THERMAL AND RADIOLYTIC PROCESSING OF ASTROPHYSICAL ICE ANALOGS

By Patrick David Tribbett

A Dissertation

Submitted in Partial Fulfillment

of the Requirements for the Degree of

Doctor of Philosophy

in Astronomy and Planetary Science

Northern Arizona University

May 2023

Approved:

Mark J. Loeffler, Ph.D., Chair

William M. Grundy, Ph.D.

Daniel J. Matthew, Ph.D.

Tyler D. Robinson, Ph.D.

Stephen C. Tegler, Ph.D.

ABSTRACT

THERMAL AND RADIOLYTIC PROCESSING OF

ASTROPHYSICAL ICE ANALOGS

PATRICK DAVID TRIBBETT

Volatile molecules (water (H_2O), carbon dioxide (CO_2), methane (CH_4), hydrogen sulfide (H_2S), etc.) present in astrophysical environments condense as ices onto surfaces as large as planetary bodies, and as small as interstellar dust grains. Once condensed, these ices are exposed to both ionizing radiation and thermal processing, which alters their chemical history. To understand the distribution of molecular ices in the solar system and the interstellar medium (ISM), determine reaction pathways to complex molecules in the condensed phase, and interpret spectral data from observational, mission, and modeling studies, it is fundamental to describe the processes that alter molecular ices at low temperatures and pressures.

Here I present experimental studies characterizing these astrophysically-relevant ices and several of the radiolytic and thermal processes that alter these ices. Experiments are performed in a new ultra-high vacuum chamber in the Processes Environments and Astrochemistry on Extraterrestrial Surfaces (PEAXS) Laboratory at Northern Arizona University (NAU), which was constructed in partial fulfillment of this dissertation.

Charged particle bombardment of H_2O ice surfaces simultaneously produces radiolytic products and sputters material, providing source material for the tenuous atmospheres around icy satellites, including Europa. We measure the total sputtering yield, or number of ejected molecules per incident ion, for low energy argon ions, analogous to the cold, heavy ion population within the magnetosphere of Jupiter, at temperatures relevant to Europa. We find that current theoretical sputtering models over predict our empirical radiolytic oxygen sputtering yields, and consequently the contribution of sputtered molecular oxygen (O_2) due to the cold, heavy magnetospheric ions that irradiate Europa.

The observational absence of the stable low temperature phase of H_2O ice, microporous amorphous solid water (ASW), in the outer solar system and ISM is surprising given that temperatures should favor the formation of microporous ASW during ambient condensation. However, we demonstrate that energetic electrons efficiently compact amorphous ice, destroying porosity and internal surface area. We find that microporous ASW should only be expected in the youngest ices in interstellar molecular clouds. To enable future detection of microporous ASW using the James Webb Space Telescope (JWST), we identify several new near-infrared (NIR) features indicative of microporous ASW and demonstrate how they may also probe,

the currently elusive homonuclear molecules.

Thermally-driven chemical reactions within astrophysical ices receive significantly less attention than radiation-driven chemistry due to the low temperatures and minimal diffusion associated with astrophysical ices. However, we find several instances of thermally-driven oxidation reactions that occur at temperatures as low as 70 K. We demonstrate that a reaction occurs in ice mixtures of H_2S, ozone (O_3), and H_2O producing sulfur dioxide (SO_2), sulfur anions, and O_2 at low temperatures, and hydrated sulfuric acid at high temperatures. This reaction is consistent with the observed hemispheric separation of sulfur species and radiolytically-produced oxidants on the Jovian satellites. We also demonstrate that a reaction occurs within ammonia (NH_3), O_3, and H_2O ice mixtures that produces the nitrate ion, which is thermally stable as ammonium nitrate salt at high temperatures. Ammonium nitrate exhibits several NIR spectral features that may be consistent with the observed 2 μm features on several icy solar system worlds, including Charon, Miranda, and Enceladus.

Copyright

Published Works

The following copyright statements apply to each respective published manuscript.

Chapter 3 – Manuscript I
The Sputtering of Radiolytic O_2 in Ion Irradiated H_2O-ice

Chapter 4 – Manuscript II
Titan in Transit: Ultraviolet Stellar Occultations Reveal Complex Atmospheric Structure

Chapter 6 – Manuscript III
Probing Microporous ASW with Near-infrared Spectroscopy: Implications for JWST's NIRSpec

Chapter 7 – Manuscript IV
Thermal Reactions between H_2S and O_3: Implications for Europa Surface Chemistry

Acknowledgements

Note: Manuscript-specific acknowledgements are found at the end of each corresponding chapter.

Indigenous Land Acknowledgement

I completed all work presented within this dissertation at NAU in Flagstaff Arizona. NAU sits at the base of the San Francisco Peaks, on homelands sacred to Native Americans throughout the region. We honor their past, present, and future generations, who have lived here for millennia and will forever call this place home.

Individuals and Groups

I am grateful for all of the support that I have received from family, friends, colleagues, and mentors. I appreciate you more than you know, and I could not have completed this Ph.D. without you.

I thank my partner, Cady, for your unwavering support and encouragement, and your willingness to proofread even the roughest of written drafts.

I thank my family for reminding me that perseverance triumphs. I thank my mom Lisa and dad David for their support, regardless of what I wanted to do when I grew up. I thank my sisters, Sydney, Maddy, and Olivia, who keep me young at heart. I am so grateful that NAU's location in Flagstaff, AZ enabled me to visit you often, and for our family dinners. I thank my Arkansas family, uncle Marcus, aunt JC, and Sierra. Thank you for the years of laughter, conversations, pop culture education, and ice cream socials. I thank my Costa Rica family, aunt Julie, Alysha, and Adam. Thank you for the adventures, both tropical and airport related, and providing me an example of what true work/life balance looks like. I thank my grandparents: Mimi, Pamp, and Grandma and Grandpa Nelson. A special thanks to Pamp — thank you for helping me find NAU Astronomy and Planetary Science and for the weekly phone calls during my first year in Flagstaff. I thank the entire Tribbett, Nelson, Barter, and DePoy families. Also, thank you to the Patcher family, Paul, Shelley, Nick, and Sam, for the great food and company. Lastly, I thank Emily Tribbett — you have listened to more presentations than you can count.

I thank all of the advisors, mentors, and teachers that have guided me through my academic career. I

thank my advisor, Mark, for all of the professional advise. I could not have asked for a more patient or kind mentor. I thank my committee members, Will, Dan, Ty, and Steve for all of the fruitful discussions and your collective guidance. I thank my previous advisors, Jonathan Merten and Ross Carroll for your continued support. Lastly, a special thanks to all of the PEAXS Lab members, past and present, Robyn, Ryleigh, Beau, Mitch, Becks, and Nicole. You have made the laboratory a wonderful and special place to work.

I thank all of the friends that I have made during my time in Flagstaff. Thank you to all of my fellow Department of Astronomy and Planetary Science classmates who created a collaborative and enjoyable learning environment. Thank you Christian, Chris, Anna, Audrey, and Diego for all of the culinary adventures. Thank you James and Andy for showing me all of my favorite Northern Arizona mountain biking trails. Thank you Colin for this LaTeX template. I thank all of my old friends who have continued to check in on me. Thank you Cody, Sam, Colin H., Colin R., Morgan, Jacob, Josh, and Gracie.

Funding

This research was supported in part by National Science Foundation (NSF) Grant # 1821919 and National Aeronautics and Space Agency (NASA) Astrophysics Research and Analysis (APRA) #80NSSC20K0359.

Contents

List of Tables

List of Figures

Dedication

This dissertation is dedicated to Paul Everett Tribbett and Sherman Burnell Nelson.

Preface

This dissertation contains chapters have been written to appear in peer-reviewed scientific journals as standalone pieces of literature. Redundancy in text is a result of reformatting to conform to University formatting requirements. References have been consolidated into a unified bibliography that appears at the end of this dissertation. Please note that Chapter 5 contains my contribution to the published work in Behr *et al.* 2020, not the full manuscript.

The following chapters have already been published:

Chapter 3 – Manuscript I: "The Sputtering of Radiolytic O_2 in Ion Irradiated H_2O-ice" (Tribbett and Loeffler 2021)

Chapter 4 – Manuscript II: "Titan in Transit: Ultraviolet Stellar Occultations Reveal Complex Atmospheric Structure" (Tribbett *et al.* 2021)

Chapter 6 – Manuscript III: "Probing Microporous ASW with Near-infrared Spectroscopy: Implications for JWST's NIRSpec" (Tribbett *et al.* 2021)

Chapter 7 – Manuscript VI: "Thermal Reactions between H_2S and O_3: Implications for Europa Surface Chemistry" (Tribbett and Loeffler 2022)

The remaining chapters will be submitted to the American Astronomical Society journals for publication as soon as possible:

Chapter 8 – Manuscript V: "Thermal Reactions between NH_3 and O_3: Salt Formation Mechanism"

Chapter 1

Introduction

Volatile molecules can condense onto the surfaces of astrophysical objects as large as planets and as small as interstellar dust grains. For example, water (H_2O) ice has been detected on the surface or in the atmosphere of nearly every planetary body in the Solar System (Schmitt et al., 1998). These detections include incredibly dry objects like Mercury and the Moon, which may have H_2O within permanently shadowed craters or buried at depth (Harcke, 2005; Spudis et al., 2013), and the possibly oceanic moons of Jupiter and Saturn (Fink et al., 1973; Fink & Larson, 1975). H_2O ice is by far the most abundant condensed volatile in the universe; however, it is not alone. Many other volatile molecules have been detected within the solid-phase both in the outer solar system, and the interstellar medium (ISM). These molecules include but are not limited to carbon monoxide (CO), carbon dioxide (CO_2), methane (CH_4), ammonia (NH_3), sulfur dioxide (SO_2), and hydrogen sulfide (H_2S). Decades of astronomical observations provide spectroscopic evidence for the presence of these ices through fingerprint spectral[1] features within the infrared (0.8 - 10 μm) and ultraviolet-visible (0.2 - 0.7 μm) wavelengths, though the observing geometry differs for solar system objects (reflected and/or thermal light) and the ISM (transmitted light). A slightly more comprehensive collection of solar system ices on each major planetary body is shown in Table 1.1, along with relevant spectral features. It is important to note that a majority of the known interstellar molecules have been detected in the gas phase only.[2] In fact, the number of detected ices in the ISM is dwarfed by the number of those detected within the solar system (Tielens (2005), Table 1.1). However, the number of known interstellar ices is expected to drastically increase with the recent launch of the National Aeronautics and Space Agency (NASA) James Webb Space Telescope (JWST), which has a significantly improved sensitivity and spectral resolution compared to its predecessors (Bagnasco et al., 2007).

Icy material on the surface of solar system objects and on interstellar dust grains exists in a variety of

[1] Spectral features refers to spectroscopy or the study of how light interacts with materials. Each composition of ice interacts with light differently, resulting in specific, identifiable features.

[2] Gas phase molecules can be detected from distinct rotational transitions that result in emitted or absorbed radio wavelengths. Importantly, Earth's atmosphere is transparent in the radio wavelengths.

Molecule	IR Spectral Features (μm)	ISM Detection	Planetary Object
H_2O	1.5, 1.65, 2.0, 3.1, 4.5, 12.5	Yes	Mercury[1,*], Moon[2,*], Earth[3], Mars[4], Jupiter[5], Galilean Satellites[6], Saturn's Rings[7] Saturnian Satellites[8], Uranian Satellites[9] Triton[10], Pluto[11]
CO_2	1.97, 2.01, 2.07, 2.70, 2.78, 4.25	Yes	Mars[12], Galilean Satellites[13], Saturnian Satellites[14] Uranian Satellites[9], Triton[10], Pluto[11]
CO	1.58, 2.35, 4.67	Yes	Triton[10], Pluto[11]
CH_4	1.15, 1.66, 1.72, 1.79, 2.2, 3.44, 3.55	Yes	Triton[10], Pluto[11]
NH_3	2.05 2.27, 2.98, 6.13, 9.17	Yes	Saturnian Satellites[15], Uranian Satellites[16], Pluto[11]
H_2S	3.92	No	Galilean Satellites(?)[13]
SO_2	0.2 - 0.33, 4.05, 7.5, 8.7	Yes	Galilean Satellites[13]
H_2O_2	3.5	No	Europa[17]
O_3	0.2 - 0.31, 9.67	No	Ganymede[18], Rhea[19], Dione[19]

Table 1.1: Common solar system ices and their key near- and mid-infrared spectral features. *Indirect detections based on radar bright spot near 3 and 4 cm.[1]Harcke (2005). [2]Spudis et al. (2013). [3] Flagstaff, AZ receives over 100 inches of snowfall (or H_2O ice) per year. [4]Singer et al. (1979); Vincendon et al. (2010). [5]Simon-Miller et al. (2000). [6]Fink et al. (1973); Fink & Larson (1975). [7]Fink & Larson (1975). [8]Fink et al. (1976); Cruikshank et al. (1977). [9]Grundy et al. (2006).[10]Cruikshank et al. (1998). [11]Grundy et al. (2016). [12]Calvin & Martin (1994). [13]McCord et al. (1998). [14]Cruikshank et al. (2010). [15]Emery et al. (2005). [16]Cartwright et al. (2020). [17]Hand & Brown (2013). [18]Noll et al. (1996). [19]Noll et al. (1997)

different environments (Table 1.1). For example, interstellar ices exist in dense, cold molecular clouds at temperatures as low as 10 K (Caselli & Ceccarelli, 2012) and are bombarded with ionizing radiation, both in the form of energetic particles (largely protons and secondary electrons, Webber & Yushak (1983)) and ultraviolet photons (Prasad & Tarafdar, 1983). H_2O ice on the surface of Europa experiences significantly warmer temperatures (80 - 130 K; Spencer et al. (1999)) and a distinct radiation environment due to Jupiter's magnetosphere and influences from the volcanos on the nearby moon Io (Cooper et al., 2001). These different environments alter ices through thermal and radiation processing to varying degrees, and result in changes in physical structure, chemistry or the formation of different molecules, and in the optical properties of the icy material. Even H_2O ice, which is incredibly common and considerably less complex than an organic molecule like glycine ($C_2H_6NO_2$), simultaneously experiences structural changes like compaction and amorphization (i.e. loss of crystalline structure), the formation of new molecules through radiolysis (H_2, O_2, H_2O_2), and the sputtering or ejection of material, all of which is temperature dependent and drastically alters the observable optical properties of the H_2O ice. Understanding these alterations due to thermal and radiation processing is required to interpret the spectral data acquired during observational campaigns, missions, and modeling studies. The interpretation of remote sensing data enables astronomers to address scientific questions regarding the distribution of molecular ices in the solar system and the ISM.

Laboratory measurements and techniques directly probe the thermal and radiation-driven alteration of icy surfaces and how these processes affect the observable properties of the ices. Typically, these techniques deposit thin film (e.g. thicknesses of $\sim$ 0.1 - 2 μm)[3] ice samples under ultra high vacuum (UHV) conditions, and expose these samples to varying radiation and thermal environments (Schmitt et al., 1998; Baragiola et al., 2002). To analyze the samples before, during and after thermal and radiation alteration, these studies typically use analytical tools with astronomical analogs, like multi-wavelength range spectroscopy, or tools that illustrate interactions between light and material. For example, laboratory infrared (IR) spectra show molecular bonds present within an ice sample and consequently can probe the thermal- and radiation-induced synthesis of new molecules, while providing tools for astronomical detection (e.g. new IR bands) and methods for quantification (e.g. band strengths). Identification of new, resultant molecules, indicative of a specific alteration processing, provides information that informs the distribution of molecular ices in both the solar system and the ISM.

Often times additional analysis of laboratory spectral measurements is required to extract all possible information out of laboratory studies. For example, Teolis et al. (2007b) demonstrated that reflectance geometry spectral measurements can be modeled following the Fresnel equations for specular reflectance and that these model calculations are required to extract important ice properties (e.g. thickness, density, etc.)

[3]A human hair is approximately 50 μm thick or at least 25x thicker than a vapor deposited thin film.

due to thin film interference effects. Experimental studies have incorporated these models (Raut et al., 2007b, 2008); however, many of these works use fairly crude methods for both fitting data with spectral models, and error representation. Some studies have demonstrated a more sophisticated analysis of laboratory data, with a particular emphasis on the calculation of optical constants (Gerakines & Hudson, 2020); however, there remains room for laboratory work to continue to incorporate novel statistical methods to fit spectral data with physical models and extract relevant parameters.

This dissertation provides both laboratory and model-driven studies that encompass a diverse range of astrochemical topics related to both the radiolytic and thermal processing of interstellar and solar system ice analogs. Chapter 2 details the specifications of a new UHV chamber constructed in the Processes Environments and Astrochemistry on Extraterrestrial Surfaces (PEAXS) Laboratory at Northern Arizona University (NAU). Chapter 3 and 5 demonstrate the physical and chemical alteration of ices due to radiation, typical of specific astrophysical environments, and quantify the rates of these processes, which is crucial to explain observations of these environments. Chapter 6, 7, and 8 demonstrate the physical and chemical alteration of ices due to thermal processes, and highlight the importance of ice temperature. Despite being consistently overlooked within astronomical literature, thermally-driven reactions result in chemical products that are consistent with molecular distributions throughout the solar system. Additionally, this dissertation demonstrates the utility of incorporating sophisticated statistical analyses, derived from other disciplines of astronomy and planetary science, into the analysis of laboratory data. Chapter 4 shows a traditional example of Bayesian Inference applied to an atmospheric chemistry and structure problem in planetary science, and Chapter 5 adapts this technique to laboratory astrophysics. Finally, implications of these studies and potential avenues for future work are discussed in Chapter 9.

Chapter 2

Methods and Materials

2.1 Experimental Setup

Under the guidance of Mark Loeffler, I constructed the ultra high vacuum (UHV) chamber employed throughout the remaining chapters to produce, alter, and analyze thin film astrophysical ice analogs as a part of this dissertation work. Here, I present a comprehensive description of each component of the UHV chamber system, all modifications, calibrations, and the analytical techniques and procedures used in the subsequent chapters.

2.1.1 Ultrahigh Vacuum Chamber

The base system is a custom-made stainless steel (Standard 304SS Material) vacuum chamber made by Nor Cal Products (Figure 2.1). A schematic of the UHV chamber along the polar angle 0° is shown in Figure 2.2. The chamber possesses 25 conflat ports: four 6" diameter ports, seventeen 2.75" diameter ports, four 1.33" diameter ports. The ports are located at 0°, 60°, 90°, 120°, and 180° polar angles and between 0 - 360° azimuthal angles. The base chamber pressure is $\sim 1 \times 10^{-8}$ Torr at room temperature and $\sim 3 \times 10^{-9}$ Torr at ≤ 200 K. The pressure is expected to be approximately one order of magnitude lower within the thermal-radiation shield surrounding the sample and sample holder (shown in Figure 2.5). A differential pumping system maintains the chamber base pressure. This system includes a IDP-7 Dry Scroll Vacuum Pump by Agilent Technologies (10^{-1} - 10^{-2} Torr) and a TwisTorr 304 FS turbo pump by Agilent Technologies (10^{-8} Torr). The improved pressure at the sample surface occurs due to the cold-trapping, or cryogenic pumping of the substrate and the thermal radiation shield. A UHV ionization gauge and Terranova Model 934 Wide Range Vacuum Gauge Controller continually monitors the chamber pressure.

An Advanced Research Systems closed cycle Helium cryostat cools the sample, and the temperature is monitored with a Lakeshore Model 335 temperature controller. The working temperature range is $\sim 5 - 320$ K, which is limited by the thermal-radiation shield modifications required for our analytical tools, and

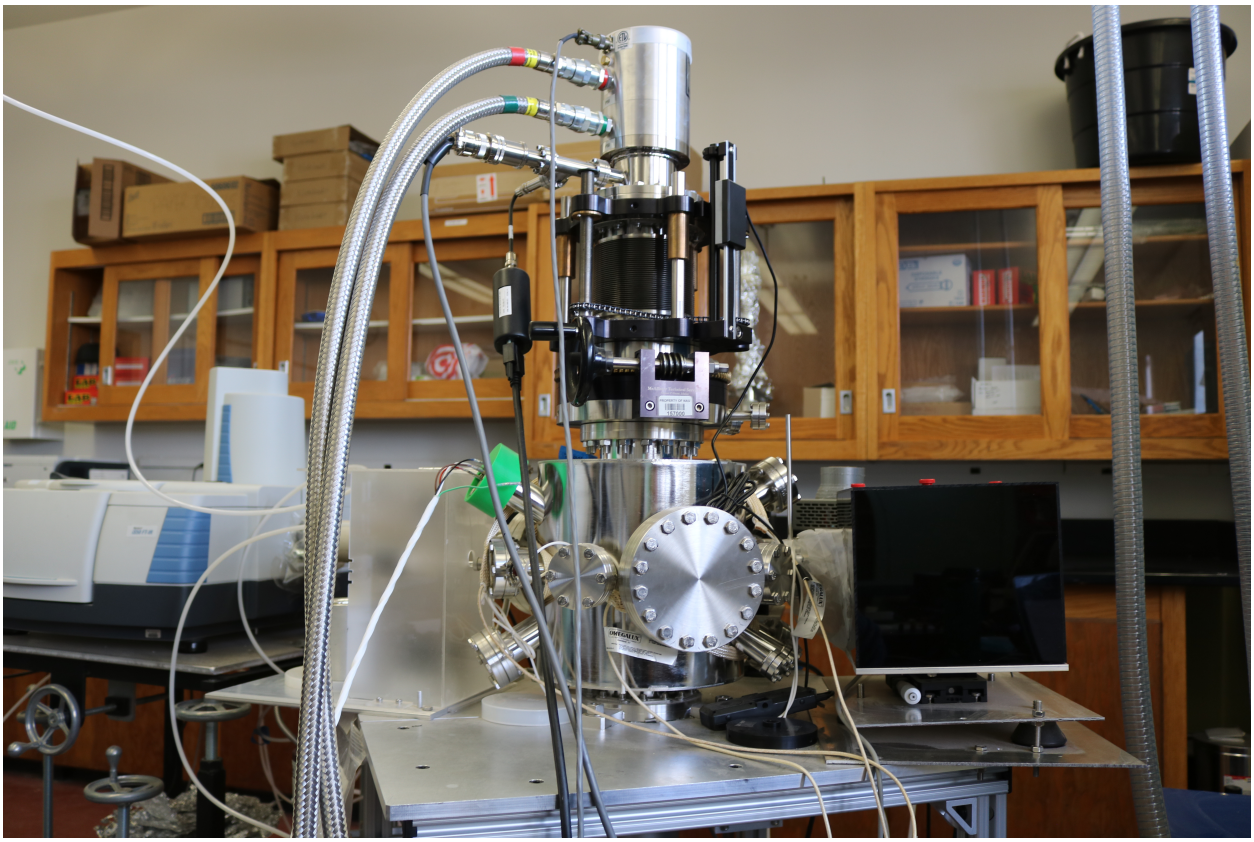

Figure 2.1: UHV chamber located in the Processes Environments and Astrochemistry on Extraterrestrial Surfaces (PEAXS) laboratory at Northern Arizona University (NAU).

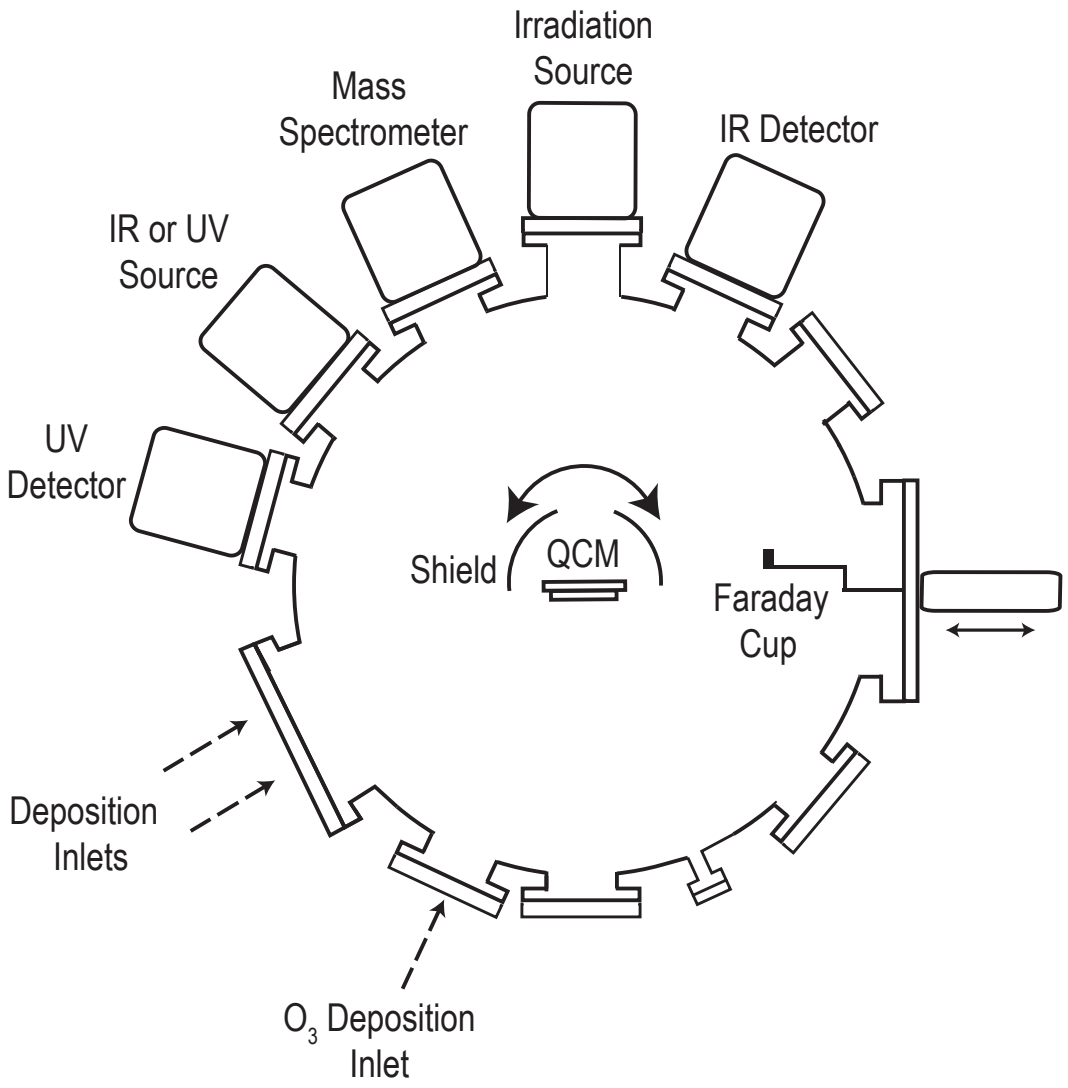

Figure 2.2: UHV chamber schematic showing the port inlets along the 0° polar angle and the corresponding analytical tools.

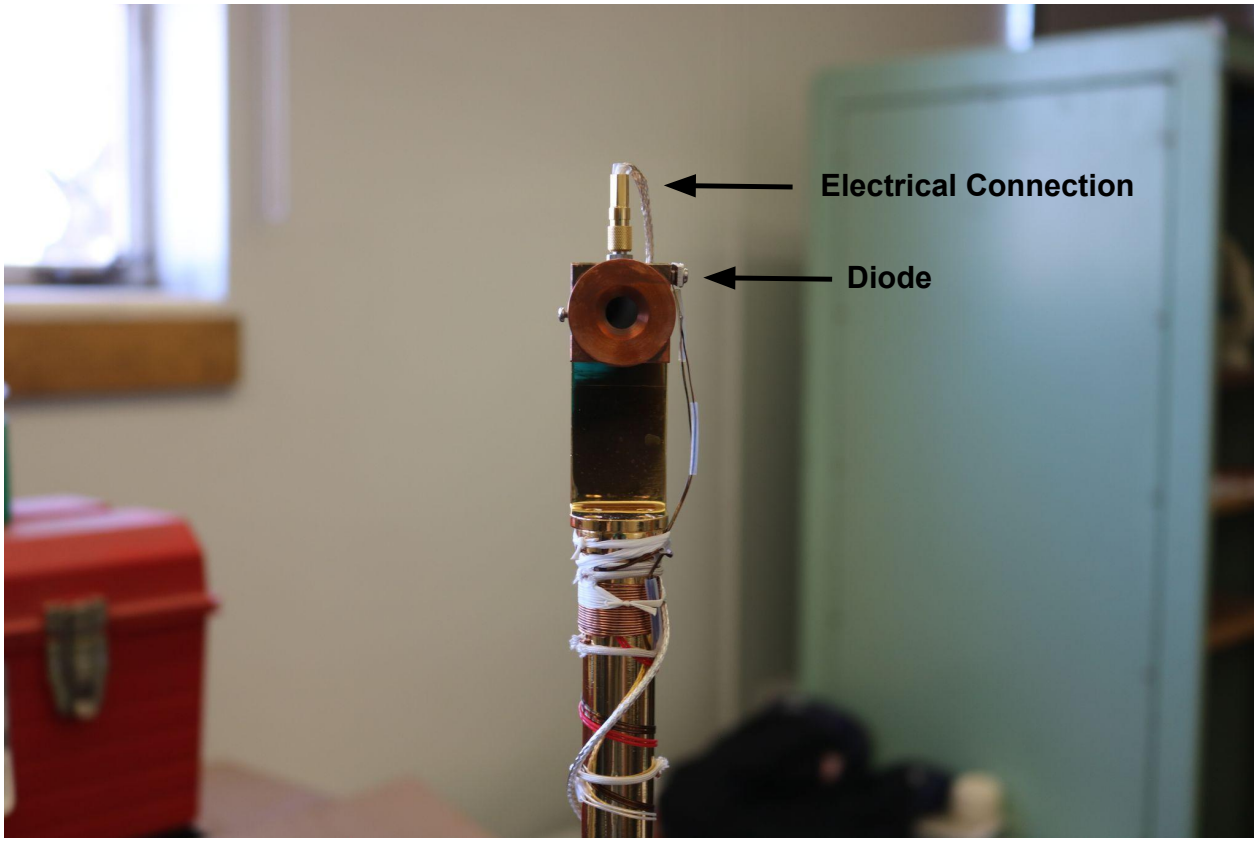

Figure 2.3: The cold finger (copper rod) and the copper block responsible for holding the quartz crystal microbalance (QCM) reflective gold substrate. Note the temperature diode attached to the right hand side of the copper block (labeled on figure). The remainder of the cold finger is attached to the cold head, which can be more easily seen in Figure 2.1 at the top of the UHV chamber.

the Indium used to improve thermal contact along the cooling stage, respectively.[1] Two diodes measure the temperature along the cooling stage: one diode is on the copper block sample holder, and one diode is further up the cooling stage closer to the cold head (Figure 2.3). Because the second diode is closer to the cold head, the temperatures of the diodes are typically offset. This temperature offset varies with temperature: the offset is nonlinear and larger at low temperatures. For temperatures $\geq$ 50K, typical of a vast majority of experiments shown throughout this dissertation, the offset is approximately 0.5 - 0.7 K. The diodes were calibrated using the temperature of liquid molecular nitrogen (N_2), which we measured to be 75.250 K. Compared to the temperature of liquid N_2 in Flagstaff, Arizona, calculated using Clausius-Clapeyron Equation, 75.30904 K (Meier, 2019), the absolute error of our sample holder diode is $\sim 0.078\%$.

The sample substrate is a highly reflective, optically flat gold mirror electrode of an Inficon IC6 QCM (Figure 2.4). The QCM substrate is mounted on the copper block, and is in thermal contact with the cooling

[1]Indium is an incredibly soft metal with a high thermal conductivity and acts a putty between copper connections within the QCM sample. This putty improves the thermal conductivity in the QCM. Indium has a low melting temperature ($\sim$ 430 K), and the QCM operating temperature range ensures that the indium does not deform.

Figure 2.4: QCM optically flat gold mirror substrate.

stage. A cylindrical thermal-radiation shield surrounds the cooling stage and sample holder minimizing sample heating due thermal-radiation from the chamber walls. To accommodate the QCM electronics, and sample exposure to the analytical tools, the thermal-radiation shield has two circular holes and two rectangular slit modifications (Figure 2.5). The sample can be rotated 360° using the McAllister Technical Services sample manipulator, which sits underneath the cryostat cold head (Figure 2.1).

2.1.2 Analysis Techniques

2.1.2.1 Infrared Spectroscopy

I acquired all infrared (IR) data presented in this dissertation using a Thermo Scientific Nicolet iS-50 Fourier Transform Infrared Spectrometer (FTIR) light source (Figure 2.6), external optics, and a Mercury Cadmium Telluride (MCT/A) detector. Figure 2.7 shows the internal components of the FTIR. Light from either an IR (10,000 - 650 cm^{-1}) or a near-infrared (NIR) source, also called the white light source, (11,500 - 2000 cm^{-1}) is collimated using an off-axis parabolic (OAP) mirror toward the interferometer through the XT-KBr beamsplitter (Thermo Scientific proprietary material, 11,000 - 350 cm^{-1}). The interferometer beamsplitter

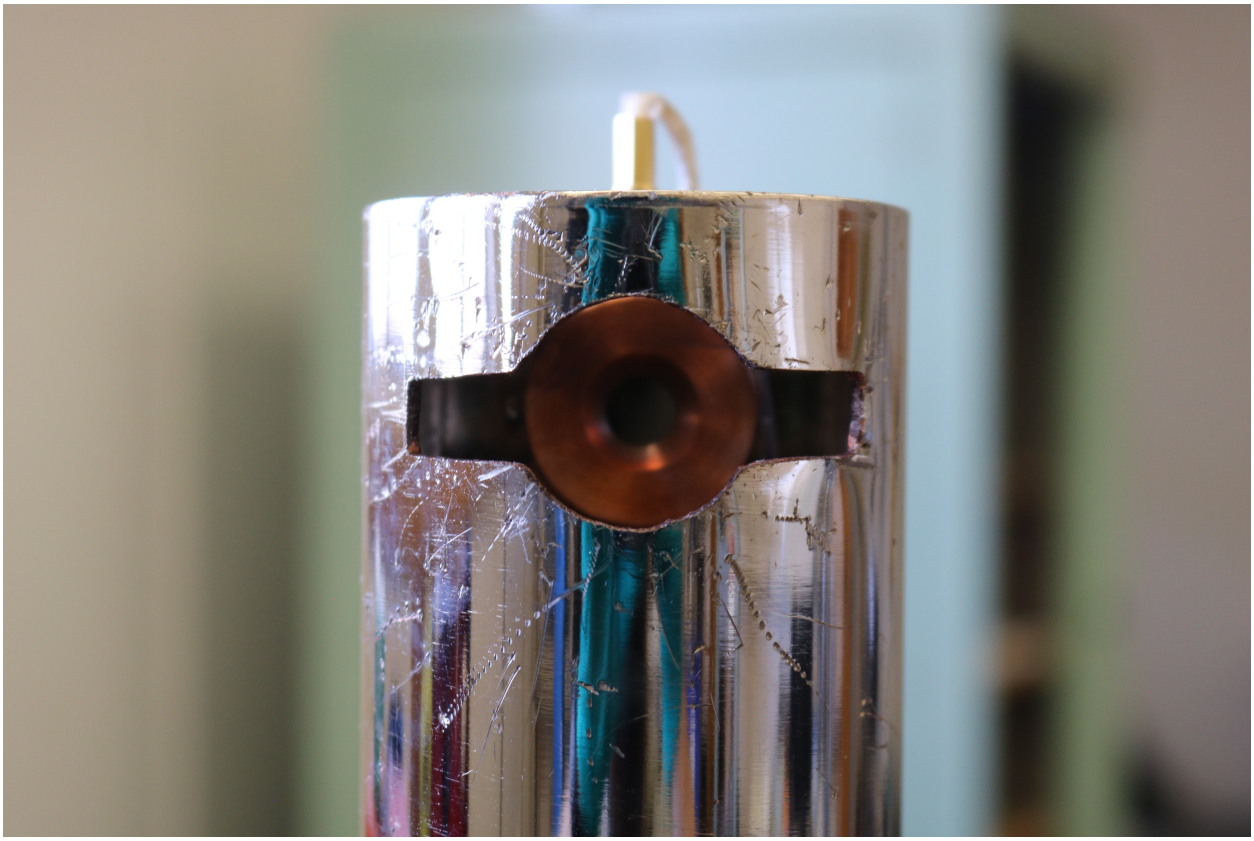

Figure 2.5: Cold finger (Figure 2.3) and QCM substrate enclosed with the thermal-radiation shield. The machined holes in the thermal-radiation shield are required for any remote sensing techniques and to allow space of the necessary QCM electronics (top).

Figure 2.6: Thermo Scientific Nicolet iS-50 FTIR used for all IR experiments throughout this dissertation. The light source can be directed through external port on either side of the FTIR, which are roughly enclosed with the 4" diameter polyvinyl chloride (PVC) pipes. These two ports enable usage for both UHV ice chambers in the PEAXS laboratory. The PVC pipe exiting toward the right is the beam path toward the UHV chamber constructed for the work described in this dissertation.

sends one beam toward a moving mirror and the second beam toward a stationary mirror. The resultant, combined beam, or interferogram exits the external FTIR port, toward the external optics.

The external optics direct the light toward the sample and substrate, and direct the reflected light from the sample and substrate to the MCT/A. Figure 2.8 shows the external optics prior to interaction with the sample and substrate. Note that both sets of external optics are enclosed in handmade acrylic plastic boxes connected to the dry air purge system (discussed below). These acrylic boxes isolate the sensitive optics from dust, and stray light, and maintain the dry air purge along the entire IR and NIR beam paths. After exiting the FTIR, the light is reflected 90° and focused onto the sample and substrate using an 14" OAP mirror. The angle of incidence is 37.5° relative to the gold substrate normal. The beam spot diameter on the sample is approximately 5 - 6 mm. Specularly reflected light (37.5°) from the sample and substrate is redirected 90° using an 14" OAP mirror toward 2" OAP mirror, which directs the reflected light another 90° and focuses the light on the MCT/A detector (Figure 2.9). The chamber port windows that the light passes through are

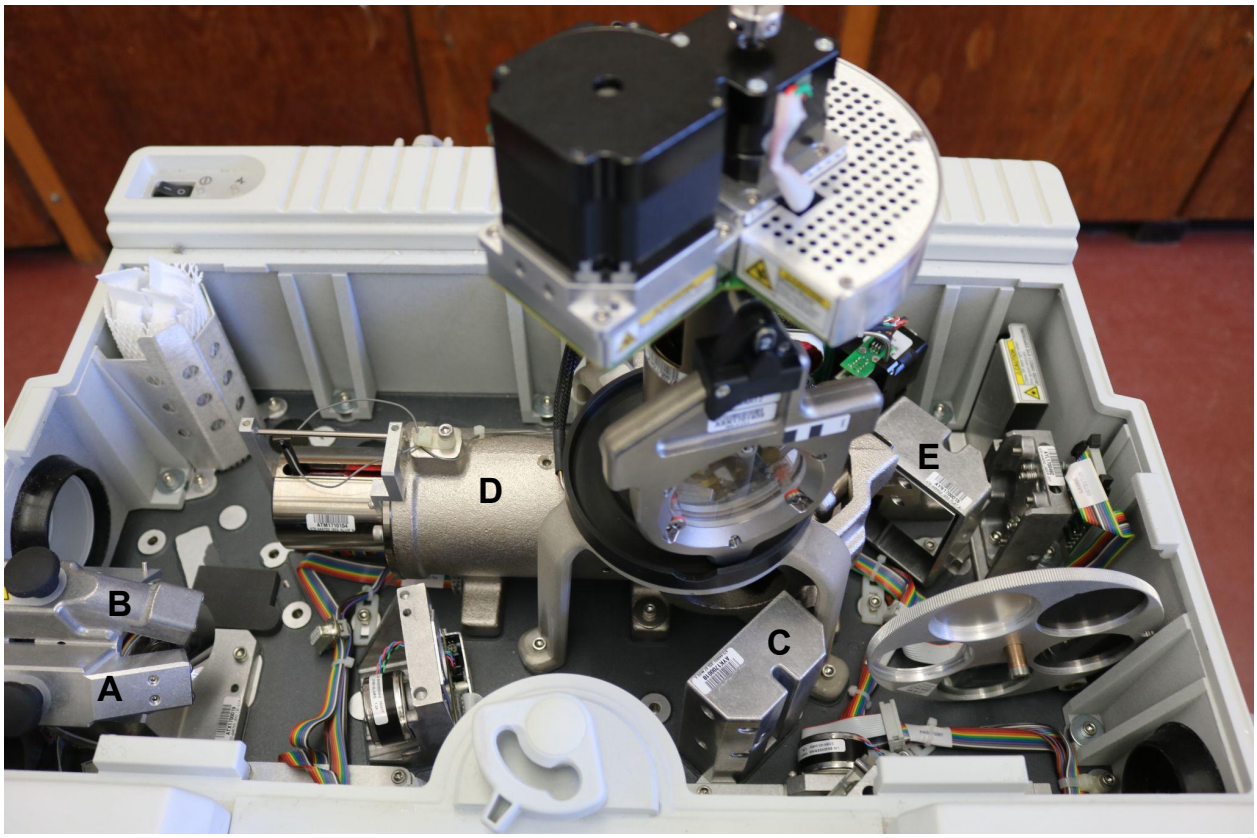

Figure 2.7: The internal components of the Thermo Scientific Nicolet iS-50 FTIR with the automatic beamsplitter exchange (ABX) system installed. (A) IR beam source. (B) White light beam source. (C) OAP mirror. (D) Interferometer. (E) OAP mirror. Note that the beamsplitter is hidden below the ABX system, which is directed out of the page, and the passport mirror is slightly out of frame below the (C) mirror.

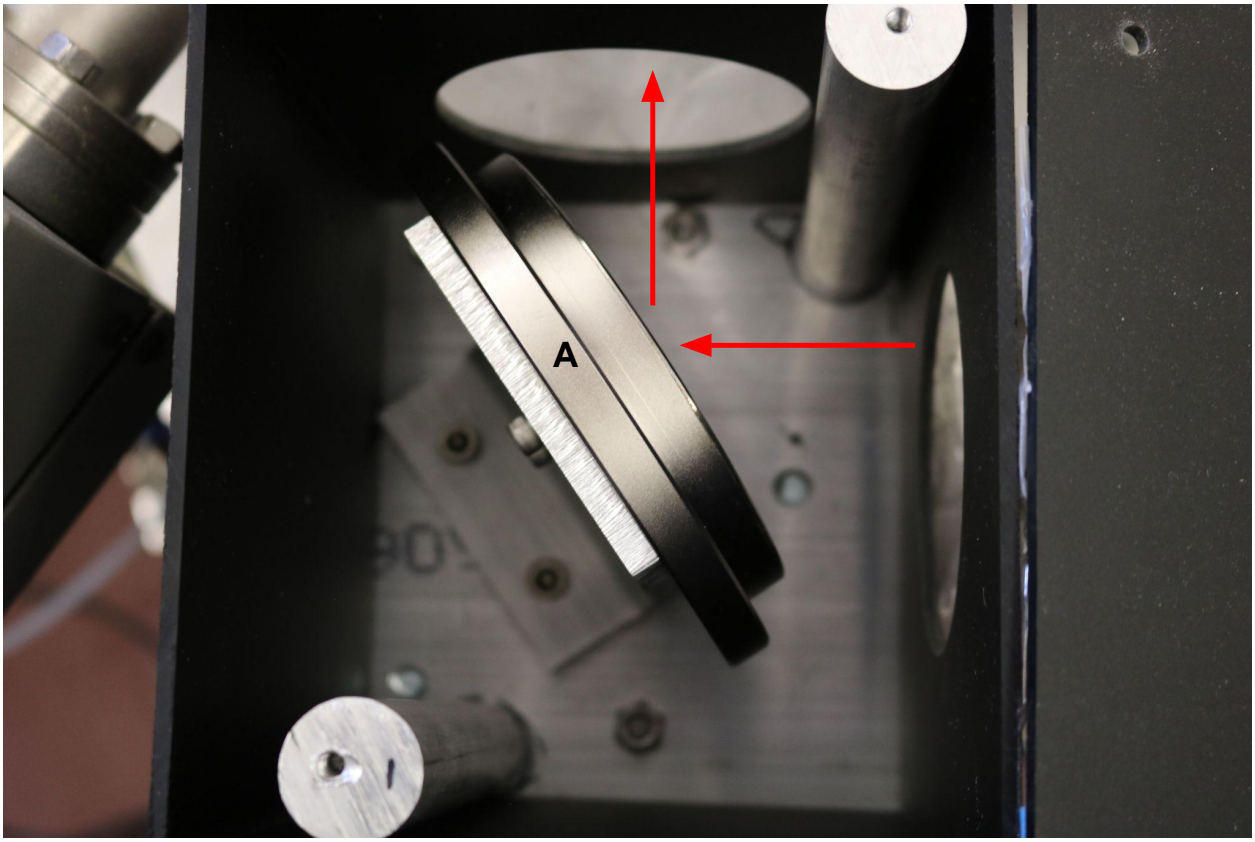

Figure 2.8: External optics that direct the light exiting the FTIR toward the sample within the UHV chamber. Light enters from the right, and is reflected off the OAP mirror toward the sample. The beam path is denoted with red arrows.

KBr. Liquid N_2 cools the MCT/A detector. The MCT/A reads the interferogram and the native software, Omnic, converts the reflected intensity into a wavelength-dependent spectrum. For overnight experiments (isothermal annealing experiments), I added liquid N_2 to the MCT/A every 8 - 10 hours. The entire beam path is purged continuously using dry air from a Parker Balston Model 75-62 Dry Air Compressor. This purge removes most of the IR spectral features due atmospheric carbon dioxide (CO_2) and water (H_2O) vapor from the final reflected light spectra.

I acquired all IR spectra as reflected intensity (arbitrary units), and subsequently converted the spectra into units of optical depth (τ). Optical depth is determined through the following relationship:

$$\tau = -\ln\left(\frac{R}{R_0}\right) \tag{2.1}$$

where R is the reflectance intensity from the sample, and R_0 is the reflectance intensity from the bare gold substrate. Figure 2.10 shows a raw reflectance spectrum of the gold substrate, the gold substrate with a deposited H_2O-ice sample, and the resultant spectrum in units of optical depth. The optical depth spectrum

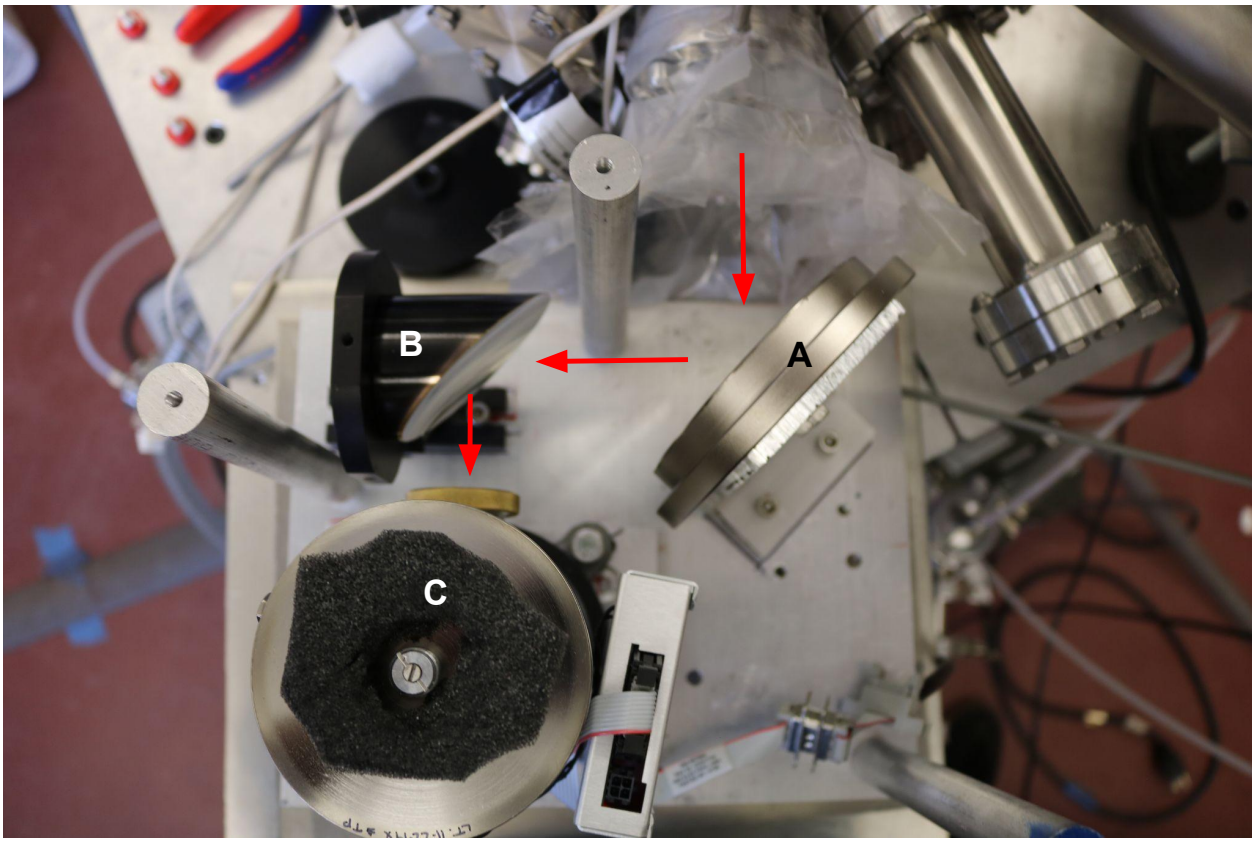

Figure 2.9: External optics that direct the interferogram toward the MCT/A detector after interacting with the sample within the UHV chamber. Light exits the chamber from the port at the top of the image and is reflected 90° from the OAP mirror, and another OAP mirror reflects the light 90° on the MCT/A detector inlet. The beam path is denoted with red arrows.

enables easy visualization of the IR bands of interest, which are identified in the figure caption. The spectral acquisition is automated and uses the a labview script written in-house by Robyn Meier and Mark Loeffler. This script writes the QCM frequency before and after acquisition, sample diode temperature before and after acquisition, and timestamp to a text file for each spectrum acquired and saves each spectrum as the Omnic native file type (.spa). Once the experiment is completed, I convert each of the files into ascii type files (.csv) manually using another labview script written in-house by Robyn Meier and Mark Loeffler. This script converts each file into units of optical depth, given an input reference spectrum, and writes all data into a single ascii file for additional analysis. In some cases, I manually remove remove excess water vapor or atmospheric CO_2 from the spectra using a spectrum of atmospheric water vapor. I apply a background subtraction to some of the spectra shown in the remaining chapters of this dissertation either for visual clarity (5^{th} order polynomial baseline) or to integrate spectral bands (linear baseline). I wrote a python script to automate spectral band integration, which was especially important for the isothermal annealing experiments discussed below where I generated between 1300 and 1400 individual spectra. Within the script I provided integration boundaries, subtracted a linear baseline between the boundaries, and calculated the band area for each spectra, which I saved in a single ascii file for later use. This script is located on the PEAXS laboratory computers for future use.

2.1.2.2 Ultraviolet Visible Spectroscopy

I acquired all Ultraviolet-Visible (UV-Vis) measurements presented in this dissertation using an Avantes 2048XL fiber optic spectrometer, and halogen and deuterium light source (Figure 2.11). The halogen and deuterium light source, emitted along a fiber optic, is incident on the sample substrate at 37.5°, and the specular reflection is detected by the fiber optic spectrometer. The final reflectance spectra (R) shown in this dissertation are calculated by the following relationship:

$$R = \frac{I_{\lambda,s} - I_{\lambda,d}}{I_{\lambda,r} - I_{\lambda,d}} \tag{2.2}$$

where $I_{\lambda,s}$ is the intensity of light reflected by the sample and substrate, $I_{\lambda,r}$ is the intensity of light reflected by the bare gold substrate or the reference spectrum, and $I_{\lambda,d}$ is the dark signal or signal recorded when the light source is off.

2.1.2.3 Mass Spectrometry

Mass Spectrometry (MS) enables the determination of the composition of molecules ejected from the ice sample through sublimation during linear heating. I acquired all mass spectra using a Stanford Research

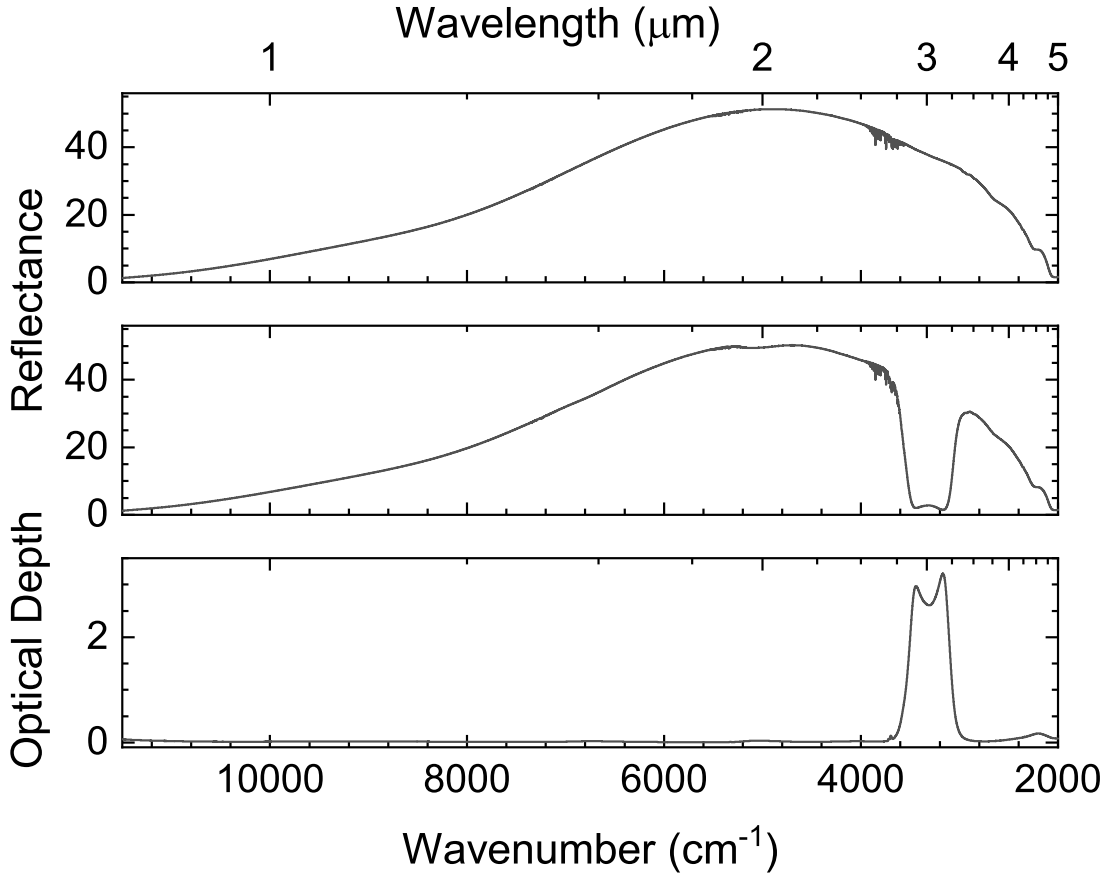

Figure 2.10: Representative infrared data required to derive an optical depth spectrum. Top: IR reflected intensity of the bare gold substrate (i.e. no ice sample present) using the white light source beam. Note the minimal atmospheric H_2O vapor absorption lines near $\sim 3\mu$m. Middle: IR reflected intensity from a representative H_2O ice sample deposited onto the gold substrate using the white light source beam. Bottom: calculated optical depth spectrum of a representative H_2O ice sample deposited onto the gold substrate using the white light source beam. The large feature around 3300 - 3000 cm^{-1} is the symmetric and asymmetric O-H stretch. Minor features are visible around 3700 cm^{-1} (O-H stretch of 3-coordinated H_2O molecules; discussed in detail in Chapter 6) and 2200 cm^{-1} (2$^{\text{nd}}$ overtone of the H_2O lattice vibration[a] or a combination bending and lattice vibration[b]). [a] Hardin & Harvey (1973); Hagen et al. (1981). [b] Giguère & Harvey (1956).

Figure 2.11: Avantes UV-Vis Spectrometer halogen (360 - 2500 nm) and deuterium (190 - 400 nm) source. Note that the wavelength range of interest for the studies does not exceed 700 nm.

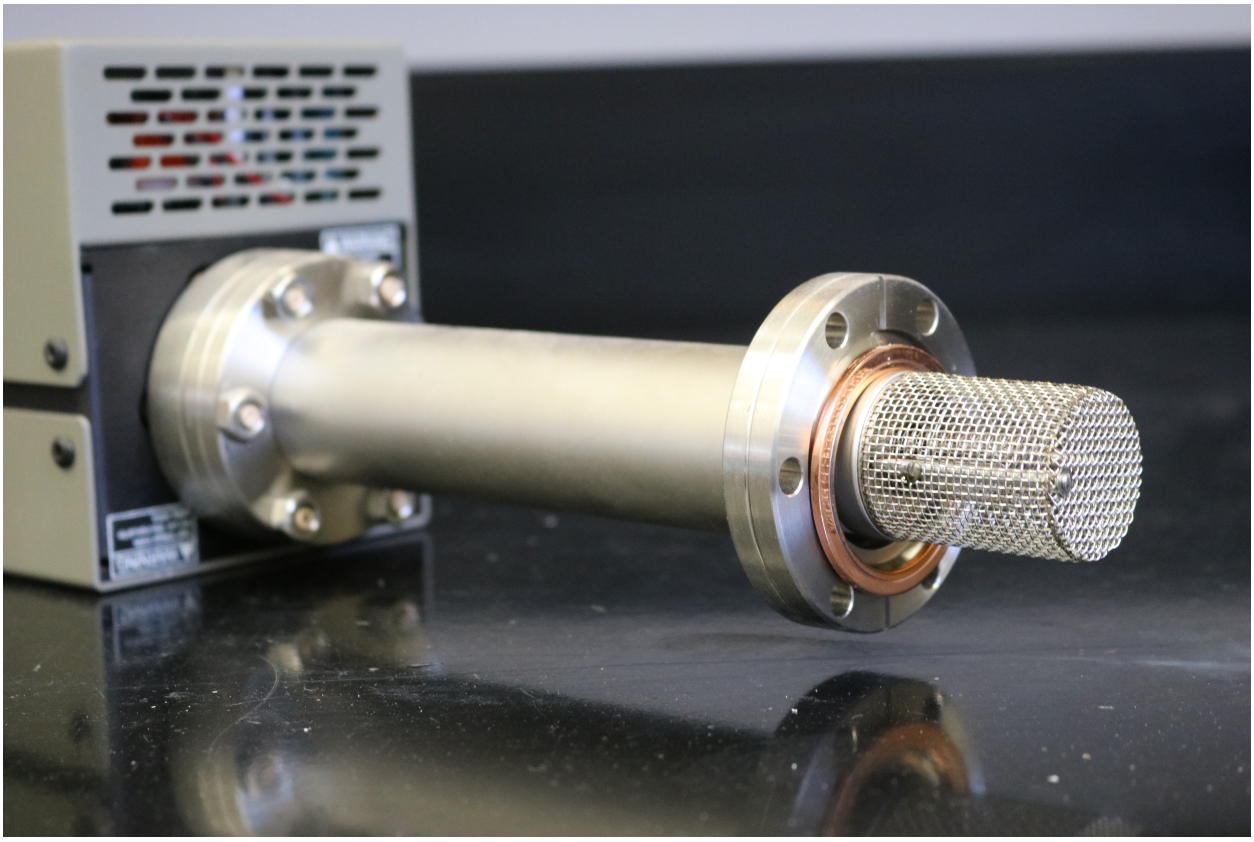

Figure 2.12: Enclosed mass spectrometer used for several studies within this dissertation work. The ionization grid is highlighted here, along with the copper gaskets required to seal the conflat UHV chamber ports.

Systems Residual Gas Analyzer (RGA-100) Quadrupole Mass Spectrometer, which is shown in Figure 2.12. The mass spectrometer operates by heating a filament to produce an electron source, which are accelerated by applying a voltage across a metal grid, resulting in electron impact ionization. Then a quadrupole mass filter separates the ionized gas based on their mass-to-charge ratio. I operated this instrument in one of two modes, analog or pressure vs. time. The analog mode monitored mass-to-charge ratios between 1 and 100 atomic mass units (amu) by individually scanning the partial pressure of each mass-to-charge ratio channel. This mode was used during initial leak testing of the UHV chamber to determine the baseline partial pressure of contaminant gases. The pressure vs. time mode enabled real-time monitoring of individual mass-to-charge ratio channels during experiments. Common mass-to-charge channels monitored include 18 (H_2O^+), and 32 (O_2^+).

2.1.2.4 Quartz Crystal Microbalance Gravimetry

As briefly mentioned in Section 2.1.1, ice samples condense onto the optically flat gold mirror electrode of an Inficon IC6 QCM. This QCM substrate enables constant monitoring of the sample areal mass, which I

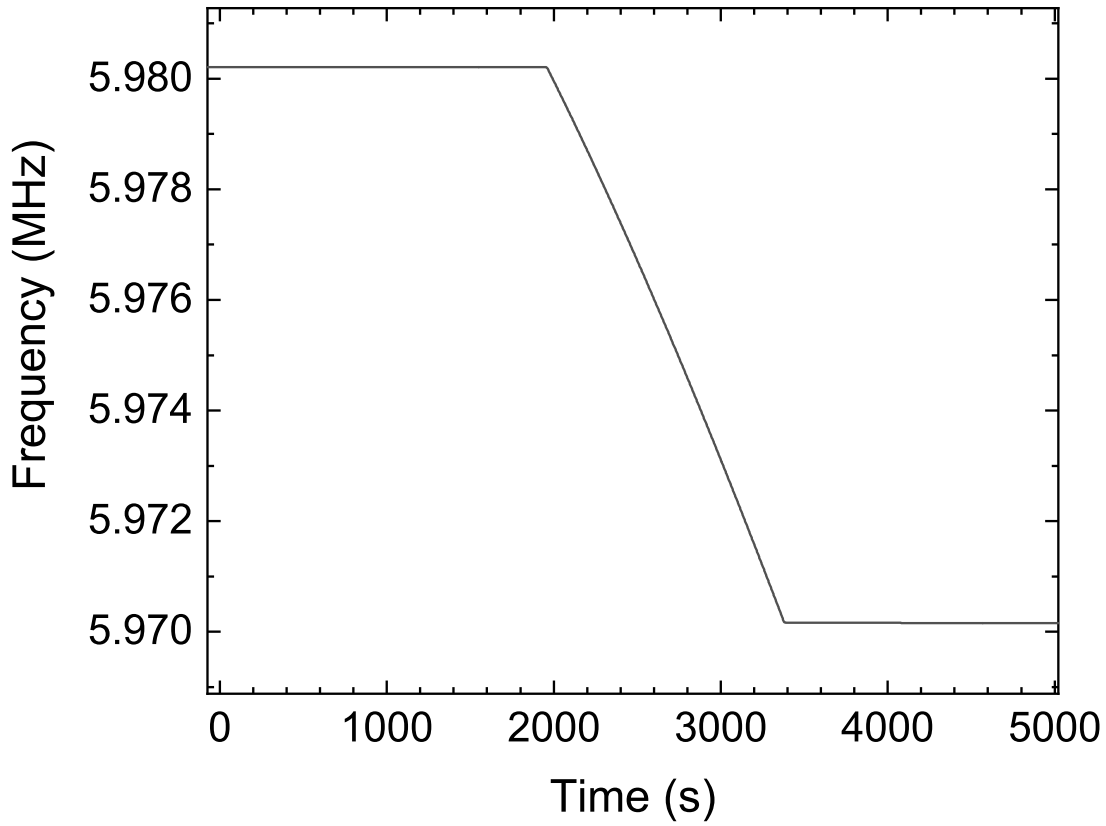

Figure 2.13: QCM frequency as a function of time during the growth of a $\sim 10,000$ Hz H_2O ice sample at 20 K. Note that the removal or sublimation of material would result in an increase in QCM frequency.

use to calculate a sample column density assuming relative concentrations, and a sample thickness assuming an ice density. The quartz crystal within the QCM is a piezoelectric material, or a material that oscillates at a resonant acoustic frequency when an electric voltage is applied across the crystal. This fundamental frequency varies slightly for each substrate but is approximately 5.879 MHz. This frequency is sensitive to the areal mass deposited onto the reflective gold substrate. As mass adsorbs or desorbs from the sample, the frequency becomes lower or higher, respectively. As a representative example, Figure 2.13 shows the quartz crystal frequency changing while depositing a pure H_2O ice sample at a constant deposition rate and constant temperature. Note that the crystal frequency also changes with temperature. Figure 2.14 shows the QCM frequency while changing the temperature of a blank sample (i.e. no deposited ice sample). This temperature dependence is consistent for an individual crystal, and allowed for the determination of sublimation during linear heating.

From the measured oscillation frequency, the change in areal mass of the sample is determined from the

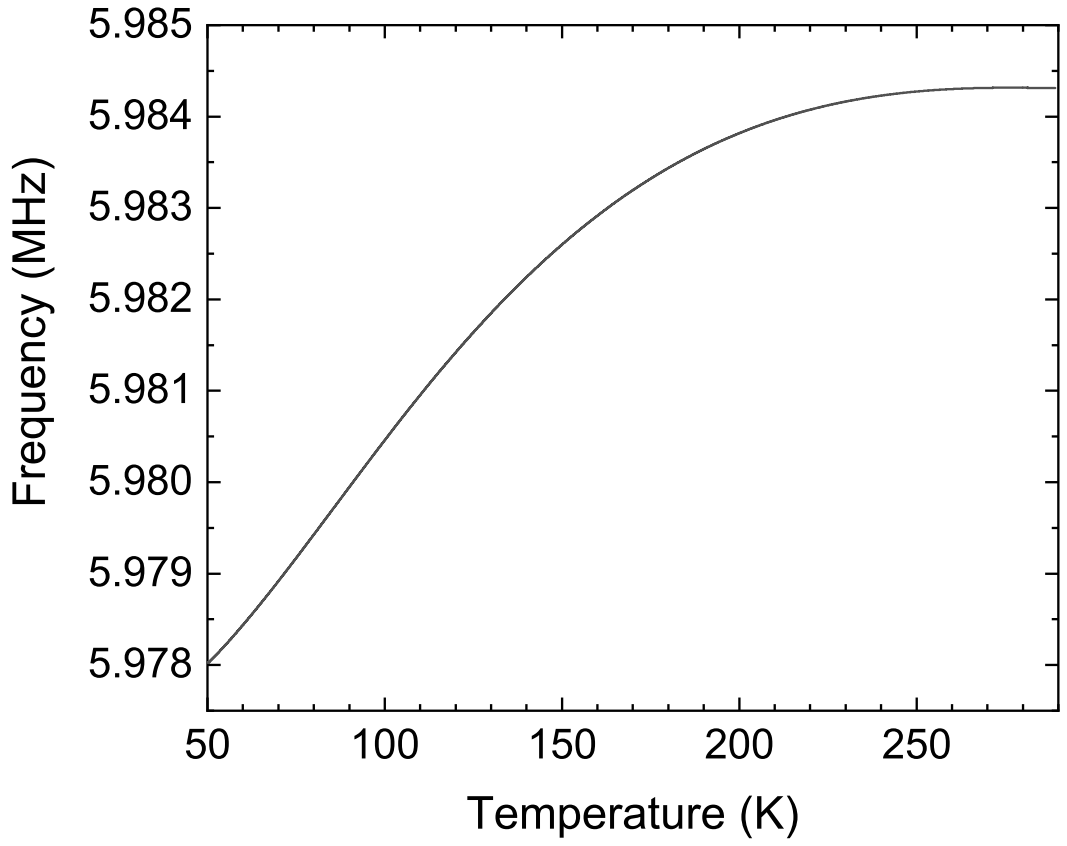

Figure 2.14: QCM frequency curve as a function of temperature for the bare gold substrate (i.e. no deposited ice sample). This curve is reproducible for a given gold substrate assuming the full sublimation of a previous sample, and is reversible with temperature.

following relationship:

$$\Delta Q = -\frac{k(f_1 - f_0)}{f_0 f_1} \tag{2.3}$$

where ΔQ is the change in areal mass, f_0 is the initial frequency of the crystal, f_1 is the final frequency of the crystal, and k is a proportionality constant, $k = 4.417 \times 10^5$ Hz g cm^{-2} (Lu & Lewis, 1972). The QCM frequency is sensitive to changes as small as 0.1 Hz or $\sim$ 1 ng cm^{-2}, which for a minimally microporous, amorphous H_2O ice sample with a density of 0.82 g cm^{-3}(Westley et al., 1998) is a column density of 4.13×10^{13} H_2O cm^{-2}.

2.1.3 Chemicals

Each section below describes the purity and supplier of each chemical used throughout these studies.

2.1.3.1 Water

Nearly all ice samples described in subsequent chapters contain H_2O. Regardless of experimental conditions and consequently, deposited ice structure, all ices are derived from high performance liquid chromatography (HPLC) grade H_2O vapors (CAS# 7732-18-5). HPLC H_2O was purchased from Sigma Aldrich (Product# 270733-1L).

2.1.3.2 Argon

We purchased ultra-high purity argon (Ar) gas (CAS# 7440-37-1), 99.998% from Matheson gas (Product# G1901175).

2.1.3.3 Methane

We purchased ultra-high purity methane (CH_4) gas (CAS# 74-82-8), 99.97% from Matheson gas (Product# G1949175).

2.1.3.4 Carbon Dioxide

We purchased CO_2 gas (CAS# 124-38-9), 99.99% chemical purity from Matheson gas (Product# G1123175).

2.1.3.5 Oxygen

We purchased ultra-high purity molecular oxygen (O_2) gas (CAS# 7782-44-7), 99.999% from Matheson gas (Product# G1979175).

2.1.3.6 Hydrogen Sulfide

We purchased 99.95% purity hydrogen sulfide (H_2S) gas (CAS# 7783-06-4) from Matheson gas (Product# G1540275).

2.1.3.7 Ammonia

We purchased 99.95% purity, anhydrous ammonia (NH_3) gas (CAS# 7664-41-7) from Matheson gas (Product# G1501275).

2.1.3.8 Nitric Acid

We purchased 15 M (i.e. conc.) nitric acid (HNO_3) (CAS# 7697-37-2), 70% v/v ACS grade reagent from Sigma Aldrich (Product# 438073). HNO_3 was required as both an ice mixture constituent, and as a cleaning

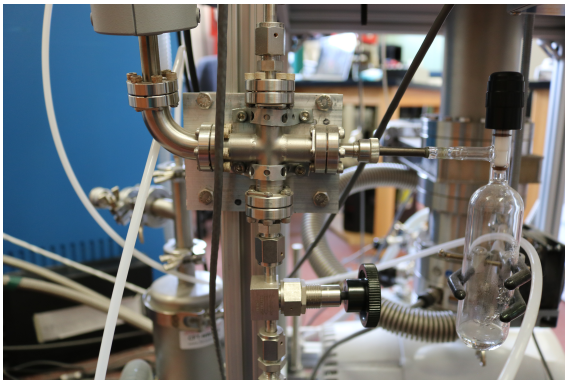

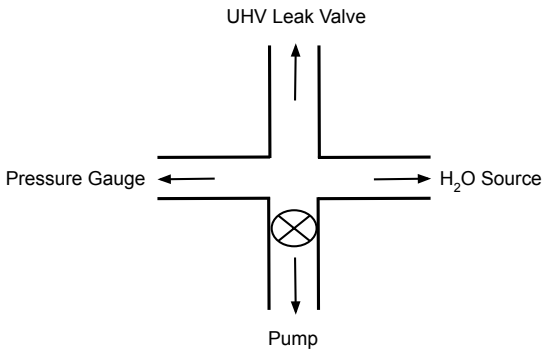

Figure 2.15: H_2O portion of the manifold system picture (left) and drawn schematic (right).

agent for all glass manifolds (H_2O and non-reactive manifolds).

2.1.3.9 Acetone

We purchased HPLC Grade, $\geq$ 99.9% purity, acetone ($(CH_3)_2CO$) (CAS# 67-64-1) from Sigma Aldrich (Product# 650501). $(CH_3)_2CO$ was used as a cleaning agent for organic soluble materials (greases, oils) and as a UHV chamber port leak testing agent, due to its high volatility/vapor pressure.

2.1.4 Gas and Vapor Manifold

The gas and vapor manifold is a single unit manifold that enables the deposition of either non-oxidizing gases or vapors. The manifold is split into two components, a H_2O vapor manifold and a "variable" gas manifold. Both sections will be described in the sections below. The entire manifold system is pumped down to $\sim 2.3 \times 10^{-2}$ Torr using a refurbished Varian SD-200 mechanical oil pump from Duniway Stockroom. This base manifold pressure is approximately an order of magnitude higher for the variable gas manifold due to the 5 L glass bulb ballast, which will be discussed in the next section. The pressure within both sections is monitored using a Baratron 626C capacitance manometer from MKS instruments. Both manifold sections are connected to the UHV chamber by a Variable Leak Valve Model 203 from MKS instruments.

2.1.4.1 H_2O Manifold

The H_2O manifold section schematic is shown in Figure 2.15. The H_2O manifold section is comprised of a 1.33" conflat port cross, bolted to a piece of aluminum, that interfaces a piece of borosilicate glassware, the capacitance manometer, the leak valve, and pumping system.

The borosilicate glassware, shown in Figure 2.16, is filled with HPLC grade H_2O. I purify the H_2O by opening the glassware stopcock and the mechanical valve to the pumping system. This process removes all

Figure 2.16: Manifold glassware containing the H_2O vapor source. The glassware is connected to the conflat cross hardware with a cajon o-ring fitting that attaches to the kovar metal tip. The H_2O vapor source is controlled using the stopcock leak valve.

excess atmosphere trapped within the H_2O. To fill the manifold with H_2O vapor, the pumping system valve is closed, and the manifold is allowed to reach an equilibrium pressure (220 - 260 mTorr). Although this equilibrium pressure is fairly consistent across experiments, the temperature of the room, pumping time, and relaxation time affect the equilibrium pressure. H_2O vapors are leaked into the UHV chamber using the quantitative leak valve. Regardless of the manifold pressure, I inject the vapor into the chamber at the same rate using a quantitative leak valve (i.e. lower manifold pressure increasingly open leak valve, and vice versa). The injection rate is proportional to the deposition rate, which is directly monitored using the QCM substrate.

2.1.4.2 Variable Gas Manifold

The variable gas manifold section schematic is shown in Figure 2.17. The manifold section structure is similar to the H_2O manifold. A 1.33" conflat port cross is bolted to a piece of aluminum interfacing the variable gas source, the capacitance manometer, the leak valve, and the pumping system.

The variable gas source is highlighted in Figure 2.18. The gas source is connected to both a variable

Figure 2.17: Variable gas portion of the manifold system picture (left) and drawn schematic (right).

gas lecture bottle from a CGA-170 or 180 lecture bottle regulator, depending on the specific gas used, and a 2 L or 5 L borosilicate glass ballast (Figure 2.19). Note that the CGA-170 and 180 regulators were used for non-corrosive and corrosive gases, respectively. Prior to the start of a series of experiments with a given gas, I incrementally leak the gas of interest into a ballast to fill the ballast and use it as the source of the gas. Using the ballast as the gas source ensures consistency across individual experiments since the volume contained a significant pressure ($\sim$ 350 mTorr) that would not substantially change over the course of the experiment. Over the course of this dissertation work, I used the ballast and "variable" gas manifold to inject CH_4, CO_2, H_2S, and NH_3 into the UHV chamber. The ballast equilibrium pressure decreases as I conduct a series of experiments with any specific gas and I compensate by increasing the leak valve opening to achieve the desired injection rate, and the deposition rate was monitored using the QCM substrate.

2.1.5 Oxidant Manifold

In addition to the water and variable gas manifold system, this dissertation work required a manifold system for oxidizing reagents. Unlike the water and variable gas manifold, the oxidant manifold system does not contain any metal components. The oxidant manifold injects vapors of interest directly into the UHV chamber using the stopcock as a leak valve. Because of the stopcock leak valve and consequently limited control, I carefully opened the stopcock to ensure that the UHV chamber pressure did not exceed 5.0×10^{-6} Torr during deposition. The QCM substrate monitors the deposition rate while I inject the oxidant. I used the oxidant manifold for two different reactants, O_3 and HNO_3, in different configurations. Regardless of configuration, the manifold was pumped down to $\sim 0.9 \times 10^{-3}$ Torr using a IDP-3 Dry Scroll Pump from Agilent Technologies. The two different configurations are described below.

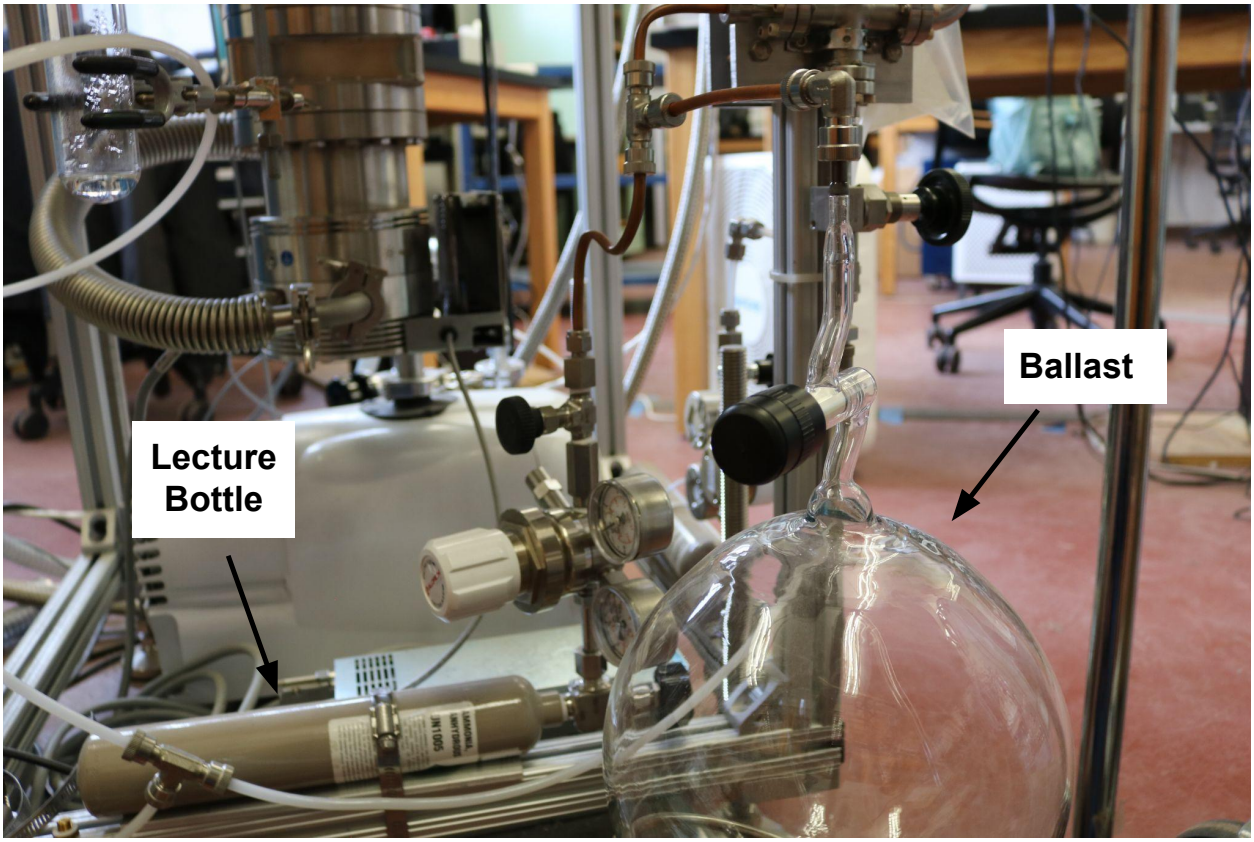

Figure 2.18: Image of Variable gas source (lecture bottle) and glass ballast. Note that this equipment is connected to the conflat cross with a cajon tee fitting.

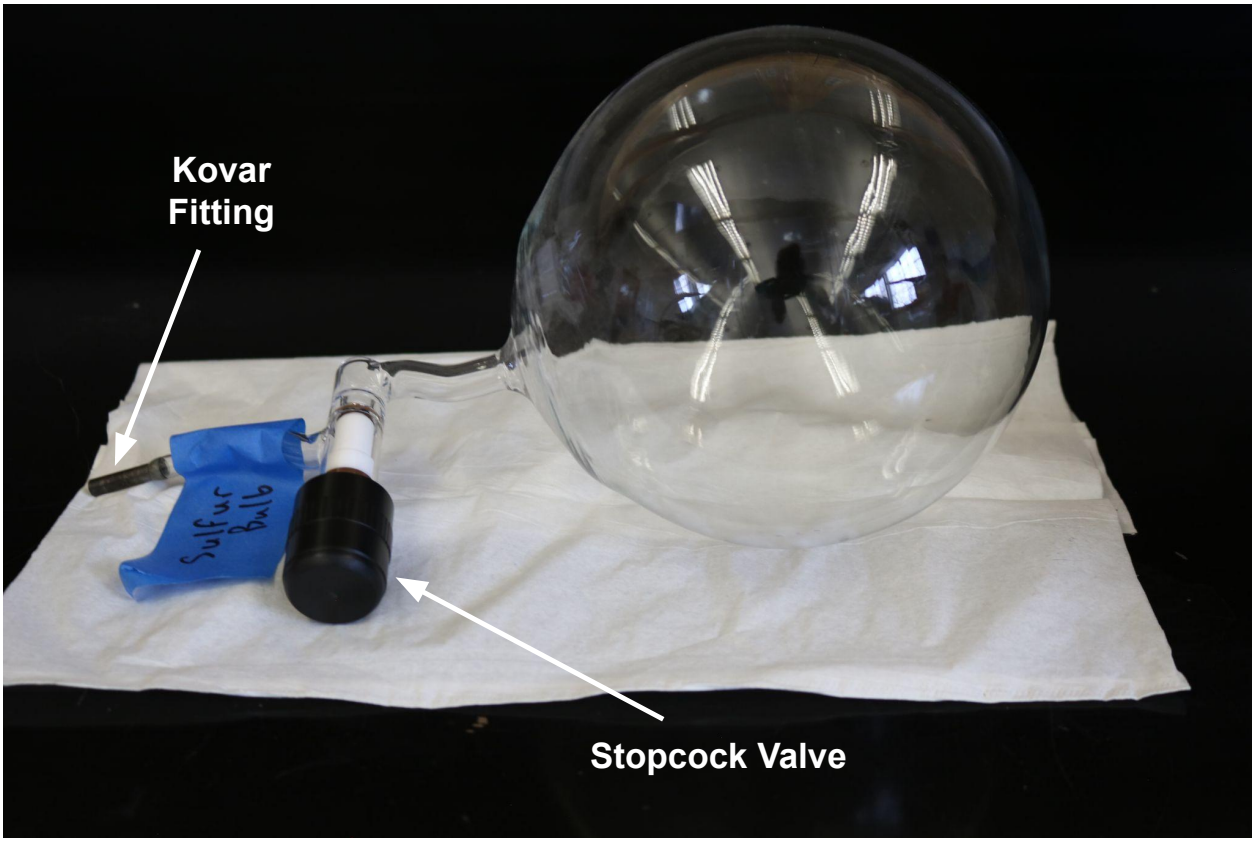

Figure 2.19: Variable gas glass ballast showing the stopcock leak valve and kovar metal fitting.

Figure 2.20: O_3 manifold (left) and schematic (right).

2.1.5.1 O_3 Manifold

Unlike all of the other gases used throughout this dissertation work, ozone (O_3) cannot be purchased from a chemical supplier. Instead, one of the oxidant manifold configurations has been optimized to produce O_3 and deposit it into the UHV chamber. The full O_3 manifold schematic, and the glassware are shown in Figure 2.20. The O_3 configuration is comprised of an O_2 source (O_2 Lecture Bottle and CGA-170 regulator), pumping system, and the O_3 glassware. The glassware is mounted to the UHV chamber table using a machined and 3D-printed mount and protected with an acrylic housing. The procedure to produce O_3 follows the subsequent steps. After the manifold has been evacuated (see above), I pressurize the small volume within the CGA-170 regulator to 1.0 bar with O_2 and I leak this O_2 into the plastic manifold lines, filling the glassware, which is then closed off from the O_2 source using the top stopcock. Once isolated, the glassware is exposed to a model BD-10AS High Frequency Generator (Tesla Coil) from Electro-Technic Products, which produces an electrical discharge that arcs from the Tesla coil tip to the glassware, for approximately 20 minutes. This arcing cracks O_2 molecules into O atoms, which react to produce O_3. These reactions are summarized in Equations 2.4 and 2.5:

$$O_2 + h\nu \rightarrow O + O^* \tag{2.4}$$

$$O + O_2 \rightarrow O_3 \tag{2.5}$$

The resultant O_3 condenses in a glassware arm that is submerged in a liquid N_2 bath. After 20 minutes and while the O_3 is still condensed, the manifold is pumped out to $\sim 3 \times 10^{-2}$ Torr to remove any residual or recombined O_2. Once the residual O_2 is removed, the N_2 bath is removed and O_3 sublimates, filling the small ballast, and the pure O_3 vapors are deposited into the UHV chamber.

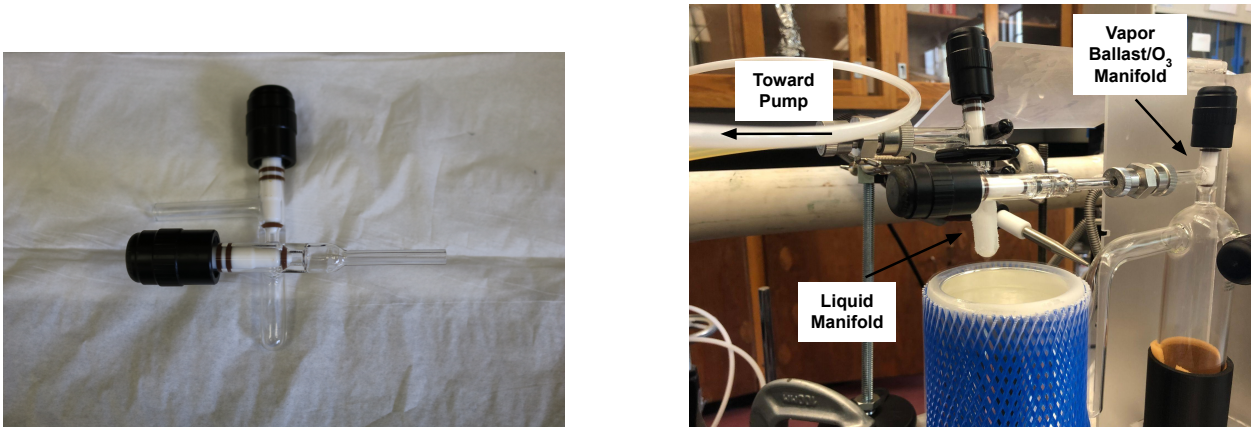

Figure 2.21: HNO_3 glassware and stopcock leak valves (left), and the HNO_3 liquid manifold attached to the O_3 manifold and UHV chamber.

2.1.5.2 HNO_3 Manifold

The HNO_3 oxidant manifold configuration is very similar to the O_3 configuration, with two exceptions. HNO_3 does not need to be produced using the Tesla coil and a smaller manifold (liquid manifold) is required to limit the quantity of concentrated HNO_3 used in the laboratory. The full HNO_3 liquid manifold glassware is shown in Figure 2.21. The HNO_3 configuration is comprised of the pumping system, liquid manifold, and vapor manifold. The vapor manifold is the same manifold used for O_3 production, and the liquid manifold is connected between the vapor manifold and the pumping line.

To prepare the sample, I transferred 15 M HNO_3 into the smaller liquid manifold using a bulb pipette. I remove the dissolved atmosphere from the HNO_3 using two freeze thaw cycles, where I freeze the 15 M HNO_3 with liquid N_2 and pump down the liquid glass manifold to $\sim 2 \times 10^{-2}$ Torr and warm to room temperature. Once purified, I open the valve to the vapor manifold and allow the two manifolds time to equilibrate ($\sim$ 15 minutes). I leak the HNO_3 into the UHV chamber using the stopcock leak valve. Despite the fact that our starting liquid manifold composition is 70% HNO_3 and 30% H_2O by volume, due to the relative vapor pressures of H_2O and HNO_3 at room temperature, we expect a deposited ice sample with a H_2O/HNO_3 composition ratio of approximately 1 assuming that the relative vapor composition at room temperature reflects the relative adsorption of each species to the sample substrate (Hanson & Mauersberger, 1988; Ritzhaupt & Devlin, 1991) .

2.1.6 Irradiation Source

Some of this dissertation work required the use of a radiation source to examine radiation-induced alteration of ice samples. Specifically, Chapter 3 examines the sputtering, or ejection, of O_2 from ion-irradiated H_2O

Ion Energy keV	Raster Voltage V
0.5	0.3
0.75	0.3
1.0	0.3
2.0	0.7
3.0	0.8
4.0	1.2
5.0	2.0

Table 2.1: Peak-to-Peak rastering voltages for each argon ion energy used.

ice samples. Here, I describe the ion irradiation source, the determination of the flux with a Faraday Cup, and calibrations.

2.1.6.1 Ion Gun

The irradiation source used throughout this dissertation is a differentially-pumped model 1401 ion gun from Nonsequitur Technologies, which is shown in Figure 2.22. This gun ionizes a source gas using accelerated electron impacts, and extracts the ion source with a negatively biased electrode at the axial exit. To ensure uniform irradiation, I externally rastered the ion beam in both the horizontal and vertical directions (200 Hz, 2000 Hz) using a Dual Channel 4050 Series Function/Arbitrary Waveform Generator by BK Precision. I determined rastering voltages based on the uniformity of the beam profile over the diameter of the sample and are shown in Table 2.1 for each ion energy of interest. I determined the beam profile using a Faraday cup (Section 2.1.6.2). I optimized the ion source gas pressure to achieve a typical flux of $\sim 1 \times 10^{13}$ ions cm^{-2} s^{-1}, which corresponded to 7.5 - 9.0 mTorr. Note that this source pressure was changed in the sputtering study (Chapter 3) to quantify the sputtering yield's flux dependence, and the scaling factor and rastering voltages were found to be independent of the source gas pressure.

2.1.6.2 Faraday and Electrometer

I measured the ion beam profile and ion fluxes using a Faraday Cup (shown in Figure 2.23). As ions enter a pinhole (6.3724748×10^5 μm^2) in the Faraday Cup they produce a current and I measure this current using a Keithy 6485 Picoammeter. Note that I prevent secondary electrons produced by ion impacts within the Faraday Cup from leaving the cup by biasing the Faraday Cup in series with the electrometer with a +9 V battery.

I attached the Faraday Cup to a linear manipulator so that I can remove the Faraday Cup from the beam line of sight after determining the initial flux. Additionally, I recorded the flux after sample irradiation to ensure that the beam flux did not change substantially over the course of the experiment. The ion

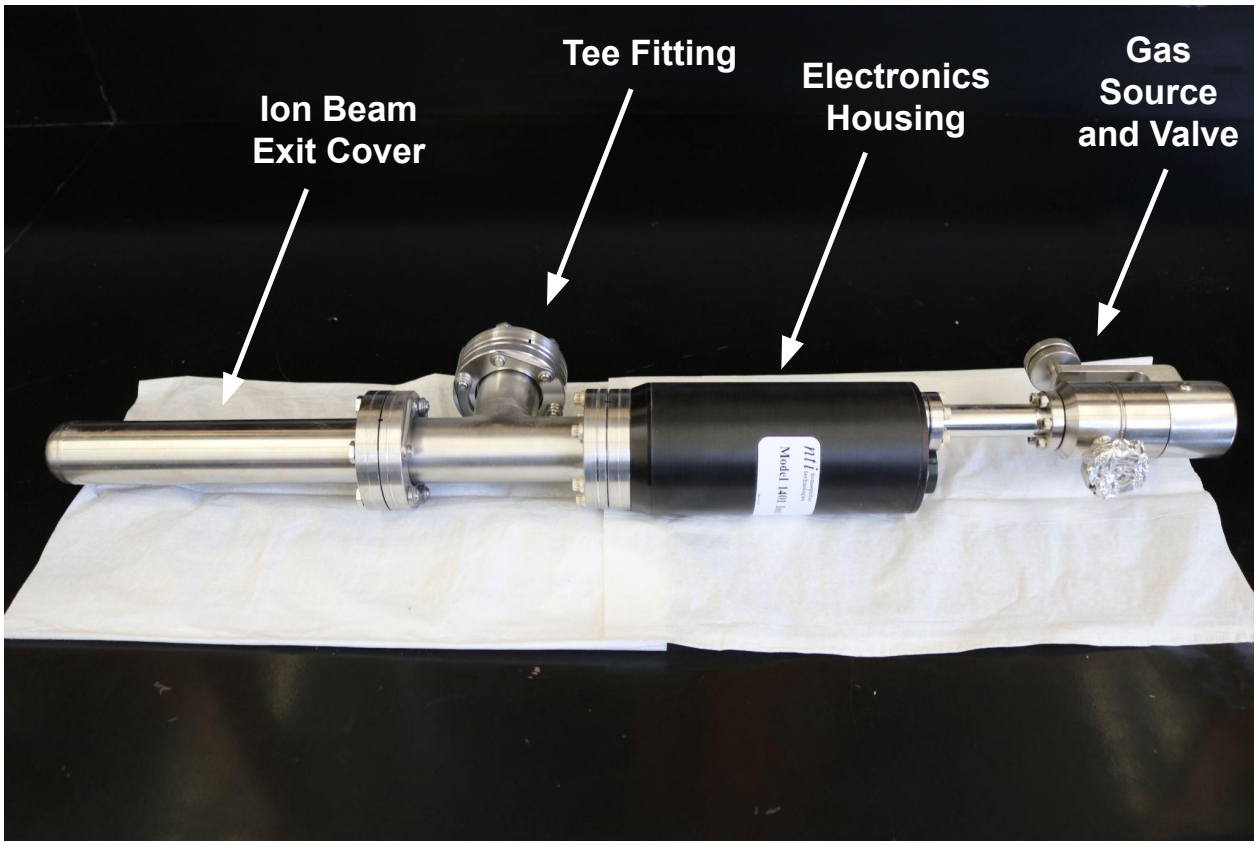

Figure 2.22: Ion gun irradiation source used during this dissertation work. From left to right: ion beam exit (covered to limit dust exposure), the tee fitting for differential pumping, the black electronics housing, and the variable gas source and gas pressure valve.

Ion Energy keV	Flux Scaling Factor
0.5	2.31335
0.75	2.57754
1.0	2.1959
2.0	2.25987
3.0	2.40273
4.0	2.48535
5.0	2.58842

Table 2.2: Flux scaling factors to calibrate the ion fluxes received at the Faraday Cup and at the sample.

flux stability was indirectly monitored using a thin wire in electrical contact with the Faraday cup. Note that I biased the thin wire placed in the beam path at -9 V to avoid attracting secondary electrons from the ionization gauge, which would drastically and inconsistently alter the thin wire current, erroneously indicating flux variations due to the ion source. The current varied by less than 10% during the experiments, and typically less than 5%. Since the ion beam diverges as the beam travels from the ion gun to the sample, and our flux measurements are made with a Faraday Cup that is several centimeters upstream, I used a scaling factor convert the measured flux to the actual flux reaching the sample. This calibration required the use of a second Faraday Cup that was placed directly in front of the sample, and I determined the scaling factor for each ion energy used (see Table 2.2). The relationship between the measured current and the flux at the sample surface is:

$$\phi_{\text{ion}} = \frac{I}{Q_e \times A \times m} \tag{2.6}$$

where ϕ_{ion} is the ion flux at the sample surface, I is the measured current, Q_e is the elementary charge (1.60×10^{-19} C), A is the area of the Faraday Cup hole (6.3724748×10^5 μm^2, measured using a calibrated digital microscope) and m is the Faraday Cup flux scaling factor.

2.1.7 Warming Procedures

Examination of the effects of thermal alteration on the deposited ice samples required specific warming procedures depending on the purpose. I used two different warming procedures: linear heating and isothermal annealing. These next sections discuss each of these techniques and their purposes.

2.1.7.1 Linear Heating

The linear heating procedure involves warming a deposited ice sample from a starting deposition temperature to a final temperature at a constant linear rate. I controlled the linear rate using the temperature controller described in Section 2.1.1, and the range of safe heating rates include rates between 0.1 - 10 K min^{-1}. The

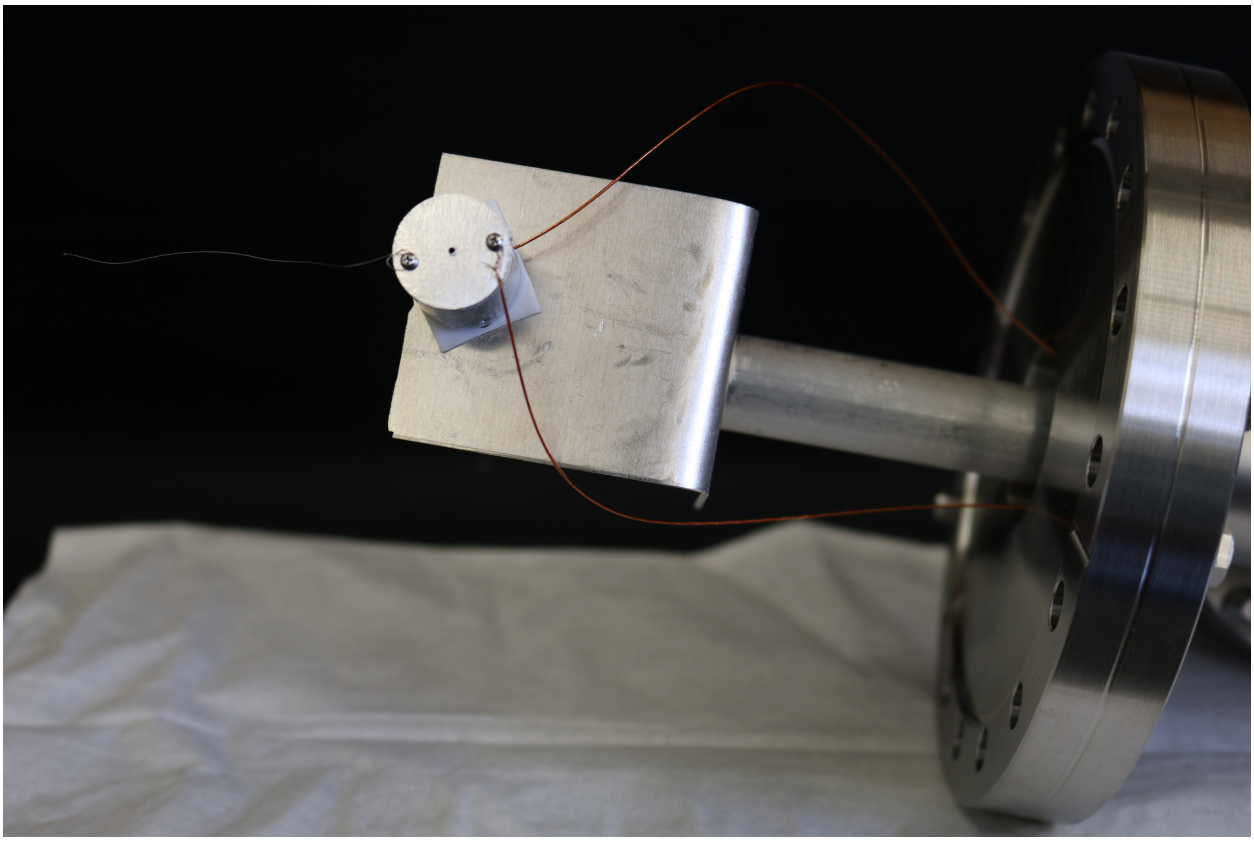

Figure 2.23: Faraday cup used for flux determination. The Faraday cup is attached and electrically isolated from the aluminum L-piece and rod using Teflon padding and screws. Ions enter the small center hole and current is read using the top copper colored wire. When conducting the experiment, the entire Faraday cup is retracted using a linear manipulator (attached to the aluminum rod), and flux stability can be monitored using the small thin wire, shown to the left of the Faraday Cup.

lower limit of 0.1 K min^{-1} is set by the experimental time required to run these experiments. For example, a warm from 50 K to 290 K at a rate of 0.1 K min^{-1} takes approximately 40 hours. The upper limit of 10 K min^{-1} is set by the heating power output, which approaches the maximum heater power output and could damage or degrade the heating element lifetime. Additionally, heating rates higher than 5 K min^{-1} result in a substantial lag between the temperature diodes. Consequently, the effective working range of heating rates is 0.1 - 5.0 K min^{-1}.

A linear heating rate allows for the acquisition of IR data using the FTIR (Section 2.1.2.1) and sublimation data from the QCM substrate (Section 2.1.2.4). I acquired IR spectra and QCM data over a small range of temperatures due to the linear rate warming, and the size of this range depends on the warming rate and the number of FTIR scans. Typically, I acquired a single spectrum or QCM data point every 1 minute or every 1 K, whichever increment results in more scans per spectrum. A typical number of scans is between 50 - 300. Regardless, the temperature associated with the spectrum and QCM data point is an average between the starting and final temperature when the spectrum was acquired. I used the linear heating procedure to identify reaction products, or sublimation products based on changes in the IR spectra and correlations between the IR spectra and QCM data.

2.1.7.2 Isothermal Annealing

During the isothermal annealing procedure, I warmed an ice sample from a deposition temperature to a temperature at a constant linear rate of 5.0 K min^{-1}. After reaching the "isothermal" temperature, I hold the sample at the temperature of interest for a specific time period, typically 24 hours. The range of temperatures of interest differ based on the ice sample composition. IR spectra and QCM data are acquired every 50 scans during both the initial warming, and the 24 hour isothermal period. Note that I acquire these 50 scans every minute (i.e. one spectrum every 5 K during warming, every minute during the isothermal period). This technique results in a substantial number of spectra over the 24 hour time period, which is necessary to determine the kinetic properties of interest (e.g. activation energy).

2.2 Standard Experimental Procedure

For each experiment described within this dissertation, I standardized several operating procedures. This section describes the standard operating procedures (SOP) and where deviations that depend on the type of experiment (e.g. irradiation, linear heating) occur.

For experiments requiring the mass spectrometer, I turned on and degassed the ionization filament to remove any residual material from the mass spectrometer (i.e. condensed H_2O). After the internal degassing

procedures, the MS was set to pressure vs time acquisition to monitor each channel of interest. I turned on the compressor to begin removing heat from the sample substrate, and cool the substrate from room temperature ($\sim$ 300 K) to 200 K at a rate of 2.5 K min^{-1}. Once the substrate was at 200 K, I allowed the chamber base pressure time to equilibrate (i.e. H_2O condensing onto the thermal-radiation shield and copper rod). While at 200 K, I took several steps depending on the expected analytical techniques. For experiments requiring IR spectroscopy, I added liquid N_2 to the MCT/A to cool the detector prior to any spectral acquisition.

Once the chamber reached its cooled based pressure, $\sim 3 \times 10^{-9}$ Torr, I cooled the substrate to the deposition temperature at a rate of 2.5 K min^{-1}. While cooling, I turned on all necessary manifold pumps to pump manifold lines to their respective base pressures. In the case of the H_2O manifold, I exposed the H_2O liquid to the manifold pump to remove any residual atmosphere gas trapped in the H_2O. Once the H_2O glassware was cold to the touch, I closed the valve to the manifold pump and allowed the H_2O vapor to fill the manifold. I allowed the H_2O manifold pressure to reach equilibrium prior to deposition ($\sim$ 250 mTorr). Once the chamber reached the deposition temperature, I acquired an IR background spectrum (800 scans) if necessary. I closed the variable gas manifold from the manifold pump, and opened the ballast to fill the manifold with the gas of interest. If O_3 was required, I used the manifold pump to evacuate the manifold lines, including the O_2 regulator, to a based pressure of $< 9 \times 10^{-3}$ Torr, then the valve to the pump was closed. I prepared the liquid N_2 bath and I describe the remaining procedures in Section 2.1.5.1. If HNO_3 was required, I prepared the liquid N_2 and I describe the remaining procedures in Section 2.1.5.2. For ice deposition, I rotated the sample substrate to face the deposition inlets at normal incidence. Note that I did not use this deposition geometry for samples composed of microporous amorphous solid water (ASW), which required background deposition or 180° from normal incidence. I deposited single component ice mixtures by opening the quantitative leak valves to the desired QCM-derived rate until the sample reached the desired ice thickness. For multi-component ice mixtures, I used a sandwich deposition method (Figure 2.24). With known QCM-derived rates, known deposition times, and the total deposited ice mass (in Hz), I calculated the column number density of each species and derived a thickness assuming a density for each species within the mixture. Note that this sandwich deposition does result in a small section of sample where the species are not intimately mixed; however, this results in $< 5\%$ error in ice composition, which is within the reproducibility of the growth conditions. Note that I measured the pressure of each manifold (excluding the oxidant manifold) prior to and after deposition, the pressure did not vary by more than 5%, typically $<$ 1%.

Once the ice sample is deposited, I rotated the sample substrate to normal incidence, with respect to the ion gun irradiation source, or 37.5° with respect to the FTIR source. In the case of irradiation experiments,

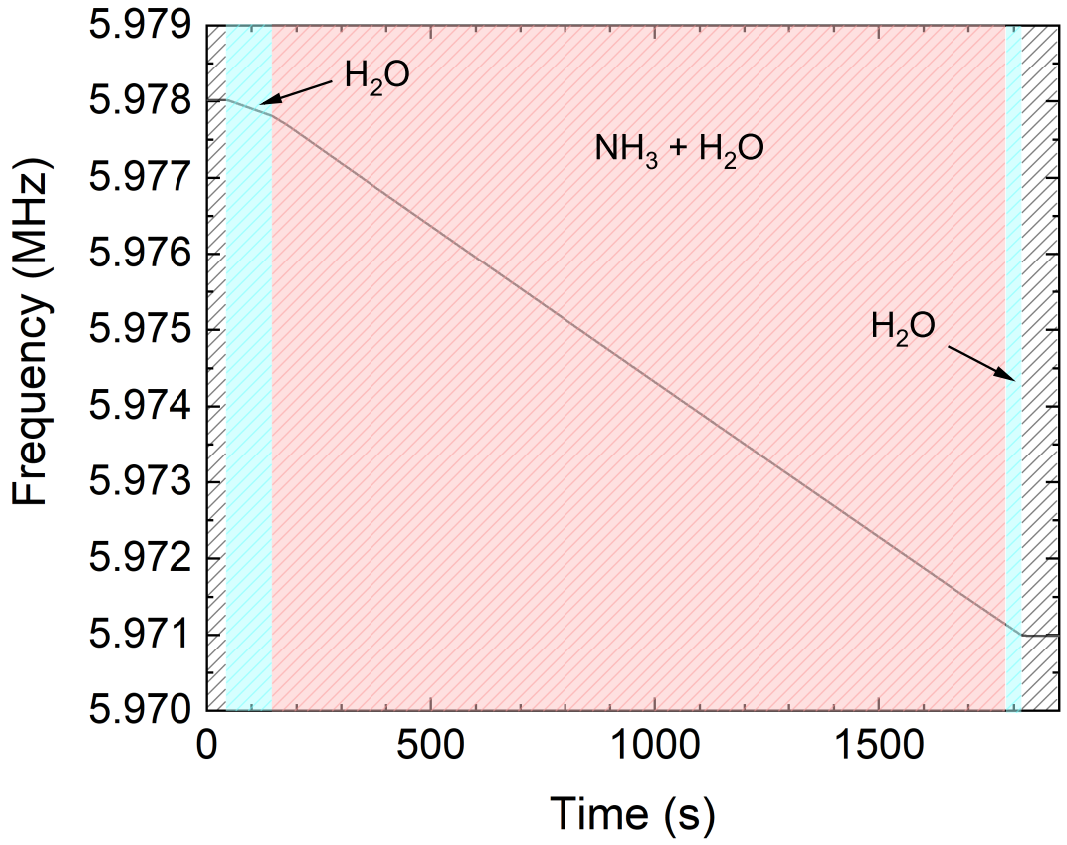

Figure 2.24: QCM frequency as a function of time during the growth of a $\sim$ 7000 Hz H_2O and NH_3 ice sample at 50 K. Color coordinated shaded regions indicate the different sandwich layers. Blue shaded regions are regions of just H_2O. The red shaded region is co-depositing H_2O and NH_3. No deposition is indicated with gray shaded regions.

I allowed the ion source to warm up for 30 minutes, prior to irradiating the sample. After the gun was warmed up, I warmed the samples to the temperature of interest and irradiated. I measured the flux of the irradiation source prior to and after irradiation to ensure beam stability. After irradiation, I turned off the ion gun and warmed the sample to 200 K, at which temperature the compressor was turned off and any residual sample sublimated. In the case of thermal experiments, I began the specific warming procedures after deposition, and turned off the compressor either at the final temperature of interest, typically between 200 - 290 K, or after the 24 hour isothermal temperature hold.

2.3 Spectral Analysis

In addition to the laboratory methods described above, this dissertation includes statistical analysis techniques to extract information from spectra. Specifically, a Markov chain Monte Carlo (MCMC) implementation of a Bayesian Inference framework is applied to spectral data, and through iteration the posterior probability is constrained, which enables determination of a best-fit model and marginal probability distributions for individual parameters. These statistical techniques are commonplace for the evaluation of astronomical data sets within the fields of exoplanet science and cosmology (Trotta, 2008; Macintosh et al., 2014; Line et al., 2015). However, these approaches are significantly less common in planetary science and virtually non-existent in laboratory-based science. For instance, laboratory science tends to apply brute force and by-hand techniques to fit physical models to generated data sets. Bayesian inference and MCMC algorithms enable the increasingly automated fitting of data, and provide more realistic picture of model parameter uncertainty. For these reasons, integration of these statistical techniques into laboratory work is crucial. To this end, this work presents the first attempts to incorporate MCMC-driven statistical analysis into laboratory studies.

In the section below, the statistical techniques and open source software are described in detail. Following this description, an example is provided in both Chapters 4 and 5. Chapter 4 demonstrates this technique's prowess in exoplanetary science, with novel applications in planetary science. The second example demonstrates the transition from modeling remote sensing spectra to laboratory driven work. Note that these examples require different forward models due to the vastly different physics and geometries; however, the overall approach is identical. In addition to the laboratory-based example provided within this dissertation work, this model and statistical approach has been successfully used by Carmack et al. (2023) to investigate the pore accessibility of ASW using the underlying forward model described in Chapter 5.

2.3.1 Bayesian Statistics and `emcee`

The statistical analysis approach used in Chapters 4 and 5 relies on a python-based MCMC implementation of Bayesian Inference called `emcee`, which was developed by Foreman-Mackey et al. (2013). This robust tool has been tested and used extensively in the exoplanet science community, and is written in python, a powerful, open source language.

Bayesian inference is a statistical method that relies on Bayes' Theorem of conditional probabilities to make inferences about the distribution of a random, unknown variable or set of variables. Very generally, conditional probability states:

$$P(B|A) = \frac{P(A \cap B)}{P(A)} \tag{2.7}$$

where $P(B|A)$ is the probability that event B occurs given that event A occurred, $P(A \cap B)$ is the probability that both events A and B occurred, and $P(A)$ is the probability that event A occurred. Let's consider an example about house cats. I apologize to any reader that is unable to relate. Let's imagine that while vacuuming your home you come across small bite marks on your house plants. Let's imagine that your cat likes to eat house plants, and event B is that your cat ate your house plant. Sometimes after eating your house plants, your cat's eyes dilate (event A). Conditional probabilities state that the probability of a cat having eaten a house plant given that it's eyes are dilated is equal to the probability that both events occurred divided by the probability that the cat's eyes are dilated. The probability that both of these events occurred ($P(A \cap B)$) is equivalent to the probability that event A occurred given B multiplied by the probability that event A occurred:

$$P(A \cap B) = P(A|B)P(B) \tag{2.8}$$

Thus, Bayes' Theorem States:

$$P(B|A) = \frac{P(A|B)P(B)}{P(A)} \tag{2.9}$$

Returning to the example, we now know that the probability that the cat ate a house plant given that it's eyes are dilated is related to the probability that the cat's eyes dilate after eating a plant, multiplied by the probability that the cat ate a plant, divided by the probability that the cat's eyes are dilated. We know from prior experience that the cat has eaten a plant on 50% of the days you have owned the cat, and you are 100% sure that you saw dilated pupils. Lastly, the likelihood that your cat's eyes dilate after eating a plant is about 90% because your cat notoriously overindulges. Then the probability that your cat did in fact eat

some house plant given that it's eyes are currently dilated is:

$$P(B|A) = \frac{0.9 \times 0.5}{1.0} = 0.45 \text{ or } 45\% \tag{2.10}$$

Now, instead of addressing the "cat's eyes are dilated because it ate too much plant" hypothesis, this statistical framework can be adapted to analyze a data set using a physical model. Bayes' Theorem is re-written as:

$$P(\theta|y) = \frac{P(y|\theta)P(\theta)}{P(y)} \tag{2.11}$$

where $P(\theta|y)$ is the posterior probability or the probability of a set of parameters (θ) given the data set y, $P(y|\theta)$ is the likelihood probability or likelihood function of the data given θ, $P(\theta)$ is the prior probability of those parameters, and $P(y)$ is the probability of the data. Since the data exists (i.e. $P(y) = 1$), this relationship is simplified. We also note that since $P(y)$ does not depend on the fitted parameters for the model, it is a constant of integration and can generally be ignored. Assuming the data follow a normal distribution, the likelihood function is expressed as:

$$\ln \mathrm{P}(\mathrm{y}|\theta) = -\frac{1}{2}\sum_{\mathrm{i}} \frac{(\mathrm{y_i} - \mathrm{f}(\theta))^2}{\sigma_\mathrm{i}^2} + \ln 2\pi\sigma_\mathrm{i}^2 \tag{2.12}$$

where y_i is the ith data point, σ_i is the uncertainty for that data point, and $f(\theta)$ is the forward model-derived values. The likelihood function maximizes as the model-derived values approach the data. The prior probabilities for each parameter is determined based on known information regarding the parameters. Note that for all studies within this work, these "priors" are uninformed or flat probabilities (e.g. binary, 1 within a specified range or 0 outside of that range). Uninformed priors truncate the model to only allow parameter values that are physical. For example, length parameters have a 0% chance of being negative. The use of informed priors is discussed briefly in Chapter 9. Within the parameter value space dictated by the priors, exploration of parameter value space determines the likelihood probability and subsequently maps posterior probability space for each parameter of interest—enter `emcee`.

`emcee` is an open source python package that couples a MCMC algorithm to Bayesian Inference. Specifically, a modified Hastings-Metropolis algorithm pseudo-randomly samples n parameter (θ) of interest to map the posterior probability distributions. `emcee` initializes a series of "walkers" with randomized initial conditions. The walkers explore n-dimensional parameter space and for each position collectively evaluate the likelihood function and consequently the posterior probability distribution for the n parameters (Foreman-Mackey et al., 2013). Movement of the walkers is determined based on a "stretch" move, which moves a

walker to a new position by randomly selecting another walker, extending a line between and beyond the two walkers, and moving the original walker along that line. The movement is made if the posterior probability for the new position improves upon the current position (acceptance condition). A more detailed description of this algorithm can be found in Goodman & Weare (2010). For the studies within this dissertation, a typical number of walkers and moves (or steps) is $\sim 100 - 500$ walkers and $\sim 500 - 10000$ steps depending on the run. Walkers were randomly initialized in clusters around the a current best guess for the marginal probability distribution mean for each parameter to ensure that walkers did not become isolated in local distribution maxima.

The goodness of fit compared to the data sets is evaluated using the reduced chi squared (χ^2_ν) criteria, which calculates the weighted sum of the squared deviations scaled by the number of free parameters:

$$\chi^2_\nu = \frac{\chi^2}{\nu} = \frac{1}{\nu} \sum_i \frac{\left(y_i - f(\theta)\right)^2}{\sigma_i^2} \tag{2.13}$$

ν is degrees of freedom or the number of data points minus the number of free model parameters, y_i is the ith data point, $f(\theta)$ is the model value, and σ_i is the uncertainty of the ith data point. χ^2_ν values close to 1 indicate a good model fit, values $<< 1$ can suggest possible overfitting of the data (i.e. too many free model parameters), and values $>> 1$ can suggest an inappropriate physical model.

The final posterior probability distributions determined by all walkers after a prescribed number of steps are visualized with corner plots (described in both Chapter 4 and 5). Briefly, these plots show the marginalized posterior distribution for each individual parameter along the diagonal axis. The marginalized posterior distribution is the posterior probability distribution integrated along all axes excluding the parameter of interest. The off-diagonal plots show the 2-dimensional marginal probability distribution for pairs of parameters which can indicate correlations between parameters. Note that corner plots are typical tools for visualizing n-dimensional parameter space (Foreman-Mackey et al., 2013; Line et al., 2015; Line et al., 2016). These corner plots often show the 16th, 50th, and 84th percentiles for each one-dimensional marginalized posterior distribution, or the mean and 1σ uncertainties (for a Gaussian distribution). This underlying `emcee` tool is easily adapted to the project of interest, which can range wildly in topics (e.g. exoplanet transit spectroscopy and spectral effects due to radiation-induced compaction). Much of the heavy lifting goes into the construction of the forward model, which is exchanged within the likelihood function. I describe each forward model used in its respective chapter. Once a forward model is formalized and the data is acquired, `emcee` hammers away (Foreman-Mackey et al., 2013).

Chapter 3

The Sputtering of Radiolytic O_2 in Ion Irradiated H_2O-ice

Patrick D. Tribbett[1], Mark J. Loeffler[1,2]

This is the Accepted Manuscript version of an article accepted for publication in Surface Science. Elsevier B.V. is not responsible for any errors or omissions in this version of the manuscript or any version derived from it. The Version of Record is available online at `https://doi.org/10.1016/j.susc.2021.121797`.

3.1 Abstract

Charged particle bombardment alters the physical and chemical properties of extraterrestrial icy surfaces by simultaneously producing radiolytic products and sputtered material. To better understand these phenomena, we measure the total sputtering yield of H_2O-ice induced by 0.5 - 5 keV Ar^+ at temperatures between 40 and 120 K, using microbalance gravimetry as our analytical tool. In addition, we also estimate the sputtered flux of radiolytic products formed during irradiation and in both cases find good agreement with comparable laboratory studies. At 120 K, we find that the O_2/H_2O sputtered ratio increases nearly linearly with the ion range suggesting that the ions are stopping at depths where O_2 is still efficiently being produced below the surface. Furthermore, we find that although theoretical models appear to over predict our O_2 sputtering yields by about of factor of three, we can make a small adjustment to this model, which improves the agreement between the model and the laboratory data significantly. This empirical adjustment may have implications for models of energetic processing that occurs on extraterrestrial icy surfaces, such as Europa, where low-energy ions are thought to be the primary source producing O_2 from sputtering of the surface H_2O-ice.

Keywords: Sputtering; Water ice; Low energy ions; Radiolysis; Europa

3.2 Introduction

Planetary surfaces with absent or tenuous atmospheres are irradiated with charged particles. These particles can significantly alter the composition of the surface, as well as erode the surface through processes includ-

[1]Department of Astronomy and Planetary Science, Northern Arizona University, PO Box 6010, Flagstaff, AZ 86011, USA
[2]Materials Interfaces in Research and Applications, Northern Arizona University, PO Box 6010, Flagstaff, AZ 86011, USA

ing sputtering. Sputtering occurs when incoming particles collisionally remove material (nuclear or elastic sputtering), electronically excite and eject material (electronic sputtering), or produce and consequently release radiolytic products (Sigmund, 1969; Brown et al., 1978; Haring et al., 1984). Sputtering by magnetospheric charged particles is responsible for the production of extended atmospheres around the Jovian and Saturnian icy satellites (Plainaki et al., 2012; Johnson et al., 2009, 2006). For this reason, the sputtering of water (H_2O)-ice via energetic ions has been extensively studied, particularly for hydrogen, helium, and argon ions (Brown et al., 1978; Christiansen et al., 1986; Shi et al., 1995; Baragiola et al., 2003; Famá et al., 2008; Teolis et al., 2005; Bahr et al., 2001; Vidal et al., 2005; Bar-Nun et al., 1985b; Muntean et al., 2016). Additionally, electrons have been shown to erode surfaces through sputtering (Meier & Loeffler, 2020; Galli et al., 2018; Heide, 1982, 1984). However, few have quantified the sputtering yields of lower energy heavy ions (Shi et al., 1995; Bar-Nun et al., 1985b; Christiansen et al., 1986; Famá et al., 2008; Teolis et al., 2010; Muntean et al., 2016), which are a substantial population of the charged particles within the Jovian magnetospheric plasma (Cassidy et al., 2013). Sputtering is quantified by a term known as the sputtering yield (Y) or the number of ejected molecules, atoms, or ions per incident particle. Nuclear sputtering occurs through billiard ball style collisions resulting in the removal of material(Sigmund, 1969). Electronic sputtering occurs through repulsive interactions between atoms when collisional energy is transferred to electronic energy promoting electrons to anti-bonding orbitals (Baragiola, 2004). Y is dependent on the projectiles's nuclear (S_N) and electronic stopping cross section (S_e); $S = \frac{1}{N}\frac{dE}{dx}$, where dE/dx is the differential loss in energy per unit path length, and N is the number density of the target. Early studies found that Y varied approximately linearly with S_N for solids, and when S_N is dominant the sputtering yield followed predictions by linear cascade theory (Sigmund, 1969). However for insulating ices like H_2O, it was later shown that $Y \propto S_e^2$, and consideration of exclusively nuclear stopping cross sections results in drastic underestimations of Y (Brown et al., 1980). Moreover, in H_2O electronic sputtering dominates at larger ion energies (>10 keV) (Baragiola et al., 2003). Lower ion energies (<10 keV) are dominated by nuclear sputtering, or some combination of nuclear and electronic sputtering. Few studies have focused on this transitional region between nuclear and electronic dominated sputtering (Bar-Nun et al., 1985b; Christiansen et al., 1986; Famá et al., 2008; Teolis et al., 2010).

Sputtering yields of H_2O-ice induced by low energy (0.5 - 6 keV) H^+ and Ne^+ at a wide range of temperatures (30 - 140 K) were first quantified employing a calibrated quadrupole mass filter by Bar-Nun *et al.* (Bar-Nun et al., 1985b). Their study confirmed a nuclear sputtering mechanism for Ne^+ and demonstrated a transition from a nuclear to electronic mechanism for H^+ within the energy range studied. Additionally, temperature dependent fluxes of ejected molecular oxygen (O_2) and molecular hydrogen (H_2) were identified. Furthermore, Y was observed to be constant at temperatures less than 80 K but increased

above 80 K, which is consistent with trends seen for higher (MeV) energy ions and believed to be a result in the increased production of radiolytic O_2 and H_2 (Boring et al., 1983; Reimann et al., 1984). Soon after, Christensen *et al.* 1986 quantified sputtering yields for 2 - 6 keV Ar^+, Ne^+, N^+, He^+, and e^- at 78 K. These yields were calculated based on resulting impact crater diameter (Christiansen et al., 1986). They found that sputtering yields of H_2O-ice at these lower energies agree fairly well with Sigmund's linear cascade theory for collisional sputtering. Famá *et al.* 2008 confirmed a sputtering yield enhancement at temperatures greater than 80 K for low energy Ar^+, which they also attributed to increased production of O_2 (Famá et al., 2008). Additionally, Famá *et al.* developed a theoretical model to predict sputtering yields of H_2O-ice. This semi-analytical model has been validated using a compilation of data from Brown et al. (1980); Rocard et al. (1986); Christiansen et al. (1986); Famá et al. (2008); Muntean et al. (2016). More recently, Teolis *et al.* 2017 generalized Famá's model for total sputtering yield, to predict sputtering yields of different ejected species including H_2, O_2, H_2O, and H_2O_2 (Teolis et al., 2017).

Interestingly, laboratory studies have also shown that the concentration of radiolytic O_2 is not constant with depth below the surface ice but reaches a maximum somewhere within the first 100 ML (300 Å) below the surface (Teolis et al., 2009, 2005). Examining this surface region in more detail using low energy ions will give direct insight into the concentration profile of radiolytic O_2. In addition, it will also test how well theoretical models predict values for O_2 sputtered from H_2O-ice in this energy range, which is of particular interest to the astronomical community, as ions in this energy range are thought to be the main producer of exospheres around icy satellites (Cassidy et al., 2013; Teolis et al., 2010). Thus, here we investigate the sputtering yield of H_2O-ice induced by 0.5 - 5 keV Ar^+ at temperatures between 40 K and 120 K, using microbalance gravimetry as our analytical technique. We compare our H_2O sputtering yields to previous work, as well as to predictions made by the Famá *et al.* 2008 sputtering model. Additionally, we estimate the sputtered flux of radiolytically produced O_2 and compare those estimates to the values predicted by the Teolis *et al.* 2017 model and give possible explanations for any observed deviations between the laboratory data and theoretical predictions.

3.3 Experimental Methods

3.3.1 Experimental Setup

All sputtering yield measurements were performed in a stainless steel ultra-high vacuum chamber with a base pressure of 2.5×10^{-9} Torr (Figure 3.1); we estimate that the pressure at the sample is significantly lower given that it is protected by a thermal-radiation shield. To prepare our samples, we vapor deposited H_2O-ice at 100 K at normal incidence onto an optically flat gold mirror electrode of an Inficon IC6 quartz-crystal

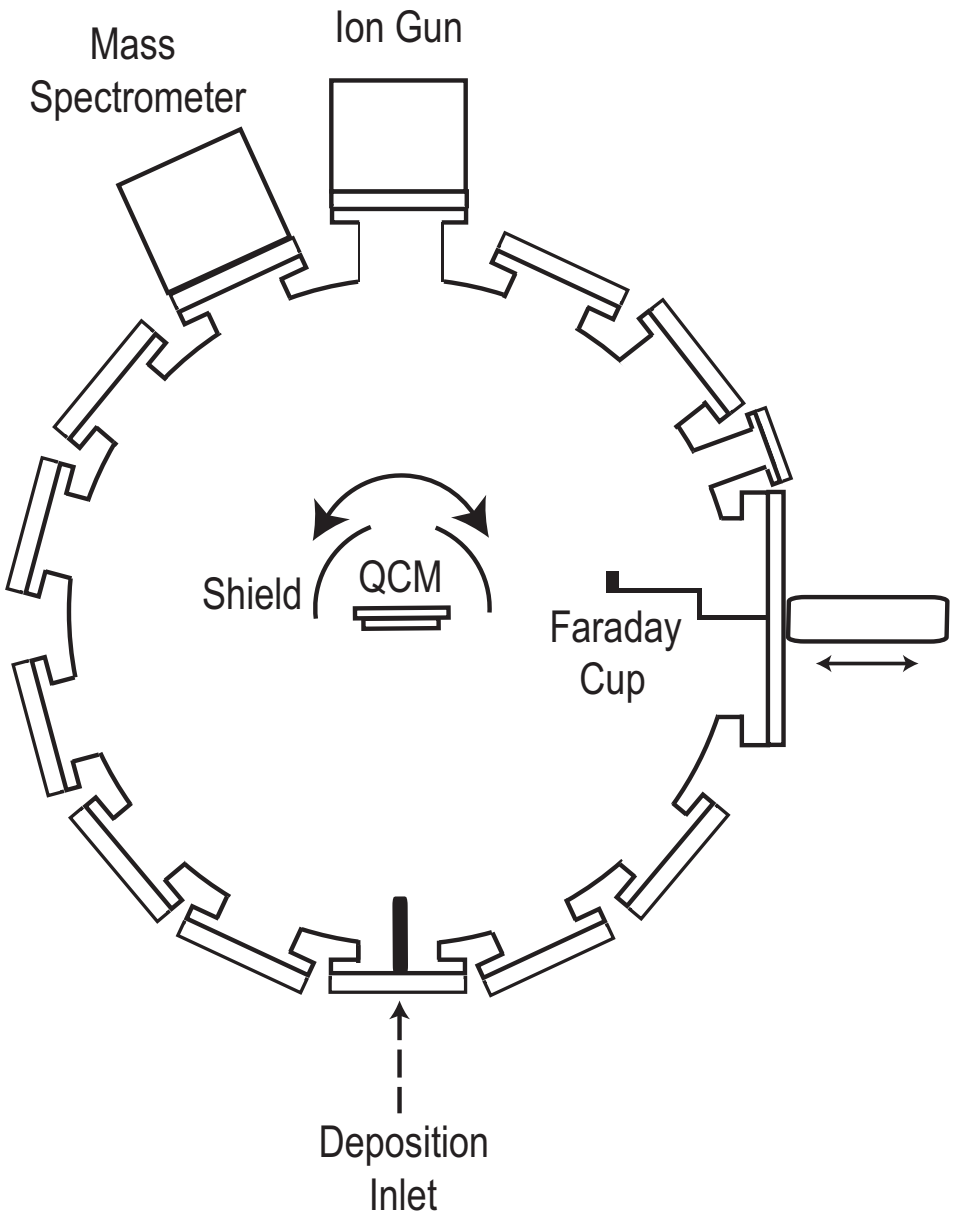

Figure 3.1: Experimental setup along the sample holder axis.

microbalance (QCM) as in our previous studies (Loeffler et al., 2020). Under these conditions, the sample is amorphous and lacks significant microporosity (Sceats & Rice, 1982; Brown et al., 1996). Ice films were grown at a rate of 2×10^{15} H_2O cm^{-2} s^{-1} to a column density of $2.9 \pm 0.1 \times 10^{18}$ molecules cm^{-2} (~ 0.87 μm), unless otherwise stated. Film thicknesses given in this paper were estimated from our QCM-derived column densities, assuming a density of 1 g cm^{-3} for H_2O-ice. We chose this value for density, so that parameters derived from our modeling efforts (see Section 3.4) would be directly comparable to previous work (Teolis et al., 2017). The QCM stability enabled us to be sensitive to changes of 0.1 Hz ($\sim 5 \times 10^{13}$ molecules cm^{-2}).

After growth, the H_2O-ice was cooled to the desired temperature and irradiated with Ar^+ (0.5 - 5 keV) at normal incidence using a differentially-pumped Non Sequitur electron impact ionization gun (Model 1401). To ensure uniform irradiation of the sample, the ion beam was externally rastered with a BK Precision 4050 Series Function/Arbitrary Waveform Generator. Optimal peak to peak function voltages and the raster frequency were determined based on the uniformity of the full width half maximum (FWHM) of the ion beam for each ion energy used in this study. Typical fluxes, measured by a Faraday Cup, were $\sim 1 \times 10^{13}$ ions cm^{-2} s^{-1}. Secondary electrons produced by ion impacts within the Faraday cup were prevented from leaving the cup by biasing it in series with the electrometer with +9 V. During the experiment, the ion flux was monitored with a thin wire placed in the beam path and biased at -9 V. The current typically varied by less than 10% during the experiment.

3.3.2 Calculating the Total Sputtering Yield

Sputtering yields were calculated based on the changes in output frequency of the QCM during irradiation (df/dt), as described in Meier and Loeffler 2020 (Meier & Loeffler, 2020). The change in areal mass is related the change in QCM frequency by:

$$\frac{dQ}{dt} = \frac{-k\frac{df}{dt}}{f^2} \tag{3.1}$$

where Q is the areal mass of the ice film, f is the frequency at which the derivative is evaluated, and k is a constant (4.417×10^5 Hz g cm^{-2}) (Lu & Lewis, 1972). Assuming the impactor flux (Φ) is constant and the total mass loss is due to H_2O, Y_{H_2O} can be calculated by:

$$Y_{H_2O} = \frac{\frac{dQ}{dt}}{\Phi}\left(\frac{N_A}{M_{H_2O}}\right) \tag{3.2}$$

where N_A is Avogadro's number, and M_{H_2O} is the molar mass of water (18 g/mol). The measured value

of df/dt was determined after a fluence of $\sim 2 \times 10^{15}$ ions cm^{-2} to ensure that sputtered flux from our sample had reached equilibrium. As was most easily seen in our higher temperature experiments (data not shown here), this chosen fluence is well past the point where df/dt has stopped increasing with fluence. This increase at low fluences has previously been attributed to production of radiolytic H_2 and O_2 (Teolis et al., 2005). We note that while we do present the total yield in terms of H_2O both for simplicity and for ease of comparison with previous experiments (Famá et al., 2008), we also consider the contribution from the main radiolytically produced species (Section 3.4.4 for more details).

3.3.3 Calculating the Total O_2 Sputtering Yield

The sputtered flux of stable radiolytic species from from H_2O-ice mainly consists of H_2O, O_2, and H_2 (Brown et al., 1982; Boring et al., 1983; Reimann et al., 1984; Bar-Nun et al., 1985b; Teolis et al., 2009). Below 80 K, the flux consists primarily of H_2O and the sputtering yield is relatively constant (Brown et al., 1984). Between 80 K and 130 K, the yield increases as a result of the radiolytic production of O_2 and H_2. Thus, as we are determining the sputtering yield via mass loss on our QCM, the changes we observe are predominantly due to the ejection of H_2O, O_2, and H_2. To provide estimates for the absolute O_2 sputtering yield, we used a two-tiered approach. First, to estimate the amount of O_2 in the sputtered flux where the total yield has been shown to be independent of temperature ($\leq$ 80 K), we use the model prediction given in (Teolis et al., 2017) (see Figure 6) for S^+ ions, which are expected to sputter in a similar manner to Ar^+ ions (Teolis et al., 2017). We used this model to estimate the O_2 component, after taking into account contribution from H_2. We utilized this approach rather than a fixed ratio for all energies, because differences in previous laboratory studies suggest that the O_2/H_2O ratio in the sputtered flux depends on energy and ion type (Brown et al., 1984; Bar-Nun et al., 1985b; Teolis et al., 2005). The model-derived O_2/H_2O ratio at each energy studied here is given in Table 3.1. At irradiation temperatures higher than 80 K, we assume that any increase in the mass loss at a given energy compared with the average mass loss of our 40 and 80 K experiments (which were within $\sim$ 5 % of one another) is exclusively due to O_2 and H_2, and that these products are produced and sputtered stoichiometrically (Brown et al., 1984; Bar-Nun et al., 1985b; Teolis et al., 2005). This "enhanced" O_2 is then added to the average O_2 sputtered at 40 and 80 K ("intrinsic" O_2) to produce the total O_2 sputtering yield. For reference, we also give the O_2/H_2O ratios derived at 100 and 120 K for each energy in Table 3.1. Based on stoichiometry, the values for the H_2/H_2O are assumed to be twice that of those given for O_2 in Table 3.1.

Ion Energy (keV)	O_2/H_2O 40 and 80 K[a]	O_2/H_2O 100 K[b]	O_2/H_2O 120 K[b]
0.5	0.082	0.070[c]	0.143
0.75	0.107	0.114	0.169
1.0	0.121	0.204	0.200
2.0	0.164	0.239	0.331
3.0	0.184	0.241	0.384
4.0	0.215	0.233	0.414
5.0	0.223	0.311	0.512

Table 3.1: O_2/H_2O ratios; [a] from reference Teolis et al. (2017) Figure 6. [b] this work. [c] we note that this ratio is anomalously lower than the ratio at 40 and 80 K due to a larger uncertainty in the total mass loss.

3.3.4 Theoretical Models

Experimental results of this study and several references herein are compiled and compared to the total sputtering yield model derived in Famá et al. (2008). Specifically, theoretical sputtering yields are computed using:

$$Y_{H_2O}(E, m_1, Z_1, \theta, T) = \frac{1}{U_0}\left(\frac{3}{4\pi^2 C_0}\alpha S_N + \eta S_e^2\right) \times \left(1 + \frac{Y_1}{Y_0} e^{-E_a/k_b T}\right) cos^{-f}(\theta) \tag{3.3}$$

where Z_1 is the atomic number of the projectile, m_1 is the mass of the projectile, U_0 is the surface binding energy of water, C_0 describes elastic scattering in a binary collision approximation, k_b is the Boltzmann constant, f is the empirically derived angular dependence, and E_a is a fitted temperature dependence constant. A detailed description of α and η can be found in Famá et al. (2008).

We also compared our estimated experimental O_2 yields to predictions given by Teolis *et al.* 2017, who developed a general relation that predicts O_2 yields from the sputtering of H_2O-ice for a given energy (E), temperature (T) and incident angle (β). The derived expression is:

$$Y_{O_2}(E, T, \beta) = \epsilon g^0_{O_2} x_0 \left(1 - \exp\left(-\frac{\mathrm{r_0 cos}\beta}{\mathrm{x_0}}\right)\right)\left(1 + \mathrm{q_0 exp}\left(-\frac{\mathrm{Q}}{\mathrm{k_b T}}\right)\right)(\mathrm{r_0 cos}\beta)^{-1} \tag{3.4}$$

where ϵ is the effective particle energy, which excludes energy contributing to lattice vibrations, $\mathrm{g}^0_{O_2}$ is the surface radiolysis yield of O_2, $\mathrm{x_0}$ is the approximate thickness of a surface layer that efficiently produces O_2, $\mathrm{r_0}$ is the projectile range at a given incidence angle, $\mathrm{q_0}$ describes the exponential temperature dependence, Q is the related to the effective activation energy, and k_b is the Boltzmann constant (Teolis et al., 2017).

We initially adopt values within the uncertainties of those used in Teolis et al. (2017) for $\mathrm{g}^0_{O_2} = 0.005$

O_2 eV^{-1}, $x_0 = 29$ Å, $q_0 = 10^3$ and Q = 0.06 eV. As $\epsilon = H \times E$, where H is the fraction of projectile energy available for radiolysis, we estimated ϵ by calculating H using Stopping and Range of Ions in Matter (SRIM) (Ziegler et al., 2010). We found that H ranged between 0.83 and 0.98 for projectile energies between 0.5 keV and 5 keV.

3.4 Results

3.4.1 Flux and Thickness Dependence

A key goal of our study is to determine the effect of sputtering due to low energy ion bombardment at temperatures and energies relevant to extraterrestrial icy surfaces. Thus, we first needed to verify that our results were independent of the ion flux and sample thickness.

To investigate whether we were in a range where the Ar^+ flux effected the sputtering yield of H_2O-ice, we irradiated a 2.9×10^{18} H_2O cm^{-2} sample with 3 keV Ar^+ at 80 K with ion fluxes between 0.085 and 2 $\times 10^{13}$ ions cm^{-2} s^{-1}. As can be seen in Figure 3.2, Y_{H_2O} is essentially constant over this range of fluxes.

There is also the potential that the sample thickness could effect the sputtering yield. For instance, it has been shown that Y_{H_2O} induced by energetic electrons increases when the penetration depth of the projectile is much greater than the film thickness (Meier & Loeffler, 2020). We note that this effect will likely not be important in our studies, as the penetration depth of the Ar^+ is always significantly less than the film thickness (Table 3.2). However, previous studies have also demonstrated that ions can induce electrostatic charging of ice (Shi et al., 2010), which could potentially alter the sputtering yield. Thus, we irradiated samples of thicknesses between 60 nm and 1.2 μm with 3 keV Ar^+ at 80 K and measured Y_{H_2O}. As is shown in Figure 3.3, there are no measurable variations in Y_{H_2O} over the range of thickness studied, suggesting that electrostatic charging effects are not significant enough in our experiments to alter the total sputtering yield, in agreement with previous work (Famá et al., 2008).

3.4.2 Energy and Temperature Dependence of the Total Mass Loss

After determining that the total mass loss is independent of our chosen sample thickness and incident ion flux, we measured Y_{H_2O} for 2.9×10^{18} H_2O cm^{-2} samples as a function of Ar^+ energy at temperatures between 40 and 120 K (Figure 3.4). We find that generally the total sputtering yield increases with temperature and energy, although this dependence in temperature is much more evident in at the higher irradiation energies. For instance, at 5 keV, Y_{H_2O} is 1.14 times higher at 100 K and 1.41 times higher at 120 K than it is at 40 K.

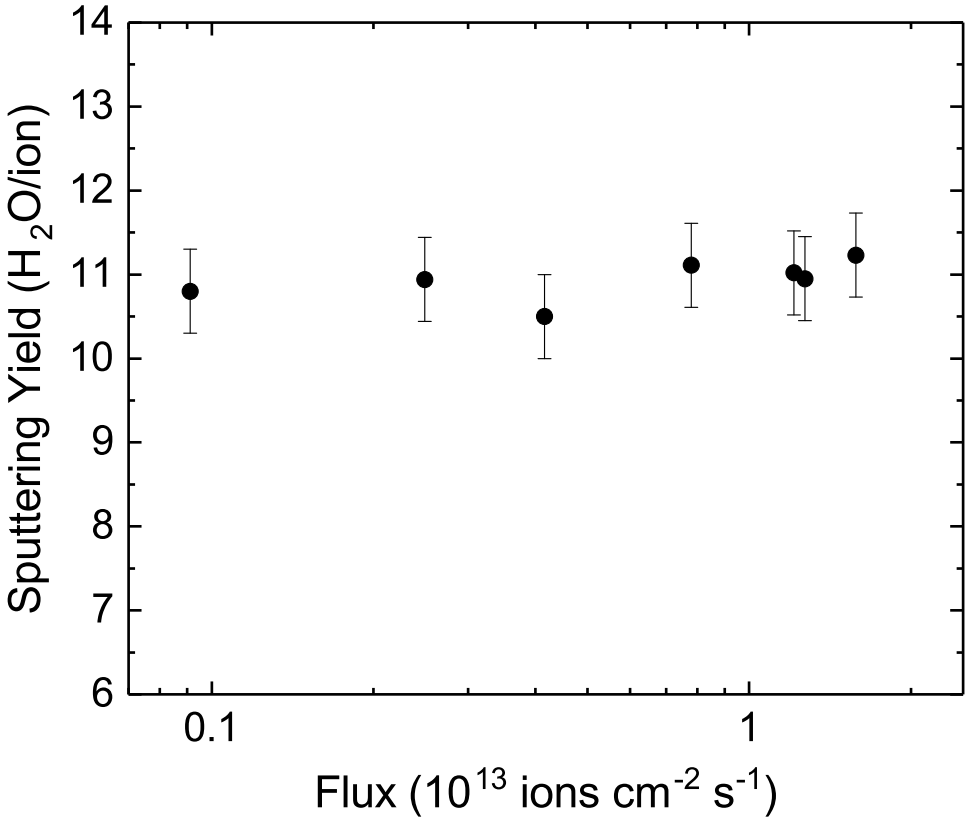

Figure 3.2: Total sputtering yield for a 2.9×10^{18} H_2O cm^{-2} sample irradiated with 3 keV Ar^+ at 80 K as a function of ion flux.

To verify that our experimental sputtering yields were not systematically offset from an absolute sputtering yield, we compared our values to those within the literature. Figure 3.5 shows our total sputtering yields as a function of energy at an irradiation temperature of 80 K, along with others compiled in Famá et al. (2008). All yields were acquired at irradiation temperatures between 60 and 80 K and corrected for angular dependence by multiplying by a factor of $\cos(\theta)^{1.78}$, where θ is the angle of incidence for the ions (Famá et al., 2008). Our experimental yields are consistent with previously studies and for the most part are transected by the theoretical values predicted by Famá et al. (2008) (i.e. Equation 3.3).

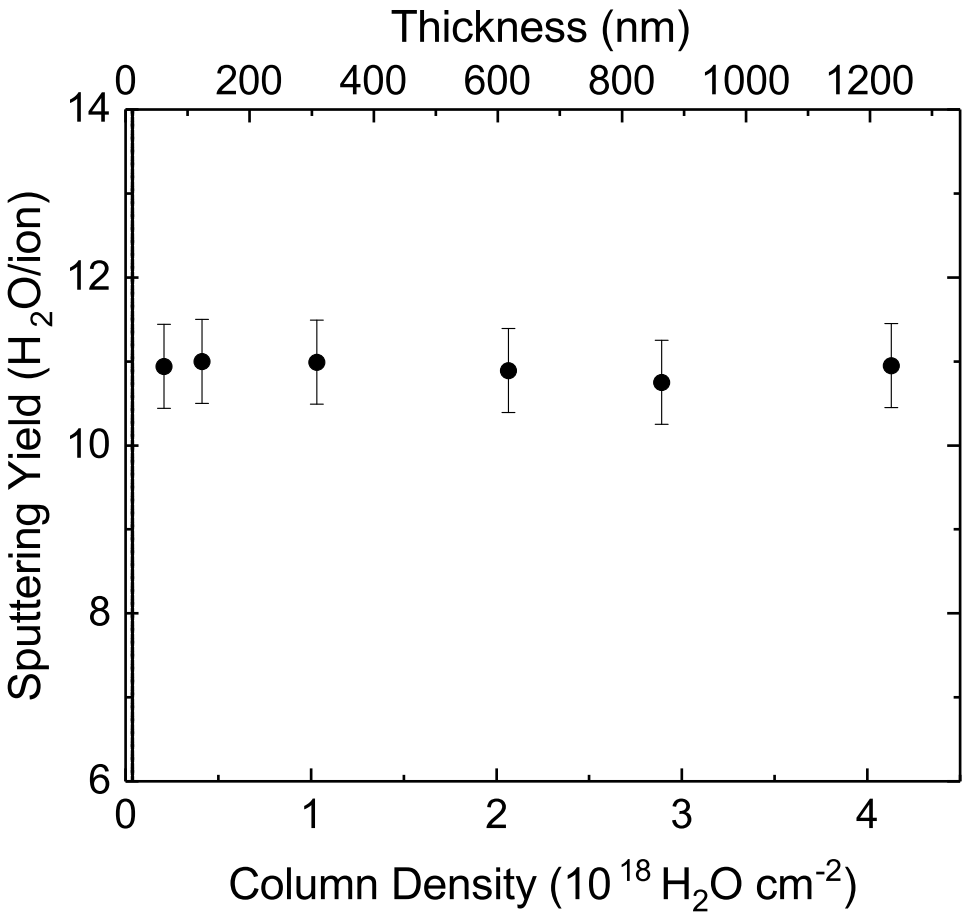

Figure 3.3: Total sputtering yield for a H_2O-ice irradiated with 3 keV Ar^+ at 80 K as a function of column density. Film thickness was calculated assuming a film density of 1 g cm^{-3}. The dashed black vertical line on the left of the figure indicates the range of a 3 keV Ar^+.

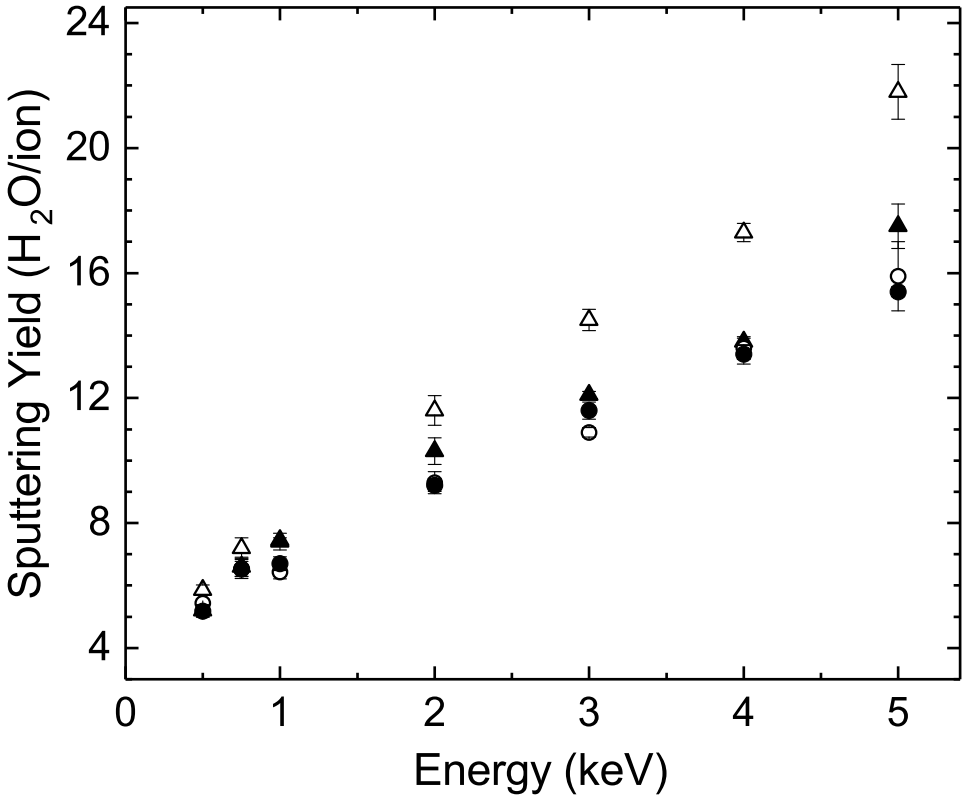

Figure 3.4: Total sputtering yield for a 2.9×10^{18} H_2O cm^{-2} sample as a function of incident ion energy for 120 K(△), 100 K(▲), 80 K(○), and 40 K(●).

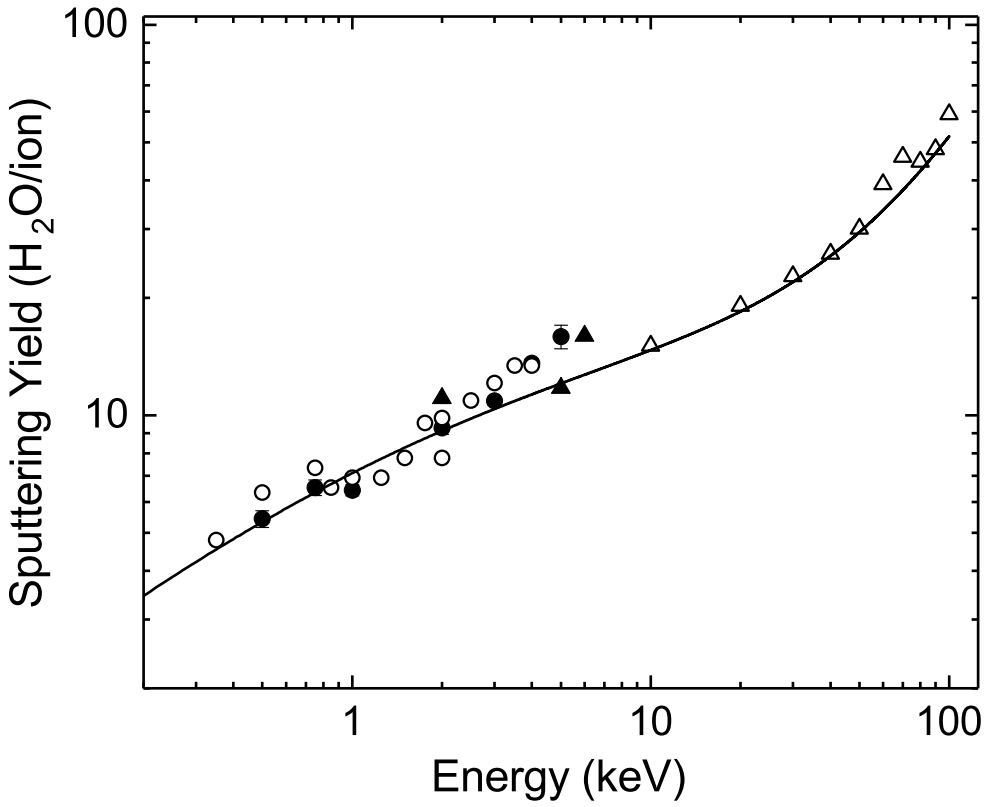

Figure 3.5: Comparison of our experimental total sputtering yields with those found in literature and compiled in (Famá et al., 2008). The symbols correspond to: this study Ar^+ 80 K (•), (Christiansen et al., 1986) Ar^+ 78 K (▲), (Baragiola et al., 2003) Ar^+ 60 K (△), and (Famá et al., 2008) Ar^+ 80 K (○).

Ion Energy (keV)	Nuclear Stopping Power eV/Å	Electronic Stopping Power eV/Å	Projected Range Å
0.5	17.86	1.30	40
0.75	20.89	1.59	50
1.0	23.15	1.83	58
2.0	28.79	2.59	87
3.0	32.02	3.17	112
4.0	34.17	3.66	135
5.0	35.71	4.10	156

Table 3.2: Nuclear and electronic stopping powers, and projected ranges for argon ions used in this study calculated using SRIM assuming a density of 1 g cm^{-3} for H_2O (Ziegler et al., 2010)

3.4.3 Energy and Temperature Dependence of the Sputtered O_2 Component

While the model comparison shown in Figure 3.5 assumes the total yield is in the form of H_2O, we can also estimate the portion of the yield that is due to sputtered O_2 using the approach described in Section 3.3.3. In Figure 3.6, we show the O_2 sputtering yield as a function of energy for 40, 80, 100 and 120 K. The observation that the O_2 yield increases as function of energy is expected from the modeling predictions. We remind the reader that the values at 40 and 80 K are derived from our total mass loss (Figure 3.4) and the O_2/H_2O ratios given in Table 3.1. Interestingly, even at 100 K the O_2 is still primarily driven by this intrinsic O_2, as the enhanced O_2 is on average 20 % of the total O_2 yield. As expected, the contribution from enhanced O_2 at 120 K is more important, as on average it is about half of the total O_2 yield. Additionally, we also find that the $Y_{O_2}(120\,\mathrm{K})/\mathrm{Y}_{\mathrm{O}_2}(40\,\mathrm{K})$ at each energy studied is within about 20% of the average value, supporting previous conclusions that the temperature dependence in the O_2 yield is independent of the particle energy (Teolis et al., 2017). An additional way to look at the data in Figure 3.6 is to evaluate how O_2/H_2O ratio in the sputtered flux changes with ion range. While this is somewhat uninformative at low temperatures, as those ratios were taken directly from the model (Table 3.1), we plot this for 120 K in the inset of Figure 3.6. The ratio increases nearly linearly from ~ 0.15 at 0.5 keV to ~ 0.5 at 5 keV. This increase of the ratio with increasing ion range (and hence energy) is a consequence of the O_2 concentration profile, as previous depth profiling studies have convincingly shown that radiolytic O_2 is most efficiently produced within the first few hundred angstroms below the surface ice and the concentration falls exponentially as one moves into the bulk (Teolis et al., 2005, 2009). Generally, this profile appears to be related to the production and out diffusion of H_2 as hydrogen loss makes the altered region more oxidizing, leading to the more efficient formation of O_2 (Johnson et al., 2003; Teolis et al., 2005, 2009). Furthermore, the observation that our measured ratios with

3 - 5 keV Ar^+ are similar to what has been seen previously using more highly penetrating Ar^+ at similar temperatures (Baragiola et al., 2002; Teolis et al., 2005), suggests that our observed trend with energy would quickly level out or possible drop slightly above 5 keV. This prediction seems reasonable considering that 5 keV Ar^+ has a range of ∼150 Å in H_2O-ice (Table 3.2) and thus is likely probing to a depth where the radiolytic O_2 is most efficiently produced.

Finally, we can also compare these derived O_2 yields to the only previous laboratory study that estimates the O_2 yield for Ar^+ in our energy range (Teolis et al., 2010, 2017). Although these experiments were only performed at T ≤ 20 K, these values should be comparable to our low irradiation temperatures (≤ 80 K), where the yield has been estimated to be nearly independent of temperature (Brown et al., 1984). These values are overlayed with our data in Figure 3.6 after accounting for the dependence of the sputtering yield on ion incidence angle (Famá et al., 2008). The overall agreement with our data is excellent, as the values are no worse than within 10-15% of one another.

3.4.4 Comparison to Theoretical Predictions of the Sputtered O_2 Component

Besides comparing our work to previous laboratory results, we were interested in determining whether the most recent theoretical model predicting O_2 sputtering yields from H_2O-ice would agree with our newly derived data. In Figure 3.7, we compare the model predictions with our O_2 sputtering yields at 40 and 120 K, as well as those given for ≤ 20 K (Teolis et al., 2010, 2017). The two parameter values used were $g^0_{O_2}$ = 0.005 O_2 eV^{-1} and x_0 = 29 Å, where the estimates of x_0 (as well as r_0) assume the H_2O-ice density is 1 g cm^{-3} (Teolis et al., 2017). While the previous laboratory results are well fit by the model, our data does not yield satisfactory results. Specifically, our measurements at 40 K are systematically lower from the predicted value by a factor of three, while our 120 K experiments are lower by about a factor of five to eight. The latter can be improved substantially if we adjust the effective activation energy (Q) in the temperature term from 0.06 eV to 0.07 eV, which is within the uncertainty given previously (Teolis et al., 2017), although the fit still is poor (see Figure 3.7 top). Superficially, the difference between our laboratory results and the model is somewhat surprising, as our Ar^+ O_2 experimental yields compare well with those derived in (Teolis et al., 2010) after correcting for the incidence angle (see above). However, this appears to be due to the difference in projectile range in the two experiments, as even at our lower irradiation energies ions penetrate to depths that fall into the "high-range" limit producing errors by as much as 50% (Teolis et al., 2017) or in our case slightly higher.

As the propensity of the model to overestimate the O_2 sputtering yield when the $r_0 cos\beta >> x_0$ is likely related to the approximation that the energy is deposited uniformly over the ion range (Teolis et al., 2017),

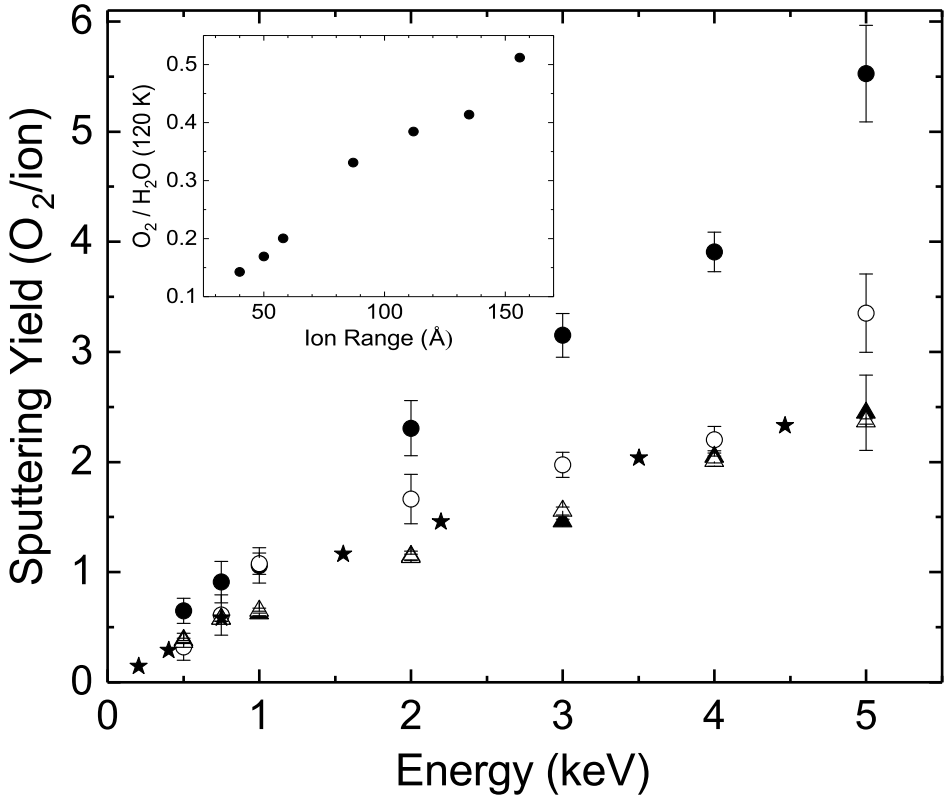

Figure 3.6: Calculated O_2 sputtering yields for a 2.9×10^{18} H_2O cm^{-2} sample as a function of incident projectile energy for 40 (△), 80 (▲), 100 (○) and 120 K (●). Additionally, data from (Teolis et al., 2010) is shown for T $\leq$ 20 K (⋆). Inset: Derived O_2/H_2O ratio at 120 K as a function of ion range.

we investigated whether a simple modification to equation 3.4 and its best fit parameters could improve the fits shown in Figure 3.6 (top). Efforts to do this by only modifying $g^0_{O_2}$ and x_0 were, as expected, unsuccessful. Additionally, adjusting these two parameters along with replacing the term representative of the average deposited energy ($\epsilon/r_0 cos\beta$) with a simple piecewise function that introduces an additional term of $x_0/(r_0(cos\beta))$ when $x_0 \geq 1$, in an attempt to account for the predicted relation between the predicted sputtering yield of O_2 at high ion ranges, were only marginally better considering the quality of the fits for both datasets. Interestingly, we found that optimizing the model with $g^0_{O_2}$= 0.001 O_2 eV^{-1} and x_0 = 90 Å after changing the average deposited energy term from $\epsilon/(r_0 cos\beta)$ to $\epsilon/(r_0(cos\beta)^{2.5})$ for all ion ranges improved the fit for our low temperature and high temperature data sets substantially, while only marginally changing the low temperature results where irradiation was performed at a high angle of incidence (Figure 3.7 bottom). More quantitatively, we found the difference between the model prediction and three laboratory datasets to be typically within $\sim$ 10% and no worse than within 30%. While the significant downward adjustment in $g^0_{O_2}$ cannot be reconciled with laboratory estimates (Teolis et al., 2017), the larger value for x_0, which is an approximation of the depth over which O_2 is produced, is reasonable considering our results on the variation of the O_2/H_2O sputtered ratio as a function of ion energy as well as those from previous depth profiling studies (Teolis et al., 2005, 2009). Although this empirical fit may prove to be fortuitous, it suggests that careful consideration of how the energy is deposited over the region where O_2 is formed could substantially extend the accuracy of the existing model at large ion ranges. Until then, it is of interest to determine whether this empirical adjustment would generally work when other parameters are varied (incidence angles, ions, energies, etc.), something that could be tested with additional laboratory studies.

3.4.5 Astrophysical Implications

Icy moons in the outer Solar System are bombarded with charged particles of varying energies that can erode and alter the composition of the surface ice. For Europa, an icy moon of Jupiter, Cassidy *et al.* (Cassidy et al., 2013) used results from previous laboratory studies to estimate the sputtering rate of the surface H_2O, as well as the sputtering rate of radiolytically-produced H_2 and O_2. They found that while the majority of the sputtered H_2O is caused by fast S^{n+} ions, the sputtered O_2 and H_2 are primarily caused by slower O^{n+} and S^{n+} ions, which not only deposit substantial energy near the surface where these products are primarily formed, but also bombard the surface at a significantly higher rate than do the fast ions (Cassidy et al., 2013). Our new data here, which suggests that the sputtered O_2 produced by low-energy ions at the higher temperatures relevant to Europa (Spencer et al., 1999) is about a factor of five lower than current theoretical predictions (assuming the use of Q = 0.06 eV), suggests that contributions from

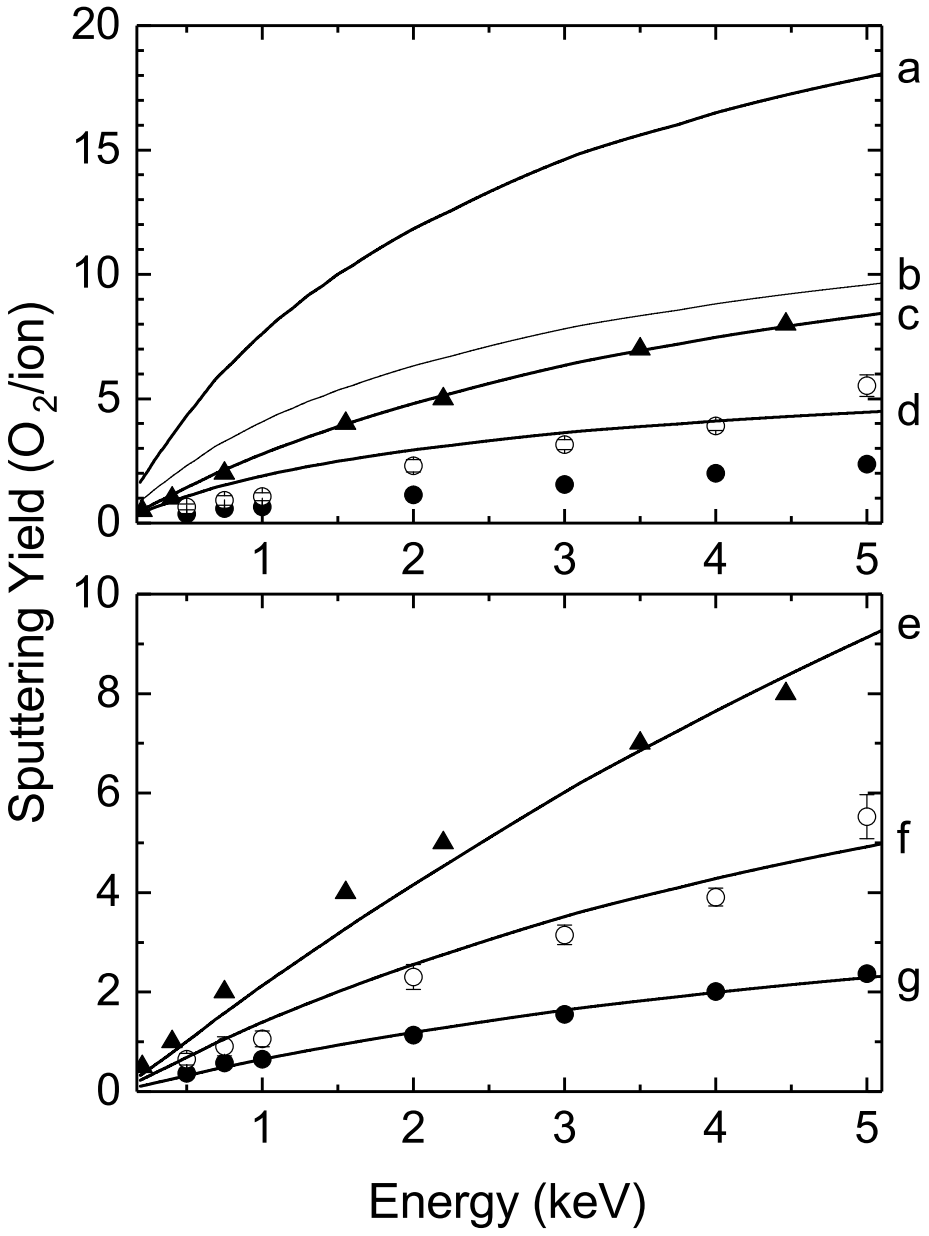

Figure 3.7: Comparison of our derived O_2 total sputtering yields at 40 K (•) and 120 K (○), as well as those given in Teolis *et al.* 2010 (▲) with the yields predicted from equation 3.4. Top: solid lines (a-d) correspond to using equation 3.4 along with the best fit parameters (g_0, x_0, Q, T, β): a) 0.005 O_2 eV^{-1}, 29 Å, 0.06 eV, 120 K, 0^0; b) 0.005 O_2 eV^{-1}, 29 Å, 0.07 eV, 120 K, 0^0; c) 0.005 O_2 eV^{-1}, 29 Å, 0.07 eV, 12 K, 60^0; d) 0.005 O_2 eV^{-1}, 29 Å, 0.07 eV, 40 K, 0^0. Bottom: solid lines (e-g) correspond to fits after modifying equation 3.4 (see text) along with the best fit parameters: (g_0, x_0, Q, T, β): e) 0.001 O_2 eV^{-1}, 90 Å, 0.07 eV, 12 K, 60^0; f) 0.001 O_2 eV^{-1}, 90 Å, 0.07 eV, 120 K, 0^0; g) 0.001 O_2 eV^{-1}, 90 Å, 0.07 eV, 40 K, 0^0.

these low-energy ions may have been significantly overestimated. For the time being, our new empirical fit may allow for more accurate predictions of sputtering yields. However, we point out that accurate modeling of the sputtering of extraterrestrial icy surfaces needs to take into account other factors (e.g., presence of a regolith, possibility of redeposition, and temperature variations), besides the sputtering yield. Thus, a more quantitative assessment on the degree to which our new laboratory data, as well as our new empirical estimate would alter previous estimates of O_2 erosion rates will require future modeling efforts.

3.5 Conclusions

We report sputtering yields for 0.5 - 5 keV Ar^+ at irradiation temperatures between 40 and 120 K. Below 80 K, our total sputtering yields cluster around the theoretical sputtering yields predicted by the Famá *et al.* 2008 model and are generally consistent with previous laboratory studies. In addition, we also estimate the sputtering yield of radiolytically produced O_2 as a function of energy for temperatures between 40 and 120 K. At 120 K, we find that the O_2/H_2O sputtered ratio increases nearly linearly with the ion range from about 0.15 to 0.5, which we attribute to the ions stopping at depths where O_2 is still efficiently being produced below the surface, consistent with previous depth profiling studies. Although our O_2 sputtering results agree well with the only comparable laboratory study, we find that theoretical models over predict the values by a factor of three or more, which is likely a consequence of the assumption that our more highly penetrating ions deposit energy uniformly throughout the sample. However, we find that making a small adjustment to this model allows us to fit the experimental data to within $\sim$ 10% in most cases and no worse than 30% in any case. Although the adjustment is primarily empirical, it could be useful to refine models predicting the sputtering of O_2 in icy extraterrestrial environments. This may be particularly important for Europa, where low-energy ions are predicted to be the primary ion producing O_2 from sputtering of the surface H_2O-ice.

3.6 Acknowledgements

This research was supported by NSF Grant # 1821919. Upon acceptance, all data will be stored in Northern Arizona University's long-term public access data archive located at https://openknowledge.nau.edu/. Currently, the data is located on our laboratory website: http://www.physics.nau.edu/ loeffler/Submitted-data.html

Chapter 4

Titan in Transit: Ultraviolet Stellar Occultations Reveal Complex Atmospheric Structure

Patrick D. Tribbett[1,2], Tyler D. Robinson[1,2,3], Tommi T. Koskinen[4]

This is the Accepted Manuscript version of an article accepted for publication in The Planetary Science Journal. IOP Publishing Ltd is not responsible for any errors or omissions in this version of the manuscript or any version derived from it. The Version of Record is available online at `https://iopscience.iop.org/article/10.3847/PSJ/abf92d/meta`.

4.1 Abstract

Transit spectroscopy is a key tool for exoplanet atmospheric characterization. However, transit spectrum observations can be limited by aerosol extinction when gas opacities are weak. The ultraviolet wavelength range contains a variety of strong molecular and atomic features, potentially enabling gas species detection even when atmospheric hazes are present. To understand the interplay between aerosol extinction and ultraviolet molecular opacities, we investigate transmission through the atmosphere of Saturn's moon Titan during an occultation observed with the Ultraviolet Imaging Spectrometer (UVIS) aboard the National Aeronautics and Space Agency (NASA) *Cassini* orbiter. We analyze the derived ultraviolet transit spectrum of Titan using exoplanet-relevant atmospheric retrieval models that both include and exclude treatments for hazes. Our retrieved gas column densities are consistent with previous studies analyzing UVIS occultation data. Despite the apparent haze impact on the underlying occultation data, our treatments fail to correctly characterize the haze in fits derived from simulated transit observations. This suggests that oversimplified haze parameterizations can hinder detection of atmospheric hazes in transit. Our work indicates that continued characterization of exoplanets in the ultraviolet wavelength regime can provide novel atmospheric constraints even if transit spectra are dominated by haze extinction at longer wavelengths.

Keywords: Transmission spectroscopy (2133); Bayesian statistics (1900); Stellar occultation (2135); Saturnian satellites (1427); Exoplanets (498)

[1]Department of Astronomy and Planetary Science, Northern Arizona University, PO Box 6010, Flagstaff, AZ 86011, USA
[2]Habitability, Atmospheres, and Biosignatures Laboratory, Northern Arizona University, Flagstaff, AZ 86011, USA
[3]NASA Astrobiology Institute's Virtual Planetary Laboratory, University of Washington, Box 351580, Seattle, WA 98195, USA
[4]Lunar and Planetary Laboratory, University of Arizona, 1629 E. University Blvd., Tucson, AZ 85721, USA

4.2 Introduction

Understanding the atmospheres of exoplanets provides essential insight into the formation, evolution, and potential habitability of these systems (Seager & Deming, 2010; Madhusudhan, 2019). Over the last two decades, transit spectroscopy (Seager & Sasselov, 2000; Brown, 2001; Hubbard et al., 2001) has emerged as the leading technique for characterizing exoplanet atmospheres. Here, atmospheric opacity sources can lead to small variations in the wavelength-dependent dimming of a stellar host during an exoplanet transit event. Despite the subtle nature of this effect, spectroscopic transit observations have yielded detections of atmospheric species in a diversity of exoplanet atmospheres (Charbonneau et al., 2002; Tinetti et al., 2007; Swain et al., 2008; Stevenson et al., 2010; Line et al., 2014; Fraine et al., 2014; Sing et al., 2016; Benneke et al., 2019; Tsiaras et al., 2019).

Of course, not all spectroscopic transit observations have revealed atmospheric features. Especially for lower-mass exoplanets, observations have sometimes revealed flat, featureless transit spectra (Kreidberg et al., 2014; Knutson et al., 2014; de Wit et al., 2016), at least to within measurement uncertainties. Here, the presence of high altitude aerosols is often used to explain such flat transit spectra. As the transit geometry implies that transit spectra probe long pathlengths along the limb of an exoplanet, even hazes or clouds with small vertical optical depths can appear opaque (Fortney, 2005).

In theory, observing transit spectra in wavelength ranges where molecular or atomic opacities are relatively large will probe the upper reaches of exoplanet atmospheres, thereby potentially avoiding the obscuring effects of hazes and providing stronger detections of atmospheric species. This, for example, leads to a key strength of NASA's upcoming *James Webb Space Telescope (JWST)* (Gardner et al., 2006), whose spectral coverage overlaps strong molecular rotation-vibration bands in the near- and mid-infrared with relevance to exoplanet transit spectra (Deming et al., 2009; Beichman et al., 2014; Greene et al., 2016; Barstow & Irwin, 2016; Batalha & Line, 2017). Another key wavelength regime with the potential for strong molecular and atomic opacities—the ultraviolet—was originally suggested as a range with likely high utility (Hubbard et al., 2001) and has recently been exploited to study the atmospheres of WASP-121 b (Sing et al., 2019) and HAT-P-41 b (Wakeford et al., 2020), both building on earlier efforts in the ultraviolet for HD 189733 b by Sing et al. (2011). In these works, Sing et al. (2019) observe strong Fe II and Mg II features for WASP-121 b, while both Wakeford et al. (2020) and Sing et al. (2011) observe sloped transit spectra in the ultraviolet that are consistent with hazes for HAT-P-41 b and HD 189733 b, respectively. In new modeling work, Lothringer et al. (2020) detailed how strong opacities at ultraviolet wavelengths due to metals and metal-bearing species could help probe rainout chemistry in exoplanet atmospheres.

To further explore the interplay between aerosol extinction and absorption due to atmospheric gas species

in ultraviolet transit observations, we turn to Titan. For Titan, solar photons, solar wind, galactic cosmic rays, and magnetospheric charged particles drive pervasive atmospheric chemistry resulting in multitudes of higher order hydrocarbons and the carbon nitrogen aggregate tholins (Yung et al., 1984; Lavvas et al., 2008; Toublanc et al., 1995; Podolak et al., 1979; Carrasco et al., 2018; Vuitton et al., 2009; Lavvas et al., 2011). Additionally, Titan has a seasonally dependent detached haze layer located between 300 and 500 km altitude (or at pressures lower than 10^{-5} bar; Lavvas et al., 2009; West et al., 2011, 2018) that is potentially analogous to the hazes responsible for some featureless exoplanet transit spectra. However, it should be noted that due to drastically different thermal conditions, aerosol haze composition and particle sizes for hot exoplanets may differ from those seen in Titan's atmosphere (Lavvas & Koskinen, 2017; Lavvas et al., 2019; Moran et al., 2020). For a recent review of Titan's atmosphere and climate, see Hörst (2017).

Here, we use Titan atmospheric stellar occultation observations from the Ultraviolet Imaging Spectrometer (McClintock et al., 1993; Esposito et al., 2004) aboard NASA's *Cassini* spacecraft to effectively study a hazy world in transit. These occultation data are converted to exoplanet-like transit spectra following techniques developed by Robinson et al. (2014) and Dalba et al. (2015). Critically, these occultation observations have already been used to derive key atmospheric properties for Titan, including number density profiles for various trace hydrocarbons (Koskinen et al., 2011), thereby helping to confirm aspects of our transit spectral analysis. Moreover, it has been suggested that Titan's hydrocarbon rich atmosphere may be representative of a fairly common class of exoplanets, reinforcing the necessity of understanding the interplay of molecular opacities and haze extinction (Lunine, 2010).

Below, we begin by describing our adopted occultation dataset and technique for converting this to an ultraviolet transit spectrum of Titan. We then present the details of an atmospheric retrieval model designed to interpret our derived transit spectrum. Following our retrieval analyses, we discuss the impact of Titan's detached haze layer on transit spectra. Finally, we conclude by interpreting our results with respect to the current state of exoplanet observations.

4.3 Methods

The following subsections describe our approach to data reduction, modeling, and analysis. First, we briefly describe the underlying occultation dataset and how this was transformed into an effective transit spectrum for Titan. Next, we present a simple forward model that we use to fit our ultraviolet transit spectrum of Titan. Finally, we describe our Bayesian approach to atmospheric characterization using our simulated transit spectrum and forward model.

4.3.1 Data Reduction and Transformation

Occultation data were acquired with the far-ultraviolet channel of the UVIS instrument on board the NASA *Cassini* orbiter, as detailed in Koskinen et al. (2011). Spectra from the far-ultraviolet channel span 110–190 nm with a spectral resolution of 0.28 nm. Further details regarding the optical specifications and design of the UVIS instrument are described in Esposito et al. (2004). Data used in our analyses are from *Cassini* flyby T41 I on 23 February 2008, where occultation observations probed 6°S. Of the 12 independent occultation observations presented in Koskinen et al. (2011), the T41 I dataset is the best option for both high signal-to-noise-ratio data as well as a strong signature of two detached haze layers. Transmissivity as a function of wavelength and altitude were calculated based on the ratio of the transmitted stellar spectrum along the instrument line of sight and the unocculted reference stellar spectrum (Koskinen et al., 2011). This inherently requires that all spectral variations are atmospheric in nature. It should be noted that variations in host star flux also affect the light transmitted through the atmosphere, which is discussed in more detail in Section 4.5. Quoted observational uncertainties are derived based on photon counting (Esposito et al., 2004; Koskinen et al., 2011). The altitude- and wavelength-dependent transmission data from *Cassini* flyby T41 I are shown in Figure 4.1. Note the two distinct vertically-isolated opacity sources in the atmosphere near 500 km and 700 km. The lower region corresponds to the detached haze layer within Titan's atmosphere (Rages & Pollack, 1983; Porco et al., 2005). The upper region can also be attributed to higher order hydrocarbons, and the structure may be due to atmospheric propagation of gravity waves (Strobel, 2006; Koskinen et al., 2011). We note that the chemistry and dynamics of this atmospheric haze are complex and are coupled to aspects of the deep atmosphere to which our study is not sensitive (West et al., 2018).

Although the process of computing transit spectra from altitude-dependent transmissivities inherently smooths over the smaller-scale effects induced by gravity waves, how gravity waves may manifest in transit analyses merits some discussion. Gravity waves transfer momentum and energy within an atmosphere, which can cause variation in thermal profiles and, consequently, density profiles of some species (Strobel, 2006; Koskinen et al., 2011). These perturbations can be substantial, particularly for hot, rotationally-locked exoplanets (Watkins & Cho, 2010). Local increases in wind speed due to the deposition of energy via gravity waves may result in Doppler shifted spectral features. Doppler shifted spectral features in exoplanet transmission spectra have been previously reported for wind speeds of order 1–10 km s^{-1} (Snellen et al., 2010; Kempton & Rauscher, 2012).

The transit depth spectrum corresponding to the altitude-dependent atmospheric transmission data was calculated following methods described in Robinson et al. (2014). Given the wavelength-dependent trans-

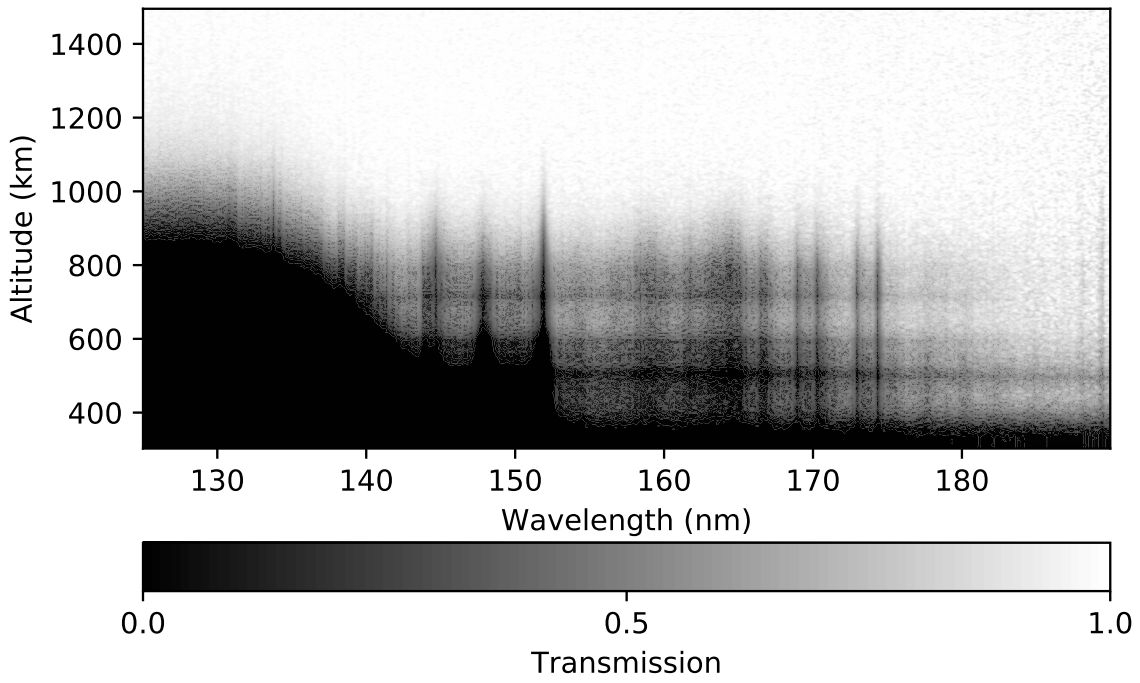

Figure 4.1: Altitude- and wavelength-dependent transmission data for Titan's atmosphere from *Cassini* flyby T41 I. An altitude of 0 km corresponds to Titan's average surface radius (2575 km), and darker colors indicate lower transmission. We note that these data are also shown in Koskinen et al. (2011) (their Figure 8a).

missivity ($t_{\lambda,i}$) on a grid of impact parameters (b_i; taken as the radial distance of closest approach for a ray), the effective area of the Sun that would be blocked by an atmospheric annulus spanning levels i to $i+1$ if Titan were observed in transit is given by,

$$\Delta A_{\lambda,i} = (1 - \bar{t}_{\lambda,i}) \cdot \pi \left(b_{i+1}^2 - b_i^2 \right) \ , \tag{4.1}$$

where $\bar{t}_{\lambda,i} = \left(t_{\lambda,i+1} + t_{\lambda,i} \right) / 2$. The wavelength-dependent transit depth is then computed by summing over annuli, with,

$$\left(\frac{R_{\mathrm{p},\lambda}}{R_\odot} \right)^2 = \left(\frac{R_\mathrm{p}}{R_\odot} \right)^2 + \frac{1}{\pi R_\odot^2} \sum_i \Delta A_{\lambda,i} \ , \tag{4.2}$$

where R_p is the solid surface radius of the planet or, for worlds without a solid surface, a sufficiently deep reference radius that all transmissivity values have reached zero. Corresponding transit depth uncertainties are calculated following standard Gaussian error propagation techniques and are described further in Section 4.4.1 (Taylor, 1997). Equation 4.2 can be solved for the wavelength-dependent planetary radius ($R_{\mathrm{p},\lambda}^2$), and subtracting the solid surface radius of Titan from this yields the so-called effective transit altitude (or height), z_{eff}. Unlike in Robinson et al. (2014), losses due to refraction can be ignored here as the occultation observations probe much greater altitudes (i.e., very low pressures and number densities). In all analyses, UVIS data between 185-190 nm are omitted due to higher-order hydrocarbon features for which we do not have sufficient absorption cross section data. Species suspected to be responsible for these unidentified features include toluene and xylene (Koskinen et al., 2011).

Figure 4.2 shows the transit spectrum that results from application of the previously described techniques, depicted here as effective transit altitude to help indicate where (vertically) in the atmosphere the transit spectrum probes. Despite the detached haze layers present over this altitude regime, the modeled spectrum is rich with molecular features. Several notable features include the broad methane absorption centered near 130 nm, acetylene and diacetylene features between 140 nm and 150 nm, and the ethylene features around 170 nm.

As a check of our UVIS-derived transit spectrum, we generated a transit depth spectrum from the species slant path column number density profiles inferred from our adopted occultation data in Koskinen et al. (2011). Here, the inferred slant column number densities were combined with known gas opacities to compute the transmissivities for Equation 4.1. Figure 4.3 shows the transit depth spectra derived from the UVIS data and from the Koskinen et al. (2011) species profiles. The dark and light blue spectra correspond to transit depth spectra derived with and without the tholin haze profile, which helps isolate and quantify the impact of haze on the UVIS-derived transits spectrum. Notably, haze impacts the transit depth spectrum

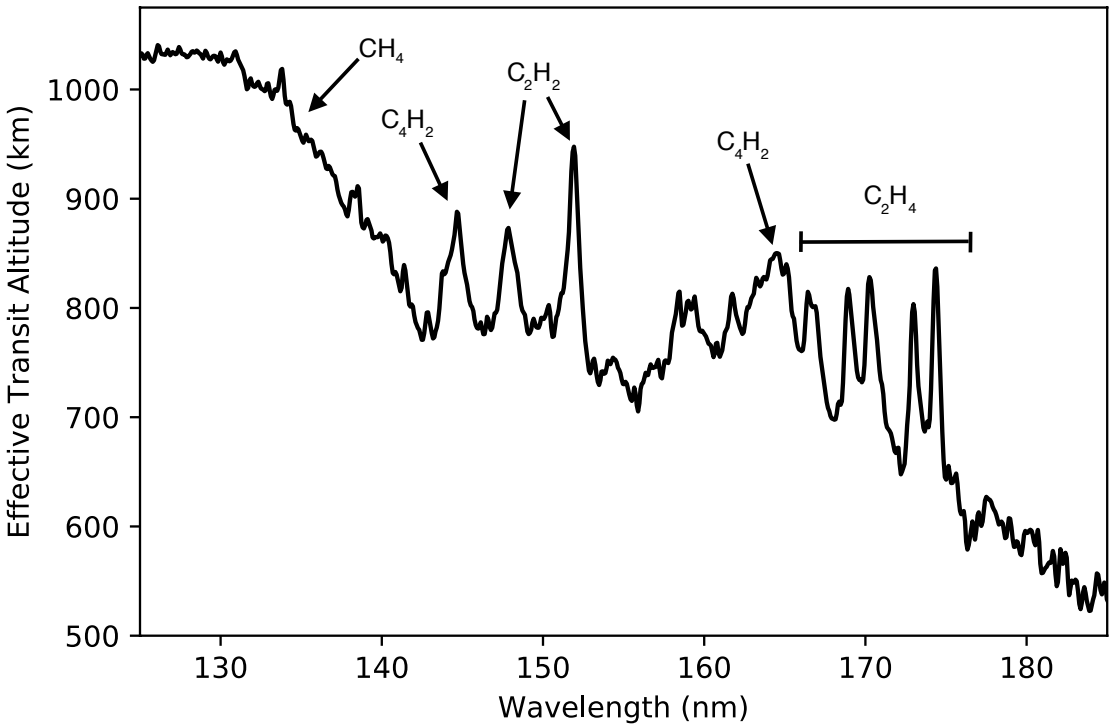

Figure 4.2: Effective transit altitude for Titan from *Cassini* flyby T41 I occultation data.

at wavelengths where the altitudes probed are at or below roughly 800 km. This observed influence of haze on the transit spectrum will be used in later sections to help explore the efficacy of cloud parameterizations often used in the exoplanet atmospheric retrieval literature.

4.3.2 Forward Model

We seek to define a forward model that: (1) will enable retrievals of key atmospheric parameters when applied to our derived transit depth spectrum, and (2) is analogous in complexity to similar models for exoplanets. Following Benneke & Seager (2012) and Robinson et al. (2014), if the number density of an extincting species is distributed exponentially with scale height H in an atmosphere, and if the extinction cross section for this species is pressure-independent, then the optical depth integrated along a slant path for an impact parameter b and for a single species is given by

$$\tau_{\lambda,j}(b) = 2N_{0,j}\sigma_{\lambda,j}\frac{b}{H}K_1\left(\frac{b}{H}\right)e^{R_0/H} \ , \tag{4.3}$$

where a sub-script 'j' indicates the species, $N_{0,j}$ is the vertical column number density above a sufficiently deep reference radius R_0, $\sigma_{\lambda,j}$ is the absorption cross section for the species, and K_n is a modified Bessel function of the second kind. Assuming all species are distributed with the same scale height, summing over all species yields the total slant optical depth,

$$\tau_\lambda(b) = 2\frac{b}{H}K_1\left(\frac{b}{H}\right)e^{R_0/H}\cdot\left(\sum_j N_{0,j}\sigma_{\lambda,j}\right) \ . \tag{4.4}$$

Given the total slant optical depth, and assuming that extinction optical depth is equivalent to absorption optical depth (see Robinson et al., 2017), the transit depth is obtained by integrating over impact parameters,

$$\left(\frac{R_{\mathrm{p},\lambda}}{R_\odot}\right)^2 = \left(\frac{R_0}{R_\odot}\right)^2 + \frac{2}{R_\odot^2}\int_{R_0}^{\infty}\left[1-e^{-\tau_\lambda(b)}\right]bdb \ . \tag{4.5}$$

Finally, for numerical implementation it is convenient to define a dimensionless parameter, $\beta = b/H$, so that,

$$\tau_\lambda(\beta) = 2\beta K_1\left(\beta\right)e^{R_0/H}\cdot\left(\sum_j N_{0,j}\sigma_{\lambda,j}\right) \ , \tag{4.6}$$

and,

$$\left(\frac{R_{\mathrm{p},\lambda}}{R_\odot}\right)^2 = \left(\frac{R_0}{R_\odot}\right)^2 + 2\frac{H^2}{R_\odot^2}\int_{R_0/H}^{\infty}\left[1-e^{-\tau_\lambda(\beta)}\right]\beta d\beta \ , \tag{4.7}$$

where a grid of β values can be straightforwardly designed to ensure vertical resolution that is (at least) finer than H. It is important to note that our forward model is consistent with common assumptions made within the exoplanet retrieval literature of isothermal atmospheres and constant mixing ratios of each species (e.g., Heng & Kitzmann, 2017).

Following Koskinen et al. (2011), our gaseous opacity sources emphasize hydrocarbon and nitrile species of substantial number densities in Titan's atmosphere and that have non-negligible absorption cross sections at deep ultraviolet wavelengths. Species used in this study are shown in Table 4.1 along with wavelength coverage, measurement temperature, and a reference paper for our adopted opacity data. Opacity data were selected on the basis of wavelength range and temperature relevance. Absorption cross sections for the eight species used in this study are shown in Figure 4.4. To treat opaque atmospheric haze layers within our forward model, we defined an altitude below which the optical depth is inflated to simulate complete extinction.

We explore two simple haze treatments in our forward model. Though we exclude a treatment of the haze chemistry or diffusion within the atmosphere, which is known to seasonally alter Titan's ultraviolet

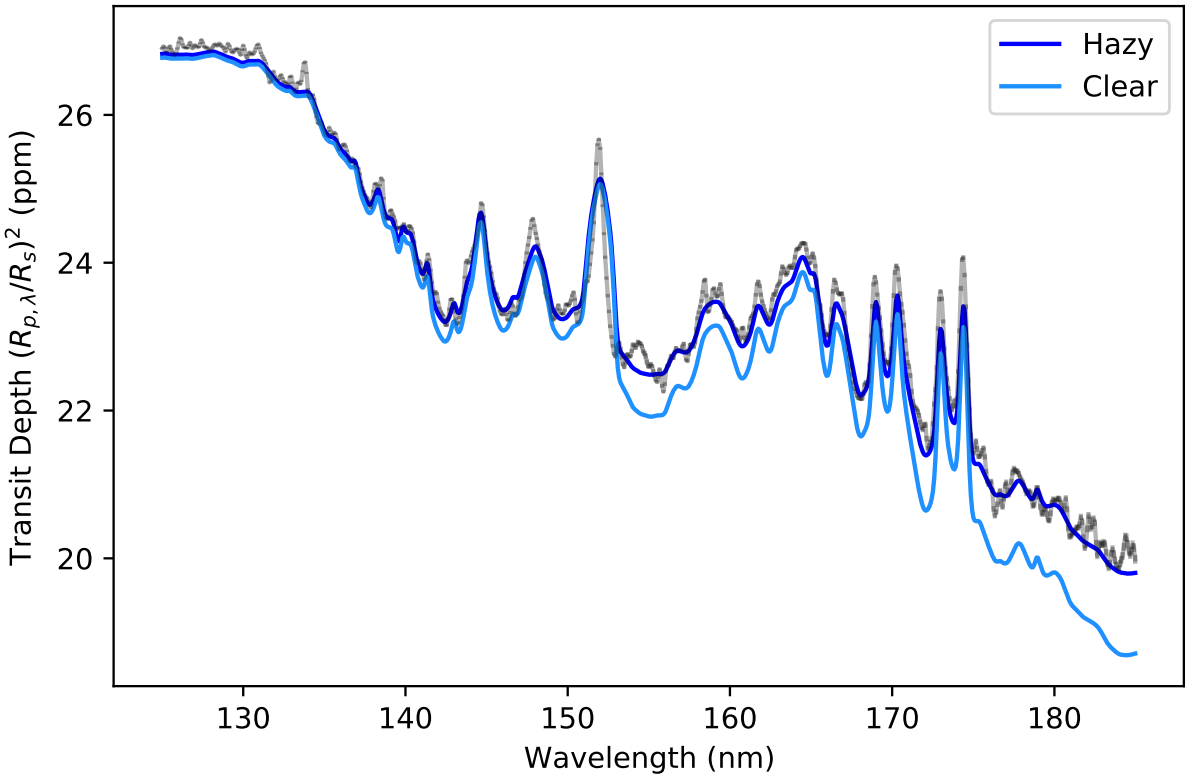

Figure 4.3: The UVIS-derived Titan transit spectrum (black), and models that do (dark blue) and do not (light blue) include the spectral impacts of a high-altitude haze detected in Koskinen et al. (2011). Models assume altitude-dependent chemical compositions from fits in Koskinen et al. (2011).

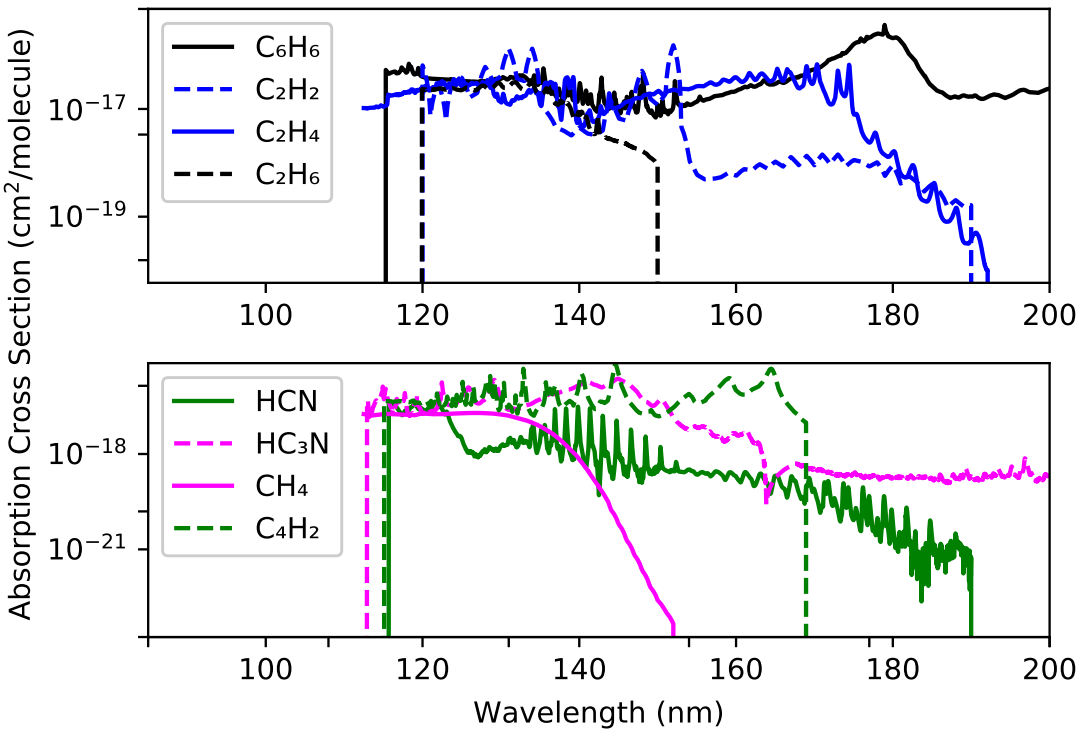

Figure 4.4: Absorption cross sections for the hydrocarbons and nitriles of interest in this study.

Species	Wavelength (nm)	Temperature (K)	Reference
Benzene (C_6H_6)	115–205	298	Capalbo et al. (2016)
Acetylene (C_2H_2)	120–190	150	Wu et al. (2001)
Ethylene (C_2H_4)	105–115	298	Lu et al. (2004)
	115–192	140	Wu et al. (2004)
Ethane (C_2H_6)	120–150	150	Chen & Wu (2004)
Methane (CH_4)	102–119	298	Ditchburn (1955)
	120–142	150	Chen & Wu (2004)
	143–152	298	Lee et al. (2001)
Hydrogen Cyanide (HCN)	115–190	255	Ferradaz et al. (2009)
Cyanoacetylene (HC_3N)	112–230	298	Koskinen et al. (2011)
Diacetylene (C_4H_2)	115–168	173	Ferradaz et al. (2009)

Table 4.1: Absorbing species included in our forward model along with wavelength range, measurement temperature, and a reference for the opacity data.

and visible spectrum, this approach will determine whether a simple haze structure can be extracted from the ultraviolet and visible transit spectrum of a Titan-like exoplanet without a priori information of the haze chemistry. Our two-parameter haze model specifies the lower boundary of a haze layer z_h, measured above R_0 as well as a grey haze vertical optical depth τ_h, which is distributed uniformly over one scale height. Slant optical depths are computed following the path distribution approach presented in (Robinson, 2017). A one-parameter haze model simply assumes the atmosphere is opaque for impact parameters that probe below z_h (see, e.g., Bétrémieux & Swain, 2016; Kempton et al., 2017), which serves to block all light that would probe atmospheric layers deeper than the haze altitude and, as we show later, is instructive for interpreting results from our two-parameter haze treatment. These simplified haze treatments are typical of many exoplanet atmospheric retrievals (Barstow, 2020, 2021).

4.3.3 Markov Chain Monte Carlo Implementation

We retrieve atmospheric parameters by fitting our forward model to our UVIS-derived transit spectrum using a standard Markov chain Monte Carlo (MCMC) approach to Bayesian inference. Specifically, we adopt the widely-used MCMC tool `emcee`, developed by Foreman-Mackey et al. (2013). Bayesian statistics describe the posterior conditional probability distribution of a set of parameters using the prior probabilities of those same parameters and their likelihood probabilities given the data. The posterior distribution enables inference of physical parameters as well as uncertainties on these parameters.

Model Parameter	Description	Units	Prior
H	Scale Height	km	$0 < H$
R_0	Reference Radius	km	$0 < R_0$
$\log N_j$	Column Number Density for Species j	$\log \mathrm{cm}^{-2}$	$12 < \log N_j < 24$
z_h	Haze Layer Altitude above R_0	km	$0 < z_\mathrm{h}$
τ_h	Haze Layer Optical Depth	-	$0 < \tau_\mathrm{h} < 10$

Table 4.2: Model parameters, their units, and our adopted priors. Column number densities are measured vertically above R_0.

Briefly, Bayes' Theorem states,

$$P(\theta|y) = \frac{P(y|\theta)P(\theta)}{P(y)} \ , \tag{4.8}$$

or

$$P(\theta|y) \propto P(y|\theta)P(\theta) \ , \tag{4.9}$$

where y are the observed data, θ is our set of atmospheric parameters (i.e., our atmospheric state parameters), $P(\theta)$ is the prior probability for these parameters, and $P(y|\theta)$ is the so-called likelihood function. The value of the likelihood function depends on the data, its associated errors, and the atmospheric state parameters. When evaluating the likelihood function, parameter values that result in poorly fit data are penalized. In our approach, the log of the likelihood function (often called the log-likelihood) is given by,

$$\ln P(y|\theta) = -\frac{1}{2}\sum_k \frac{[y_k - f(\theta)]^2}{\sigma_k^2} + \ln 2\pi\sigma_k^2 \ , \tag{4.10}$$

where y_k is the kth spectral data point, σ_k is the uncertainty for this data point, and $f(\theta)$ is the transit depth (forward) model. We adopt uninformed prior probability distributions that simply set physical limits on the values that each parameter can take. Model free parameters, their descriptions, and corresponding prior probability limits for our analyses are shown in Table 4.2. Our prior probabilities are largely based on the physical limits of the properties that the parameters represent (e.g., all lengths cannot be smaller than zero). Column number densities are retrieved in log space to ensure full exploration of parameter space over multiple orders of magnitude. We note that the lack of prior knowledge regarding the expected range of exoplanet column number densities would require careful attention to ensure the priors do not unphysically truncate the posterior distributions.

In later sections, we use the Bayesian Information Criterion (BIC) to determine if the addition of a haze layer is warranted in our forward model. The BIC has become increasingly common in the astronomy

community by providing a robust means for model comparisons (e.g., Littenberg & Cornish, 2009; Feng et al., 2016; Sharma, 2017), and is defined by,

$$\mathrm{BIC} = -2 \ln P\left(y|\theta\right)_{\max} + \nu \ln N \tag{4.11}$$

where ν is the number of model free parameters, N is the number of spectral data points, and $P(y|\theta)_{\max}$ is the maximized log likelihood. The change in the BIC, ΔBIC, between two models is then evaluated to support or reject adding additional parameters (e.g., z_{h} and τ_{h} in our case) to improve the model fits. The model with a lower BIC value is preferred over another. Following Kass & Raftery (1995), ΔBIC values between 0 and 2 suggest that the evidence against the higher BIC model is "not worth more than a bare mention." Values between 2 and 6 suggest positive evidence against the larger BIC model. Values between 6 and 10 suggest strong evidence against the larger BIC model. Values greater than 10 suggest very strong evidence against the larger BIC model. A more detailed description of the BIC and how to compare models can be found in Kass & Raftery (1995).

4.4 Results

Clear sky (i.e., haze-free) and hazy models were applied within our retrieval framework to our derived transit spectrum of Titan. As discussed immediately below, retrievals were initially performed assuming only photon counting errors in the observations. Later retrievals — more analogous to an exoplanet case — were performed with inflated error bars. As described in Section 4.3.2, adopted haze models are simplified and similar to those used in some exoplanet atmospheric retrieval studies. Given that the haze has a notable impact on the transit spectrum (Figure 4.3), our hazy retrieval models offer an opportunity to test the utility of commonly-applied exoplanet cloud/haze parameterizations.

4.4.1 Error Scaling

We initially applied our clear sky and two-parameter haze retrieval models to the acUVIS-derived transit spectrum of Titan with only propagated photon counting errors. Initial occultation data errors are 1-σ uncertainties from Koskinen et al. (2011). Using Equations 1 and 2, and following standard Gaussian error propagation techniques described in Taylor (1997), these wavelength- and altitude-dependent transmissivity uncertainties ($\sigma_{t_{i,\lambda}}$) were mapped to effective transit altitude uncertainties following:

$$\sigma^2_{z_{\mathrm{eff}}} = \frac{1}{16 R^2_{\mathrm{p},\lambda}} \sum_i \left(b^2_{i+1} - b^2_i\right)^2 \sigma^2_{t_{i,\lambda}} \ . \tag{4.12}$$

Effective transit altitude uncertainties are then propagated to transit depth uncertainties with,

$$\sigma_{R_{\mathrm{p},\lambda}/R_{\odot}} = 2\frac{R_{\mathrm{p},\lambda}}{R_{\odot}^2}\sigma_{z_{\mathrm{eff}}} \ , \tag{4.13}$$

where z_{eff} is the effective transit altitude and $\sigma_{z_{\mathrm{eff}}}$ is the 1-σ effective transit altitude uncertainties. Figure 4.5 shows fitted spectra with uncertainties for the clear sky case. While the modeled spectra appear qualitatively reasonable, the reduced chi-squared for the clear sky best-fit model was 72.1. Similarly, the reduced chi-squared for the two-parameter haze best fit model was 72.2. Moreover, the probability this reduced chi-square value would occur by chance is infinitesimal, further indicating an over-simplified model or underestimated data error (Flannery et al., 1992). Here, quantitatively poor fits likely stem from a combination of incomplete opacity data and overly-simplified model assumptions. For the former, and as can be seen in Table 4.1, the laboratory opacity data are often measured in a temperature regime that is much warmer than Titan's upper atmosphere (which has characteristic temperatures of 150–200 K). Additionally, it is worth noting that both best-fit models (our work and Koskinen et al., 2011) struggle to reproduce the acetylene and ethylene features between 145–155 nm despite having cross section data for both species at Titan-relevant temperatures. This may reflect uncertainty in the cross section measurements, which are estimated to be at 10% or less (Wu et al., 2001, 2004). Regarding model assumptions, previous analyses of the UVIS occultation observations reveal that the absorbing gaseous species do not have number density profiles that follow simple exponential decreases with a uniform scale height (Koskinen et al., 2011), as is assumed in our model. A comparison of Figures 4.3 and 4.5 demonstrates the error associated with our model assumptions.

To produce better fits (as indicated by the reduced chi-squared) and to better mimic noisy exoplanet data, we opted to inflate the error bars on our transit spectrum via a uniform multiplicative scaling factor (as is a relatively common practice; Tremaine et al., 2002; Hogg et al., 2010; Foreman-Mackey et al., 2013; Line et al., 2015). Figure 4.6 demonstrates how increasing the data uncertainty affects the resulting reduced chi-squared for a best-fit clear sky model. Based on this analysis, we chose a multiplicative scaling factor of 8 to produce reduced chi-squared values reliably close to unity without losing spectral information and potentially overfitting the data. As is discussed later, error scaling does not impact any of the conclusions we draw from subsequent retrieval analyses.

4.4.2 Clear Sky Retrievals

Retrieved atmospheric parameters for the application of our clear sky model to the UVIS Titan transit spectrum with inflated uncertainties are shown in Figure 4.7. This so-called "corners" plot depicts, along the diagonal, the posterior distributions for all retrieved parameters marginalized over all other parameters.

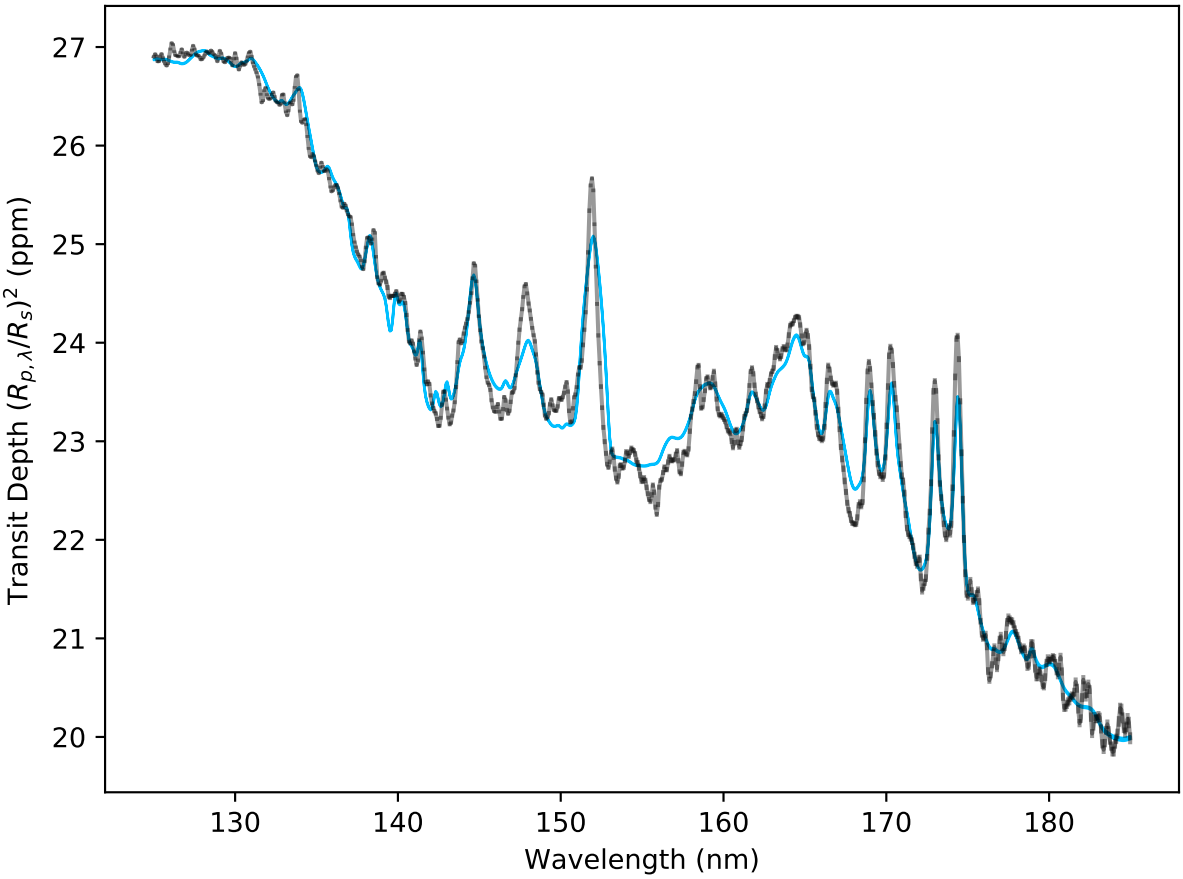

Figure 4.5: Titan transit depth spectrum is shown in black. Propagated error bars are included; however, they are small enough such that they are not visible on this scale. Modeled transit spectra from our clear sky retrieval analyses are shown as a 2-σ (95.5%) spread in blue.

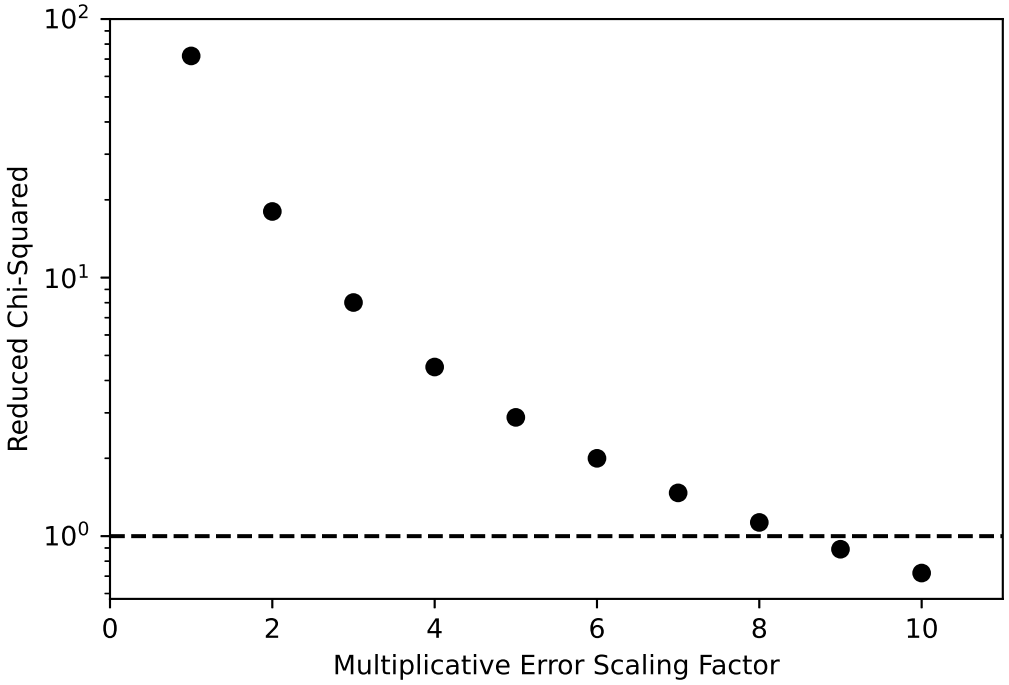

Figure 4.6: Reduced chi-squared values for the best-fit model from our retrieval framework when increasing the multiplicative error scaling factor on the UVIS-derived transit spectrum. The dotted line represents a reduced chi-squared of unity.

Off-axis plots show two-dimensional posterior distributions where all but two retrieved parameters have been marginalized over. For the one-dimensional marginal distributions, values at the 16th, 50th, and 84th percentile are indicated above each sub-plot (i.e., the distribution mean and $\pm$1-σ), and the reduced chi-squared for the best-fit model was 1.126. All one-dimensional marginal distributions are roughly Gaussian in shape. The reference radius (R_0) is anti-correlated with all gas column number densities over a narrow range of parameter space as roughly fixed number densities aloft can be maintained when the reference radius is increased but the column number densities down to this radius are decreased. These anti-correlations with R_0 then lead to correlations between all gas column number densities over narrow ranges of parameter space. Finally, Figure 4.8 shows the 1-σ (68.2%) and 2-σ (95.5%) spread in model spectra derived from our retrieval.

4.4.3 Hazy Retrievals

Marginalized posterior distributions for our two-parameter haze model applied to the UVIS-derived transit spectrum are shown in Figure 4.9. The resultant spectra are shown in Figure 4.10. As can be seen in the spectra, fits produced by the two-parameter haze model show little to negligible difference in quality as compared to the clear sky model. More quantitatively, the reduced chi-squared for the best-fit two-parameter haze model is 1.130, indicating that the models are nearly identical in their ability to fit the data.

Correlations between gas column number densities and the reference radius parameter in the two-parameter hazy model analysis are similar to those seen in the clear sky analysis. However, and as compared to the clear sky analysis, the two-parameter hazy one-dimensional posterior distributions are generally wider and non-Gaussian (excepting the scale height distribution). The detached haze vertical optical depth ($\tau_{\rm h}$) is poorly constrained, but is generally found to be optically thick in the horizontal (i.e., slant) direction. A tail in the marginal distribution for the reference radius (R_0) to smaller radii correlates with $z_{\rm h}$ to maintain the floor of the transit spectrum near 3,100 km, or about 500 km above the solid body radius of Titan, which corresponds to the deepest altitudes probed in our transit spectrum. This, in turn, leads to tails in the marginal distributions for the gas vertical column abundances towards larger values. Lastly, it should be noted that the primary benzene feature ($\sim$ 180 nm) probes near 500 km in the transit spectrum. For this reason, the distribution is likely impacted by the haze parameterization, which sets the floor of the transit spectrum near 500 km.

Results from our one-parameter haze model can be used to further understand the correlations and wide distributions seen in our two-parameter haze treatment. Marginalized posterior distributions from the application of our one-parameter model are shown in Figure 4.11 and the resulting spread in model spectra

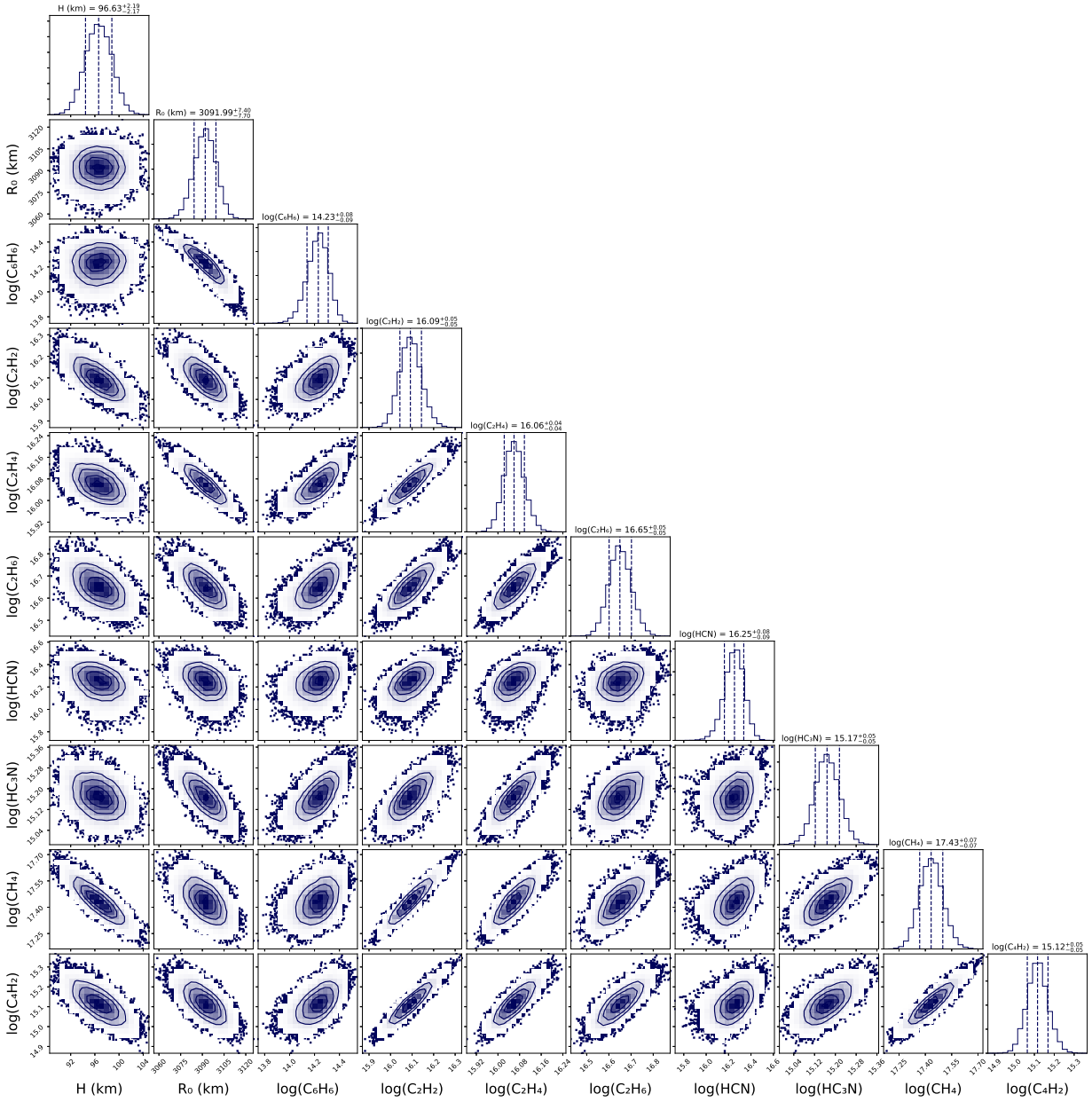

Figure 4.7: Marginalized posterior distributions for a clear sky retrieval analysis applied to the UVIS-derived transit data for Titan in Figure 4.2. Sub-plots along the diagonal show posterior distributions where all but a single parameter have been marginalized over, and distribution values at the 16th, 50th, and 84th percentile are indicated above each sub-plot. Off-diagonal sub-plots show posterior distributions where all but two parameters have been marginalized over.

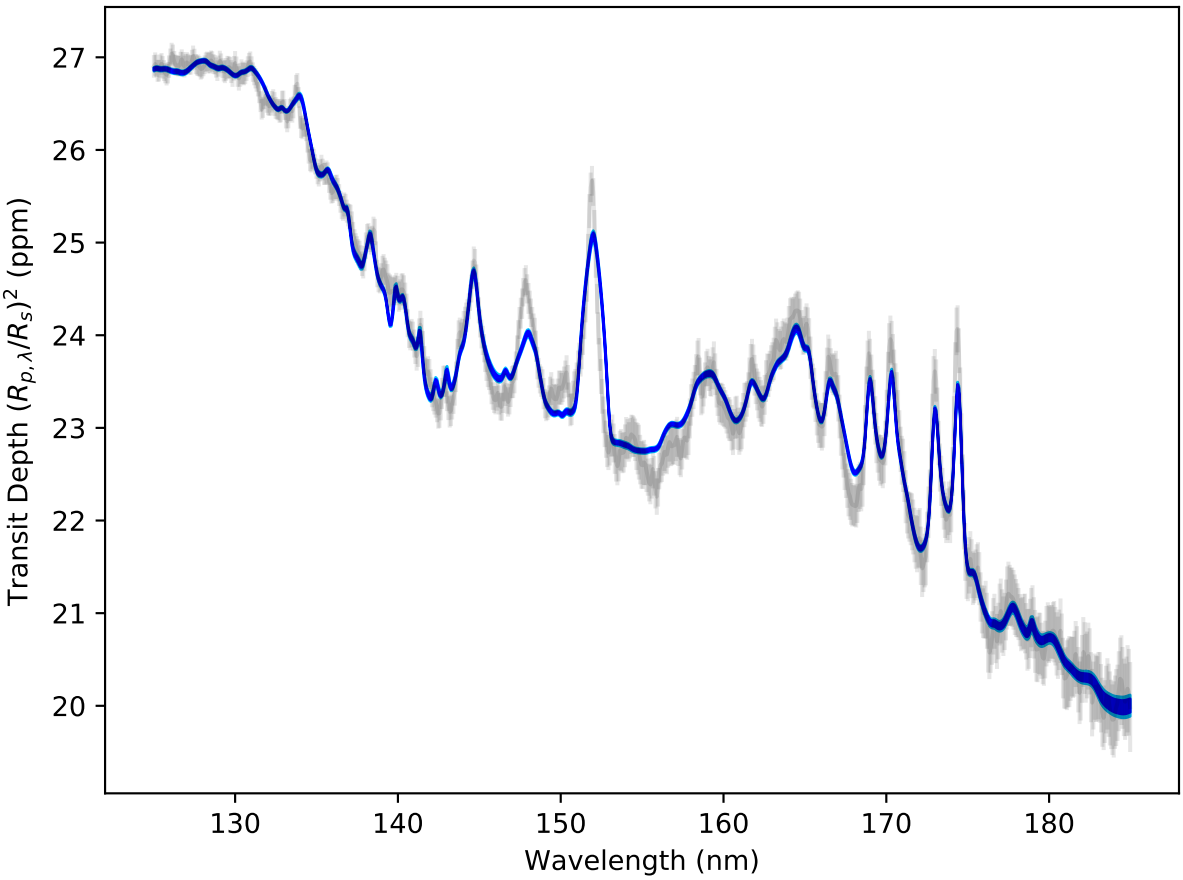

Figure 4.8: Titan transit depth spectrum with 8× inflated error bars (light grey). Modeled transit spectra from our clear sky retrieval analysis are shown as 1-σ (68.2%) and 2-σ (95.5%) spreads, dark blue and light blue respectively. Note that the difference between the 1-σ and 2-σ spreads is most discernible in the 175–185 nm range.

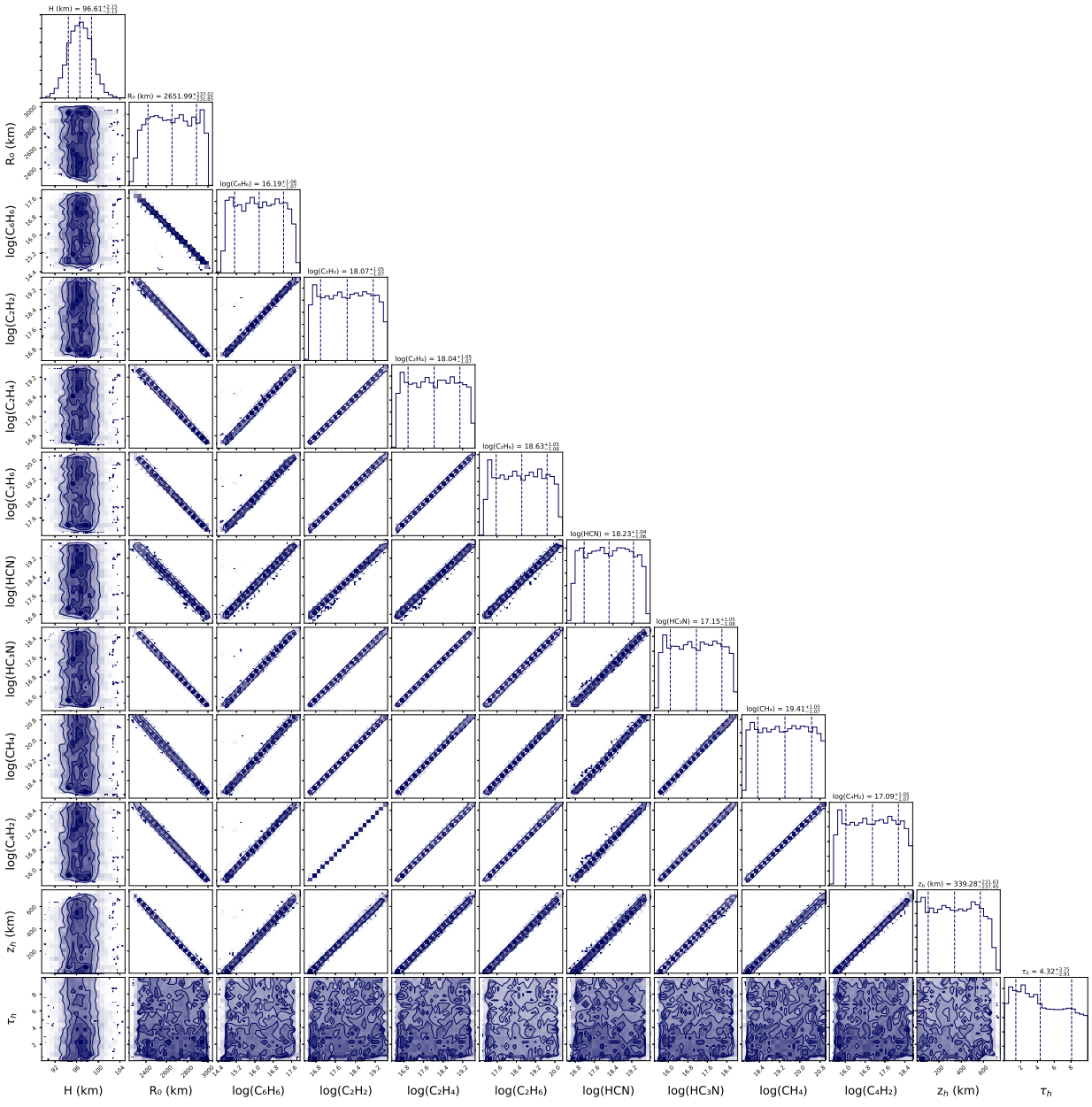

Figure 4.9: Same as Figure 4.7 except with the addition of a two-parameter haze treatment.

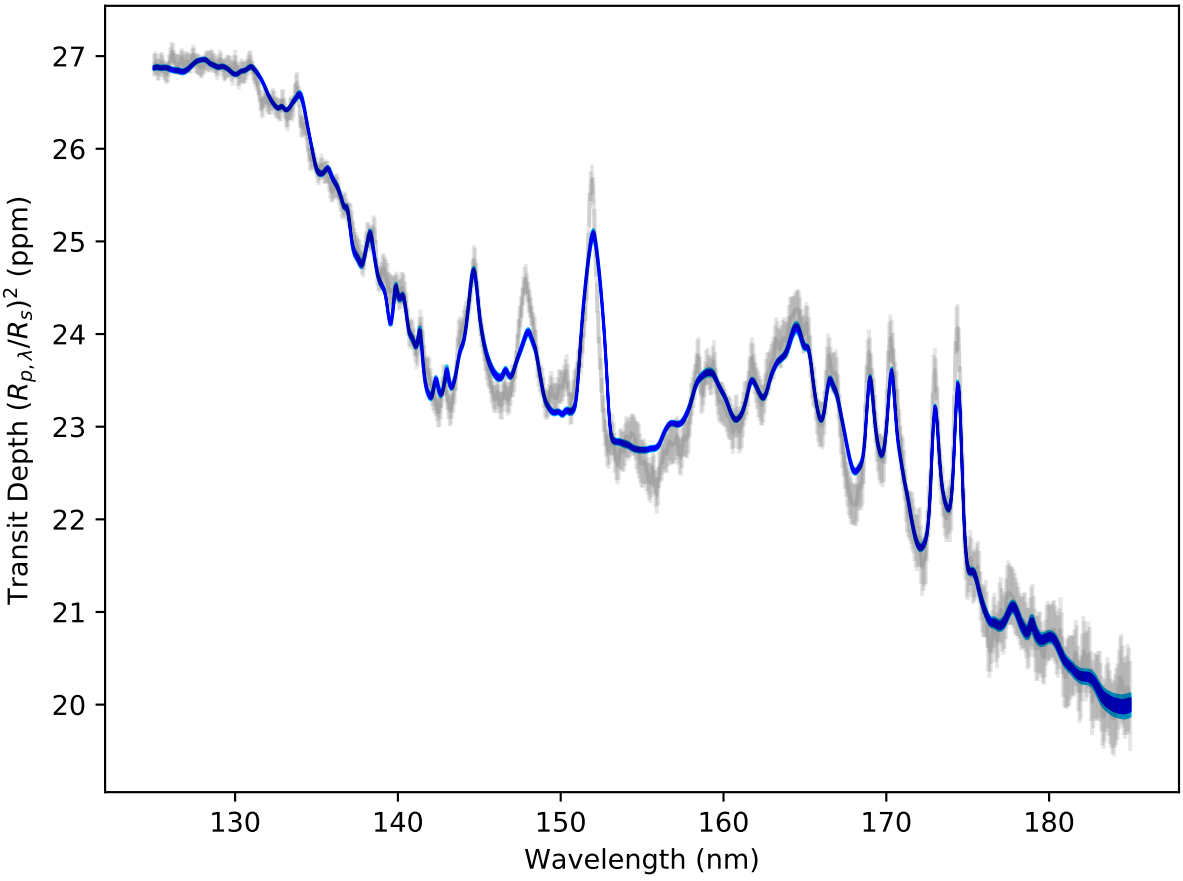

Figure 4.10: Same as Figure 4.8 except for retrieved spectra that include a two-parameter haze treatment.

are shown in Figure 4.12. Here, the reference radius and haze altitude combine to set the floor of the transit spectrum near 500 km above Titan's solid body radius. With the haze layer fixing the floor of the transit spectrum, R_0 can take on a wide range of values and, correspondingly, the column number densities also vary over a wide range of values. These behaviors are also seen in the two-parameter haze model results and are analogous to a degeneracy between the reference radius, pressure, and gas abundances discussed for retrievals applied to transiting exoplanets in Heng & Kitzmann (2017).

4.5 Discussion

Titan is a well-studied world in the Solar System, which enables intercomparisons between our retrieval analyses and previous works, as is discussed immediately below. Here, we also explore how the BIC parameter enables model selection amongst our various haze treatments (including haze-free models), and we discuss implications that stem from our non-detections of Titan's tholin haze in our retrievals. Finally, we describe how our transit spectrum results could apply to future exoplanet observations.

4.5.1 Comparisons to Previous Studies

To compare with previous studies, we convert our vertical column number densities (measured above R_0) to slant path column number densities. These two column number densities are related through,

$$N_s(z) = \frac{2\left(R_\mathrm{p} + z\right)}{H} \cdot K_1\left(\frac{R_\mathrm{p} + z}{H}\right) \cdot e^{R_0/H} \cdot N_0 \tag{4.14}$$

where N_s is the slant path column number density of some species at a tangent altitude of z above the solid body radius. Using Equation 4.14, we randomly re-sampled our MCMC-derived distributions for each species to derive slant column number density distributions at 700 km altitude (selected to best compare to results in Koskinen et al., 2011). With these derived distributions, we directly compare our slant column number densities to previous *Cassini*/UVIS retrievals.

Critically, our retrieved column number densities generally agree with previous studies that used *Cassini*/UVIS observations, as shown in Table 4.3. Thus, with sufficient signal-to-noise, transit observations can constrain atmospheric properties with uncertainties comparable to orbital measurements. Despite general agreement between our retrievals, Koskinen et al. (2011), and Shemansky et al. (2005), column number densities for ethane (C_2H_6) and benzene (C_6H_6) show more substantial deviation and merit some discussion. Ethane is a known photochemical product within Titan's atmosphere (Lavvas et al., 2008). Unfortunately, there are no apparent distinct ethane features within Titan's transit spectrum. Rather, it provides relatively grey

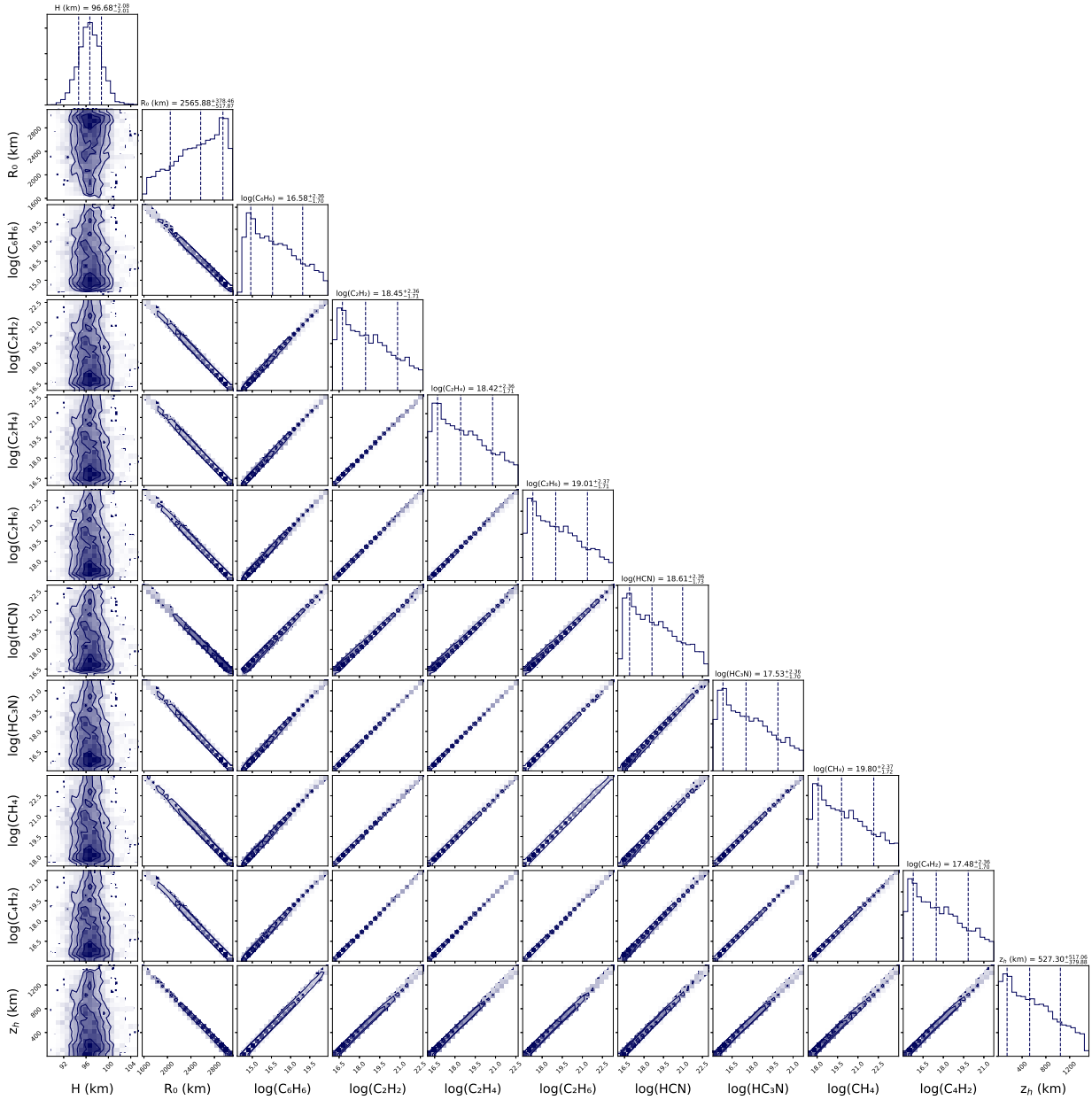

Figure 4.11: Same as Figure 4.7 except with the addition of a single-parameter haze treatment.

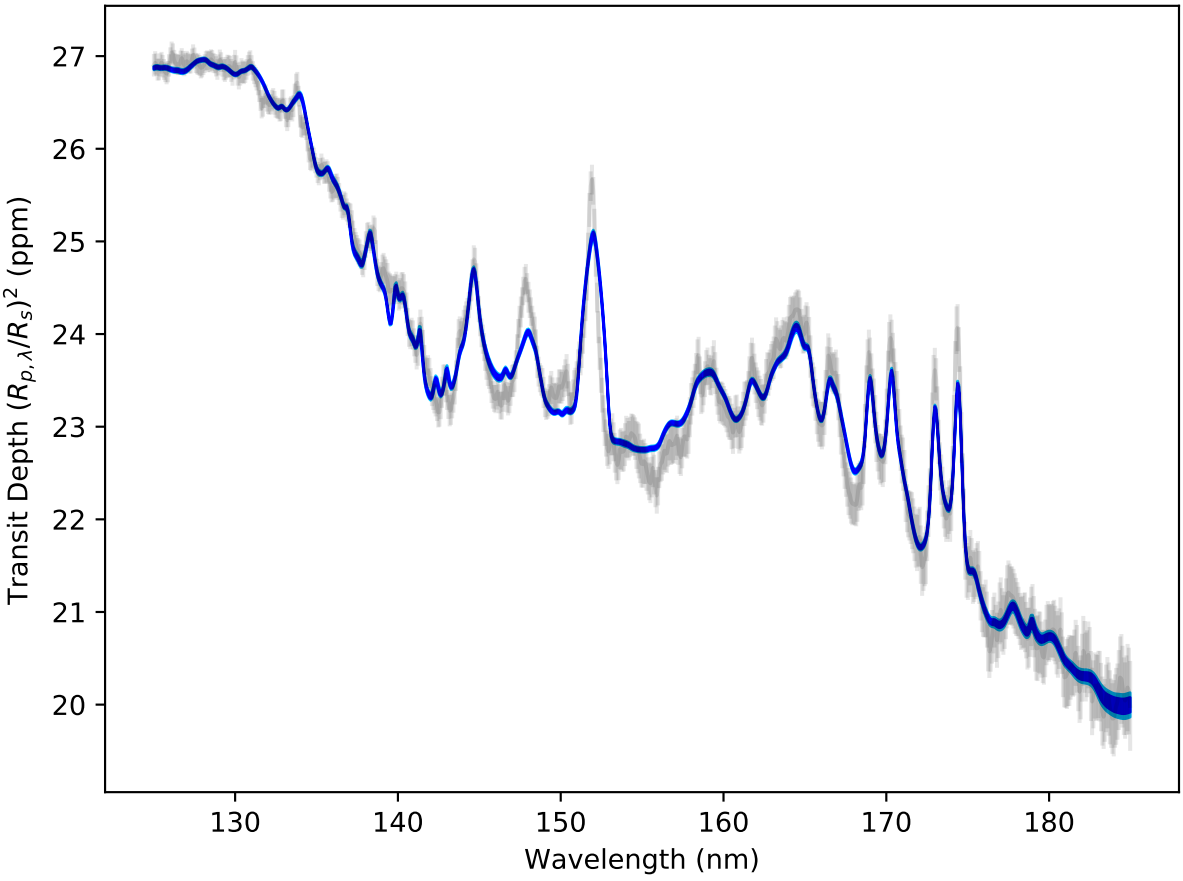

Figure 4.12: Same as Figure 4.8 except for retrieved spectra that include a single-parameter haze treatment.

opacity between 120–135 nm, with a slight slope longward. Using photochemical calculations and mixing ratio constraints Koskinen et al. (2011) estimate an upper limit for the column number density of ethane. Our retrieved column number density, which is obtained without photochemical modeling, is in agreement to within an order of magnitude of previous UVIS results. Additionally, retrieved column number densities for benzene show some variation. These discrepancies likely stem from simplifying assumptions in our model — namely that atmospheric species are distributed exponentially with scale height. Koskinen et al. (2011) demonstrate that column densities for benzene have additional structure with altitude, especially near 700 km. Generally, all retrieved column number density values across studies are fairly consistent.

Comparisons to previous results do present some issues, however. Potentially most importantly, the results from our transit retrievals can be most sensitive to the abundance of a given species at a range of altitudes that is quite distinct from the 700 km altitude level adopted for comparisons. For example, in the far-ultraviolet ($\sim$ 130nm) the transit spectrum probes much greater altitudes than the comparison altitude of 700 km. As methane is responsible for the majority of the opacity in this region, our methane constraint is primarily applicable at altitudes markedly larger than 700 km and our assumption of a constant scale height for number density distributions leads to a discrepancy at 700 km. Figure 4.13 demonstrates this effect by comparing our idealized slant path column number density profiles with those inferred in Koskinen et al. (2011). Our simplified model profiles generally agree with previous UVIS-derived profiles in altitude regions where our best-fit model is most sensitive to the species number density. Sensitivity was determined based on the contribution function, or $\partial z_{\text{eff}}/\partial N_j$. Deviations between our retrieved profiles and those of Koskinen et al. (2011) occur where our retrievals have limited or no sensitivity, either due to the extent of altitudes probed by the transit spectrum or due to the strength of the given species' opacity.

4.5.2 Model Selection Considerations

To determine a preference for either our clear sky or hazy models, we calculated the BIC for each model using Equation 4.11. Recall that differences in the BIC between fitted models can quantitatively indicate if, say, the improvement in a fit through the addition of model parameters is warranted. The ΔBIC value was 6 when comparing the clear sky and one-parameter haze model, with the higher individual BIC corresponding to the hazy model. This evidence suggests that there is no reason to include an additional free parameter to fit for an opaque haze layer. For the clear sky and two-parameter haze model comparison, the ΔBIC value was 14. This indicates strong evidence that supports excluding the two-parameter detached haze layer treatment. These findings remain true for data even without inflated error bars, indicating that error inflation did not result in substantive losses in spectral information.

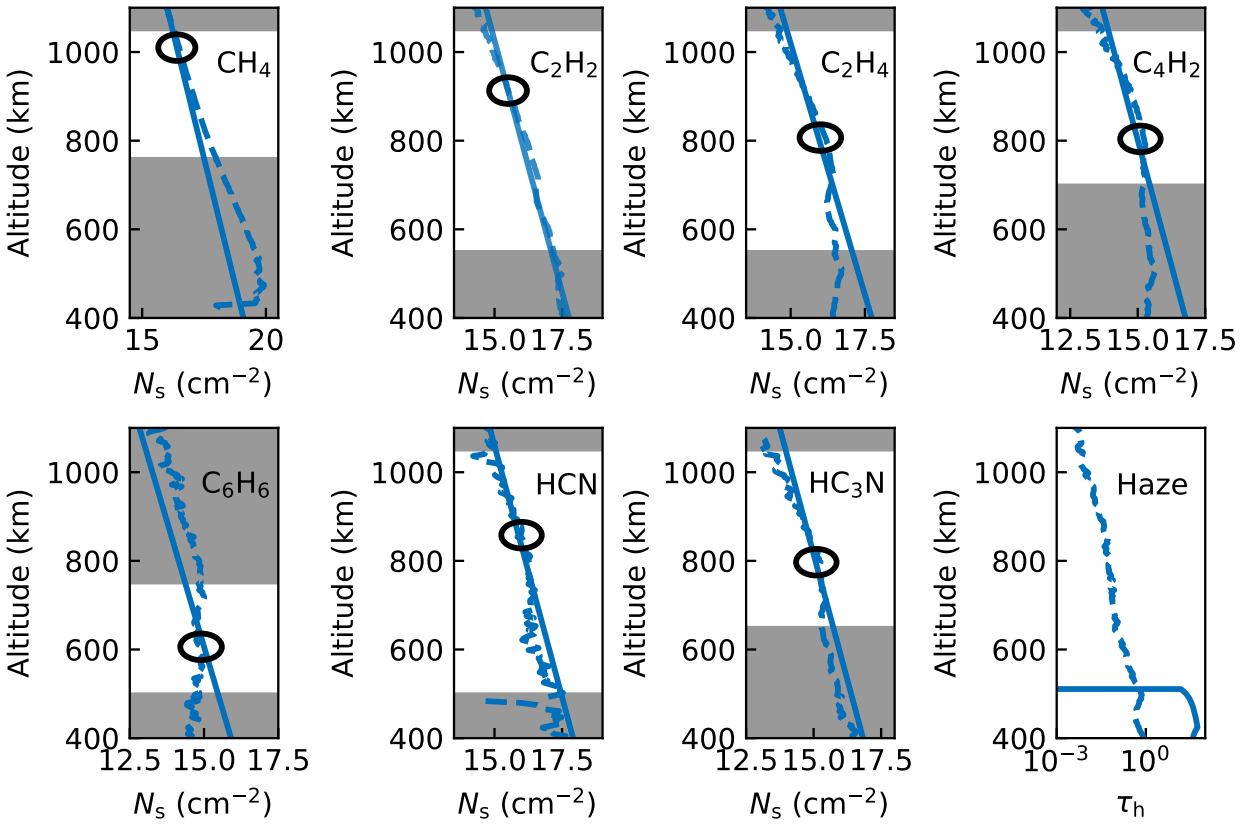

Figure 4.13: Best-fit model slant column number density profiles for each species retrieved in this work (solid lines) compared with those inferred in Koskinen et al. (2011) (dashed). Circles indicate where our model is most sensitive to the column number density of that species based on the maximum of the contribution function (i.e., $\partial z_{\rm eff}/\partial N_j$). Grey regions indicate where the contribution function is zero, either due the strength of the opacity or the extent of the altitudes probed by the transit spectrum. Note that the haze panel compares slant path optical depth profiles at 180 nm.

It is tempting to interpret results from our two-parameter haze treatment in Figure 4.9 as showing a slight preference for models with a detached haze layer near 500 km above Titan's solid body radius with a slant optical depth near unity (i.e., τ_h near 0.1). This would correspond to the haze density maximum near 500 km seen in the altitude-resolved transmission data (Figure 4.1). Future work might find stronger evidence for the detection of this "detached" haze layer (and, potentially, the haze layer/maximum near 700 km) in our transit spectrum by including wavelength-dependent (i.e., non-grey) opacity data for organic hazes and/or exploring haze models that do not assume a uniform distribution of aerosol opacity across a scale height. Regarding the latter point, the transmission data in Figure 4.1 show a sharper increase in aerosol number density near the base of the haze layer near 500 km (Koskinen et al., 2011). Along these lines, future work might also investigate how atmospheric constraints are degraded as observational uncertainties are artificially inflated to increasingly larger levels than are investigated here.

4.5.3 Relevance to Exoplanet Cloud/Haze Parameterizations

Given the quantifiable impact of haze on the UVIS-derived transit spectrum of Titan (Figure 4.3), it is striking that none of the hazy retrieval models confidently detected a haze layer (regardless of error scaling). This suggests that common models for parameterizing the distribution of hazes/clouds in exoplanet atmospheric retrieval models could lead to false negative non-detections of aerosols. Furthermore, and as can be seen by comparing Figures 4.7 and 4.9, false negative results can also be associated with degradations in the inferred distributions of other atmospheric parameters. In the particular case here, the false negative and degradations likely stem from two distinct over-simplifications. First, hazy retrieval models applied here assume a grey haze opacity. Future work could explore other parameterizations of haze opacity, although we caution against any heavy reliance on Titan's aerosol optical properties as these may not be particularly relevant given conditions in hotter exoplanet atmospheres (Lavvas & Koskinen, 2017; Lavvas et al., 2019; Moran et al., 2020). Additional laboratory work addressing the optical properties of relevant haze compositions will be increasingly important given the varied and extreme conditions of the numerous classes of exoplanets (He et al., 2020; Moran et al., 2020).

A second over-simplification stems from our assumption that the haze either truncates the transit spectrum below a fitted altitude (i.e., our one-parameter haze model) or that the fitted haze optical depth is distributed uniformly over one scale height above a fitted altitude (i.e., our two parameter haze model). In reality, results from Koskinen et al. (2011) show that the haze profile is continuous below about 1,000 km with regions of local increases in density (e.g., near 500 km and 700 km for the dataset adopted here). While a two-parameter haze model is common in the exoplanet retrieval literature (for a review see Barstow,

2020, 2021), Titan's high-altitude haze demonstrates the importance of exploring other haze parameterizations (e.g., an exponential vertical haze distribution, potentially with its own distinct scale height) when applying retrieval analysis to exoplanet observations. The inability of our retrieval models to detect Titan's tholin haze highlights the importance of appropriately balancing simplicity with physicality in treatments of clouds/hazes.

4.5.4 Considerations for Future Exoplanet Observations

While our results demonstrate the rich atmospheric information that can be provided by observations of exoplanet transits at ultraviolet wavelengths, the acquisition of such data comes with additional complications. Perhaps most fundamentally, the overall faintness of Sun-like and cool stars at ultraviolet wavelengths implies that reaching even 10–100 parts per million (ppm) accuracy on transit spectrum observations is difficult. Specifically, shortward of 140 nm, Sun-like stellar spectra exclusively consist of atomic emission lines and minimal continuum severely limiting the signal-to-noise (SNR) (Young et al., 2018). Beyond this, the so-called "transit light source effect" will be most pronounced at short wavelengths (see, e.g., Rackham et al., 2018). Here, occulted heterogeneities on the stellar photosphere — namely spots and faculae — can introduce systematic biases in transit spectra, and the contrast between these heterogeneities and the background photosphere is strong in the ultraviolet regime (Oshagh et al., 2014; Llama & Shkolnik, 2015). To consider how our results for Titan might translate to other star-planet systems, we note that the transit features we observe span 6–12 scale heights. For a sub-Neptune with a gravity of 10 m s^{-2} and an atmospheric temperature of 500 K, this range of scale heights translates to 100–200 km for a water-dominated atmosphere and 1,000–2,000 km for a H_2/He-dominated atmosphere. This range of thicknesses (100–2000 km) corresponds to transit depths of 10–100 ppm for a Sun-like host and 200–3,000 ppm for a mid-M dwarf (at $0.2R_\odot$). For comparison, Sing et al. (2019) reach uncertainties of ~ 20 parts per thousand in 1 nm bins for WASP-121b with *Hubble Space Telescope (HST)*/Space Telescope Imaging Spectrometer (STIS) while Wakeford et al. (2020) obtain 100–1,000 ppm uncertainties in 10 nm bins for HAT-P-41b with Wide Field Camera 3 (WFC3)/UVIS aboard *HST* — both at longer ultraviolet wavelengths than studied here. Thus, while the quality of atmospheric characterization obtained from *Cassini*/UVIS-derived transit spectra of Titan may be out of reach for *HST*, it may be that next-generation ultraviolet-capable space telescopes (e.g., the Large UltraViolet-Optical-InfraRed [LUVOIR; Roberge & Moustakas (2018)] surveyor, or the Habitable Exoplanet Observatory [HabEx; Gaudi et al. (2018)]) could better leverage exoplanet transit observations at ultraviolet wavelengths.

4.6 Conclusions

In this paper we have investigated the interplay between absorption by atmospheric hydrocarbon and organonitrile species and haze extinction in an occultation-derived ultraviolet transit spectrum of Titan. Critically, Titan's complex atmospheric chemical structure may be analogous to hazy exoplanet atmospheres rich in hydrocarbon species. Our findings are summarized as follows:

- Despite extensive haze structures in Titan's atmosphere, numerous ultraviolet molecular gas absorption features are easily detected in our occultation-derived transit spectrum. The subtle impact of high-altitude hazes on the ultraviolet transit spectrum of Titan differs from the results of similar analyses of the near-infrared transit spectrum of Titan, which demonstrated a spectral impact of the main haze layer and strong detections of primarily CH_4 (Robinson et al., 2014). This difference suggests that various wavelength regimes (ultraviolet, visible, infrared, etc.) can have dramatically different sensitivities to gas and aerosol species, ultimately imploring for complementary analyses to derive a whole picture.

- Solar System observations provide valuable, often ground-truthed, tests of exoplanet atmospheric characterization techniques.

- Application of various haze parameterizations within our atmospheric retrieval framework to our ultraviolet transit spectrum of Titan all resulted in inferred gas column densities that are consistent with previous analyses of *Cassini*/UVIS observations

- Despite the apparent impact of haze extinction on the underlying occultation data and Titan's UVIS-derived transit spectrum, retrievals using a simplified haze parameterization were unable to detect these haze layers in transit. Thus, oversimplified haze parameterizations, which are conventional within exoplanet atmospheric characterizations, may result in false negative results for detections of atmospheric clouds and hazes.

4.7 Acknowledgements

The authors thank Robert West and an anonymous reviewer for helping to substantially improve an earlier version of this article. TDR gratefully acknowledges support from NASA's Exoplanets Research Program (No. 80NSSC18K0349) and Exobiology Program (No. 80NSSC19K0473), as well as the Nexus for Exoplanet System Science and NASA Astrobiology Institute Virtual Planetary Laboratory (No. 80NSSC18K0829).

Species	Clear	One-Parameter Haze	Two-Parameter Haze	Koskinen et al. (2011)	Shemansky et al. (2005)
CH_4	$(6.1 \pm 0.6) \times 10^{17}$	$(6.0 \pm 0.6) \times 10^{17}$	$(6.1 \pm 0.6) \times 10^{17}$	$(1.60 \pm 0.03) \times 10^{18}$	$(2.5 \pm 0.5) \times 10^{18}$
C_2H_2	$(2.8 \pm 0.1) \times 10^{16}$	$(2.7 \pm 0.2) \times 10^{16}$	$(2.8 \pm 0.2) \times 10^{16}$	$(3.40 \pm 0.05) \times 10^{16}$	$(6 \pm 2) \times 10^{16}$
C_2H_4	$(2.55 \pm 0.05) \times 10^{16}$	$(2.55 \pm 0.05) \times 10^{16}$	$(2.55 \pm 0.05) \times 10^{16}$	$(2.50 \pm 0.02) \times 10^{16}$	$(3.2 \pm 0.7) \times 10^{16}$
C_2H_6	$(1.00 \pm 0.07) \times 10^{17}$	$(0.99 \pm 0.07) \times 10^{17}$	$(0.99 \pm 0.07) \times 10^{17}$	$< 2.7 \times 10^{16}$	$(4 \pm 2) \times 10^{16}$
C_4H_2	$(2.9 \pm 0.2) \times 10^{15}$	$(2.9 \pm 0.2) \times 10^{15}$	$(2.9 \pm 0.2) \times 10^{15}$	$(1.70 \pm 0.05) \times 10^{15}$	$(2.5 \pm 0.9) \times 10^{15}$
C_6H_6	$(3.7 \pm 0.5) \times 10^{14}$	$(3.8 \pm 0.5) \times 10^{14}$	$(3.7 \pm 0.6) \times 10^{14}$	$(7.8 \pm 0.3) \times 10^{14}$	-
HCN	$(4.0 \pm 0.7) \times 10^{16}$	$(3.9 \pm 0.7) \times 10^{16}$	$(4.0 \pm 0.7) \times 10^{16}$	$(2.3 \pm 0.2) \times 10^{16}$	$(5 \pm 2) \times 10^{16}$
HC_3N	$(3.3 \pm 0.2) \times 10^{15}$	$(3.2 \pm 0.2) \times 10^{15}$	$(3.3 \pm 0.2) \times 10^{15}$	$(2.40 \pm 0.06) \times 10^{15}$	-

Table 4.3: Calculated slant column densities (cm^{-2}) at an altitude of 700 km above Titan's solid body radius compared to previous UVIS studies.

Chapter 5

Compaction of Microporous H_2O ice via Energetic Electrons

Some figures appearing in this chapter have been reproduced from Behr, P. R., Tribbett, P. D., Robinson, T. D., and Loeffler, M. J. (2020), Astrophys. J. 900, 2, 147. IOP Publishing Ltd is not responsible for any errors or omissions in this version of the manuscript or any version derived from it. The Version of Record is available online at `https://iopscience.iop.org/article/10.3847/1538-4357/abad3f/meta`.

5.1 Abstract

Here we provide experimental evidence for the compaction of microporous amorphous solid water (ASW) via energetic electron irradiation using Ultraviolet-Visible (UV-Vis) spectroscopy. While this project, and the published version of this data, included analysis of infrared (IR) spectra to demonstrate the disappearance of the dangling bond (DB) absorption features, which serve as a proxy for porosity and internal surface area, this chapter will focus on our analysis with UV-Vis spectroscopy. The experimental data (both UV-Vis and IR spectra were acquired by first author Patrick R. Behr, a summer 2019 research experience for undergraduates (REU) student at Northern Arizona University (NAU). Additionally, Behr analyzed the infrared spectra. My contribution to the project focuses on the analysis of the UV-Vis data using a Fresnel reflectance model coupled to a Markov chain Monte Carlo (MCMC)-implementation of Bayesian Inference. This chapter includes an introduction to motivate compaction of microporous ASW and previous work addressing irradiation-induced compaction, the Fresnel reflectance model and a brief description of the UV-Vis spectra, results, and discussion. For access to all published information, see the DOI located in the disclaimer above.

Keywords: Astrochemistry (75); Interstellar medium (847); Cosmic rays (329); Solid matter physics (2090); Surface ices (2117); Laboratory astrophysics (2004); Spectroscopy (1558)

5.2 Introduction

Microporous ASW should preferentially form on interstellar dust grains from the ambient condensation of H_2O vapor within cold ($\sim$ 10 K; Caselli & Ceccarelli (2012)), dense molecular clouds in the interstellar

medium (ISM). Laboratory studies have demonstrated that background deposition (analogous to ambient condensation) creates microporous ASW (Sceats & Rice, 1982; Brown et al., 1996), which can be easily identified remotely using several absorption features in the IR region that have been attributed to dangling O-H bonds or DBs (Buch & Devlin, 1991; Rowland et al., 1991). More specific information regarding these DBs can be found in Chapter 6. These DBs occur at surface vacuum interfaces. Due to the cold temperatures during condensation, they are not locked within a crystal lattice and do not participate in intermolecular lattice bonding, which results in their having unique IR features. This phase of H_2O ice could have critical implications for the chemical history of interstellar ices since the significant pore volume (Mayer & Pletzer, 1986) could trap additional volatiles (Bar-Nun et al., 1985a) and the surface area may facilitate gas phase chemical reactions. Moreover, recent work by Carmack et al. (2023) demonstrated that all micropore networks within ASW are accessible from the surface regardless of sample thickness, further highlighting the importance of volatile trapping. However, to date, microporous ASW has not been detected anywhere.

While non-detections (Dartois et al., 2013) of ASW may be attributed to the presence of other IR active molecules with absorption features near the DB absorption bands or due to constraints on the previous generations of telescopes (discussed in Chapter 6), previous laboratory studies have demonstrated that heavy ion bombardment destroys the DB absorption bands and induces compaction. For example, Raut et al. (2007b) demonstrated that microporous ASW compacts (i.e. decrease in thickness and porosity) when irradiated with H^+, He^+, Ne^+, and Ar^+ with energies between 80 and 400 keV. However, this work found that compaction scaled linearly with the stopping power of each projectile above a stopping power threshold of 4 eV $Å^{-1}$. This threshold suggested that complete compaction would take approximately the entire lifetime of a molecular cloud, which would suggest that ASW should still be present. To address the stopping power threshold of compaction, and improve estimates for the lifetime of microporous ASW, we grew microporous ASW samples and irradiated these samples with 5 keV electrons, which have a stopping power of 0.35 eV $Å^{-1}$ (i.e. below the threshold). We acquired UV-Vis spectra during irradiation, and fit these spectra using a Fresnel reflectance forward model coupled to a MCMC-implementation of Bayesian Inference (`emcee`; see Chapter 2) to derived model parameters, including the ice thickness. Using the model-derived thickness and the QCM-derived areal mass, we demonstrate that electrons compact ASW and the implications are discussed in Section 5.5.

5.3 Methods

5.3.1 Experimental Methods

We deposited microporous ASW samples in a similar ultra high vacuum (UHV) chamber to that described in Chapter 2. A detailed description of this UHV chamber can be found in Loeffler et al. (2020). We background deposited microporous ASW samples onto a quartz crystal microbalance (QCM) substrate to a column density of 1.68×10^{18} H_2O cm^{-2} or a thickness of $\sim 0.7\mu$m, which we determined using the UV-Vis analysis technique described below. We irradiated samples at an incidence angle of 12.5° with 5 keV electrons produced by a EGG-3103C Kimball Physics electron gun with typical electrons fluxes of $\sim 2 \times 10^{12}$ electrons cm^{-2} s^{-1}. We determined the electron fluxes using a Faraday Cup, nearly identical to that described in Chapter 2. We acquired UV-Vis spectra before, during, and after irradiation using the instrument described in Section 2.1.2.2.

5.3.2 Fresnel Reflectance Model

To analyze the UV-Vis spectra, we generated synthetic spectra using a forward model derived from the Fresnel equations for specular reflectance (Heavens, 1965). This technique is similar to previous studies modeling the radiation-induced compaction of porous ASW ice (Raut et al., 2007b, 2008) and is described previously in Teolis et al. (2007b). Note that all of these previous studies fit this forward model to spectral data by-eye.

The Fresnel equations for specular reflectance calculate the wavelength-dependent Fresnel Coefficients for both parallel and perpendicularly polarized light reflected from the ice and vacuum interface (Equations 5.1 and 5.2) and reflected from the ice and substrate interface (Equations 5.3 and 5.4):

$$r_{\perp,\mathrm{ice}} = \frac{n_0 cos(\theta_{ice}) - n_{ice} cos(\theta_0)}{n_0 cos(\theta_{ice}) + n_{ice} cos(\theta_0)} \tag{5.1}$$

$$r_{\parallel,\mathrm{ice}} = \frac{n_{ice} cos(\theta_{ice}) - n_0 cos(\theta_0)}{n_{ice} cos(\theta_{ice}) + n_0 cos(\theta_0)} \tag{5.2}$$

$$r_{\perp,\mathrm{sub}} = \frac{n_{film} cos(\theta_{sub}) - n_{sub} cos(\theta_{ice})}{n_{ice} cos(\theta_{sub}) + n_{sub} cos(\theta_{ice})} \tag{5.3}$$

$$r_{\parallel,\mathrm{sub}} = \frac{n_{sub} cos(\theta_{sub}) - n_{ice} cos(\theta_{ice})}{n_{sub} cos(\theta_{sub}) + n_{ice} cos(\theta_{ice})} \tag{5.4}$$

where r denotes the Fresnel coefficient for either parallel ($\parallel$) or perpendicularly ($\perp$) polarized light for either the vacuum/ice interface or the ice/substrate interface, n_0 is the incident real index of refraction

or the real index or refraction of a vacuum (assumed to be 1), θ_0 is the angle of incidence, n_{ice} is the wavelength-dependent real index of refraction of the ice (H_2O, or H_2S in the case of Chapter 7), n_{sub} is the wavelength-dependent complex index of refraction of the gold substrate, θ_{ice} is the angle of refraction for the ice, and θ_{sub} is the angle of refraction for the substrate. The angles of refraction are calculated from Snell's Law:

$$\theta_{ice} = \arcsin n_0/n_{ice} \sin\theta_0 \tag{5.5}$$

$$\theta_{sub} = \arcsin n_0/n_{sub} \sin\theta_0 \tag{5.6}$$

Since H_2O-ice is transparent within the wavelength range 0.25 - 0.7 μm (Warren & Brandt, 2008), we use the Sellmeier equation to approximate the wavelength-dependent, real index of refraction:

$$n(\lambda) = \frac{A + B(\lambda)^2}{\lambda^2 - C^2} \tag{5.7}$$

where n is the wavelength-dependent, real index of refraction of H_2O, and A, B, and C are the fitted Sellmeier coefficients. Note that this technique is frequently used to estimate the real index of refraction within the field of material science (Voronin & Zheltikov, 2017). The Sellmeier approximation also works for the H_2S ice samples in Chapter 7 since H_2S is also transparent within 0.3 - 0.7 μm. The slight difference in wavelength range is due absorptions of H_2S in the deep UV. The complex optical constants (n - ik) for the gold substrate were taken from Babar & Weaver (2015).

From the Fresnel coefficients, we calculated the parallel and perpendicular reflectance components:

$$R_\perp = \left(\frac{r_{\perp,\mathrm{ice}} + r_{\perp,\mathrm{sub}} e^{(-2i\phi)}}{1 + r_{\perp,\mathrm{ice}} r_{\perp,\mathrm{sub}} e^{(-2i\phi)}} \right)^2 \tag{5.8}$$

$$R_\parallel = \left(\frac{r_{\parallel,rmice} + r_{\parallel,\mathrm{sub}} e^{(-2i\phi)}}{1 + r_{\parallel,\mathrm{ice}} r_{\parallel,\mathrm{sub}} e^{(-2i\phi)}} \right)^2 \tag{5.9}$$

where i is an imaginary number, and ϕ is the phase angle. The phase angle is related to the ice thickness (d) through the following relationship:

$$\phi = 2\pi n_{ice} d \cos\theta_{ice} \frac{1}{\lambda} \tag{5.10}$$

The total reflectance from the ice and the substrate is assumed to be an equal parts mixture of parallel and perpendicularly polarized light. A similar exercise is completed to calculate the total reflected light from the

bare substrate, though substantially simplified:

$$r_{\perp,\text{bare}} = \frac{n_0 \cos\theta_{sub} - n_{sub} \cos\theta_0}{n_0 \cos\theta_{sub} + n_{sub} \cos\theta_0} \tag{5.11}$$

$$r_{\parallel,\text{bare}} = \frac{n_{sub} \cos\theta_{sub} - n_0 \cos\theta_0}{n_{sub} \cos\theta_{sub} + n_0 \cos\theta_0} \tag{5.12}$$

$$R_{\text{bare}} = 0.5 \left(r^2_{\perp,\text{bare}} + r^2_{\parallel,\text{bare}} \right) \tag{5.13}$$

Additionally, we included a scattering efficiency factor in the forward model to account for the increased light scattering at high irradiation fluence. This scattering is a consequence of radiation-induced roughness on the surface at a length scale significantly smaller than the UV-Vis wavelengths analyzed. For this reason, the scattering is approximated as Rayleigh scattering. We evaluated the total light reflected from the sample as:

$$R = \left(\frac{R_{\text{ice}}}{R_{\text{bare}}} \right) \left(1 - \frac{\sigma_s}{\lambda^4} \right) \tag{5.14}$$

where σ_s is the scattering efficiency factor.

5.3.3 Optimization of Synthetic Spectra

We fit the synthetic spectra produced from the Fresnel reflectance forward model to the UV-Vis laboratory data using a MCMC-implementation of Bayesian Inference using the open source `emcee` python package (Foreman-Mackey et al., 2013). Note that this is the same python package that I used for the atmospheric forward model retrievals in Chapter 4. I explain this technique in detail in Chapter 2. Briefly, Bayes Theorem states that the posterior probability distribution for a given set of physical parameters (θ) and a given set of data (x) is proportional to the prior probabilities of those parameters and the likelihood probability of the data given those parameters:

$$P(\theta|x) \propto P(\theta) P(x|\theta) \tag{5.15}$$

where $P(\theta|x)$ is the posterior probability distribution, $P(\theta)$ is the prior probability, and $P(x|\theta)$ is the likelihood probability. A modified Hastings-Metropolis algorithm psuedorandomly samples the the parameters to effectively map the posterior probability distribution space for each individual parameter. The likelihood probability or likelihood function effectively compares the laboratory data and associated error with the reflectance forward model for a given set of parameters:

Model Parameter	Description	Priors
A	Sellmeier Coefficient	$A > 0$
B	Sellmeier Coefficient	$B > 0$
C	Sellmeier Coefficient	$-200 < C < 200$
d	Film Thickness	$d > 0$
σ_s	Scattering Efficiency Parameter	$7 < \sigma_s < 9$

Table 5.1: Model fitted parameters, their descriptions, and their prior probabilities.

$$lnP(x|\theta) = -\frac{1}{2}\sum_i \frac{(x_i - R_i)}{\sigma_i^2} + ln2\pi\sigma_i^2 \tag{5.16}$$

where x_i is the ith reflectance data point, σ_i is the associated uncertainty for the ith data point, and R_i is the Fresnel reflectance forward model. The likelihood probability (and consequently posterior probability distribution) maximizes as the differences between the data and model are minimized. As in Chapter 4, I assume uniformed (flat) prior probability distributions to truncate the parameter values and limit the MCMC algorithm to physical parameter values (e.g. an absolute length cannot be negative). The parameters of interest, their description, and the prior probability limits are shown in Table 5.1. Note that the scattering efficiency factor is retrieved in log space to ensure that multiple orders of magnitude are sufficiently explored.

5.4 Results

We background deposited microporous ASW ice samples at 30 K, and irradiated with 5 keV electrons, acquiring UV-Vis spectra before, during, and after irradiation. Figure 5.1 shows the UV-Vis reflectance as a function of wavelength, acquired prior to (top) and after (bottom) irradiation to a fluence of 3.18×10^{16} electrons cm^{-2}. Since H_2O ice is transparent with this wavelength range, these periodic dips in reflectance are due to interference between the light reflected from the surface of the ice and the surface of the gold substrate, rather than light absorbed by the H_2O ice sample. Prior to irradiation, the spectrum shows large interference fringes with minimal scattering at the deep UV wavelengths. Additionally, the modeled best fit spectrum (shown in red) agrees well with the laboratory data, indicating an appropriate physical model. More quantitatively, the reduced chi-squared (defined in Chapter 2) is 0.82, confirming the quality of model fit. After irradiation (bottom), the spectrum shows evidence for wavelength-dependent scattering due to irradiation-induced surface roughness. However, the model accounts for this and qualitatively agrees with the laboratory spectrum. The reduced chi squared for this spectrum is 1.28, again suggesting a good model fit. Notably, the model and data deviate around 500 nm. This discrepancy is likely due to the assumed optical constants of the gold substrate. Additionally, both laboratory spectra show a small artifact of the halogen light source near 650 nm.

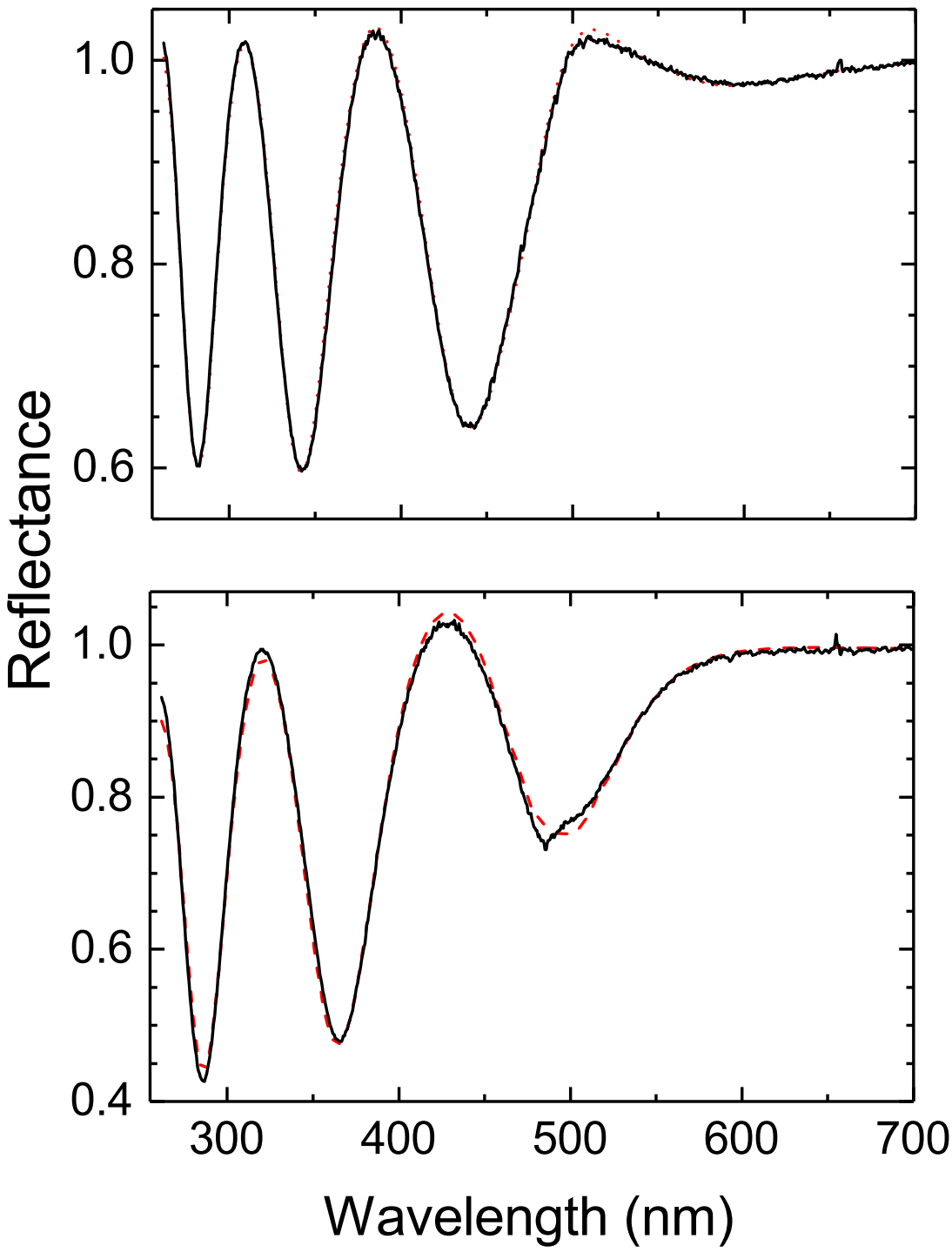

Figure 5.1: UV-Vis reflectance spectra of a ASW ice deposited with a column number density of 1.68×10^{18} H_2O cm^{-1} after deposition at 30 K (top), and after irradiation with 5 keV at 30 K to an electron fluence of 3.18×10^{16} electrons cm^{-2}. Laboratory spectra are shown in solid black lines. Best fit modeled spectra are shown in dotted red lines.

Importantly, Figure 5.1 shows that after irradiation, the number of interference fringes decreases, qualitatively indicating that as the electron fluence increases, the ice thickness decreases (i.e. compacts). The model-derived thickness confirms the qualitative fringe counting. Figure 5.2 shows the marginalized posterior probability distributions for each individual parameter along the diagonal axis showing the distributions 16th, 50th, and 84th percentiles (i.e. distribution mean and 1σ uncertainty). Off axis plots show the two-dimensional marginalized posterior probability distributions for each pair of parameters. Note that there are correlations between the Sellmeier coefficients, which is expected; however, these values do not extend over the entirity of parameter space. Importantly, from these distributions, we determine the mean ice thickness and uncertainty. Our initial ice thickness is ~ 704 nm and our final thickness after irradiation is ~ 527 nm, with a modeled uncertainty of $< 0.1\%$.

Following this method for determining the ice thickness, we derive a sample thickness at incremental fluences using the UV-Vis spectra. With the known column density (or areal mass) of the sample, known independently from the QCM data, we calculate the density for each UV-Vis spectra. As the sample is irradiated, the density increases from an initial value of 0.72 g cm^{-3} to a final compact value of 0.95 ± 0.02 g cm^{-3}, which is consistent with the previously determined density for compact H_2O-ice (0.94 g cm^{-3}) (Narten et al., 1976). Assuming a final compact density (ρ_c) of 0.95 g cm^{-3}, we calculate the sample porosity:

$$\phi = 1 - \frac{\rho}{\rho_c} \tag{5.17}$$

Figure 5.3 shows the porosity of the microporous ASW sample as a function of fluence. As the fluence increases, the porosity decreases and the sample becomes fully compact. Note that the remote indication of porosity (DB absorption bands) also decreases as a function of fluence. For additional information regarding the DB IR analysis, see Behr et al. (2020).

5.5 Discussion

MCMC-based analysis of the UV-Vis spectra indicate that the thickness of microporous ASW ice samples decreases as a function of electron fluence. As the QCM-derived areal mass remains constant, this decrease in thickness requires an increase in density and consequently a decrease in porosity. Note that 5 keV electrons do sputter a small amount of material resulting in a small loss in areal mass as a function of fluence. Meier & Loeffler (2020) demonstrated that 5.0 keV electrons sputter ~ 0.03 H_2O electron^{-1} at 60 K, which should be similar to 30 K (Davis et al., 2021). Given that the fluence reached in our study is $\sim 2 \times 10^{16}$ electrons cm^{-2}, this results in an insignificant loss in the total areal mass of our samples ($\sim 0.03\%$ by number). A fluence of $\sim 2 \times 10^{16}$ electrons cm^{-2} is required to full compact the ice samples. The complete compaction

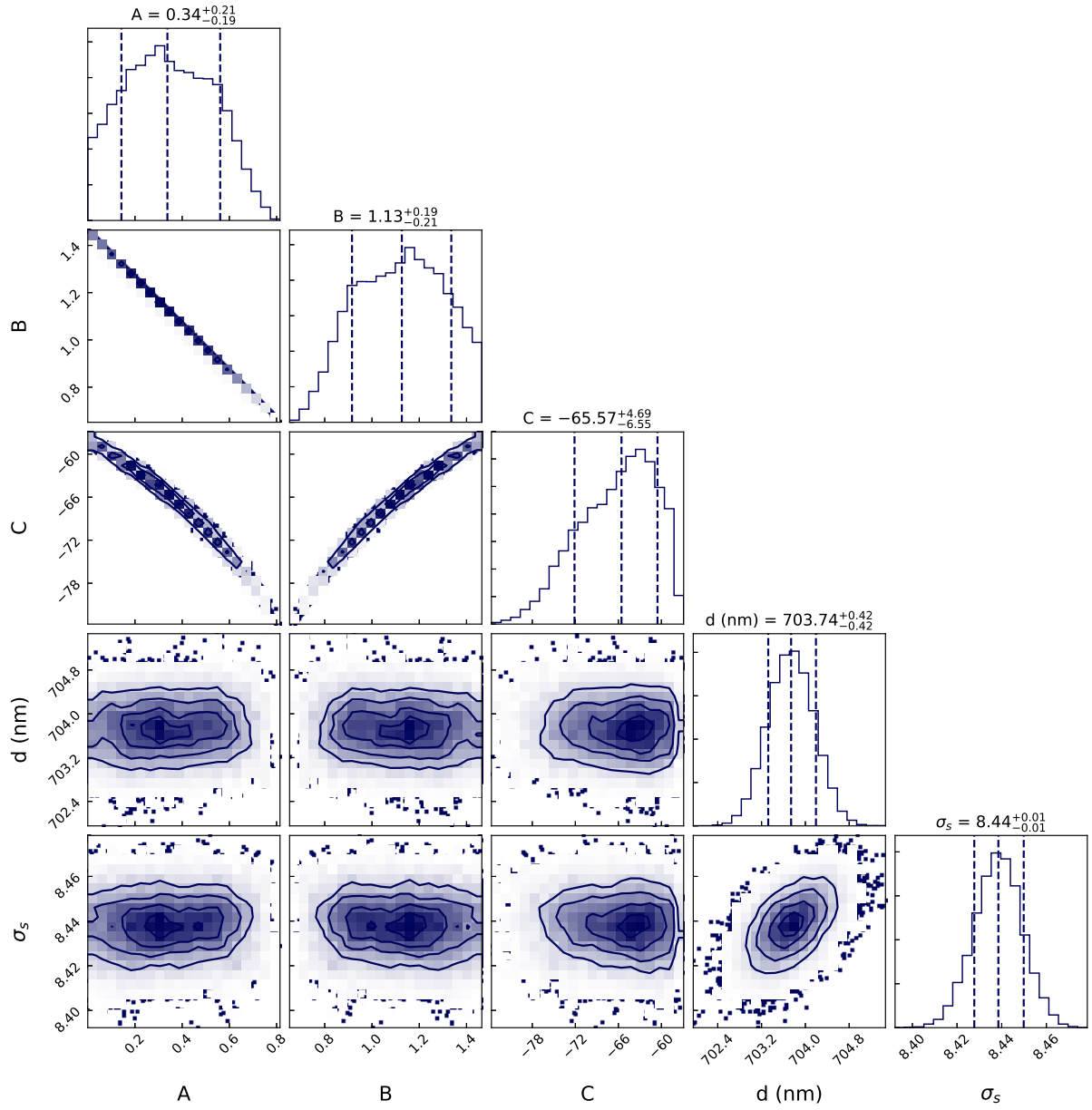

Figure 5.2: Marginalized posterior probability distributions for each individual model parameter along the diagonal, and the two-dimensional posterior probability distributions for each pair of parameters.

of microporous ASW with energetic electrons is of fundamental interest because it demonstrates that the proposed stopping power threshold of 3 eV Å^{-1} is not necessary to achieve compaction and the destruction of micropores and any remotely detectable features. Because energetic particles with lower stopping power than this threshold were not previously included in compaction timescale estimates, the time period required for compaction is significantly less than that estimated in Raut et al. (2008). Specifically, Behr et al. (2020) estimated the lifetime of microporous ASW to be on the order of 10^5 years, which is significantly shorter

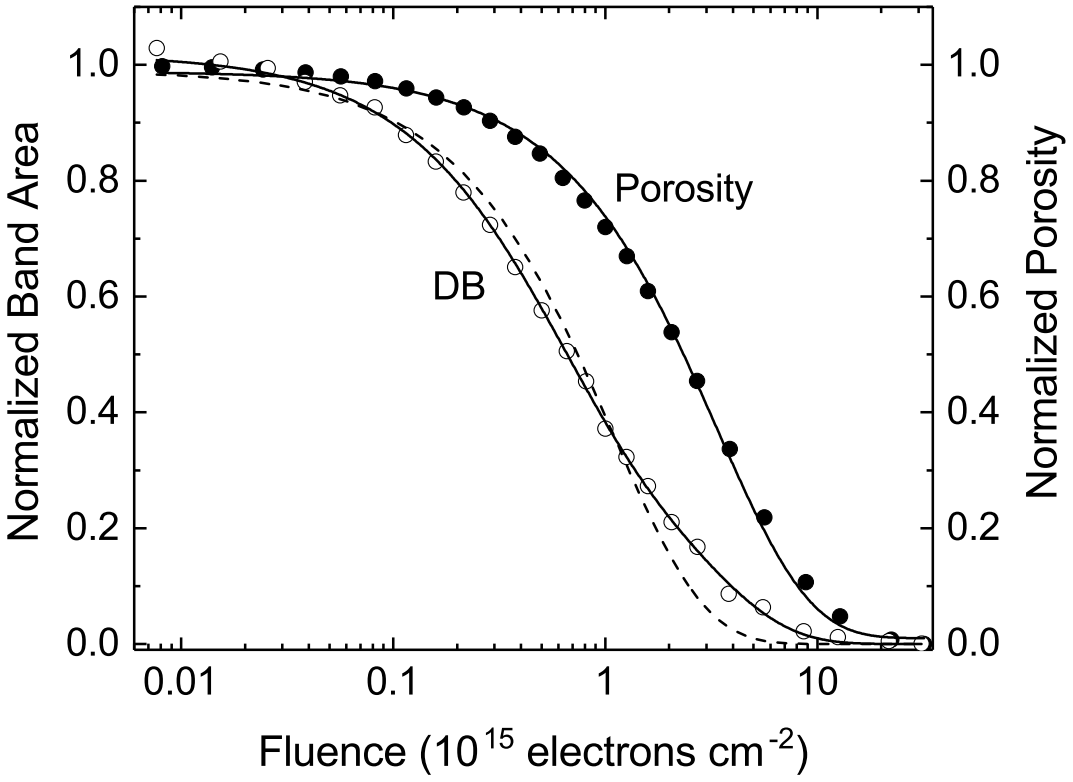

Figure 5.3: Normalized porosity and dangling bond (DB) absorption normalized band area of a 1.68×10^{18} H_2O cm^{-2} ASW sample as a function of fluence. Fits to this data are described further in Behr et al. (2020).

than the lifetime of a molecular cloud (Blitz & Shu, 1980). Radiation-induced compaction likely explains the lack of abundant microporous ASW; however, it does not explain the absense of microporous ASW in the youngest of molecular clouds. The anticipation of microporous ASW detections in young molecular clouds is addressed in depth in Chapter 6.

5.6 Acknowledgements

This research was supported by NSF grant # 1821919. Data can be found in Northern Arizona University's long-term repository (https://openknowledge.nau.edu/5519/). PDT would also like to thank PRB for their work collecting all laboratory data, and analyzing the IR data, and the NAU Department of Astronomy and Planetary Science REU program.

Chapter 6

Probing Microporous ASW with Near-infrared Spectroscopy: Implications for JWST's NIRSpec

Patrick D. Tribbett[1], Stephen C. Tegler[1], Mark J. Loeffler[1,2]

This is the Accepted Manuscript version of an article accepted for publication in The Astrophysical Journal. IOP Publishing Ltd is not responsible for any errors or omissions in this version of the manuscript or any version derived from it. The Version of Record is available online at `https://iopscience.iop.org/article/10.3847/1538-4357/abff55`.

6.1 Abstract

The presence of porous amorphous solid water (ASW) in interstellar ice mantles has long been suspected but, to date, has not been identified. With the upcoming launch of the James Webb Space Telescope (JWST), future detections of porous ASW seem promising. To this end, we investigated the near-infrared spectra of ASW to confirm that two features that have been seen sporadically in literature and have either not been identified or only tentatively identified were indeed due to dangling bond (DB) absorption bands. These bands may provide an additional way to identify porous ASW with remote sensing spectroscopy. Our systematic study tested the thermal stability of these features and their spectral shifts during gas adsorption. We correlated these changes to what we observed in the well-studied fundamental DB absorptions at 3720 cm^{-1} and 3696 cm^{-1}. We find excellent agreement between the behavior of the fundamental DB absorption bands with those centered at 5326 cm^{-1} and 7235 cm^{-1}, as well as a shoulder located at 7285 cm^{-1}, confirming that all these features are due to DBs present in porous ASW. We estimate that these weaker DB absorptions should be identifiable after 4 - 5 hrs of observation time with JWST's NIRSpec instrument. These new features may not only prove useful in future observational campaigns in search of porous ASW but also may serve as a powerful way to indirectly detect weakly absorbing species that challenge the ability of remote sensing spectroscopy.

Keywords: Laboratory astrophysics (2004); Solid matter physics (2090); Surface ices (2117); Astrochemistry (75); Interstellar medium (847); Spectroscopy (1558)

[1]Department of Astronomy and Planetary Science, Northern Arizona University, PO Box 6010, Flagstaff, AZ 86011, USA
[2]Materials Interfaces in Research and Application, Northern Arizona University, PO Box 6010, Flagstaff, AZ 86011, USA

6.2 Introduction

At cold temperatures (< 100 K), water vapor condenses to form amorphous solid water (ASW) (Blackman & Lisgarten, 1958). ASW will contain pores, and the characteristics of these pores will depend strongly on the growth conditions (Sceats & Rice, 1982; Brown et al., 1996; Stevenson et al., 1999; Horimoto et al., 2002). Porous ASW is believed to be of particular importance for astronomical environments, as the pores within the ice can trap volatile gas species and may promote gas-solid phase chemistry altering the chemical history of the ice (Bar-Nun et al., 1985a; Mayer & Pletzer, 1986). One consequence of ASW's porosity and large internal surface area is that the intermolecular bonding at the internal surfaces can differ compared to what occurs in the bulk of the ice (Mayer & Pletzer, 1986). More specifically, the water molecules at the pore surface partially dangle off into the pore and cannot participate in lattice bonding. These dangling bonds (DBs) are characteristic of porous ASW and are typically identified in laboratory studies using the pair of infrared (IR) bands centered at 3696 cm^{-1} and 3720 cm^{-1} (or 2.705 μm and 2.688 μm) (Buch & Devlin, 1991; Rowland et al., 1991). These bands have been assigned to vibrations of 3-coordinated (one free hydrogen bond) and 2-coordinated water (two free hydrogen bonds) molecules.

Although the temperatures within the interstellar medium (ISM) and the outer Solar System are sufficiently low to form porous ASW from ambient condensation of H_2O, the DB IR spectral features have not been detected anywhere. Previous laboratory studies have demonstrated that energetic particle bombardment can efficiently destroy the DB absorption bands (Palumbo, 2006; Raut et al., 2007b; Dartois et al., 2013; Mejía et al., 2015; Behr et al., 2020), as well as compact the pore volume (Palumbo, 2006; Raut et al., 2007b, 2008; Behr et al., 2020). In fact, most recent laboratory estimates (Behr et al., 2020) suggest that the DB features will be destroyed 10-100 times faster than the average lifetime of a molecular cloud (Blitz & Shu, 1980), which is consistent with these features' absence in remote sensing spectra.

The absence of the DB features in remote sensing spectra taken to date could also be a consequence of other more basic factors. For instance, the proximity between the fundamental DB bands and the fundamental OH stretch of H_2O-ice could inhibit clear detection of these features, especially in spectra that do not have the high signal to noise ratios ($\sim 10 - 100$) that are typically observed in laboratory spectra. Moreover, IR-active species, such as CO_2, which have absorption features in this spectral region may also inhibit clear detections of DB features (Dartois et al., 2013). Thus, in this study, we were interested in determining whether we could confidently identify any other absorption bands present in the spectrum of ASW that could be attributed to the DBs and hence identify porous ASW. We note that near-infrared spectral features for the DBs, where overtones and combination modes typically occur, are expected. Yet, to our knowledge, there are only a few instances in literature where these potential features are either seen

Identification	References			SNR[d]
	[a]	[b]	[c]	
DB2 (DB1)+ ν_2^e	5320	5313	5326	31.06
2DB2	7230	-	7235	10.83
2DB1	-	-	7285	3.08

Table 6.1: Compilation of previous laboratory work characterizing NIR DB features: [a]Mastrapa et al. (2008), 25 K, [b]Zheng et al. (2009), 10 K, and [c]this work, 21 K. See Palumbo (2006) and Mejía et al. (2015) for a review of the fundamental DB features. [d]Signal to noise ratios are calculated by dividing the absorption feature's peak height by the peak-to-peak signal adjacent to the absorption feature (noise). These SNR values are for this work only. Note that these features can also be seen in Fig. 3 in Schmitt et al. (1998); however, band centers are not reported. [e]Assignment for ν_2 is from Hagen et al. (1981).

or tentatively identified (Schmitt et al., 1998; Mastrapa et al., 2008; Zheng et al., 2009). For instance, two absorption features are observed near 5320 cm^{-1} and 7230 cm^{-1} by Schmitt et al. (1998) but not identified, while in more recent works**,** one or two features are seen and tentatively assigned to the DB absorptions (Mastrapa et al., 2008; Zheng et al., 2009).

In an effort to confidently identify any new potential DB absorption bands, we deposited ASW films between $\sim$ 20 and 150 K and studied their near-infrared spectra in detail after growth, during warming and during adsorption of methane. Finally, we point out that this work was also motivated by the upcoming launch of the James Webb Space Telescope (JWST). The near-infrared spectrometer (NIRSpec) instrument on JWST is expected to have a significantly better sensitivity and resolution than its predecessors (Bagnasco et al., 2007; Milam et al., 2016), opening up new opportunities for detection of previously unidentified species, as well as more robust characterizations of the physical properties of the icy materials in extraterrestrial environments.

6.3 Experimental Methods

Experiments were performed within a stainless steel ultra-high vacuum chamber with a base pressure of 1.5×10^{-9} Torr. The specifications of this chamber are detailed in Tribbett & Loeffler (2021); modifications to include reflectance spectroscopy are similar to those described in Loeffler et al. (2020). To prepare our ASW samples, we background deposited H_2O (high-performance liquid chromatography (HPLC) grade, Sigma Aldrich) at 21 K onto an optically flat gold mirror electrode of an Inficon IC6 quartz-crystal microbalance (QCM) as described in our previous studies (Loeffler et al., 2020). Note that in all cases, the thermal-radiation shield was removed to allow molecules from all angles to deposit on the sample, which should more closely mimic an extraterrestrial environment, while maximizing the sample's porosity (Loeffler et al., 2016b). Samples were deposited at a rate of $\sim 4 \times 10^{14}$ H_2O cm^{-2} s^{-1} to a column density of 4.13×10^{18} H_2O cm^{-2} or an ice thickness of ~ 1.76 μm assuming a density of 0.70 g cm^{-3} (Behr et al., 2020).

For analysis, the specular reflectance between 12,000 cm^{-1} and 2000 cm^{-1} was acquired using a halogen light source from a Thermo-Nicolet iS50 Fourier Transform Infrared Spectrometer (FTIR) and an MCT-A detector at a spectral resolution of 2 cm^{-1}. The incident angle of the light source was 37.5° with respect to the surface normal of our gold-mirror QCM. IR spectra reported here are given in units of optical depth, -ln(R), where R is the ratio of the intensity of reflected light from the sample divided by the intensity reflected from the bare substrate. All reflectance spectra were collected without rotating the substrate (i.e. collected at the same viewing geometry).

To determine temperature dependence of the spectral features, H_2O-ice samples were warmed at a rate of 2 K min^{-1} and allowed to equilibrate at the acquisition temperature before taking an IR spectrum. To quantify the band area of any DB absorption bands, we used a 5^{th} order polynomial to reproduce and remove the baseline continuum from the absorption region prior to integration, as we have done in previous studies (Loeffler et al., 2006b; Behr et al., 2020). In some experiments, we also deposited methane (ultra-high purity, 99.97 %, Matheson Gas) onto the ASW samples via background deposition at 21 K at a rate of $\sim 2 \times 10^{14}$ CH_4 cm^{-2} s^{-1}, which was monitored using the QCM. The low deposition temperatures allowed us to avoid competition between adsorption and desorption of the CH_4 (Raut et al., 2007a).

6.4 Results

6.4.1 Thermal Stability of DB Absorption Bands

Figure 6.1 shows the near-infrared spectrum of an ASW sample after deposition at 21 K and during warming to 150 K. As expected, the spectra are dominated by two broad absorption bands, which are due to combination ($\nu_2 + \nu_3$; 5041 cm^{-1}) and overtone ($2\nu_3$; 6748 cm^{-1}) modes of H_2O-ice (Gerakines et al., 2005; Mastrapa et al., 2008). The sharp rise beginning near $\sim$ 3800 cm^{-1} is due to the fundamental stretching mode of H_2O-ice. These near-infrared features change slightly during warming with the most drastic changes being due to the crystallization of ASW that occurs at higher temperatures (Jenniskens & Blake, 1994).

In addition to these large absorption features, there are three spectral regions that contain smaller absorption bands that appear at higher wavenumbers than each large feature, which we show in Figure 6.2. It is well-known that the bands located at 3720 cm^{-1} (DB1) and 3696 cm^{-1} (DB2) are indicative of dangling bonds present in 2- and 3-coordinated H_2O molecules (Buch & Devlin, 1991; Raut et al., 2007a; Dartois et al., 2013; Mejía et al., 2015; Behr et al., 2020). In addition, we also assign these other smaller features present in Figure 6.2a and 6.2b to dangling bond absorptions (see Table 6.1 for more details). The absorption band centered at 5326 cm^{-1} (DB3) is consistent with what was previously tentatively identified as a DB combination feature at 5313 cm^{-1} (Zheng et al., 2009) and at 5320 cm^{-1} (Mastrapa et al., 2008),

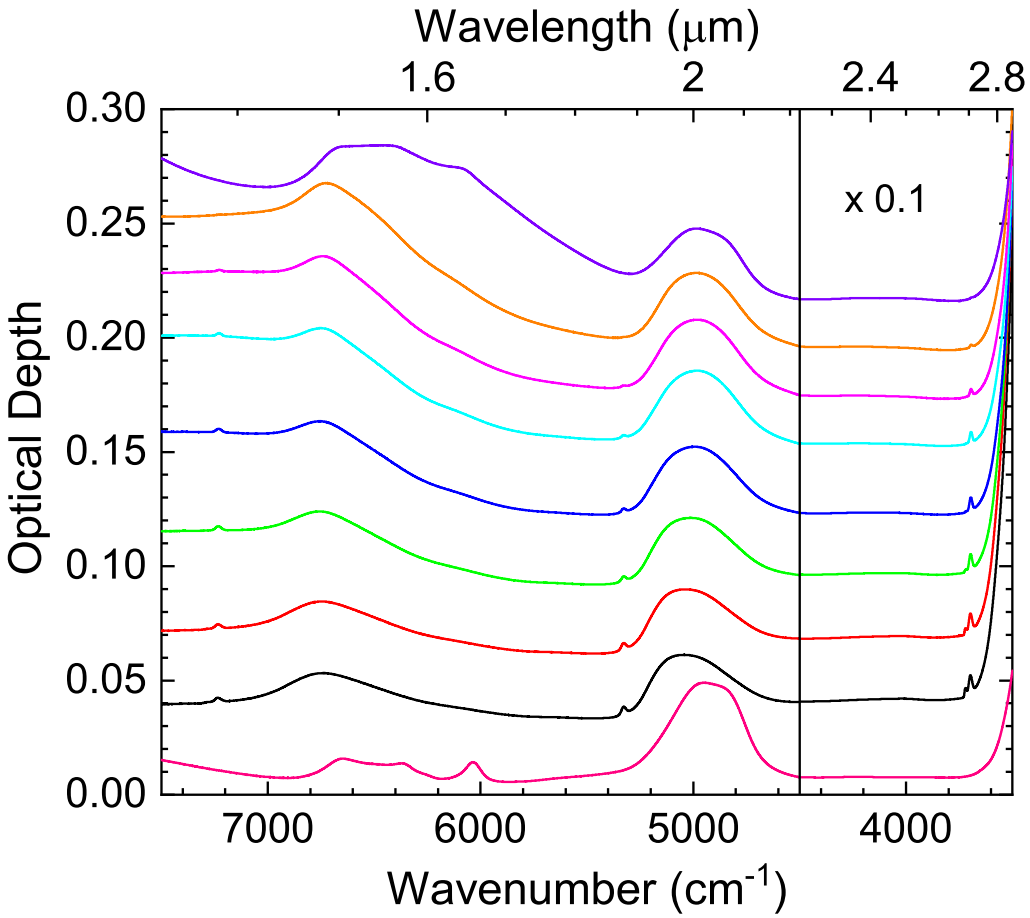

Figure 6.1: IR spectra of a 4.13×10^{18} H_2O cm^{-2} sample deposited at 21 K and incrementally warmed to 150 K. Spectra correspond to (2^{nd} from the bottom to top): 21 K, 30 K, 50 K, 70 K, 90 K, 110 K, 130 K, and 150 K. For comparison, the bottom spectrum is a 4.13×10^{18} H_2O cm^{-2} crystalline sample deposited at 150 K and cooled to 21 K. Note that the optical depth at < 4500 cm^{-1} is divided by 10 for comparison. Spectra are vertically offset for clarity.

as well as what was observed in one of our recent works (see Figure 3 in Loeffler et al., 2020). Furthermore, we suspect that the DB3 combination band is due to both 2- and 3-coordinated H_2O molecules, as previous studies have shown that peak position of the O-H stretching and H_2O bending modes shift in opposite directions as the coordinate state changes (Falk, 1984), which likely prevents the two transitions from being resolved in our spectra. Finally, there appear to be two absorptions located at 7285 cm^{-1} (DB4) and at 7235 cm^{-1} (DB5). Similar to DB3, this is consistent with the tentative identification of a feature at 7230 cm^{-1} (Mastrapa et al., 2008), although the smaller absorption feature (DB4) was not reported in that work. By comparing the band areas of each DB absorption region, we estimate that DB3 and DB4+DB5 are ~ 20 times smaller than DB1+DB2, which is typical of an overtone or combination mode absorption (Hudson et al., 2017). Admittedly, it would be better to refine this estimate in future laboratory measurements,

as the relative strength of the absorption features can change with film thickness in our setup, which is a consequence of thin film interference effects present in reflectance spectroscopy (Teolis et al., 2007b).

As can be most clearly seen in Figure 6.2, all DB features weaken during warming, eventually dissipating. Both shoulder bands (DB1 and DB4) are unidentifiable at temperatures warmer than 70 - 90 K, supporting that they are both indicative of 2-coordinated water molecules. DB2, DB3, and DB5 dissipate by 150 K; generally agreeing with the temperature dependence of the larger DB feature (DB2) shown in earlier studies (Horimoto et al., 2002). We point out all of these DB features are absent, as expected, within the crystalline H_2O-ice reference sample (Figure 6.2, bottom spectrum), which was background deposited at 150 K and acquired at 21 K.

We also studied the decrease in the DB absorption bands during warming more quantitatively by measuring the normalized band areas for each DB region as a function of temperature (Figure 6.3a). Band areas were normalized to unity based on the band areas at 21 K. Note that both DB pairs (DB1, DB2, and DB4, DB5) overlapped enough that we calculated the total band area for those spectral regions. As can be seen in Figure 6.3a, the normalized band area for each region decreases as a function of temperature at a nearly identical rate, further supporting that all these features are indeed due to dangling bonds in ASW.

6.4.2 Gas Adsorption

To further confirm that these new absorption bands are due to dangling bonds in ASW, we adsorbed CH_4 onto the surface of our ASW samples after deposition at 21 K. This effort was motivated by previous work that has shown the position of DB1 and DB2 shifts to lower wavenumbers as gas attaches to the DBs (Rowland et al., 1991; Chaabouni et al., 2000; Palumbo & Strazzulla, 2003; Raut et al., 2007a). Figure 6.4a shows the spectra of DB1 and DB2 during deposition of CH_4. Previous studies have shown that CH_4 adsorbs onto the pore surfaces of ASW prior to condensing on the surface of the sample as a thin film (Raut et al., 2007a). The appearance of the 2904 cm^{-1} CH_4 absorption feature (Figure 6.4b) during adsorption supports this expectation. This feature is only found in amorphous CH_4 or amorphous H_2O + CH_4 mixtures (Hudson et al., 2015; Mejía et al., 2020) and our relatively high deposition temperature (21 K) should produce crystalline CH_4 if it deposited as a multilayered thin film. Thus, we estimate the CH_4 uptake into the pores with our QCM data. As expected, DB1 and DB2 shift by approximately 30 cm^{-1}, agreeing with previous studies (Palumbo, 2006; Raut et al., 2007a). Interestingly, the percentage of CH_4 required to induce a spectral shift in our sample is greater in our experiments than reported previously (Raut et al., 2007a). While this difference is not entirely clear, it seems likely due to slightly different experimental parameters (thickness, deposition temperature, etc.) employed in each study. Analogously, DB3 also shifts

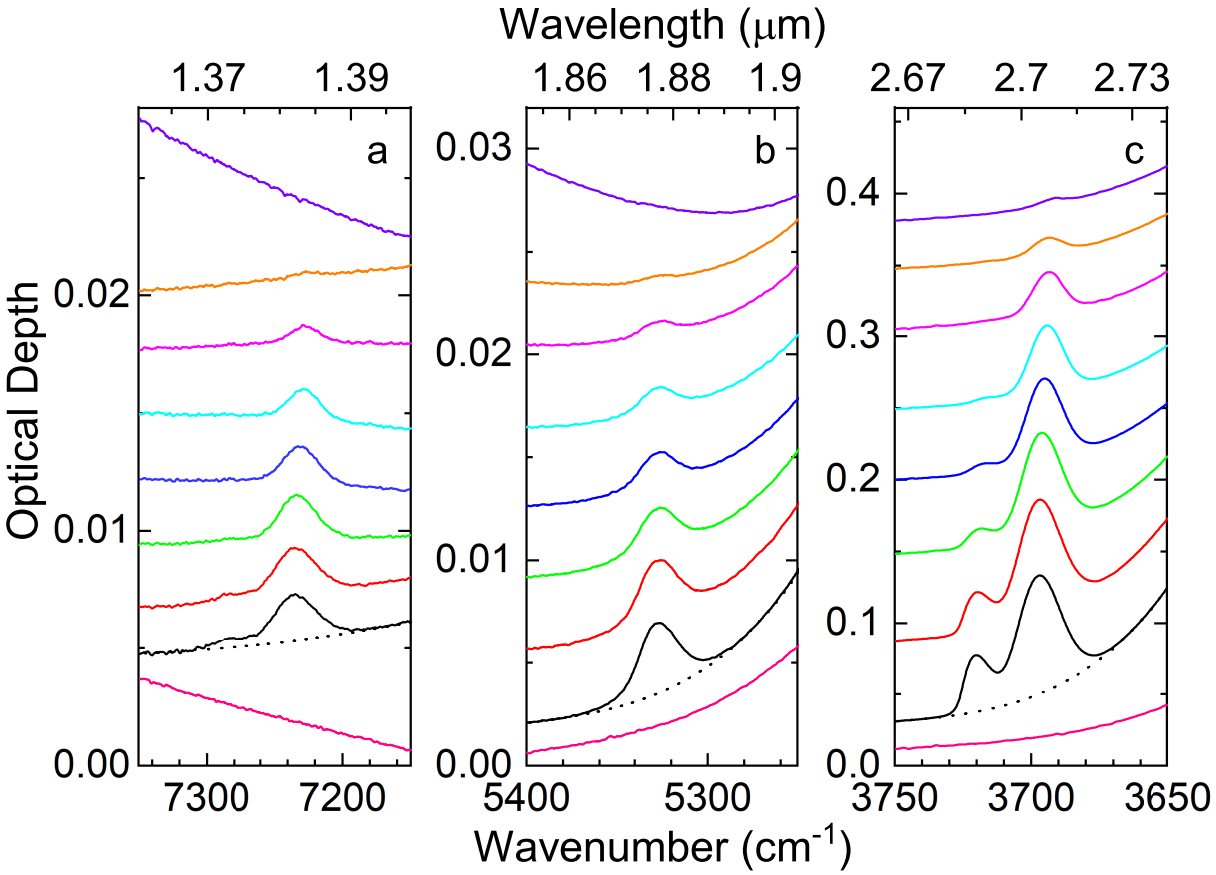

Figure 6.2: IR spectra focusing on the regions containing (a) DB4 and DB5, (b) DB3, and (c) DB1 and DB2 for a 4.13×10^{18} H_2O cm^{-2} sample deposited at 21 K and incrementally warmed to 150 K. Spectra correspond to (2^{nd} from the bottom to the top): 21 K, 30 K, 50 K, 70 K, 90 K, 110 K, 130 K, and 150 K. For comparison, the bottom spectrum is a 4.13×10^{18} H_2O cm^{-2} crystalline sample deposited at 150 K and cooled to 21 K. Spectra are vertically offset for clarity. The dotted line shows an example of our baseline fit for each DB feature at 21 K (see Section 6.3 for more details).

approximately 30 cm^{-1} as CH_4 adsorbs to the ice surface (Figure 6.5b). In addition, we also observe an absorption band at 5384 cm^{-1}, which is a combination band of CH_4 (Grundy et al., 2002). Figure 6.5a shows the DB4 and DB5 region with increasing CH_4 uptake. Admittedly, this spectral region is not as easily interpreted as the other spectral regions, due to the appearance of multiple combination bands of CH_4 that occur near and overlap the DB bands (Calvani et al., 1992; Quirico & Schmitt, 1997; Grundy et al., 2002). However, after the smallest amounts of CH_4 uptake, we can clearly resolve the shifted DB5 feature at 7185 cm^{-1} (see arrow in Figure 6.5a). There may also be two additional CH_4 absorptions that overlap with the two DB features in the spectrum with the highest CH_4 uptake (Figure 6.5a, top spectrum), yet their presence is not obvious here, likely because they are two to three times weaker than the CH_4 absorption at 7130 cm^{-1} (Calvani et al., 1992; Grundy et al., 2002). Future studies using a gas other than CH_4 would likely better

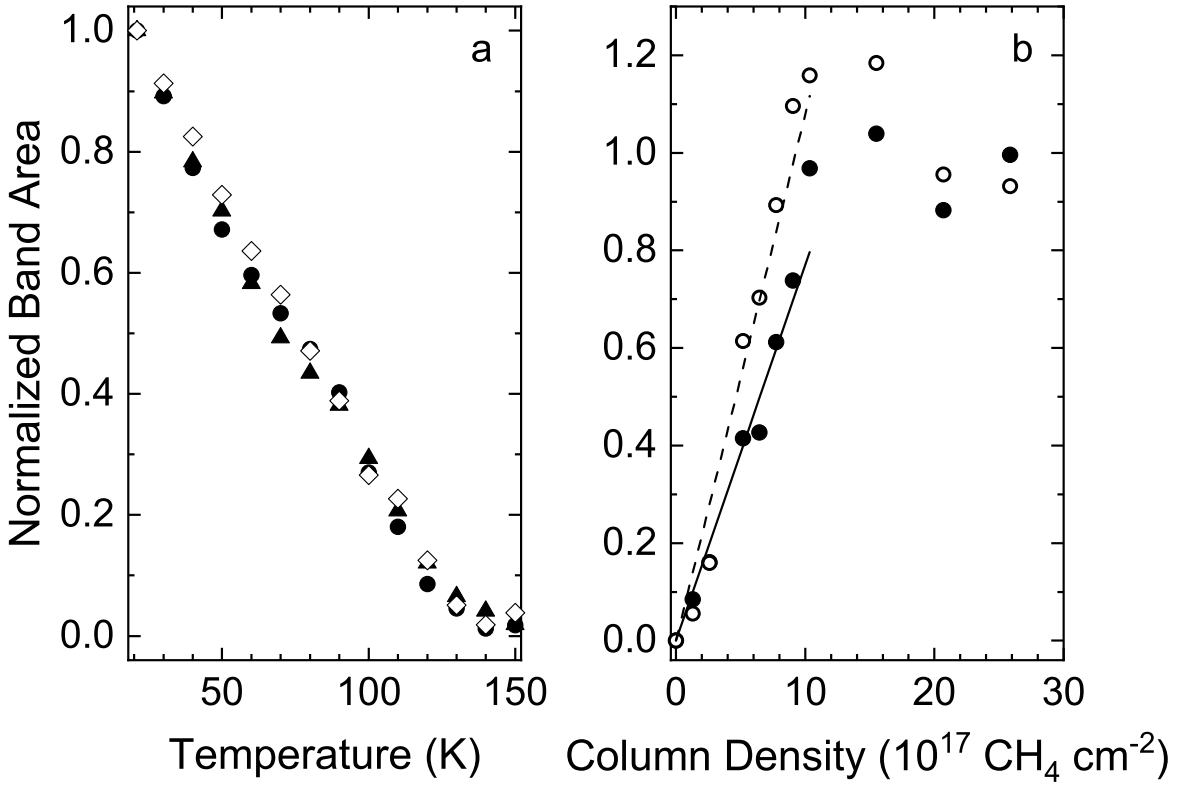

Figure 6.3: (a) Normalized band area of the $\sim$ 3700 cm^{-1} DB band pair (•), the 5326 cm^{-1} DB band (○), and the $\sim$ 7200 cm^{-1} DB band pair (▲) for a 4.13×10^{18} H_2O cm^{-2} sample deposited at 21 K and incrementally warmed to 150 K. (b) Normalized band area of the shifted DB2 (3669 cm^{-1}; ○) and the shifted DB3 (5296 cm^{-1}; •) bands for a 4.13×10^{18} H_2O cm^{-2} sample deposited at 21 K as a function of adsorbed CH_4. Dashed and solid lines correspond to the best linear fits during the initial linear increase in band area for the 3669 cm^{-1} and 5296 cm^{-1} bands, respectively. Oscillation of the band areas above $\sim 10^{18}$ CH_4 cm^{-2} is likely due to thin film interference effects (Teolis et al., 2007b).

elucidate these shifts in DB4 and DB5.

6.4.3 Estimating the Fraction of Water with a Dangling Bond

In addition to confirming multiple absorption bands that are to dangling bonds in our samples, it is also of interest to estimate the fraction of H_2O molecules that contain dangling bonds. Although doing this in more than a qualitative manner is challenging, below we make a rough estimate based on two different approaches.

As the DB3 absorption band appears to be due to both the 2- and 3-coordinated H_2O molecules (see Section 6.4.1), we can use the gas adsorption experiments to estimate an upper limit of the fraction of H_2O molecules that contain dangling bonds in our deposited sample. To do this, we calculated the band area of the DB3' (shifted DB3) during CH_4 adsorption, which we plot (Figure 6.3b) after normalizing each band

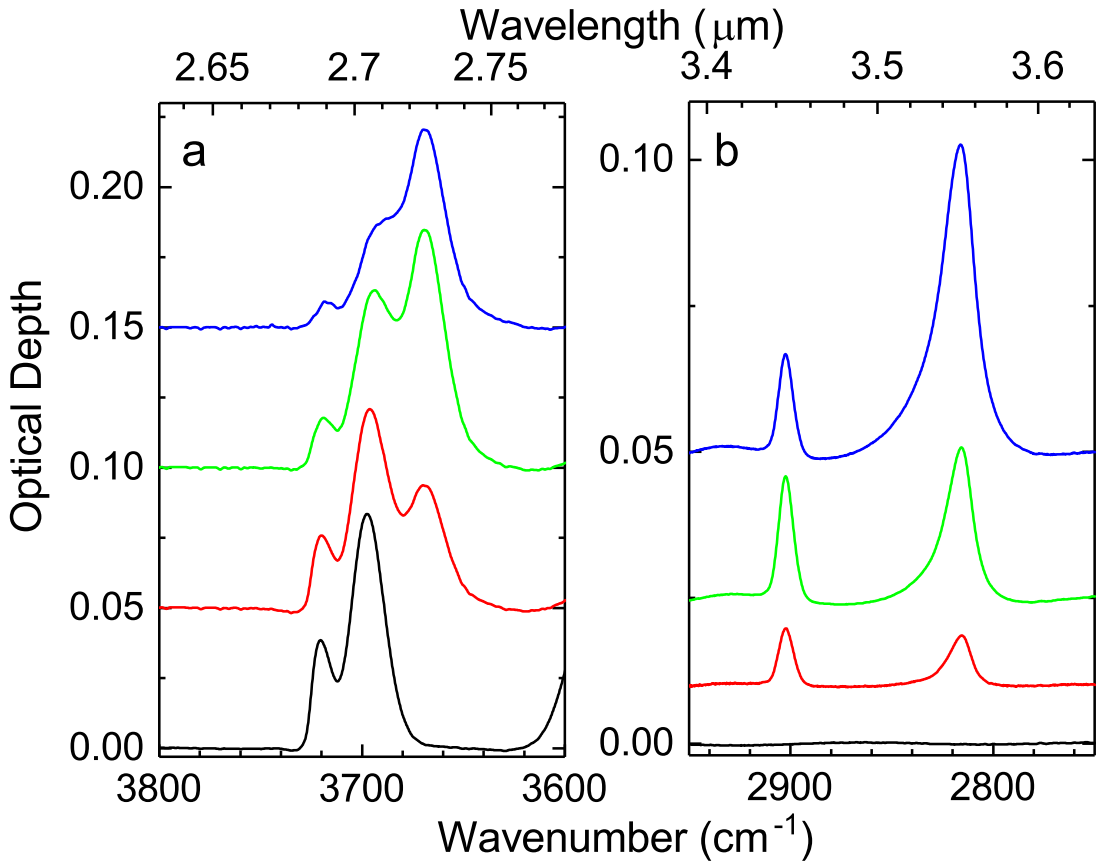

Figure 6.4: (a) IR spectra of the DB absorption features near ~ 3700 cm^{-1} and (b) the weak CH_4 features near ~ 2900 cm^{-1} for a 4.13×10^{18} H_2O cm^{-2} sample deposited at 21 K with increasing CH_4 uptake. From bottom to top, spectra correspond to (in units of 10^{17} CH_4 cm^{-2}): 0, 4.68, 9.34, and 23.4. For clarity, each spectrum has been vertically offset after removal of the baseline continuum (see Section 6.3 for more details).

area to the initial band area of the unshifted band. The increase with CH_4 uptake is initially linear and then slows down, which we interpret as the CH_4 initially going into the pores and attaching to a dangling bond, and then later beginning to deposit on the outer surface layers of the sample. Fitting the initial linear rise of band and setting the y-value to unity, we estimate that $\sim 1.3 \pm 0.1 \times 10^{18}$ CH_4 cm^{-2} would be needed to shift 100 % of the DB3 band if all the DB bonds could be accessed. Assuming each CH_4 molecule adsorbs to a single H_2O molecule, we estimate that $\sim$ 30 % of the H_2O molecules contain dangling bonds. We suspect this is an upper limit, as the CH_4 may also adsorb to interior and exterior surfaces of our sample, which lack dangling bonds, or two CH_4 molecules could potentially attach to a 2-coordinated H_2O molecule. Our interpretation is consistent with our separate analysis of the DB2' feature, also shown in Figure 6.3b, which is only sensitive to 3-coordinated H_2O molecules. In that case, the shape of the curve is still the same, yet has a smaller slope, which we can use to estimate that $9.3 \pm 0.5 \times 10^{17}$ CH_4 cm^{-2} would be needed to shift 100 % of the DB2 band or that up to $\sim$ 23 % of the H_2O in the sample consists of 3-coordinated

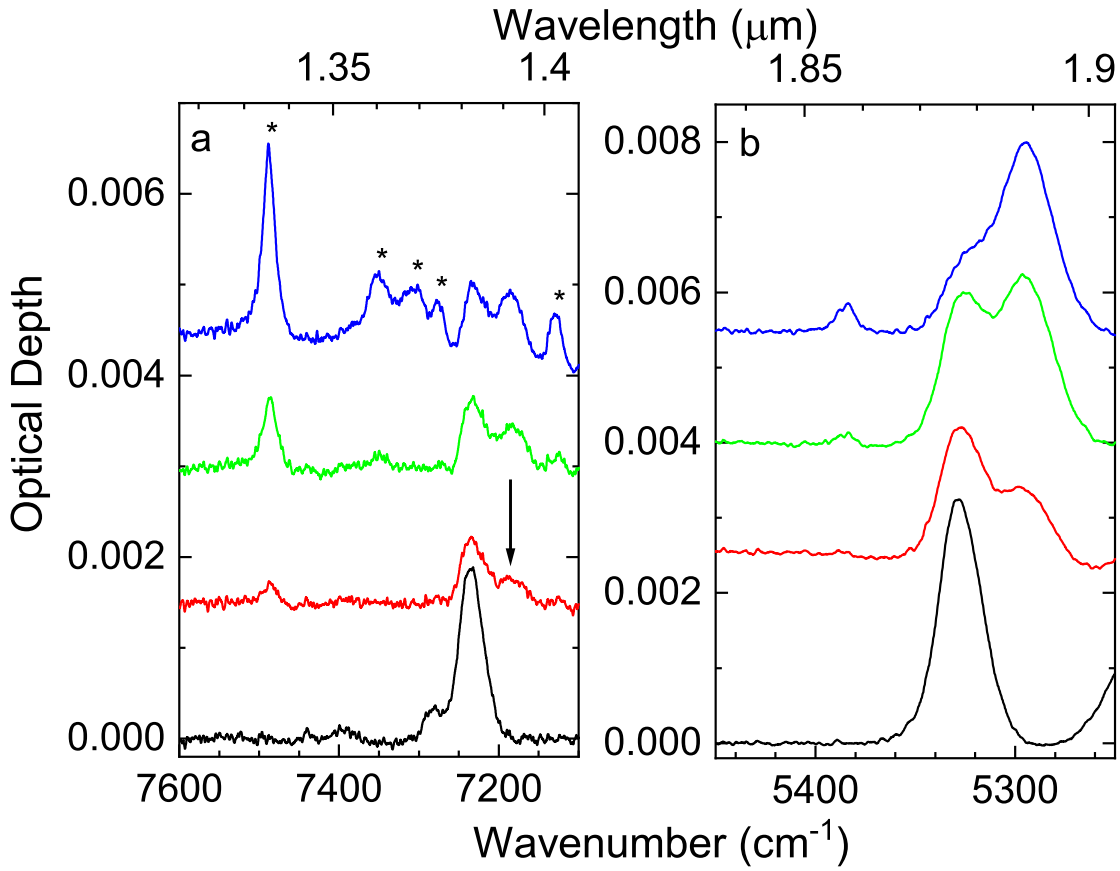

Figure 6.5: (a) IR spectra of the DB absorption features near $\sim$ 7200 cm^{-1} and (b) $\sim$ 5300 cm^{-1} for a 4.13×10^{18} H_2O cm^{-2} sample deposited at 21 K with increasing CH_4 uptake. From bottom to top, spectra correspond to (in units of 10^{17} CH_4 cm^{-2}): 0 , 4.68, 9.34, and 23.4. Resolved CH_4 features in the $\sim$ 7200 cm^{-1} are indicated with stars; from left to right these correspond to: $\nu_2 + 2\nu_3$, 7488 cm^{-1}; $\nu_1 + \nu_2 + \nu_3$, 7351 cm^{-1}; $2\nu_2 + \nu_3 + \nu_4$, 7303 cm^{-1}; $2\nu_3 + \nu_4$, 7279 cm^{-1}; $\nu_1 + \nu_3 + \nu_4$, 7130 cm^{-1} (Grundy et al., 2002). Note the single CH_4 feature in the $\sim$ 5300 cm^{-1} region at 5384 cm^{-1} (Grundy et al., 2002). For clarity, each spectrum has been vertically offset after removal of the baseline continuum (see Section 6.3 for more details).

H_2O molecules. Interestingly, the slopes for DB2' and DB3' represent the number of 3-coordinated H_2O molecules and the total H_2O molecules with dangling bonds, respectively. Assuming that the CH_4 adsorbing to surfaces without dangling bonds affects both bands similarly, the ratio of the two slopes suggests that the 3-coordinated H_2O molecules make up $\sim$ 70 % of the total H_2O molecules with dangling bonds. This estimate is qualitatively consistent with the size of DB1 and DB2 (Figure 6.2c), especially considering that the absorption strength of the 2-coordinated H_2O molecule (DB1) will likely be slightly weaker than the 3-coordinated H_2O molecule (DB2) (Moudens et al., 2009).

Another way to estimate the fraction of H_2O molecules that contain dangling bonds is by noting that the band area of the DB3 combination absorption band is $\sim$ 124 times smaller than the corresponding band area of the combination mode for fully coordinated H_2O molecules in our fresh sample. Previous work has shown

that the IR absorption strength of the free O-H bond (DBs) stretch is between $\sim$ 8 - 17 % the strength of the fundamental O-H stretch of H_2O-ice due to fully coordinated molecules (Hagen et al., 1981; Moudens et al., 2009). Assuming this decrease in strength is similar for these combination bands, then we estimate that 5 – 10 % of the H_2O molecules in the sample contain dangling bonds. Of course this could also be an underestimate, as the IR absorption strength of the fundamental H_2O bending mode may be weaker in the 2- and 3-coordinated H_2O molecules than it is in the fully coordinated H_2O molecule. Regardless, this value is somewhat higher than the 1 - 2 % (or 0.5 - 1 % fraction of OH bonds in the sample are dangling bonds) value estimated by Dartois et al. (2013), although this discrepancy may be at least partially due to a difference in sample porosity, which is strongly dependent on conditions under which the ice is deposited (Brown et al., 1996; Stevenson et al., 1999; Horimoto et al., 2002). At any rate, assuming that the resulting band strength (A-value) of DB3 would scale similarly to previous measurements of 1.2×10^{-18} cm H_2O^{-1} for the fully coordinated combination mode at 5040 cm^{-1} (Gerakines et al., 2005), we estimate that the A-value in transmission, which could be used directly for measurements in the ISM, is between $9.6{\times}10^{-20}$ and $2.1{\times}10^{-19}$ cm H_2O^{-1}. This somewhat crude estimate should be refined with direct transmission measurements, where interference effects are typically less prominent (Teolis et al., 2007b), which is something we hope to do in the future.

6.5 Astrophysical Implications

As noted previously, there have been no detections of the fundamental DB absorption bands (DB1 and DB2) in the spectra of interstellar ices. While the particular susceptibility of these features to energetic particle irradiation may be largely responsible for the absence of these features (see above), it also seems reasonable that there may be some regions in interstellar space where porous ASW exists, such as in very young molecular clouds. Dartois et al. (2013) showed spectra in the fundamental DB region ($\sim$ 3700 cm^{-1}) of several younger stellar objects, finding that CO_2 absorptions and spectral noise prevented any detection of porous ASW. While the increased sensitivity predicted for JWST's NIRSpec, compared to prior generation telescopes (Milam et al., 2016), may enable future detections of porous ASW through the identification of the fundamental DB absorptions, these features may still be obstructed by other IR active species. Our new results, which clearly show two additional spectral regions that could be used to identify porous ASW through detection of DB absorption bands, may serve as an alternative way to identify porous ASW with remote sensing spectroscopy. The 5326 cm^{-1} DB band (DB3) may be particularly useful given that unlike the fundamental and overtone DB bands, this combination band is well separated from CO, CO_2, and CH_4 absorption features in this spectral region (Gerakines et al., 2005; Dartois et al., 2013).

Admittedly, these near-infrared DB absorption features are ~ 20 times weaker than the fundamental DB absorption features. As the column density of our samples are similar to what is typical of H_2O-ice detected in the ISM $\sim 1 \times 10^{19}$ H_2O cm^{-2} (Whittet et al., 1996; Gibb et al., 2000), we suspect that the DB3 and DB5 (Figures 6.2b and 6.2c) features will have optical depths on the order of $\sim 10^{-3}$. This small of an optical depth would make these features difficult if not impossible to detect with even large prior generation telescopes, where previous estimates (Sandford & Allamandola, 1993) suggested that integration times on the order of hours were required to observe an absorption feature with an optical depth of ~ 0.03 at a SNR of 3 (3σ confidence). However, given that the minimum detectable flux estimated for JWST's NIRSpec is about a factor of 10 - 100 better than any prior generation telescopes (Milam et al., 2016; Rivkin et al., 2016), it is of interest to estimate the integration time that would be required to observe these new dangling bond features with JWST. To do this, we used the JWST Exposure Time Calculator for JWST's NIRSpec operating in its fixed slit observation mode with the G235M/F170LP grating/filter pair (Pontoppidan et al., 2016), which has a resolving power of ~ 1000 for wavelength coverage that includes DB3, which is the mostly likely of the new DB features to be well separated from other absorption features potentially present (see above). Similar time estimates are expected for the DB5 absorption band. Given a typical continuum flux of 40 mJy at 2 microns for the bright embedded source W33A (Capps et al., 1978), which is a common target for weak ice absorption features (Whittet et al., 1996; Gibb et al., 2000), and binning every four wavelength resolution elements (~ 0.002 μm), we estimate that this feature should be observable at a SNR of 3 after an integration time of ~ 4.5 hrs. Thus, we suspect that these features should be large enough to be identified by JWST's NIRSpec in future observing campaigns.

Finally, we also speculate that much of the ASW in the ISM will have molecules trapped in its pores, which will alter the position of each DB feature, as shown here for CH_4 or for other gases previously (Rowland et al., 1991; Chaabouni et al., 2000; Palumbo & Strazzulla, 2003; Loeffler et al., 2006c). This complication may, in some cases, inhibit the success of using remote sensing spectroscopy to identify porous ASW and any adsorbed species present, while in other cases, it may enhance it. In the former case, adsorbates may appear at similar peak positions as these shifted DB features, as we show for DB4 and DB5 in Figure 6.5a, making unique identifications difficult. In the latter case, where adsorbates don't have a feature appearing near or overlapping with the DB features, the peak position of the shifted DB band may not only identify ASW but also possibly the adsorbed species, as the magnitude of the shift will vary depending on the adsorbed molecule. This characteristic of the DB absorption bands may be particularly valuable for cases where the adsorbates are weakly absorbing, such as with homonuclear molecules (H_2, N_2 and O_2), which are likely important components of many interstellar ice mantles (Sandford & Allamandola, 1993; Ehrenfreund et al., 1993).

6.6 Acknowledgements

This research was supported by NASA Astrophysics Research and Analysis Award #80NSSC20K0359. Upon acceptance, all data shown in the paper, as well as the raw spectral data (i.e. before continuum removal or vertically shifting the spectra) will be stored in Northern Arizona University's long-term public access data archive located at https://openknowledge.nau.edu/. Currently, the data is located on our laboratory website: http://www.astro.nau.edu/ loeffler/Submitted-data.html.

Chapter 7

Thermal Reactions between H_2S and O_3: Implications for Europa Surface Chemistry

Patrick D. Tribbett[1], Mark J. Loeffler[1,2]

This is the Accepted Manuscript version of an article accepted for publication in The Planetary Science Journal. IOP Publishing Ltd is not responsible for any errors or omissions in this version of the manuscript or any version derived from it. The Version of Record is available online at `https://iopscience.iop.org/article/10.3847/PSJ/ac9236`.

7.1 Abstract

Here we present a laboratory study demonstrating a low temperature thermal oxidation reaction within H_2O + H_2S + O_3 solid ice mixtures that produces observable sulfur anion products at temperatures as low as 90 K. This reaction primarily produces SO_2, sulfur anions (including HSO_3^-, HSO_4^-, and SO_4^{2-}) and O_2 at lower temperatures (90 - 140 K) and hydrated states of sulfuric acid (H_2SO_4: nH_2O, where n = 0, 1, 4) at higher temperatures (150 - 250 K). We estimate that the overall activation energy to initiate these reactions is $20 \pm 3\,\mathrm{kJ\,mol^{-1}}$, which is significantly lower than the activation energy required to oxidize SO_2 to the sulfate ion. Given the detection of sulfur species on the surfaces of the Galilean satellites, and the prevalence of radiolytically produced oxidants, we expect that these thermal reactions will play an important role in explaining results obtained from future observations and missions that can measure the spatial distribution of these species.

Keywords: Laboratory astrophysics (2004); Astrochemistry (75); Surface ices (2117); Galilean satellites (627)

7.2 Introduction

The radiolytic chemistry of icy surfaces within the Solar System and in the interstellar medium (ISM) has been studied for several decades. However, the thermal chemistry of surface and subsurface ices has received

[1]Department of Astronomy and Planetary Science, Northern Arizona University, PO Box 6010, Flagstaff, AZ 86011, USA
[2]Center for Materials Interfaces in Research and Applications (MIRA), Northern Arizona University, PO Box 6010, Flagstaff, AZ 86011, USA

significantly less attention due to the characteristically low temperatures ($\sim$ 60 - 160 K on the Galilean and Saturnian satellites (Squyres, 1980; Hanel et al., 1982; Spencer et al., 1999); $\sim$ 20 - 40 K in the outer Solar System (Stern et al., 1993; Earle et al., 2017); $\sim$ 10 K in the ISM (Caselli & Ceccarelli, 2012)). Despite the low temperatures in these astronomical environments and the limited diffusion associated with solid state materials, recent studies have demonstrated that many chemical systems are thermally reactive at temperatures as cold as 80 K (Moore et al., 2007b; Bossa et al., 2008; Loeffler & Hudson, 2010). Low temperature acid-base reactions (Demyk et al., 1998; Noble et al., 2013) proceed through proton transfer; and increasingly complex reaction mechanisms, including oxidation reduction (Loeffler & Hudson, 2013, 2016) and nucleophilic additions (Bossa et al., 2008; Noble et al., 2012), also occur at low temperatures. For a recent review of thermally reactive astrochemical systems see Theulé et al. (2013).

One environment of particular interest is the Galilean system, which is exposed to substantial ionizing radiation (Cooper et al., 2001; Nordheim et al., 2019), is geologically active (Greeley et al., 2004), and possesses surface and near-surface diurnal temperatures potentially conducive to low temperature thermal reactions (Spencer et al., 1999). Decades of laboratory studies have demonstrated that the irradiation (H^+ and e^-) of H_2O-ice produces a number of radiolytic products including H_2, O_2, and H_2O_2 (Moore & Hudson, 2000; Orlando & Sieger, 2003; Loeffler et al., 2006b; Zheng et al., 2006). If enough radiolytic O_2 is produced, then O_3 will also be produced, as has been shown directly in experiments that deposited H_2O-ice, while actively irradiating the sample with heavy ions (Teolis et al., 2006). Despite the overwhelming number of laboratory studies demonstrating solid state radiolysis and the production of strong oxidants (H_2O_2 and O_3), and a magnetospheric radiation environment encompassing the Galilean satellites, the observational evidence for these two solid state species is both underwhelming and complex. In fact, only H_2O_2 has been definitively observed on Europa's surface, and it is largely confined to the leading hemisphere (Carlson et al., 1999b; Hand & Brown, 2013). Conversely, O_3 has only been detected in ultraviolet reflectance spectra of the trailing hemisphere of Ganymede (Noll et al., 1996). While it seems likely that the conditions of the local surface environment (radiation flux, composition, temperature, etc.) strongly influence the formation and survival of these two species, to date, there is no unanimously accepted solution that can explain these observations.

Interestingly, Noll et al. (1997) noted a possible anti-correlation between these oxidant populations and other resident species, specifically sulfur species. SO_2 is largely confined to the trailing hemisphere of Europa (Hendrix et al., 2011), while H_2O_2 has primarily been detected on the leading hemisphere (Hand & Brown, 2013). Low temperature thermal reactions may play an important role in these hemispheric dichotomies especially in the near sub-surface. Previous laboratory studies by Loeffler & Hudson (2013, 2016) demonstrate that SO_2 reacts readily with both H_2O_2 and O_3 at temperatures as low as 80 K. For a

recent review of sulfur ice astrochemistry see Mifsud et al. (2021a). H_2S has also been tentatively identified on the surface of the Galilean satellites (McCord et al., 1998). Though H_2S does not react with the oxidant H_2O_2 in the solid phase (Loeffler & Hudson, 2015), H_2S reacts readily with the oxidant O_3 in the gas phase (Cadle & Ledford, 1966; Hales et al., 1969; Glavas & Toby, 1975). A low temperature thermal oxidation reaction between an additional sulfur compound and the strong oxidant O_3 may have implications for the surface and sub-surface chemistry of the Galilean satellites. Here, we demonstrate the efficacy of a thermal oxidation reaction within H_2O + H_2S + O_3 ice mixtures at temperatures relevant to the icy satellites. We identify the reaction products using a combination of infrared spectroscopy, microbalance gravimetry, and mass spectrometry as our analytical tools. In addition, we derive an overall reaction activation energy and discuss this reaction's implications for both Europa, Ganymede, and Callisto in anticipation of the upcoming NASA's Europa Clipper Mission.

7.3 Experimental Methods

We performed all experiments within a stainless steel ultra-high vacuum (UHV) chamber with a base pressure of 10^{-9} torr ($\sim 10^{-10}$ torr within the thermal-radiation shield). Figure 7.1 shows the current setup used for this study, which has been slightly modified from our recent work (Tribbett & Loeffler, 2021; Tribbett et al., 2021). To prepare our samples, we co-deposited H_2O (high performance liquid chromatography (HPLC) grade, Sigma Aldrich), H_2S (99.95% purity, Matheson Gas), and O_3 at 50 K from separate mixing lines onto an optically flat gold-mirror electrode of an Inficon IC6 quartz-crystal microbalance (QCM). We produced O_3 within a glass manifold filled with O_2 (99.999% purity, Matheson Gas) by sparking the manifold with a Tesla coil for $\sim$ 20 min. Resultant O_3 condensed in a portion of the manifold submerged in a liquid nitrogen bath, and all residual O_2 was pumped away. We determined the composition of our H_2O + H_2S + O_3 (71:23:6 $\pm$ 2:2:1) ices by first leaking in a small amount of H_2O, then adding H_2S, and finally adding in O_3, all while monitoring the change in deposition rate with our QCM. The amount of pure H_2O and H_2O + H_2S was $\sim$5% of the total mass of the sample, and the derived composition includes these first two layers. We estimate that the uncertainty of our composition measurements due to the unmixed layers is less than 5%, which is within the reproducibility of our growth conditions. We estimate the thickness of our mixture to be $\sim$ 0.85 - 1. μm, assuming a density of 0.82 g cm^{-3} for H_2O (Westley et al., 1998), 1.65 g cm^{-3} for O_3 (Teolis et al., 2007a; Raut et al., 2011), and 1.15 g cm^{-3} for H_2S. Due to the sparse density measurements of solid H_2S and density's dependence on deposition method (Loeffler et al., 2016b), we opted to determine the density of amorphous H_2S deposited at 50 K within our UHV chamber using ultraviolet-visible spectroscopy (see Behr et al. (2020) for additional information regarding the methods). Our derived density of 1.15 g

cm^{-3} is consistent with the Lorentz-Lorenz estimate by Hudson & Gerakines (2018) ($\sim$ 1.1 g cm^{-3}) for background deposited amorphous H_2S ice and the more recent measurement by Yarnall & Hudson (2022a) for crystalline H_2S ice (1.22 g cm^{-3}).

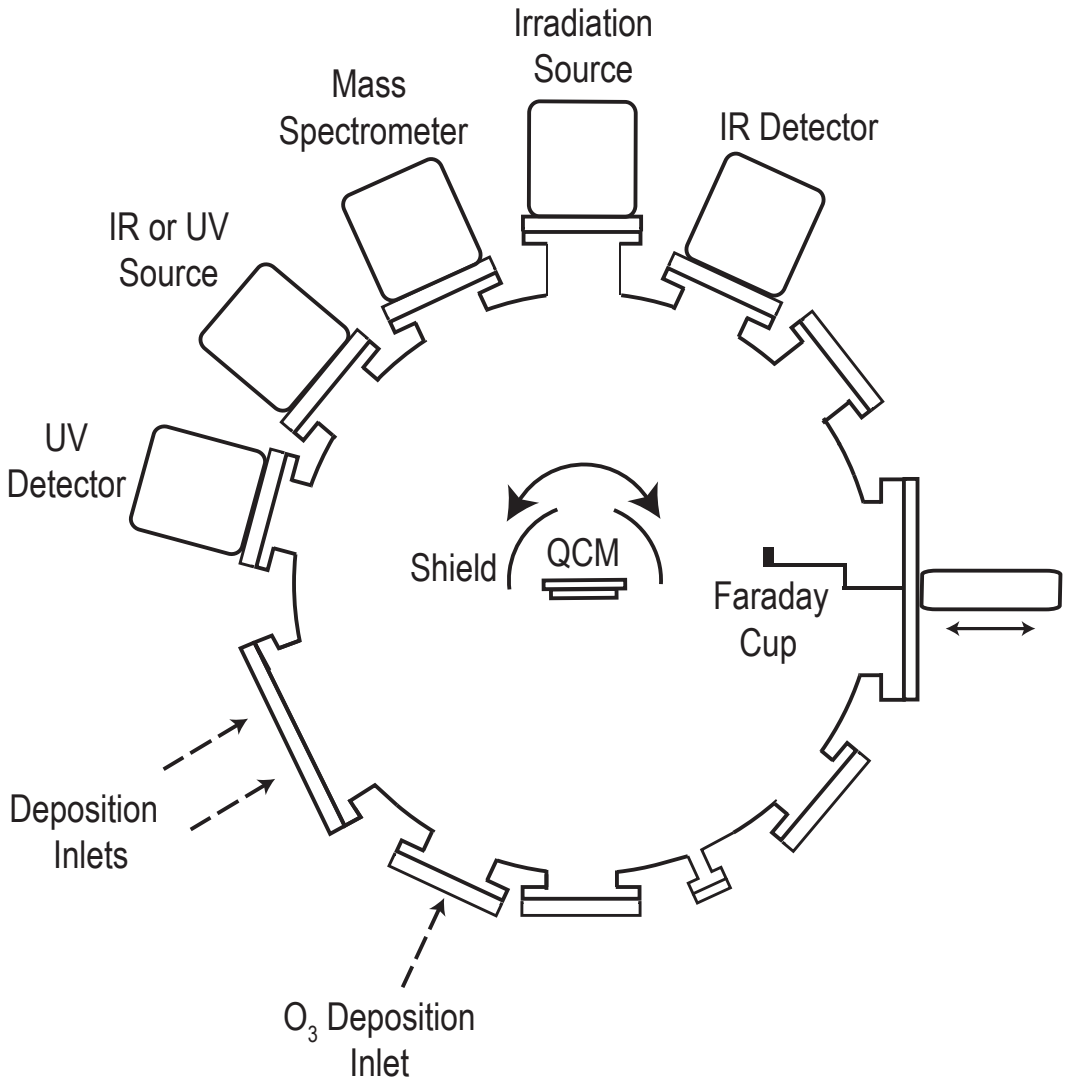

Figure 7.1: Experimental setup.

We monitored the ice samples using a combination of infrared (IR) spectroscopy, mass spectrometry (MS), and the QCM. We acquired specular reflectance spectra between 10000 cm^{-1} and 650 cm^{-1} using the infrared light source from a Thermo-Nicolet iS50 Fourier Transform Infrared Spectrometer (FTIR) that is incident on the sample at 37.5°, and analyzed the reflected light using a MCT-A detector at a spectral resolution of 2 cm^{-1}. Here, we report spectra in units of optical depth ($-\ln(R/R_0)$), where R is the reflected

intensity from the sample and R_0 is the reflected intensity from the bare gold substrate.

Once the ice samples were deposited, we performed one of two heating approaches: linear heating or isothermal annealing. During the linear heating experiments, we warmed the ice samples from 50 K to 290 K at a rate of 0.1 K min^{-1}, while monitoring for reactions using IR spectroscopy and the QCM. QCM data indicated that sublimation of O_3 within an H_2O-ice matrix between 50 K and 130 K is negligible (see section 7.4). However, the band area of the O_3 combination band at 2104 cm^{-1} decreases by $\sim$ 15% between 50 K and 130 K, which is consistent with Loeffler & Hudson (2016) and is taken into account in our analysis. During the isothermal annealing experiments, we warmed the ice samples from 50 K to an annealing temperature between 95 K and 125 K at a rate of 5.0 K min^{-1}. Samples remained at the annealing temperature for 24 hours, where we monitored them using IR spectroscopy to derive reaction kinetic parameters (Loeffler & Hudson, 2013). To determine the extent of the reaction, we monitored the 2104 cm^{-1} O_3 band, since sulfur anions products appear and overlap with the stronger fundamental O_3 feature at 1032 cm^{-1} (Teolis et al., 2007a; Loeffler & Hudson, 2016). Lastly, during both warming techniques, we monitored the composition of the ejected flux using a Stanford Research Systems (SRS 100) Residual Gas Analyzer, aimed at an incident angle of $\sim$19° with respect to the QCM substrate.

7.4 Results

Figure 7.2 shows the mid-infrared spectrum of a H_2O + H_2S + O_3 ice mixture after deposition at 50 K and at several temperatures during warming to 150 K at a rate of 0.1 K min^{-1}. The initial spectrum is dominated by several large absorption features attributed to H_2O (O-H bending mode, 1654 cm^{-1}; lattice mode, 806 cm^{-1}) and H_2S (S-H stretching modes, 2551 cm^{-1}, S-H bending mode, 1175 cm^{-1}), as well as several sharper peaks attributed to O_3 (1032 cm^{-1} and 2104 cm^{-1}). Spectral assignments for these reactants can be found in Table 7.1. We note that there is a small amount of CO_2 and OCS contamination within our ice mixture, indicated with asterisks in the 150 K spectrum. The CO_2 is evident by the absorption feature between 2400 - 2300 cm^{-1} (C=O stretch). Instead of using the band strength of the CO_2 (Gerakines et al., 1995; Gerakines & Hudson, 2015), which can be problematic due to the interference effects typical of thin film reflectance spectroscopy (Teolis et al., 2007b), we estimated the CO_2 column density by co-depositing a mixture with known amounts of H_2O and CO_2 to a thickness of $\sim 0.9 - 1\mu$m and compared the integrated band area of the fundamental CO_2 feature to the integrated band area of the feature in our H_2O + H_2S + O_3 ice. With this approach, we determined the amount of CO_2 in our ice mixtures to be $\sim 1.10 \times 10^{15}$ CO_2 cm^{-2} or $\sim$ 0.04% of our sample by number. Regardless, previous work has shown that CO_2 is not oxidized by O_3 at these temperatures and thus does not participate in the observed reactions (Loeffler & Hudson,

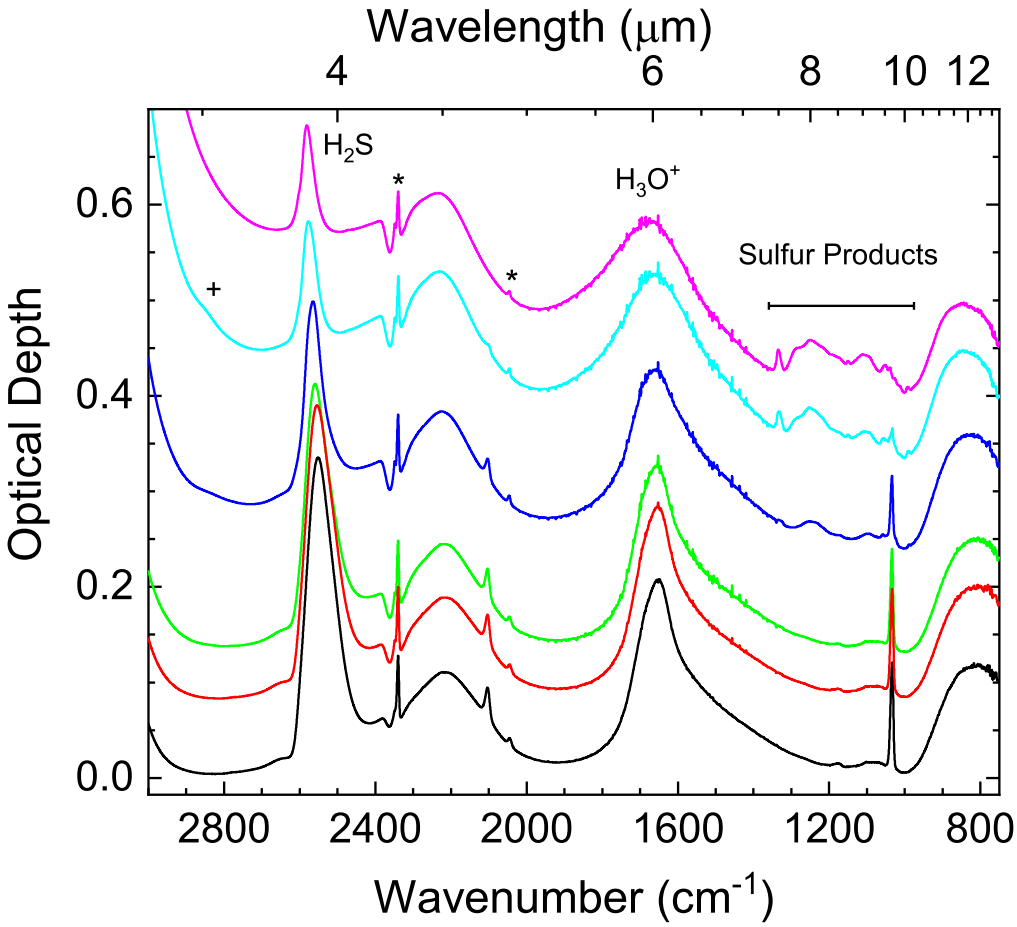

Figure 7.2: IR spectra of a H_2O + H_2S + O_3 sample (75:20:5) during warming at a rate of 0.1 K min^{-1}. Spectra correspond to approximate temperatures of (from bottom to top): 50 K, 71 K, 91 K, 110 K, 130 K, and 151 K. Asterisks denote contaminants within the ice (CO_2 and OCS). The plus sign corresponds to the H_2O_2 band at $\sim$ 2850 cm^{-1}.

2016). CO_2 has also been shown to react with H_2O to create H_2CO_3 or carbonic acid; however, this reaction is endothermic (31.4 kJ mol^{-1}) and unlikely to occur at low temperatures in the absence of ionizing radiation (Zheng & Kaiser, 2007). The OCS contamination is apparent from the small band centered at 2045 cm^{-1} (Ferrante et al., 2008), and is likely introduced by the H_2S source, which lists OCS as a possible contaminant at 0.2% by volume. Despite being fairly dilute, the band strength for the C=O stretch of OCS is comparable to CO_2 (Yarnall & Hudson, 2022b) and minimal contamination from this compound is reasonable. Moreover, this feature can be seen in the spectra of mixtures of H_2S and H_2O ice throughout the literature, where similar qualities of H_2S are used (Jiménez-Escobar & Muñoz caro, 2011; Yarnall & Hudson, 2022b). Recent work has demonstrated that OCS can undergo thermal nucleophilic addition in the presence of methylamine (CH_3NH_2)((Mahjoub & Hodyss, 2018)); however the kinetics of a simple addition reaction between OCS and H_2O are unfavorable (Ghosh et al., 2010). Given the minimal change in band area and shape during

our experiments and the minor amount present, it is also unlikely OCS contributes to our thermal reactions with O_3. Regardless, we hope to investigate this as a chemical system (H_2O + OCS + O_3) in the future.

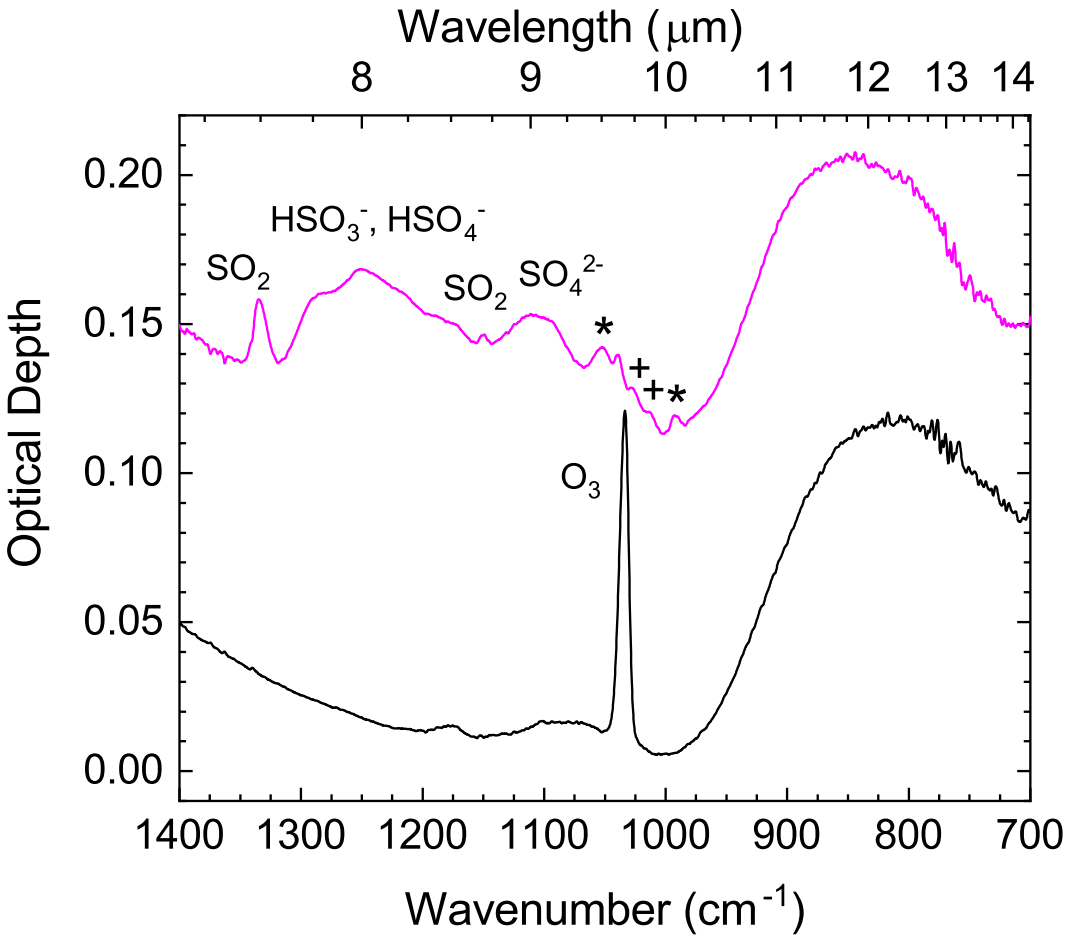

Figure 7.3: Mid-infrared spectra of a H_2O + H_2S + O_3 sample (75:20:5) during warming at a rate of 0.1 K min^{-1}, highlighting the spectral region containing features attributed to the sulfur products (see Table 8.1 for spectral assignment details). Spectra correspond to 50 K (bottom) and 151 K (top). Note that the broad and unresolved feature at 1235 cm^{-1} has been a attributed to both HSO_3^- and HSO_4^- (see Table 8.1 for additional details). Asterisks correspond to HSO_4^-, and plus signs correspond to HSO_3^-.

During warming, both H_2S and O_3 absorption features begin to decrease by around 70 K despite negligible mass loss from the sample at these temperatures (Figure 7.4). We suspect that this decrease corresponds to the formation of an intermediate sulfur compound that we cannot uniquely identify with infrared spectroscopy (see Section 7.5.1 for more details) (Glavas & Toby, 1975). Above 90 K, several spectral changes include the broadening of the H_2O bending feature, and the appearance of HSO_3^- (1038 cm^{-1}), HSO_4^- (992 cm^{-1}), SO_4^{2-} (1111 cm^{-1}), and the broader feature at 1235 cm^{-1} which has been attributed to both the bisulfite and bisulfate anions (Moore et al., 2007b; Loeffler & Hudson, 2016). Above 110 K, an additional band attributed to HSO_3^- appears at 1013 cm^{-1}, and two sharp stretching bands of SO_2 appear at 1333 cm^{-1}

and 1149 cm^{-1}. Several of these smaller features are more evident in Figure 7.3, which highlights the wavelength region (1400 - 800 cm^{-1}) most affected by the presence of the sulfur anions. Additionally, we see the appearance (between 110 - 130 K) and disappearance (150 K) of a small band at 2848 cm^{-1}, which we attribute to H_2O_2 (Loeffler et al., 2006b; Zheng et al., 2006). The feature's disappearance at temperatures below where it will sublimate (Loeffler et al., 2006c) is consistent with known thermally-driven reactions between H_2O_2 and HSO_3^- (Loeffler & Hudson, 2013). Figure 7.4 shows the mass loss rate during warming of our H_2O + H_2S + O_3 ice mixtures from 50 K to 290 K at a rate of 0.1 K min^{-1} and the O_2 (32 amu) flux measured with the MS. Over the temperature range of interest for these thermal reactions (80 - 130 K), there is negligible desorption from our samples as indicated by the QCM and MS. Between 135 and 140 K, we observe our first peak in the mass loss rate spectrum, which, based on our MS measurements, we attribute to thermally-produced oxygen diffusing from our sample as the H_2O-ice begins to crystallize. The desorption of trapped O_2 prior to the desorption of H_2O is consistent with previous laboratory studies examining the thermal desorption of O_2 within H_2O-ice mixtures (Vidal et al., 1997; Loeffler et al., 2006c). The presence of O_2 is also consistent with the reaction mechanisms discussed below (see section 7.5.1), which yields O_2 as a major reaction product. Further warming results in two large, unresolved peaks at 155 K and 160 K, which we attribute to O_2, H_2S, and H_2O. Similar to the O_2, residual H_2S desorbs from the ice as the H_2O crystallizes, and ultimately sublimates from the sample. Following the large H_2O desorption peak, we find several additional desorption peaks that we attribute to H_2O desorbing from stable states of hydrated sulfuric acid. Based on previous studies (Moore et al. (2007b); Loeffler et al. (2011)), the desorption peak at 174 K is due to the decomposition of sulfuric acid tetrahydrate, while the peak at 203 K is due to the decomposition of sulfuric acid monohydrate (H_2SO_4:$4H_2O$ and H_2SO_4:H_2O). We note that an additional peak occurs around 193 K. While this peak may indicate another stable hydrated state of sulfuric acid (Zhang et al., 1993), our samples were too thin at this point to allow us to determine whether there was a unique spectral signature associated with this peak (data not shown). We intend to pursue this unidentified peak further in future studies using additional chemical systems that are not oxidant limited (e.g. H_2O:SO_2:H_2O_2). Once the final H_2O peak desorbs, a film of solid crystalline sulfuric acid remains until it begins to desorb at $\sim$ 240 K, which is consistent with previous studies examining the radiolytic and thermal stability of H_2SO_4 (Moore et al., 2007b; Loeffler et al., 2011).

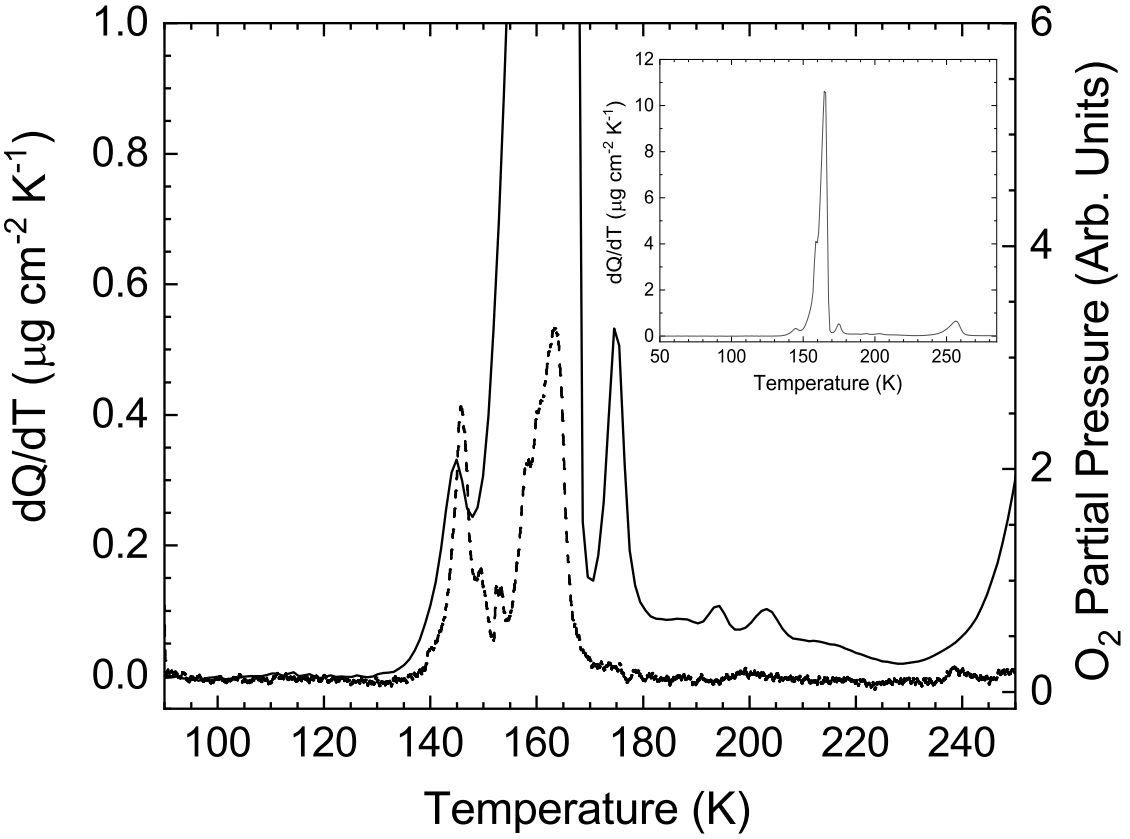

Figure 7.4: QCM-derived mass loss rate (solid line) and O_2 partial pressure (dashed line) during warming of a H_2O + H_2S + O_3 sample (75:20:5) at a rate of 0.1 K min^{-1}. Inset: QCM-derived mass rate shown in main figure but with an expanded scale to show the entire mass-loss rate curve.

7.5 Discussion

7.5.1 Reaction Chemistry and Spectral Assignments

The thermal oxidation of H_2S with O_3 has been studied in the gaseous and aqueous phases due to the reaction's implications for Earth's atmospheric chemistry (Hales et al., 1969; Glavas & Toby, 1975; Mark et al., 2011); however, the exact mechanism is still unclear. Early works suggested that the primary reaction sequence produces SO_2 and O_2 through a five-membered ring (HSO_3H) and the more stable intermediates HSO, HSO_2, and SO (see Equations 7.1 - 7.3).

$$H_2S + O_3 \longrightarrow HO_2 + HSO \tag{7.1}$$

$$HSO + O_3 \longrightarrow HO + SO + O_2 \tag{7.2}$$

$$SO + O_3 \longrightarrow SO_2 + O_2 \tag{7.3}$$

This sequence was later corroborated by chemical luminescence experiments identifying HSO within H_2S and O_3 gaseous mixtures (Schurath et al., 1977). Moreover, several previous studies have also demonstrated an oxidative addition reaction between photolyzed oxygen atoms and H_2S at low temperatures within an argon matrix forming SO_2 through the intermediate HSOH (Smardzewski & Lin, 1977; Smardzewski, 1978). Additionally, we note the presence of H_2O_2 in our thermally altered samples, which may form through the recombination of hydroxyl radicals formed in Equation 7.2 (Loeffler et al., 2006b; Zheng et al., 2006):

$$2OH \longrightarrow H_2O_2 \tag{7.4}$$

The insertion of excited oxygen radicals into water molecules is also a possible H_2O_2 formation mechanism as suggested by Zheng et al. (2006); however, we find no evidence of the formation of H_2O_2 in our thermally altered $H_2O + O_3$ reference samples, which indicates that this formation pathway is significantly less efficient.

Mark et al. (2011) argue that the oxidation of H_2S by O_3 may primarily occur through the intermediate HS^- and a peroxysulfinate anion ($HS(O)O_2^-$) based on the overall molar ratio of O_3 and SO_4^{2-} within their aqueous system (2.4 O_3/SO_4^{2-} rather than the predicted 4 O_3/SO_4^{2-}, or a series of 4 O-transfer reactions):

$$H_2S + H_2O \longrightarrow HS^- + H_3O^+ \tag{7.5}$$

$$HS^- + O_3 \longrightarrow HS(O)O_2^- \tag{7.6}$$

$$HS(O)O_2^- + H_3O^+ \longrightarrow 2H_2O + SO_2 \tag{7.7}$$

More recent computational studies agree that at low temperatures SO_2 and H_2O are major products formed via the peroxysulfinate intermediate (Mousavipour et al., 2013). We can estimate our O_3/SO_4^{2-} by integrating the rate of mass loss QCM data (Figure 7.4) between $\sim$ 230 K and 270 K, which is mass loss due to pure anhydrous sulfuric acid (Moore et al., 2007b; Loeffler et al., 2011), and our known concentration of O_3 initially deposited at 50 K. We estimate that our O_3/SO_4^{2-} molar ratio is 2.8 $\pm$ 0.6. This molar ratio suggests that the peroxysulfinate anion intermediate may also facilitate this reaction. Regardless of the mechanism, the

strong SO_2 band at 1333 cm^{-1} appears in our spectra between 100 and 110 K indicating that the H_2S is ultimately oxidized to SO_2 producing some O_2 in the process (Moore et al., 2007b).

The remainder of our reaction sequence agrees with additional atmospheric studies (Erickson et al., 1977; Hoffmann, 1986) and solid state astrochemical work (Loeffler & Hudson, 2016) addressing the thermal oxidation of SO_2, beginning with the formation of bisulfite (HSO_3^-):

$$SO_2 + 2H_2O \longrightarrow HSO_3^- + H_3O^+ \tag{7.8}$$

Features previously attributed to bisulfite (1038 cm^{-1} and 1235 cm^{-1}; Moore et al. (2007b); Loeffler & Hudson (2010); Kaňuchová et al. (2017); Mifsud et al. (2021b)) appear in the IR spectra at nearly the exact temperature as in previous studies. Their appearance suggests that any produced SO_2 is immediately converted to HSO_3^- via autoionization of H_2O, which is consistent with work by Loeffler & Hudson (2016) where this reaction occurs at temperatures as low as 80 K. Remaining O_3 then converts the bisulfite to bisulfate (HSO_4^-), with prominent features at 992 cm^{-1}, 1057 cm^{-1}, and 1235 cm^{-1}. These absorption features are consistent with features found in hydrated states of sulfuric acid (Moore et al., 2007b; Loeffler et al., 2011; Loeffler & Hudson, 2016).

$$HSO_3^- + O_3 \longrightarrow HSO_4^- + O_2 \tag{7.9}$$

Unlike the thermal reactions within SO_2 + O_3 + H_2O (Loeffler & Hudson, 2016), we did not find any evidence for the sulfur anion, metabisulfite ($S_2O_5^{2-}$) within our heated ice samples, suggesting that the reaction between H_2S and O_3 does not produce enough stable bisufite to facilitate the following reaction:

$$2HSO_3^- + \longrightarrow S_2O_5^{2-} + H_2O \tag{7.10}$$

This reaction is likely limited by the number of O_3 molecules required to fully oxidize the initial H_2S.

7.5.2 Reaction Kinetics

Extrapolating laboratory kinetic data to astronomical temperatures and timescales is crucial for understanding thermal processes in realistic astrochemical environments. For thermal chemical reactions within the gas and aqueous phases, Arrhenius parameters (activation energy, and pre-exponential factors) are commonly extracted from laboratory data. Though solid state environments uniquely challenge the assumptions of Arrhenius behavior (e.g. limited motion and orientation within solids, etc.), Vyazovkin & Wight (1997) suggest that these kinetic parameters have parallels within the solid state. Some previous works have had

success determining a reaction's overall activation energy by employing an isothermal annealing technique and fitting the data with first order Arrhenius kinetics (Bossa et al., 2009b; Noble et al., 2013; Loeffler & Hudson, 2013). Figure 7.5 shows the 2104 cm^{-1} O_3 band during warming and isothermal annealing at 120 K, which we integrate after removing the linear continuum to determine the O_3 band area, a proxy for O_3 abundance or the extent of the reaction. Figure 7.6 shows the normalized O_3 band area as a function of time (50 K; $t = 0$) for three annealing temperatures (98.5 K, 105.5 K, and 110.5 K). Assuming first order Arrhenius reaction kinetics, our reaction rate constant (k) is related to our O_3 column number density by the following:

$$\mathrm{N(t) = N_0 e^{-kt}} \tag{7.11}$$

We calculate the rate constant using the time at which half of the O_3 is consumed by the reaction ($\mathrm{k = \frac{ln(2)}{t_{1/2}}}$). We note that for the case of 120 K, over half of the initial O_3 is consumed prior to reaching the annealing temperature. For this reason, we only use annealing temperatures below 110.5 K to calculate the reaction's activation energy.

The inset for Figure 7.6 shows the Arrhenius plot for nine different annealing temperatures, where the linear fit is proportional to $-\mathrm{E_a/R}$ and R is the universal gas constant. We derive an activation energy of 20 $\pm$ 3 kJ mol^{-1}, which is significantly lower than the activation energy required to oxidize SO_2 (Loeffler & Hudson, 2016). Whether this difference in activation energy is due to the use of different techniques (isothermal annealing vs. linear heating (Vyazovkin & Wight, 1997; Loeffler & Hudson, 2016)) or a fundamental difference in the chemistry is something we hope to investigate in the future. Regardless, our activation energy seems reasonable compared to literature values derived using this isothermal annealing technique (Bossa et al., 2009b; Noble et al., 2013; Loeffler & Hudson, 2013).

7.5.3 Astrophysical Implications

Our recent studies demonstrate the importance of considering low temperature thermal reactions in astronomical environments. Specifically, H_2S is readily oxidized to sulfur anions and hydrated states of sulfuric acid in the presence of O_3 within a H_2O-ice matrix. This oxidation sequence agrees well with gas phase literature (Glavas & Toby, 1975), and solid state studies focusing on SO_2 and O_3 (Loeffler & Hudson, 2016). We suspect that these results will not only be important for interpreting data from future outer Solar System Missions focusing on Europa, such as Europa Clipper (Phillips & Pappalardo, 2014) and JUICE (Grasset et al., 2013), but also for future observations of Ganymede and Callisto, as sulfur compounds and O_3 or its precursor (O_2) are likely present and mixed within the surface of all these satellites. Below, we discuss our

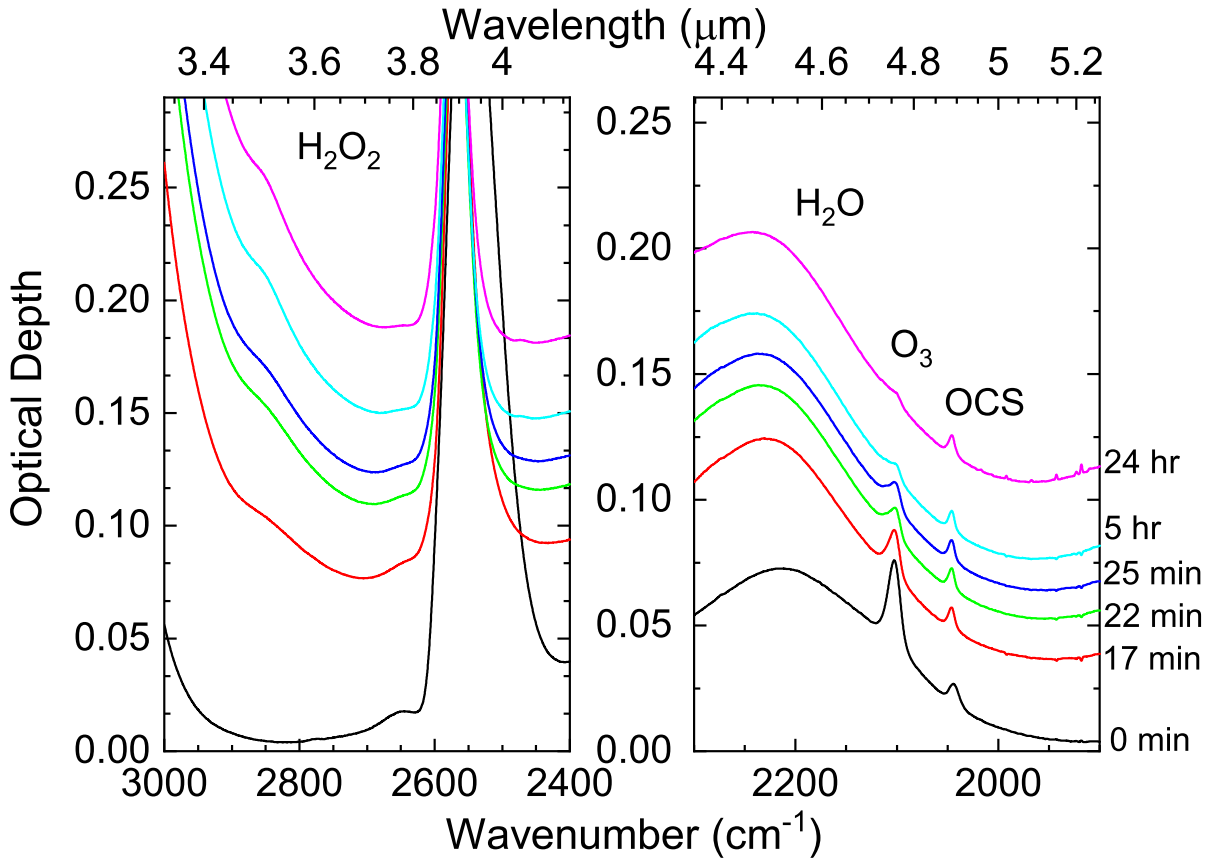

Figure 7.5: IR spectra of the region containing the O_3 2104 cm^{-1} band in an H_2O + H_2S + O_3 ice during warming at 5 K min^{-1} and isothermal annealing at 120 K. From the bottom to the top, these spectra correspond to time elapsed since beginning warming: 0 min, 17 min, 22 min, 25 min, 300 min, and 24 hr. The first spectrum was acquired at 50 K, and the rest were acquired after equilibrating at 120 K.

results in more detail with regards to each of these three Jovian satellites.

The detection of O_2 on both hemispheres of Europa (Spencer & Calvin, 2002) is expected given the strong radiation environment present on the surface (Cooper et al., 2001, 2009; Paranicas et al., 2009; Cassidy et al., 2013; Nordheim et al., 2019) and the numerous laboratory studies that have shown that O_2 can be formed via radiolysis (H^+, Ar^+, and e^-) of H_2O-ice (Haring et al., 1984; Teolis et al., 2005; Sieger et al., 1998; Davis et al., 2021). However, the lack of detection of O_3 on Europa is a bit more puzzling, as laboratory studies have shown that O_3 is easily produced from ion and electron irradiation of O_2-ice (Famá et al., 2002; Bennett & Kaiser, 2005) and from heavy ion irradiation of H_2O-ice that is deposited while being actively irradiated (Teolis et al., 2006). While it is unclear why O_3 is absent on the leading hemisphere of Europa, we have noted previously that the lack of O_3 on the trailing hemisphere of Europa could be due to thermal reactions with SO_2 (Loeffler & Hudson, 2016), which has been detected on the surface of the trailing hemisphere (Lane et al., 1981; Hendrix et al., 2011; Becker et al., 2022). Here we show that H_2S will also react with O_3 on

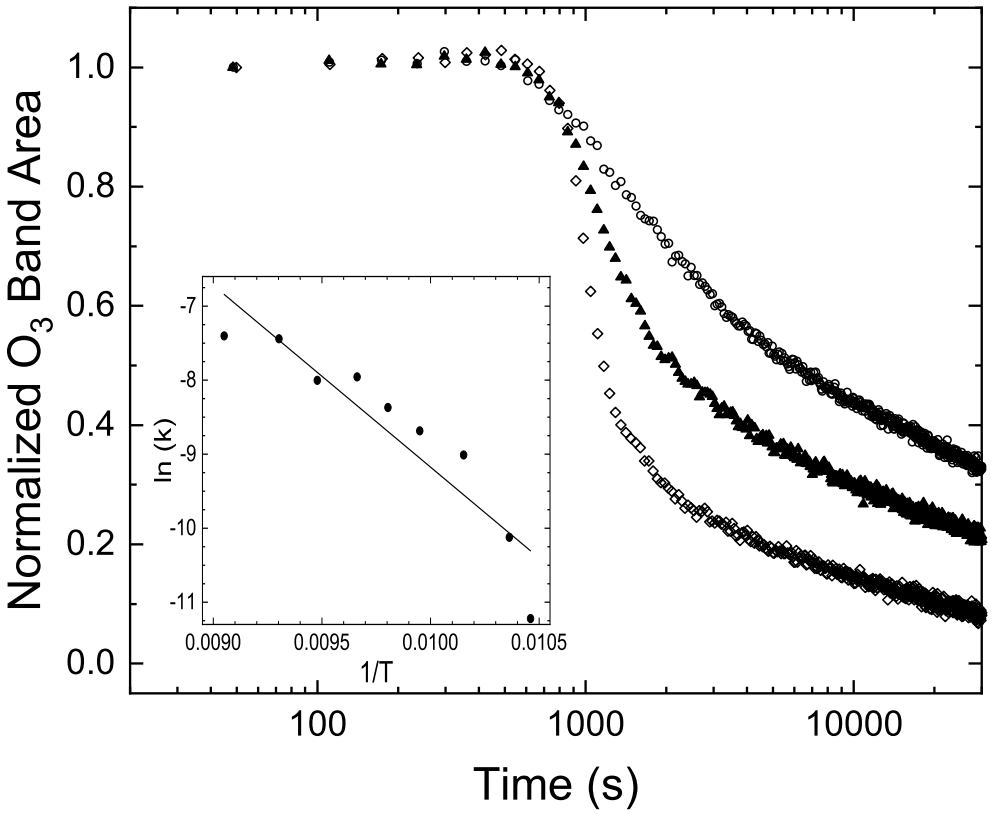

Figure 7.6: Normalized integrated O_3 2104 cm^{-1} band area in a H_2O + H_2S + O_3 ice mixture deposited at 50 K during warming at a rate of 5 K min^{-1} to the following annealing temperatures: (98. K, ○; 105.5 K, ▲; 110.5 K, ◇) . Inset: Arrhenius plot of the H_2O + H_2S + O_3 reaction. Isothermal annealing temperatures used were: 95.6, 96.5, 98.5, 100.5, 102.0, 103.5, 105.5, 107.5, and 110.5 K The linear fit is proportional to the reaction activation energy (see text for more details). The R^2 for this linear fit is 0.86.

the order of hours or days at the temperatures found on Europa ($\sim$ 90 - 130 K). The potential involvement of H_2S in the thermal chemistry occurring on Europa's surface would also explain its lack of detection on Europa, as H_2S should form from implantation of iogenic ions into the surface ice or from the irradiation of other numerous sulfur bearing compounds present (Carlson et al., 1999a, 2002; Strazzulla et al., 2009). Moreover, the radiolytic lifetime of H_2S on the surface of Europa is on the order of several years (Carlson et al., 1999a), whereas its thermal lifetime in the presence of O_3 is $\sim$ 5 hours at 120 K. These lifetimes further highlight the potentially significant role these reactions play in the overall sulfur cycle on Europa, especially below the surface, where there is significantly less radiation (Cooper et al., 2001).

For Ganymede, surface O_2 is primarily located in the mid- and low-latitudes of the trailing hemisphere (Trumbo et al., 2021), which is consistent with current flux models, O_2 production via the radiolysis of

H_2O-ice (Poppe et al., 2018; Johnson & Jesser, 1997) and more recent comparisons of Ganymede's spectra and laboratory spectra of oxygen rich H_2O-ice (Migliorini et al., 2022). O_3 has mainly been identified in the trailing hemisphere (Noll et al., 1996; Hendrix et al., 1999) and has been found to be most abundant near the poles of the trailing hemisphere (Hendrix et al., 1999). Moreover, Hendrix et al. (1999) found that the O_3 abundance correlates with the solar zenith angle, suggesting that the O_3 is destroyed by photolysis more easily at lower latitudes, where the sunlight is most intense. H_2S has also been tentatively attributed to a feature at 3.88 μm in observations of Ganymede's surface using the Galileo NIMS instrument (McCord et al., 1998). Although the geographic distribution of this feature has not been studied, more recent work using the Very Large Telescope or VLT (Ligier et al., 2019; King et al., 2022) shows minor amounts of sulfuric acid hydrates and sulfates at low-latitudes on the trailing hemisphere, which are thermal products of O_3 and H_2S, as well as reaction products between SO_2 and O_3 (Loeffler & Hudson, 2016). Thus, it is also possible that the lower abundance of O_3 found at lower latitudes is due to the presence of sulfur-bearing compounds. More observational work is necessary to further constrain the compositional variation across Ganymede's surface.

On Callisto, O_2 has been detected on the trailing side (Spencer & Calvin, 2002); however, there have been no definitive detections of O_3. Additionally, H_2S and SO_2 have been tentatively identified on Callisto using the Galileo NIMS instrument (McCord et al., 1998). While these features may be due to another species entirely (H_2CO_3 or other carbon-bearing compounds; Johnson et al. (2004)) or be an artifact of the method of analysis as suggested by Hendrix & Johnson (2008); the presence of H_2S and SO_2 in the absence of O_3 is consistent with our thermal oxidation reactions.

7.6 Conclusions

We have shown that thermal oxidation reactions occur within H_2O + H_2S + O_3 ice mixtures on laboratory timescales at temperatures relevant to Europa, Ganymede, and Callisto. These reactions produce sulfur anion and O_2 products at low temperatures and hydrated sulfur acid at higher temperatures, and the activation energy to initiate these reactions is significantly lower than the activation energy required to oxidize SO_2 to the sulfate ion. These results are generally consistent with the observed geographic distributions of sulfur compounds on the Galilean icy satellites, and this study further highlights the importance of considering thermal chemical alteration on astrophysical surfaces, despite the low temperatures. Finally, we suspect that thermal reactions with sulfur bearing species will be important for interpreting observations made by NASA's upcoming Europa Clipper Mission, as well as future compositional investigations of the Galilean icy satellites.

7.7 Acknowledgements

This research was supported by NSF grant No. # 1821919. Data from this publication can be found in Northern Arizona University's long-term repository (https://openknowledge.nau.edu/5947).

Reactants			
Species	Peak Position (cm^{-1})	Assignment	Reference
H_2O	3359	ν_1 and ν_3	Hardin & Harvey (1973); Hagen et al. (1981)
	2201	$3\nu_L$	Hardin & Harvey (1973); Ritzhaupt et al. (1976); Hagen et al. (1981)
	1654	ν_2	Hardin & Harvey (1973); Ritzhaupt et al. (1976); Hagen et al. (1981)
	806	ν_L	Bertie & Whalley (1964)
H_2S	2551	ν_1 and ν_3	Reding & Hornig (1957); Moore et al. (2007b); Hudson & Gerakines (2018)
	1175	ν_2	Reding & Hornig (1957); Fathe et al. (2006); Hudson & Gerakines (2018)
O_3	1032	ν_1	Teolis et al. (2007a); Raut et al. (2011); Loeffler & Hudson (2016)
	2104	$\nu_1 + \nu_3$	Teolis et al. (2007a)
Products			
SO_2	1333	ν_3	Wiener & Nixon (1956); Moore et al. (2007b)
	1149	ν_1	Wiener & Nixon (1956); Moore et al. (2007b)
HSO_3^-	$\sim$ 1235		Moore et al. (2007b); Kaňuchová et al. (2017)
	1038	-	Moore et al. (2007b); Loeffler & Hudson (2016)
	1013	-	Moore et al. (2007b)
HSO_4^-	$\sim$ 1235	-	Moore et al. (2007b)
	1057	-	Moore et al. (2007b); Loeffler & Hudson (2016)
	992	-	Loeffler & Hudson (2016)
SO_4^{2-}	1111	-	Moore et al. (2007b)

Table 7.1: Peak positions for the species identified within H_2O + H_2S + O_3 ice mixtures at 50 K (reactants) and 150 K (products).

Chapter 8

Thermal Reactions between NH_3 and O_3: Salt Formation Mechanism

Patrick D. Tribbett[1], Mark J. Loeffler[1,2], Stephen C. Tegler[1], William M. Grundy[3]
In Prep..

8.1 Abstract

We demonstrate the efficacy of a low temperature, thermal oxidation reaction between NH_3 and O_3 within a laboratory ice sample (H_2O + NH_3 + O_3) at temperatures as low as 70 K. This reaction produces NO_3^- and NH_4^+ at low temperatures (70 - 120 K), and the salt NH_4NO_3, which is stable under vacuum to temperatures as high as 260 K. We estimate that the overall reaction activation energy to initiate this reaction is $\sim 17 \pm 2$ kJ mol^{-1}, which is reasonable given the activation energies for other thermally-driven reactions involving NH_3. In addition to being an efficient pathway to remove NH_3 and O_3 from an icy surface, we also find that the product NH_4NO_3 has an absorption feature near 2.2 μm. A spectral feature in this region has been previously attributed to NH_3, hydrated NH_3, NH_4^+-bearing salts, and NH_3-bearing phyllosilicates. Given the similar positions of our product and the one found on icy body surfaces, we suggest that a low temperature reaction pathway such as this may be important to explain observations. Thus, we intend to measure its optical constants in the near future to enable its detection within the spectra of outer solar system objects.

8.2 Introduction

Through its near-infrared (NIR) absorption feature near 2.2 μm, ammonia (NH_3) has been tentatively detected on the surface of Charon (Brown & Calvin, 2000; Cook et al., 2007), Pluto (Dalle Ore et al., 2019); several Uranian satellites, including Miranda and Ariel (Bauer et al., 2002; Cartwright et al., 2020); Quaoar (Jewitt & Luu, 2004), Orcus (Barucci et al., 2008), and possibly Enceladus (Emery et al., 2005; Verbiscer et al., 2006; Hendrix et al., 2010). Additionally, solid NH_3 likely exists at depth within the atmospheres

[1]Department of Astronomy and Planetary Science, Northern Arizona University, PO Box 6010, Flagstaff, AZ 86011, USA
[2]Materials Interfaces in Research and Applications (MIRA), Northern Arizona University, PO Box 6010, Flagstaff, AZ 86011, USA
[3]Lowell Observatory, 1400 W Mars Hill Rd, Flagstaff, AZ 86001, USA

of Uranus and Neptune (Hueso et al., 2020) and may provide a source for the activity on active Centaurs (Chandler et al., 2020).

Due to the prevalence of these NH_3-bearing compounds, decades of laboratory studies have investigated their physical and chemical properties. Radiation studies have demonstrated the efficient and fluence-dependent sputtering of pure NH_3 and mixtures of NH_3 and H_2O (Lanzerotti et al., 1984; Loeffler et al., 2010), and the radiolytic production of nitrogen- or N-bearing compounds. Loeffler et al. (2006a) demonstrated that H^+ irradiation and the subsequent heating of H_2O and NH_3 resulted in the formation and eruption of N_2 and H_2 bubbles, a possible small-scale source of the H_2O vapor and nitrogen within the plumes detected on Enceladus during NASA's *Cassini* flybys (Waite et al., 2006; Hansen et al., 2006). Additionally, irradiating NH_3 and H_2O mixtures results in the formation of of small amounts of increasingly complex N-bearing molecules including hydrazine (N_2H_4), hydroxylamine (NH_2OH) (Zheng & Kaiser, 2007), and ammonium (NH_4^+) (Moore et al., 2007a), as well as results in the amorphization of crystalline ammonia hydrates (Moore et al., 2007a). Laboratory studies have also demonstrated that NH_3 participates in a number of different thermally-driven reactions, including acid-base reactions (Schutte et al., 1999; Noble et al., 2013; Loeffler & Hudson, 2015), and nucleophilic additions (Bossa et al., 2009a,b). Notably, recent work by Potapov et al. (2019) demonstrates that, in general, this reactivity in the absence of irradiation is likely underestimated in laboratory work due to catalytic effects of dust grain surfaces, which tend to be difficult to effective recreate experimentally. Many of these thermally-driven reactions result in the formation of NH_4^+-bearing salts, and Kruczkiewicz et al. (2021) demonstrate that these salts remain stable under a wide range of thermal conditions.

Solid NH_3 also interacts strongly with H_2O ice and can produce various hydrates (Bertie & Morrison (1980)). NH_3 can also react with other material and produce semi-volatile ammonium-bearing (NH_4^+) salts, including but not limited to ammonium hydrosulfide or NH_4SH (Loeffler et al., 2016a), ammonium carbonate or $(NH_4)_2CO_3$ (De Sanctis et al., 2016) and ammonium acetate or NH_4HCO_2 (Kruczkiewicz et al., 2021); these salts also have an absorption feature near 2.2 μm due to NH_4^+. The formation of salts has been used to explain the relative depletion of NH_3 in cometary ices (Filacchione et al., 2019; Poch et al., 2020; Kruczkiewicz et al., 2021). Lastly NH_3-bearing phyllosilicates may explain the NH_3 spectral features identified on warmer astronomical bodies, like the dwarf planet Ceres (King et al., 1992; Singh et al., 2021). NH_3- and NH_4^+-bearing compounds are seemly present on surfaces of astronomical objects throughout the Solar System under vastly different radiation and thermal environments.

In addition to the thermally-driven acid-base and nucleophilic addition reactions, many recent studies have demonstrated the importance of oxidative reactions, specifically for simple sulfur-bearing molecules expected on several outer Solar System satellites (Loeffler & Hudson, 2010, 2013, 2015; Tribbett & Loeffler,

2022; Mifsud et al., 2021a). The strong oxidants hydrogen peroxide (H_2O_2) and ozone (O_3) have been detected or are expected on a number of planetary bodies since both oxidants are radiolytic byproducts of H_2O (Loeffler et al., 2006b; Teolis et al., 2006) and O_2 (Famá et al., 2002; Bennett & Kaiser, 2005). O_3 has been detected on Ganymede (Noll et al., 1996), and on Rhea and Dione (Noll et al., 1997) using ultraviolet observations of each satellite. Both hydrogen sulfide (H_2S) (Tribbett & Loeffler, 2022) and sulfur dioxide (SO_2) (Loeffler & Hudson, 2016) undergo thermally-driven oxidation reactions when exposed to O_3 to produce increasingly complex sulfur anions (HSO_3^-, HSO_4^-, and SO_4^{2-}) at low temperatures, and hydrated sulfuric acid at higher temperatures. While H_2O_2 does not react with H_2S, H_2O_2 does oxidize SO_2 in the presence of H_2O (Loeffler & Hudson, 2013, 2015).

Early literature suggests that O_3 oxidizes NH_3 to the oxidized nitrogen anion, nitrate (NO_3^-). However, Loeffler & Hudson (2015) found that NH_3 and H_2O_2 ice mixtures undergo a simple acid-base proton transfer. This difference suggests that the NH_3 and O_3 system should be revisited to further investigate the chemical properties of NH_3. Here, we present evidence for a thermally-driven oxidative reaction between NH_3 and O_3 at temperatures as low as 70 K in both H_2O-dominated and NH_3-dominated H_2O + NH_3 + O_3 ice mixtures. We identify the reaction products using a combination of infrared spectroscopy, and mass gravimetry, provide estimates for the overall activation energy of this reaction, and place our results in the context of extraterrestrial environments.

8.3 Experimental Methods

We performed all experiments at Northern Arizona University in an ultra high vacuum (UHV) chamber with a base pressure of 10^{-9} torr ($\sim 10^{-10}$ within the thermal radiation shield). Note that we describe the specifications for this UHV chamber in detail in a recent publication (Tribbett & Loeffler, 2022). To prepare ice samples, we codeposited H_2O (high-performance liquid chromatography grade, Sigma Aldrich), NH_3 (99.99% purity, Matheson Gas), and O_3 from separate mixing lines onto an optically flat gold mirror electrode of a quartz crystal microbalance (QCM). We produced O_3 by sparking a glass manifold containing $\sim$ 750 torr of O_2 (99.999%, Matheson Gas) with a Tesla coil for $\sim$ 20 minutes. O_3 condenses into the portion of the manifold submerged in liquid nitrogen, and the residual O_2 is pumped out leaving the residual O_3 to be leaked into the UHV chamber.

We determined the relative abundances of molecules in our ice samples following the QCM technique described in Tribbett & Loeffler (2022). We estimate the thickness of our ice samples to be $\sim$ 1.1 μm assuming a density of 0.82 g cm^{-1} for H_2O (Westley et al., 1998), 1.65 g cm^{-3} for O_3 (Teolis et al., 2007a; Raut et al., 2011), and 0.68 g cm^{-3} for NH_3 (Hudson et al., 2022). Note that discrepancies exist in the

literature regarding the density of amorphous NH_3 at low temperatures (Wood & Roux, 1982; Satorre et al., 2013; Hudson et al., 2022), and we opt to use the most recent literature values available. For experiments requiring nitric acid (HNO_3), we deposited 15 M HNO_3 (70% v/v, Sigma Aldrich) from the ozone glass manifold, purified with two liquid nitrogen freeze thaw cycles. We note that the ratio of HNO_3/H_2O in the deposited mixtures is ~ 1 due to the vapor pressure of both constituents (Hanson & Mauersberger, 1988; Ritzhaupt & Devlin, 1991). We estimate the thickness of these ice samples to be $\sim 0.9\,\mu$m, assuming a density of 0.82 g cm^{-3} for H_2O (Westley et al., 1998) and 1.51 g cm^{-3} for HNO_3 (Stern et al., 1960).

We monitored our ice mixtures using a combination of infrared (IR) spectroscopy, mass spectroscopy, and QCM gravimetry. We acquired IR specular reflectance between 10,000 - 650 cm^{-1} (1 - 15.38 μm) with a spectral resolution of 2 cm^{-1} at an incidence angle of 37.5^{o} using the IR light source from a Thermo-Nicolet iS50 Fourier Transform Infrared Spectrometer (FTIR) and an Mercury Cadmium Telluride (MCT/A) detector. Infrared spectra reported here are in units of optical depth ($\tau = -\ln(I/I_0)$), where I is the reflected intensity from the sample and I_0 is the reflected intensity from the bare gold substrate. After deposition, we warmed our samples following one of two different heating treatments: linear heating or isothermal annealing. In the linear heating experiments, we warmed our samples from 50 K to 290 K at a 0.1 K minute^{-1}. For the isothermal annealing experiments, we first warmed our ice samples from 50 K to the desired annealing temperature (75 K - 90 K) at 5 K minute^{-1}. The ice sample remained at the prescribed annealing temperature for 24 hours, and we monitored it using IR spectroscopy to derive the reaction kinetic parameters following a technique common in the astrochemical literature (Bossa et al., 2008; Loeffler & Hudson, 2013; Tribbett & Loeffler, 2022) (see Section 8.5 for details). Several of our previous studies focused on sulfur molecule chemical systems use the O_3 combination band at 2104 cm^{-1} as a proxy for the extent of the reaction rather than the stronger ozone fundamental band at 1034 cm^{-1} (Teolis et al., 2007a), since the combination band is well separated from the reaction products of interest (Loeffler & Hudson, 2013, 2016; Tribbett & Loeffler, 2022). For the NH_3 ice mixtures, we find that reaction products strongly overlap with the O_3 combination band (see Table 8.1). Thus, we use the fundamental O_3 band as a proxy for the extent of the reaction. Additionally, we note that the O_3 fundamental band is temperature dependent and decreases $\sim 7\%$ between 50 K and 90 K, which we take into account in our analyses.

8.4 Results

Figure 8.1 shows the mid-IR spectra acquired for a water-dominated H_2O + NH_3 + O_3 (70:25:5) ice mixture deposited at 50 K, and incrementally warmed to 123 K and 207 K at a rate of 1 K min^{-1}. The 50 K spectrum is dominated by several large overlapping spectral features attributed to H_2O (O-H stretch, 3295

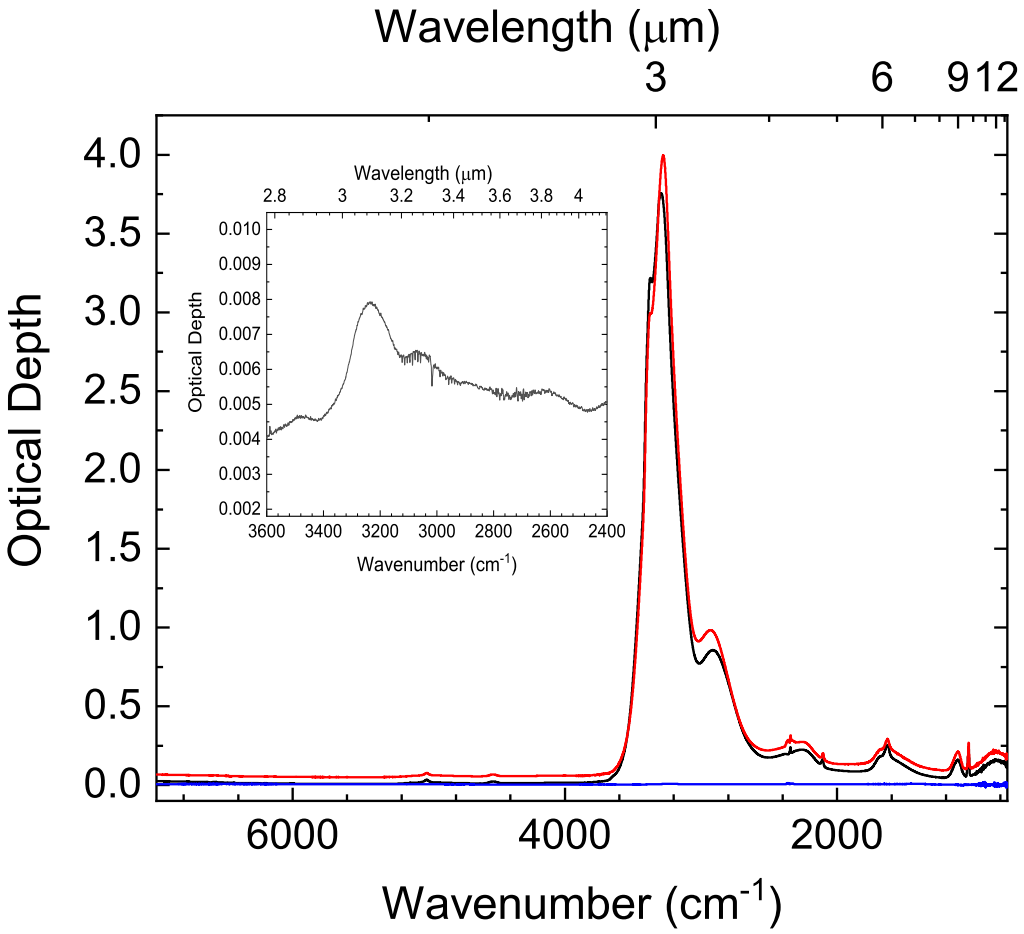

Figure 8.1: IR spectra of a H_2O + NH_3 + O_3 sample (70:25:5) during warming at 1.0 K min^{-1}. Spectra correspond to 50 K (black), 123 K (red), and 207 K (blue). The 50 K and 120 K spectra are vertically offset for clarity. Inset: Highlighting the fundamental O-H stretching region of the sample at 207 K.

cm^{-1}), NH_3 (N-H stretch, 3376 cm^{-1}), and intermolecular interactions between the H_2O and NH_3 (N$\cdots$O-H, 2912 cm^{-1}) (Moore et al., 2007a). Deeper into the infrared, the broad H_2O lattice mode overtone (2250 cm^{-1}), bending mode ($\sim$ 1654 cm^{-1}), and lattice mode (835 cm^{-1}) are accompanied by several more narrow NH_3 features (1629 cm^{-1}, 1112 cm^{-1}) and O_3 features (2108 cm^{-1}, 1034 cm^{-1}). In the near-infrared, we find two additional NH_3 combination features at 5014 cm^{-1} and 4526 cm^{-1}. The broad baseline structure underlying these combination features is consistent with NH_3 well mixed in H_2O-dominated mixtures (Moore et al., 2007a). The spectral assignments and references for each reactant are shown in Table 8.1. We note that CO_2 contamination is evident from the absorption feature (C=O stretch) between 2400 and 2300 cm^{-1}. Although we cannot easily determine the column number density of CO_2 based on the band strength of CO_2 (Gerakines et al., 1995; Gerakines & Hudson, 2015) due to the interference effects typical of thin film reflectance spectroscopy (Teolis et al., 2007b), we can approximate the CO_2 concentration from previous calibration experiments described in Tribbett & Loeffler (2022). We determine a CO_2 contamination upper limit of $\sim 1.10 \times 10^{16}$ molecules cm^{-2} or $\sim$ 0.04% of our sample by number. Regardless, literature demonstrates that CO_2 is not oxidized by O_3 (Loeffler & Hudson, 2016; Tribbett & Loeffler, 2022) and is unlikely to react with H_2O or NH_3 without the presence of ionizing radiation (Zheng & Kaiser, 2007; Chen et al., 2011). At 123 K, our sample looks qualitatively similar to our freshly deposited sample, showing no obvious product features. However, we note a decrease in intensity of each NH_3 and O_3 feature and a slight broadening of the H_2O bending feature centered at 1654 cm^{-1}. Upon further warming, the 207 K spectrum shows the sublimation of a majority of the sample material; however, several unresolved features appear in both the 3600 - 2600 cm^{-1} (Figure 8.1 inset) and 1600 - 1300 cm^{-1} regions. QCM data (data not shown here) confirm the presence of 0.5 μg cm^{-2} of material present on the substrate. While the products remain unidentifiable, the spectral changes prior to sample desorption and the presence of spectral features at 207 K suggests that a reaction occurs within this ice mixture.

While H_2O and O_3 are expected to interact when exposed to ionizing radiation (Sauder et al., 1992), the stable high temperature product shown in the Figure 8.1 inset is likely due to a reaction between NH_3 and O_3. Gas phase literature (Olszyna & Heicklen, 1971; De Pena et al., 1973), aqueous literature (Singer & Zilli, 1975; Khuntia et al., 2013), and a single low temperature, condensed study (Huston et al., 1983a) suggests that NH_3 can be oxidized to the NO_3^- ion. Thus, we transitioned to a NH_3-dominated ice mixture to highlight this potential reaction, and enable the identification of the reaction products. For the remainder of this study, we used H_2O + NH_3 + O_3 (22:72:6) ice samples. Figure 8.2 shows the infrared spectra of a H_2O + NH_3 + O_3 (22:72:6) ice mixture deposited at 50 K and incrementally warmed to 120 K at 0.1 K min^{-1}. Generally, the initial ice spectrum at 50 K is similar to the H_2O-dominated ice mixture with the exception of sharper peaks attributed to NH_3, as well as the shifting of several H_2O and NH_3 peaks.

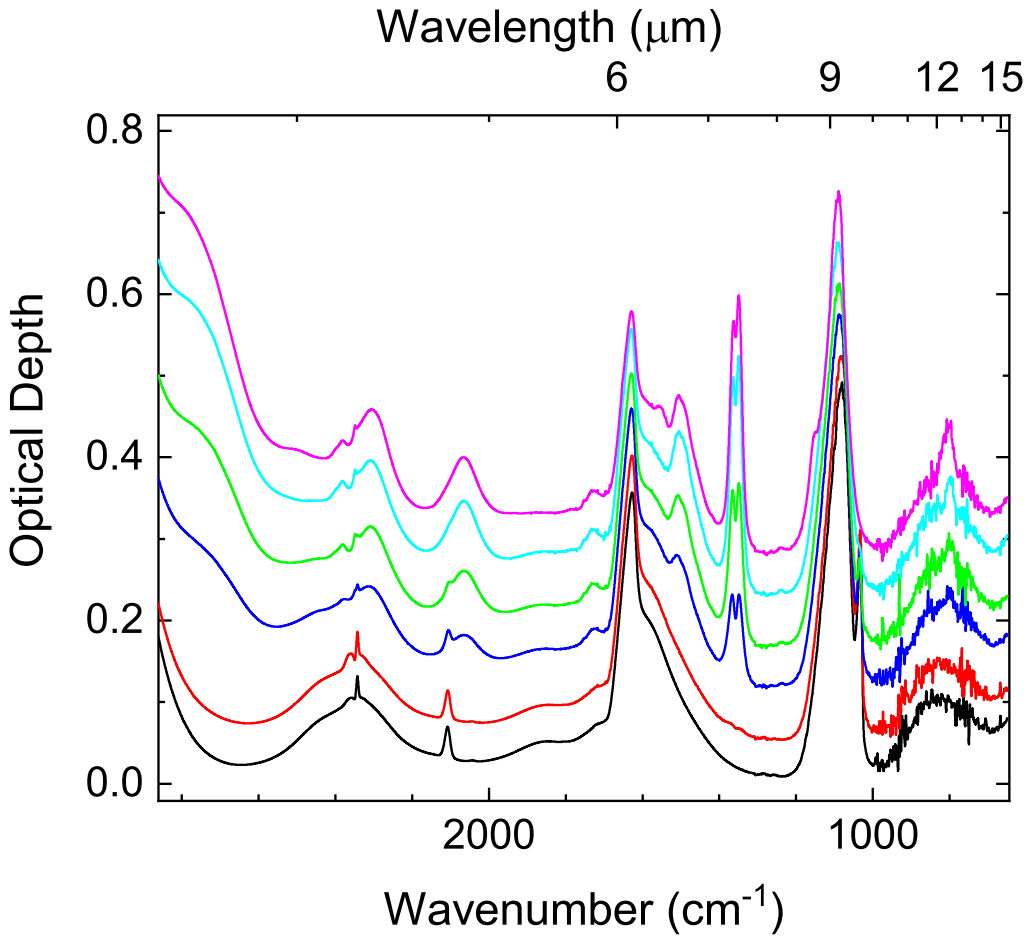

Figure 8.2: IR spectra of a H_2O + NH_3 + O_3 sample (22:72:6) during warming at a rate of 0.1 K min^{-1}. Spectra correspond from bottom to top: 50, 70, 90, 100, 110, and 120 K. Spectra are vertically offset for clarity.

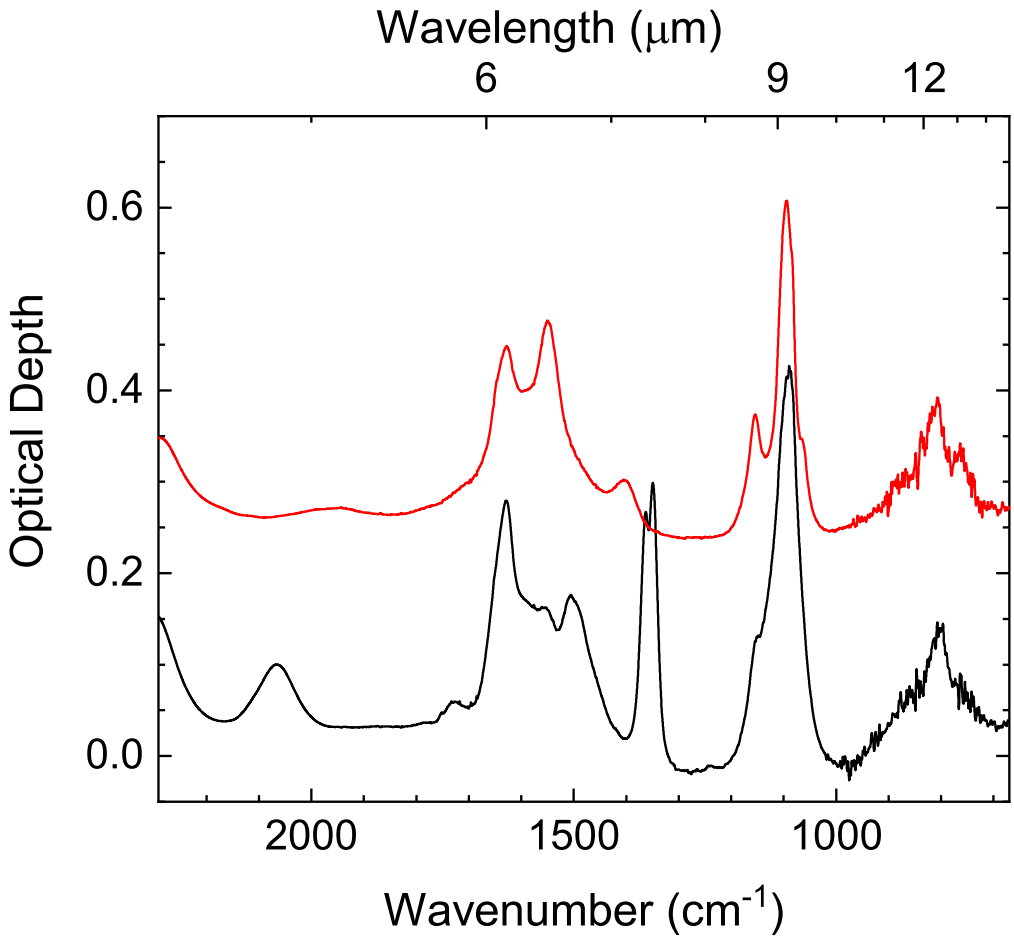

Figure 8.3: IR spectrum of a H_2O + NH_3 + O_3 sample (22:72:6) warmed at a rate of 0.1 K min^{-1} to 120 K (bottom, black) and of partially crystalline ammonia hemihydrate or $2NH_3$:H_2O at 123 K (top, red). Spectra are vertically offset for clarity.

These shifts are consistent with the spectral assignments of features within H_2O and NH_3 ice mixtures of varying relative concentrations (Moore et al., 2007a). At temperatures between 70 and 90 K, we see the formation of two distinguishable, sharp peaks at 1364 and 1348 cm^{-1}, in addition to a shoulder at 1506 cm^{-1} and a broader feature centered around 2058 cm^{-1}. The sharp doublet feature is consistent with absorption features produced by the NO_3^- ion in studies examining the IR spectrum of both NO_3^--bearing salts (Keller & Halford, 1949; Theoret & Sandorfy, 1964; Huston et al., 1983a) and solid-phase mixtures containing nitric acid (HNO_3) (McGraw et al., 1965; Ritzhaupt & Devlin, 1991; Smith et al., 1991). We attribute the 1506 cm^{-1} shoulder feature to the NH_4^+ ion (Loeffler & Hudson, 2015), and the broad 2058 cm^{-1} is consistent with a feature produced by the NH_4^+ ion in the presence of excess NH_3 (Lundeen & Tobias, 1975; Huston et al., 1983a).

Above 110 K, three new absorption features at 1549, 800, and 753 cm^{-1} appear, which are consistent with

the formation of hydrated ammonia compounds at higher temperature (Moore et al., 2007a). Specifically, ammonia hemihydrate ($2NH_3$:H_2O) readily forms within H_2O and NH_3 ice mixtures (1:2) deposited at 50 K and warmed to temperatures between 120 - 140 K (Moore et al., 2007a). Figure 8.3 shows the IR spectrum of a H_2O + NH_3 + O_3 (22:72:6) warmed to 120 K (black) and the IR spectrum of a H_2O + NH_3 (1:2) ice mixture warmed to 123 K (red). The ice mixture without O_3 shows a spectrum of partially crystalline $2NH_3$:H_2O, and is consistent with the $2NH_3$:H_2O spectra published by Moore et al. (2007a). We note that the three absorption bands located at 1549 cm^{-1}, 800 cm^{-1}, and 753 cm^{-1} within the ice containing O_3 agree with those in the $2NH_3$:H_2O spectrum. This comparison suggests that at higher temperatures (110 - 140 K), the hemihydrate is contributing to spectra containing O_3. However, importantly, these hemihydrate features are visually distinguishable from the features that we have attributed to the NO_3^- and NH_4^+ ions indicating that, while these two processes are likely occurring simultaneously, the formation of hydrates is not responsible for the perceived reaction products. We note that as NH_3 and H_2O begin to sublimate above 130 K, our IR spectra do not show evidence for ammonia monohydrate (NH_3:H_2O) or ammonia dihydrate (NH_3:$2H_2O$).

In addition to the emergence of several new absorption features, Figure 8.4 shows the fundamental O_3 absorption band during warming. Previous studies have demonstrated that both the O_3 fundamental band and the combination band at 2108 cm^{-1} decrease linearly with temperature (Loeffler & Hudson, 2016; Tribbett & Loeffler, 2022). However, over this temperature range (50 - 120 K), the O_3 band is expected to only decrease by $\sim 10\%$. Additionally, O_3 does not sublimate from the ice (Figure 8.5) which is consistent with our previous work with H_2O + H_2S + O_3 mixtures (Tribbett & Loeffler, 2022). Thus, these changes in band area suggest that NH_3 is being oxidized by O_3 to produce NO_3^-.

Figure 8.5 shows the QCM-derived rate of mass loss while warming a H_2O + NH_3 + O_3 ice mixture between 50 and 290 K at a rate of 0.1 K min^{-1}. As previously mentioned, there is negligible mass loss prior to 115 K suggesting minimal O_3 loss due to sublimation from the sample during the temperature range of interest for this reaction (70 - 120 K). At 120 K, we observe our first broad mass loss peak likely due to the release of O_2 as the residual NH_3 becomes increasingly mobile and crystallizes. This desorption temperature is consistent with previous studies that demonstrate the release of O_2 from proton-irradiated H_2O-ices (Bahr et al., 2001). The following desorption peak occurs at 130 K and is largely due the desorption of residual excess NH_3. We observe four additional peak between 135 and 165 K. We note that these desorption peaks and the underlying structure within the peaks is likely due to the presence of ammonia hydrates, each with slightly different binding energy to H_2O. However, due to the relatively thin samples, we cannot confirm the identity of these hydrates the corresponding IR spectra. We find two desorption peaks at higher temperatures. The first peak occurs near 190 K, and we attribute this peak to H_2O within hydrated nitric

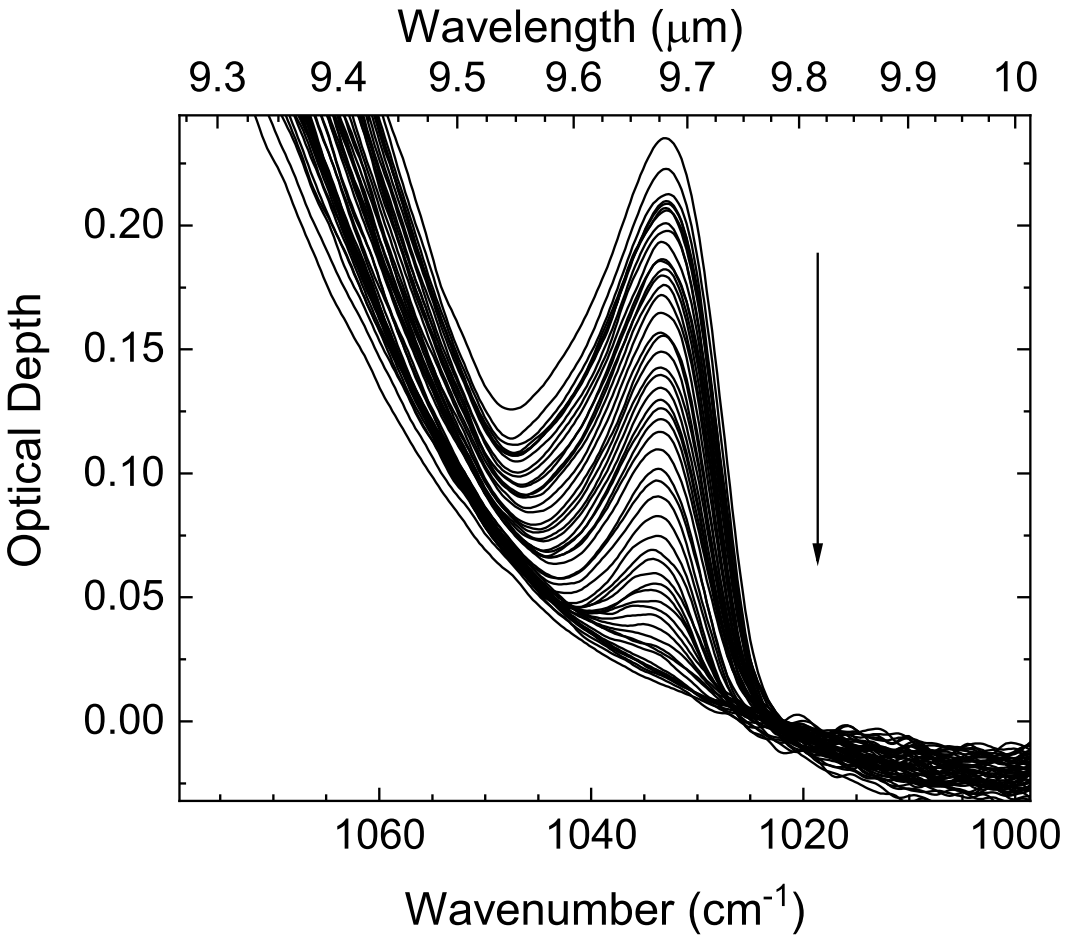

Figure 8.4: IR spectrum of a H_2O + NH_3 + O_3 sample (22:72:6) warmed at a rate of 0.1 K min^{-1}. Spectra highlight the O_3 fundamental absorption feature as the sample is warmed between 50 K and 120 K. Black arrow indicates the direction of increasing temperature.

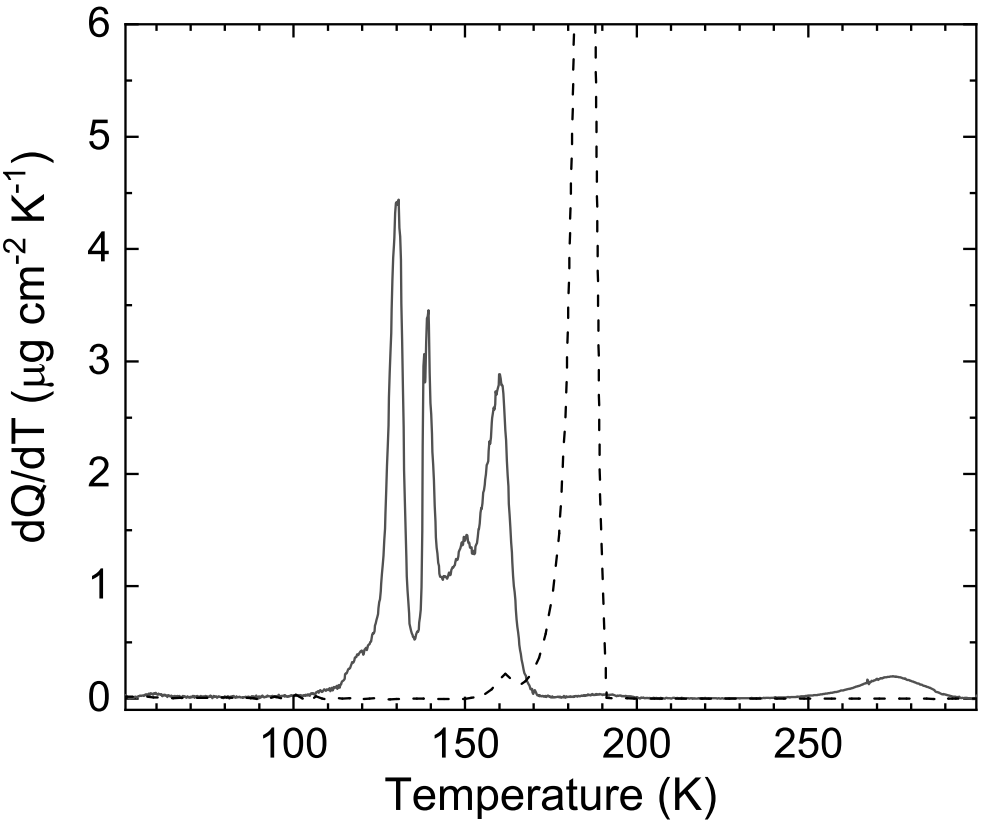

Figure 8.5: QCM-derived rate of mass loss during warming of a H_2O + NH_3 + O_3 sample (22:72:6) (solid line) and of a H_2O:HNO_3 sample (dotted line).

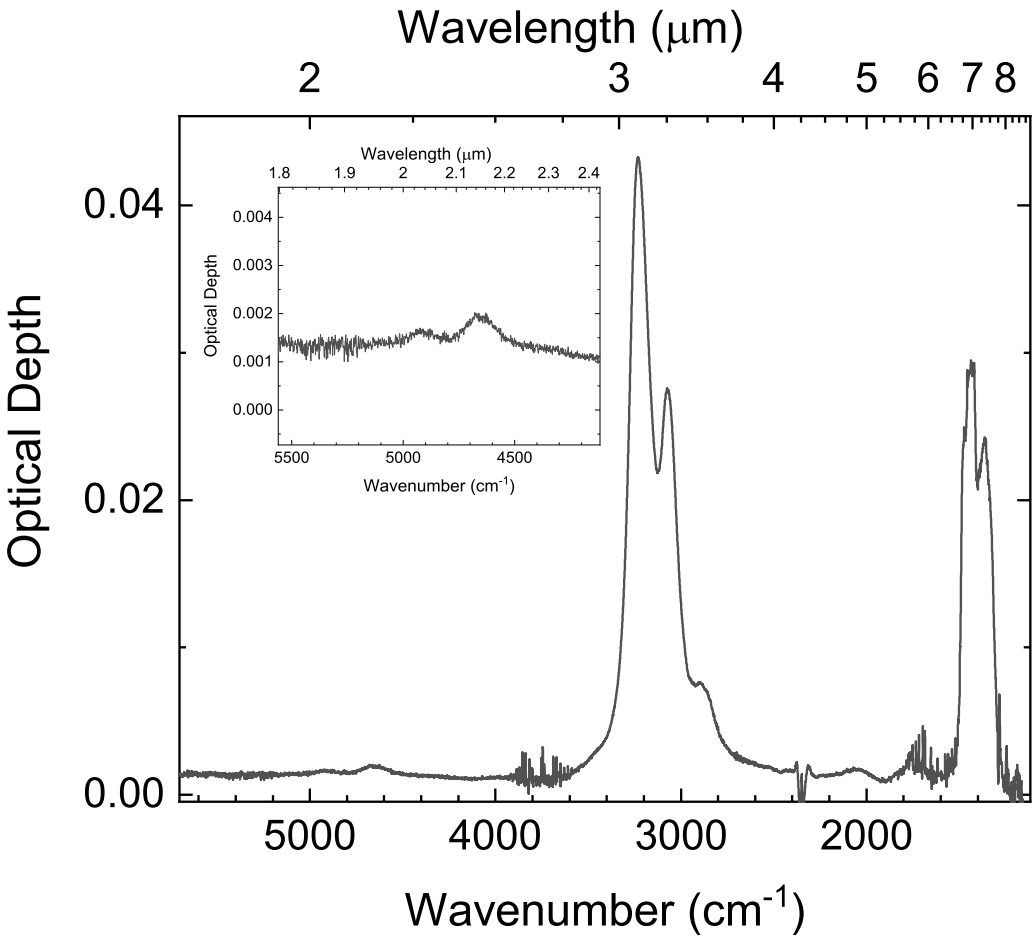

Figure 8.6: IR spectrum of a H_2O + NH_3 + O_3 sample (22:72:6) warmed at 0.1 K min^{-1} to 200 K. Inset: Highlighting the near-infrared region of the absorption spectrum.

acid (see Discussion). Finally, we observe a desorption peak near 275 K, indicating the presence of a high temperature product, consistent with what we found in the H_2O-dominated ice mixtures. Interestingly, this desorption peak corresponds to an areal mass of $\sim 5.1\,\mu$g cm^{-2}, which is approximately 10× more material than the H_2O-dominated ice produced. Figure 8.6 shows an IR spectrum of the thermally-stable product at 250 K, which is characteristic of a semi-volatile NO_3^- compound (1500 - 1300 cm^{-1}).

8.5 Discussion

8.5.1 Reaction Chemistry and Spectral Assignments

Due to the importance of NH_3-bearing atmospheric particulates and the presence of NH_3 in wastewater, the oxidation of NH_3 with O_3 has been previously demonstrated in both the gas-phase (Olszyna & Heicklen, 1971; De Pena et al., 1973; Olszyna et al., 1974) and the aqueous literature (Singer & Zilli, 1975; Kuo et al.,

1997; Khuntia et al., 2013). Olszyna & Heicklen (1971) demonstrated the production of O_2, H_2O, N_2O, N_2, and solid NH_4NO_3 within gaseous mixtures of O_3 and excess NH_3. The mechanism described required a free radical chain reaction mechanism, assuming an OH radical chain carrier (Equations 8.1 - 8.6):

$$O_3 + NH_3 \longrightarrow O_2 + OH + NH_2 \tag{8.1}$$

$$O_3 + NH_2 \longrightarrow O_2 + NH_2O \tag{8.2}$$

$$O_3 + NH_2O \longrightarrow O_2 + OH + HNO \tag{8.3}$$

$$O_3 + HNO \longrightarrow O_2 + HNO_2 \tag{8.4}$$

$$O_3 + HNO_2 \longrightarrow O_2 + HNO_3 \tag{8.5}$$

$$NH_3 + HNO_3 \longrightarrow NH_4NO_3 \tag{8.6}$$

While the authors provide constraints on the reaction mechanism, the radical chain initiation step remains unclear, and the majority of these intermediate N-bearing species were not detected (Olszyna & Heicklen, 1971). Subsequent studies have largely focused on the product, NH_4NO_3, and kinetics of particulate growth (De Pena et al., 1973; Olszyna et al., 1974) assuming an overall reaction of:

$$2NH_3 + 4O_3 \longrightarrow 4O_2 + NH_4NO_3 + H_2O \tag{8.7}$$

More recent efforts have coupled this overall reaction to photochemical models to produce steady state distributions of NH_3 and NO_3^- aerosols globally and in regions of high localized pollution (Feng & Penner, 2007; Wen et al., 2015). Aqueous literature, with an emphasis on wastewater treatment, demonstrates a similar overall oxidation mechanism between O_3 and the free NH_3 within NH_4^+-salt solutions, typically NH_4Cl (Singer & Zilli, 1975) or $(NH_4)_2SO_4$ (Khuntia et al., 2013). In each case, the NH_3 reacts readily with O_3 forming NO_3^- following:

$$NH_3 + 4O_3 \longrightarrow H_3O^+ + NO_3^- + 4O_2 \tag{8.8}$$

Unlike the studies mentioned above, which monitored this reaction at or near room temperature, Huston et al. (1983a) found that this reaction occurs readily at cryogenic temperatures. NH_3 and O_3 gases were introduced into a cryogenic cell cooled with liquid nitrogen, where the gases condensed and formed the salt NH_4NO_3 in the presence of excess NH_3 through an ozonide ($NH_3^+O_3^-$) intermediate, which was identified based on an infrared absorption band at 800 cm^- and a yellow color change:

$$NH_3^+O_3^- + O_3 + NH_3 \longrightarrow NH_4NO_3 + H_2O + O_2 \tag{8.9}$$

While it is clear that each of these studies agree that NH_3 and O_3 react to produce NO_3^-, the intermediate N-bearing species and the state of the NO_3^- ion remain unclear. The aqueous reaction suggests that the presence of an H_2O solution results in the formation of nitric acid in solution, while the gas and condensed phase studies form the solid salt NH_4NO_3 in the absence of H_2O. Both the aqueous and gas phase studies indicate that the reaction occurs through single O-atom transfers, however, the condensed phase study suggests a significantly different stoichiometry. This discrepancy is similar to what has been observed for another chemical system, namely H_2S and O_3 (Glavas & Toby, 1975; Mark et al., 2011). In fact, the low temperature solid-phase reaction between H_2S and O_3 shows competition between the O-atom transfer and complex O_3 intermediate mechanism (Tribbett & Loeffler, 2022).

To elucidate the reaction mechanism, we used our IR spectra and QCM data. Above 70 K, we see the immediate conversion of NH_3 to the NO_3^- ion. Two distinct NO_3^- features emerge at 1364 cm^{-1} and 1348 cm^{-1} (McGraw et al., 1965), and the fundamental O_3 is attenuated, despite negligible sublimation from the sample. Additional N-bearing intermediates, like the NO_2^- ion, nitrite, are IR active, and have absorption features shifted from the NO_3^- features (Weston Jr & Brodasky, 1957). However, we see no underlying structure in the $\sim$ 1350 cm^{-1} region that would indicate the presence of NO_2^-. This absence may suggest that either the single O-atom transfer reaction occurs quickly, or that the ozonide intermediate is preferred in a solid mixture. While we do see a new feature around 800 cm^{-1} consistent with the presence of an ozonide (Huston et al., 1983a), this feature appears at temperatures above 110 K well after the appearance of NO_3^-, within a temperature range typically associated with the formation of ammonia hemihydrate, which also has a spectral feature near 800 cm^{-1} (Moore et al., 2007a). Moreover, the initial O_3 is entirely depleted above 120 K (Figure 8.4), which further suggests that the 800 cm^{-1} feature is a consequence of ammonia hydrate formation. We can estimate the stoichiometry of this reaction using our QCM data (5.1 μg cm^{-2} of NO_3^--bearing product) and the known concentration of O_3 in our ice sample, since a the gas phase reaction mechanism would require a molar ratio of 5 O_3/NO_3. We calculate a molar ratio of 3.4 $\pm$ 0.4 O_3/NO_3 indicating that the reaction may involve the ozonide intermediate.

In addition to NO_3^-, we also find the NH_4^+ ion in our thermally-altered samples above 70 K, indicated by an absorption feature at 1506 cm^{-1}. Loeffler & Hudson (2015) found NH_4^+ within warmed ice mixtures of H_2O + NH_3 + H_2O_2 do to the relative acidity of H_2O_2 compared to H_2O, and Moore et al. (2007a) only found NH_4^+ present in irradiated H_2O and NH_3 mixtures. In the absence of radiation, it seems likely that our NH_4^+ is the counter ion for the NO_3^-.

From the previously mentioned reaction mechanisms, we expect that the NO_3^- ion is in the form of either the salt NH_4^+, or hydrated HNO_3. To identify the high temperature product, we grew ice mixtures from 15 M HNO_3 solutions. Due to the vapor pressures of both HNO_3 and H_2O, we expect that our resultant ices had a HNO_3/H_2O ratio of 1 (Hanson & Mauersberger, 1988; Ritzhaupt & Devlin, 1991). We warmed these HNO_3 + H_2O mixtures at 1.0 K min^{-1} and monitored the QCM for sublimation (Figure 8.5). We find that all of the sample has sublimated prior to 200 K, which is reasonably consistent with previous studies examining the infrared spectra of nitric acid and water clusters (Ritzhaupt & Devlin, 1991; Smith et al., 1991). While there may be a small amount of HNO_3 produced during the reaction as indicated by the H_2O + NH_3 + O_3 desorption curve structure from 180 - 200 K, after the H_2O has desorbed from the sample, the product that remains is the salt, NH_4NO_3. Moreover, the NH_4NO_3 spectrum (Figure 8.6) is consistent with the infrared spectrum of low temperature phase NH_4NO_3 crystals produced by Theoret & Sandorfy (1964).

8.5.2 Reaction Kinetics

In addition to determining the mechanism and products of this reaction, we are interested in determining the kinetic parameters, which provide constraints on the reaction time at lower, astronomical temperatures outside of the range of temperatures studied here. We follow the isothermal annealing technique, which is been successfully used previously to determine the overall activation energy of a chemical system (Bossa et al., 2008; Loeffler & Hudson, 2013; Tribbett & Loeffler, 2022). Figure 8.7 shows the O_3 fundamental absorption band at 1033 cm^{-1} while warming to an isothermal annealing temperature of 90 K (t = 0 at 50 K), which we integrate after subtracting a linear baseline as a proxy for the extent of the reaction. We choose the O_3 fundamental band as a proxy because it is well-separated from any product bands that could distort the band or substantially change the continuum background. Figure 8.8 shows the normalized integrated O_3 band area as a function of time (t = 0 at 50 K) for three of our isothermal annealing temperatures (75.6 K, 80.6 K, and 90.6 K). We assume first-order kinetics for this reaction, and we write the rate of reaction (k) as a function of O_3 column number density:

$$N(t) = N_0 e^{-kt} \tag{8.10}$$

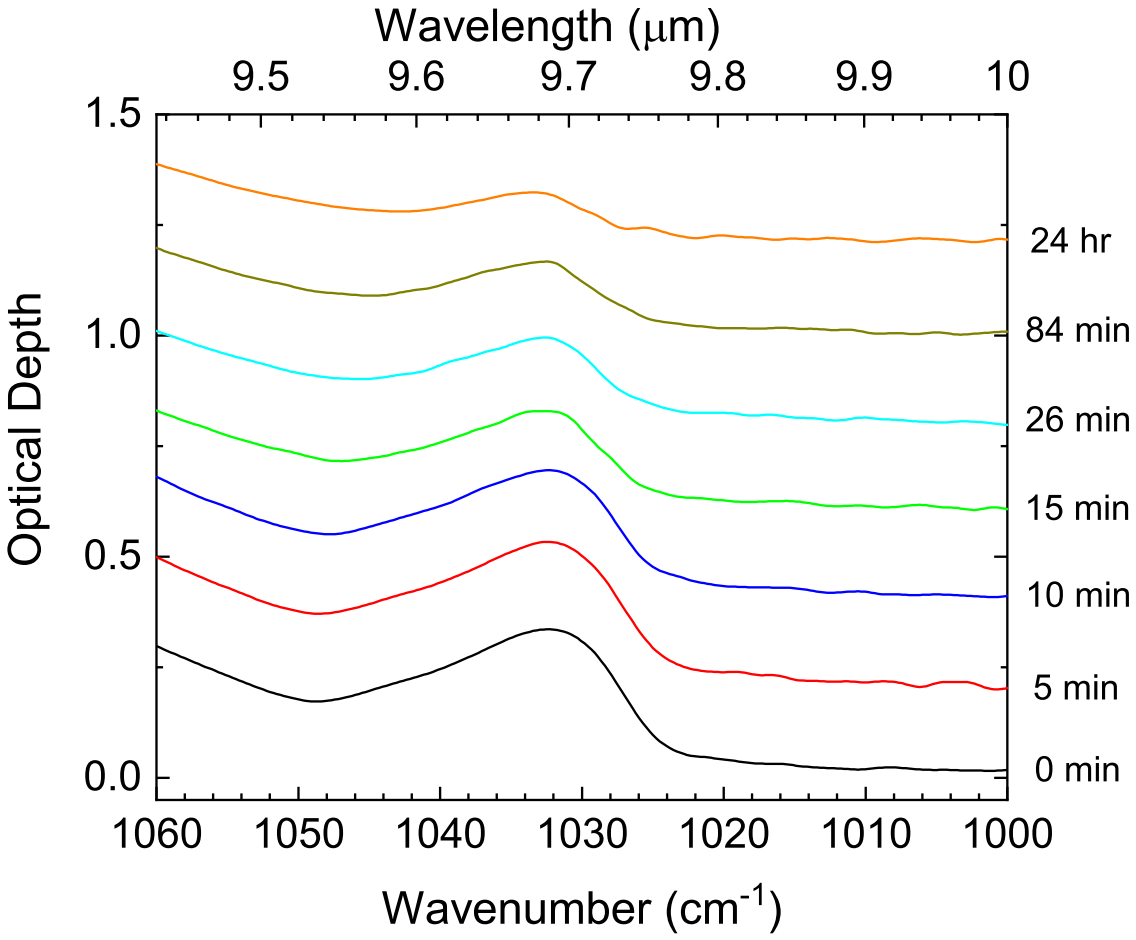

Figure 8.7: The IR spectral region containing the fundamental O_3 absorption feature of a H_2O + NH_3 + O_3 sample (25:70:5) warmed at 5.0 K min^{-1} to 90 K, where it was annealed. Spectra are vertically offset for clarity, and correspond to the time elapsed since beginning warming: 0 min, 5 min, 10 min, 15 min, 26 min, 84 min, and 24 hr.

where N_0 is the initial ozone column number density, and t is the time elapsed. We calculate the rate of reaction (k) at the time at which half of the ozone is consumed:

$$k = \frac{\ln 2}{t_{1/2}} \tag{8.11}$$

Note that we cannot use this calculation for temperatures at which half of the O_3 is consumed prior to reaching the annealing temperature, and thus we opted to calculate k for annealing temperatures between 75 and 90 K. Figure 8.8 inset shows the Arrhenius plot (i.e. rate of reaction for various temperatures) for several different isothermal annealing temperatures between 75 and 90 K. The linear fit of this data is proportional to the overall reaction activation energy, which we determine to be 17 ± 2 kJ mol^{-1}. The activation energy is consistent with values determined for other chemical systems using this experimental technique (Bossa et al., 2008; Loeffler & Hudson, 2013; Tribbett & Loeffler, 2022). We note that this reaction occurs at lower temperatures than the analogous sulfur oxidation reactions and requires a small activation energy (Loeffler & Hudson, 2013; Tribbett & Loeffler, 2022). This oxidation reaction does require more overall energy that many single-step acid base reactions involving NH_3. For example, the reaction between HCN and NH_3 forming the salt NH_4CN requires an activation energy of ~ 2.7 kJ mol^{-1} (Noble et al., 2013). However, oxidation with O_3 requires significantly less energy than the nucleophilic addition reaction between NH_3 and CH_3CHO (acetaldehyde), which requires ~ 33 kJ mol^{-1} (Duvernay et al., 2010).

8.5.3 Astrophysical Implications

Here we demonstrate that NH_3 ice is readily oxidized by the radiolytically-produced oxidant O_3 to the N-bearing anion NO_3^-, which upon warming forms a NH_4^+-bearing salt (NH_4NO_3). Moreover, this reaction occurs in the absence of radiation, at temperatures as low as 70 K on a laboratory timescale. For example, at 75 K half of the O_3 column number density is consumed within 24 hours, and within 30 minutes at 85 K. Critically, several Uranian satellites contain observable near-infrared bands that have been attributed to ammonia hydrates and ammonium-bearing salts (Cartwright et al., 2020), which have been correlated to geologically-active terrain, and these satellites have average surface temperatures between 70 - 85 (Hanel et al., 1986; Grundy et al., 2006), although the range has been suggested to extended above (90 K) and well below (20 - 40 K) the average surface temperatures (Sori et al., 2017; DeColibus et al., 2022). Our results indicate that this thermally-driven reaction can quickly produce the NH_4NO_3 salt at these average temperatures, and likely at low temperatures given a geologic timescale. This reaction provides an additional candidate for the NH_4^+-bearing salts responsible for the NIR spectral features in the 2.0 - 2.2 μm region. NH_4NO_3 may provide a considerably more refractory nitrogen-atom sink compared to ammonia or hydrated

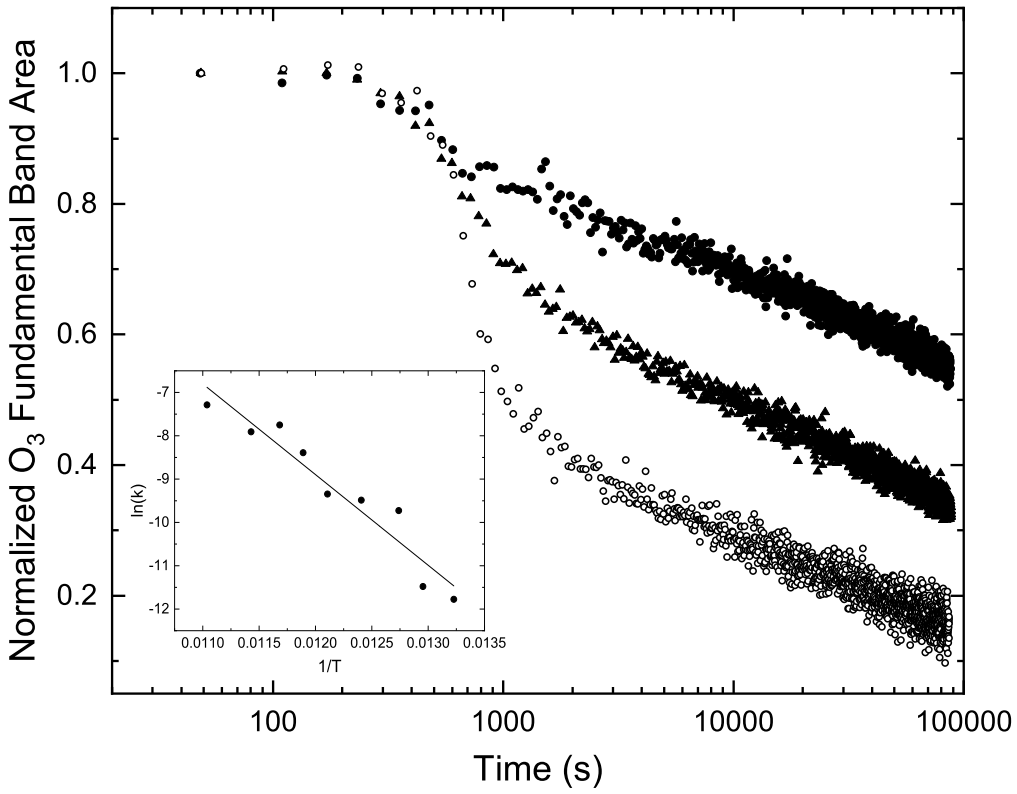

Figure 8.8: Normalized integrated O_3 fundamental band area for H_2O + NH_3 + O_3 (25:70:5) samples deposited at 50 K and warmed at a rate of 5 K min^{-1} to an isothermal annealing temperature (75 K, circles; 80 K, triangles; open circles, 90 K) and held for 24 hours. Inset: Arrhenius plot for the H_2O + NH_3 + O_3 reaction. The temperatures used correspond to: 75.6, 77.2, 78.5, 80.6, 82.6, 84.1, 85.6, 87.5, and 90.6 K

ammonia, similar to other NH_4-bearing salts which have been postulated to contain a reservoir of nitrogen-atoms on comet nuclei (Filacchione et al., 2019; Poch et al., 2020; Kruczkiewicz et al., 2021). Additionally, NH_3, NH3 hydrates, and NH_4^+-bearing salts have been postulated to be on the surface of Pluto's satellite Charon (Cook et al., 2023). While Charon is expected to be significantly colder than the Uranian satellites (35 - 40 K), this reaction could proceed over a geologic time frame or during a heating or resurfacing event (Stern et al., 1993; Grundy et al., 2016). Given that this reaction occurs readily at astrochemical temperatures and the resultant salt contains spectral features consistent with features detect on several outer solar system objects, we intend to derive optical constants for this salt in the near- and mid-IR spectral regions in the near future.

8.6 Conclusion

We provide evidence for an efficient thermally-driven oxidation reaction between NH_3 and O_3 at temperatures as low as 70 K. This reaction produces the NO_3^- anion at low temperatures, which interacts with excess NH_3 to produce the cation NH_4^+. These species are thermally stable in the form of the salt NH_4NO_3, which does not begin to sublimate under vacuum until above 250 K. We determined the overall activation energy of this reaction to be 17 $\pm$ 2 kJ mol^{-1}, which is consistent with other chemical systems that react at cryogenic temperatures. The salt product within this sample contains near-infrared spectral features near ones that have been previously attributed to NH_3 hydrates and NH_4^+-bearing material on several outer Solar System objects, including Miranda and Ariel.

8.7 Acknowledgements

P.D.T would like to acknowledge the assistance of Joshua Ellsworth, NAU Environmental Health and Safety (EHS), who provided corrosive storage and fume hood space. This research was supported by NSF Grant # 1821919. Upon acceptance, all data shown in the paper will be stored in Northern Arizona University's long-term public access data archive located at https://openknowledge.nau.edu/. Currently, the data is located on our laboratory website: http://www.astro.nau.edu/∼loeffler/Submitted-data.html.

Reactants			
Species	Peak Position (cm^{-1})[a]	Assignment	Reference
H_2O	$\sim$ 3250 (3295)	ν_1 and ν_3	Hardin & Harvey (1973); Hagen et al. (1981)
	$\sim$ 2250 (2250)	$3\nu_L$	Hardin & Harvey (1973); Ritzhaupt et al. (1976); Hagen et al. (1981)
	$\sim$ 1600 (1654)	ν_2	Hardin & Harvey (1973); Ritzhaupt et al. (1976); Hagen et al. (1981)
	840 (835)	ν_L	Bertie & Whalley (1964)
NH_3	5002 (5014)	$\nu_3 + \nu_4$	Ferraro et al. (1980); Hudson et al. (2022)
	4499 (4526)	$\nu_3 + \nu_2$	Ferraro et al. (1980); Hudson et al. (2022)
	3385 (3376)	ν_3 and ν_1	Ferraro et al. (1980); Hudson et al. (2022)
	1637 (1629)	ν_4	Ferraro et al. (1980); Hudson et al. (2022)
	1080 (1112)	ν_2	Ferraro et al. (1980); Hudson et al. (2022)
$H_2O + NH_3$	3108 (2912)	ν_{OH--N}	Waldron & Hornig (1953); Bertie & Morrison (1980); Moore et al. (2007a)
O_3	2108 (2108)	$\nu_3 + \nu_1$	Teolis et al. (2007b)
	1033 (1034)	ν_3	Teolis et al. (2007b); Raut et al. (2011)

Table 8.1: Peak positions for the species identified within H_2O + NH_3 + O_3 ice mixtures at 50 K (reactants). [a] Peak positions listed in parentheses are from the H_2O-dominated ice mixtures.

Low Temperature Products			
Species	Peak Position (cm^{-1})	Assignment	Reference
NO_3^-	1364	$2\nu_4$	McGraw et al. (1965); Ritzhaupt & Devlin (1977); Smith et al. (1991)
	1348	ν_3	McGraw et al. (1965); Ritzhaupt & Devlin (1977); Smith et al. (1991)
	800	ν_2?	Keller & Halford (1949); Ritzhaupt & Devlin (1991)
NH_4^+	1506	ν_4	Miller & Wilkins (1952); Knop & Glguère (1959); Loeffler & Hudson (2015)
$NH_4^+ + NH_3$	2058	...	Lundeen & Tobias (1975); Huston et al. (1983b)
$2NH_3$:H_2O	1549	$2\nu_L$	Bertie & Devlin (1984); Moore et al. (2007a)
	800	ν_L	Moore et al. (2007a)
	753	ν_L	(Moore et al., 2007a)
High Temperature Product[a]			
NH_4NO_3			
(NH_4^+)	4925	$\nu_3^{'} + \nu_4^{'}$	
	4670	$\nu_3^{'} + \nu_2^{'}$	
	3226	$\nu_3^{'}$	Keller & Halford (1949); Theoret & Sandorfy (1964)
	3085	$\nu_2^{'} + \nu_4^{'}$	Keller & Halford (1949); Theoret & Sandorfy (1964)
	2880	$2\nu_4^{'}$	Keller & Halford (1949); Theoret & Sandorfy (1964)
	1435	$\nu_4^{'}$	Keller & Halford (1949); Theoret & Sandorfy (1964)
(NO_3^-)	1377	$2\nu_4$	Theoret & Sandorfy (1964)
	1330	ν_3	Theoret & Sandorfy (1964)

Table 8.2: Peak positions for the species identified within H_2O + NH_3 + O_3 ice mixtures at 140 K (low temperature products) and 200 K (high temperature products). [a] Assignments indicated with the primes are attributed to the cation (NH_4^+) to remain consistent with the cited reference.

Chapter 9

Discussion and Conclusions

My co-authors and I demonstrate that thermal and radiolytic processing significantly alters the physical structure and composition of laboratory astrophysical ice analogs. Understanding these alterations is critical to enable the interpretation of astronomical observations and to describe the inventory and distribution of ices in the solar system and in the interstellar medium (ISM). Here I discuss the key implications for each of the previous chapters and briefly discuss potential avenues for future work.

Chapter 2 describes the newly constructed ultra high vacuum (UHV) chamber in the Processes Environments and Astrochemistry on Extraterrestrial Surfaces (PEAXS) laboratory at Northern Arizona University (NAU). This chamber boasts a suite of analytical tools, including Ultraviolet-Visible (UV-Vis) and infrared (IR) spectroscopy, Mass Spectrometry (MS), and quartz crystal microbalance (QCM) gravimetry. These techniques enable detailed characterization of astrophysical ice analog thin film samples at multiple wavelengths, probing both the physical and chemical properties of the ice mixtures. This chamber is versatile, and I effectively operated it to address the astrochemical questions discussed in each individual chapter. This chamber is easily adaptable to new research questions, and importantly, will provide opportunities for future graduate students.

Chapter 3 provides the QCM-derived sputtering yields of H_2O and the radiolytic decomposition product O_2 for low energy (0.5 - 5 keV) heavy (Ar^+) ion-irradiated H_2O ice samples at temperatures relevant to Jupiter and Saturn's icy satellites. These derived sputtering yields agree nicely with the single laboratory study performed under similar conditions; however, these yields are inconsistent with the current sputtering yield models, which overestimate our yields by nearly an order of magnitude. This discrepancy may indicate that the low energy ion sputtering contribution of O_2 into the tenuous atmosphere of icy satellites is overestimated. Given that the difference between the two experimental studies is the irradiation angle of incidence (0°, Chapter 3; 60°, Teolis et al. (2010)), a study addressing angular dependence of O_2 is warranted. O_2 sputtering is likely more dependent on the irradiation angle of incidence than H_2O sputtering since O_2 production preferences the near-surface layer of the ice and the angle of incidence significantly affects the

energy deposition profile of low energy, heavy ions.

In Chapter 4, we demonstrate the efficacy of molecular species detection within an ultraviolet (UV) occultation-derived transit spectrum of Titan acquired by the National Aeronautics and Space Agency (NASA) *Cassini* UVIS instrument. However, using simplified haze parameterizations typical of exoplanet characterization within our atmospheric retrieval model, we failed to constrain the well-documented haze structure within Titan's atmosphere. This non-detection suggests that simplified haze models may be biased toward false-negative detections of exoplanetary atmospheric hazes, which can affect our understanding of the temperature, and structure of those atmospheres. We anticipate using this Titan data set to refine and expand the simplified haze parameterizations by including wavelength dependent haze attenuation and increasingly complex haze distributions to detect Titan's haze structure. Importantly, this chapter provides an example of the spectral analysis tool that I applied to laboratory astrophysics. From this project, I learned how to use a MCMC-implementation of the Bayesian Inference tool (`emcee`) to fit a model to data to derive probability distributions for model parameters. In Chapter 5, I use this tool to fit a Fresnel reflectance model to laboratory UV-Vis spectra of irradiated microporous H_2O ice samples, which allowed me to derive a thickness or density as a function of fluence. We demonstrated that energetic electrons compact microporous H_2O ice and improve estimates for the radiation-induced compaction timescales of H_2O ice in the ISM. These estimates suggest that compaction happens quickly on an astronomical timescale, and thus may explain why microporous H_2O has not been observed in the ISM.

In Chapter 6, we identify three new near-infrared absorption features within microporous ASW ice samples. We attribute these absorption bands to the dangling bonds within microporous ASW based on their thermal stability, and band shifts due to the adsorption of CH_4. These bands provide additional spectral features that NASA's JWST can target with the NIRSpec instrument to identify microporous ASW within the youngest molecular clouds in the ISM. We estimate that the integration time required to detect one of these features with an SNR of 3 is on the order of 4 - 5 hours of telescope time. Logical next steps for this project include a detailed laboratory characterization of the spectral shifts due to different adsorbed species, specifically O_2, N_2, and H_2, as a method for probing ISM column densities of condensed IR-inactive molecules.

Finally, we demonstrate that thermally-driven reactions occur readily at astrophysical temperatures with two different chemical systems. In Chapter 7, we demonstrate an oxidation reaction within H_2O + H_2S + O_3 ice mixtures at temperatures as low as 90 K. O_3 readily oxidizes H_2S to form SO_2 and increasingly complex sulfur anions (HSO_3^-, HSO_4^-, and SO_4^{2-}) at low temperatures and hydrated sulfuric acid at higher temperatures. The overall activation energy for this reaction is $\sim$ 20 kJ mol^{-1}, which is consistent with previous studies that have used the isothermal annealing technique. We find that this reaction is consistent

with the geographical distribution of oxidant and sulfur populations on the surface of Europa, and that this reaction may occur on a shorter timescale than competing radiation-driven reactions. In Chapter 8, we demonstrate an analogous oxidation reaction within $H_2O + NH_3 + O_3$ ice mixtures at temperatures as low as 70 K. O_3 reacts with NH_3 to produce NO_3^-, which is thermally stable until 260 K as the salt NH_4NO_3. The overall activation energy for this reaction is ~ 17 kJ mol^{-1}, which is consistent with other thermally-driven acid/base reactions and nucleophilic addition reactions with NH_3 (Theulé et al., 2013). We also show that NH_4NO_3 possesses near-infrared absorption features that are consistent with previous detections of NH_4^+-bearing salts on several outer solar system objects. Thus, NH_4NO_3, due to its low temperature thermal reactivity, is a candidate for salts on these surfaces. These studies highlight the potential significance of thermally-driven reactions in astrophysical systems. We identify OCS and CH_3OH as potential candidates for oxidation reactions with O_3, and will focus on these in the near future. Moreover, observational and modeling studies would greatly benefit from the inclusion of these reactions in their discussions of icy outer solar system chemistry.

Acronyms

amu atomic mass units

APRA Astrophysics Research and Analysis

Ar argon

ASW amorphous solid water

BIC Bayesian Information Criterion

CH_4 methane

$(CH_3)_2CO$ acetone

CO carbon monoxide

CO_2 carbon dioxide

DB dangling bond

FTIR Fourier Transform Infrared Spectrometer

FWHM full width half maximum

H_2 molecular hydrogen

H_2O water

H_2S hydrogen sulfide

HNO_3 nitric acid

HPLC high performance liquid chromatography

HST Hubble Space Telescope

IR infrared

ISM interstellar medium

JWST James Webb Space Telescope

MCMC Markov chain Monte Carlo

MCT/A Mercury Cadmium Telluride

MS Mass Spectrometry

NAU Northern Arizona University

NASA National Aeronautics and Space Agency

NH_3 ammonia

NH_4^+ ammonium

NIR near-infrared

N_2 molecular nitrogen

NO_3^- nitrate

NSF National Science Foundation

O_2 molecular oxygen

O_3 ozone

OAP off-axis parabolic

PEAXS Processes Environments and Astrochemistry on Extraterrestrial Surfaces

ppm parts per million

PVC polyvinyl chloride

QCM quartz crystal microbalance

REU research experience for undergraduates

SNR signal-to-noise

SO_2 sulfur dioxide

SOP standard operating procedures

SRIM Stopping and Range of Ions in Matter

STIS Space Telescope Imaging Spectrometer

UHV ultra high vacuum

UV ultraviolet

UVIS Ultraviolet Imaging Spectrometer

UV-Vis Ultraviolet-Visible

WFC3 Wide Field Camera 3

Y sputtering yield

References

Babar, S., & Weaver, J. H. *2015*, *Optical constants of Cu, Ag, and Au revisited*, Applied Optics, 54, 477

Bagnasco, G., Kolm, M., Ferruit, P., et al. *2007*, Overview of the near-infrared spectrograph (NIRSpec) instrument on-board the James Webb Space Telescope (JWST), in Cryogenic Optical Systems and Instruments XII, Vol. 6692, International Society for Optics and Photonics, 66920M

Bahr, D. A., Fama, M., Vidal, R. A., & Baragiola, R. A. *2001*, *Radiolysis of water ice in the outer solar system: Sputtering and trapping of radiation products*, J. Geophys. Res. Planets, 106, 33285

Bar-Nun, A., Herman, G., Laufer, D., & Rappaport, M. L. *1985a*, *Trapping and release of gases by water ice and implications for icy bodies*, Icarus, 63, 317

Bar-Nun, A., Herman, G. B., Rappaport, M. L., & Mekler, Y. *1985b*, *Ejection of H2O, O2, H2 and H from water ice by 0.5–6 keV H+ and Ne+ ion bombardment*, Surf. Sci., 150, 143

Baragiola, R. A. *2004*, *Sputtering: survey of observations and derived principles*, Philos. T. R. Soc. A, 362, 29

Baragiola, R. A., Atteberry, C. L., Dukes, C. A., Fama, M., & Teolis, B. D. *2002*, *Atomic collisions in solids: astronomical applications*, Nucl. Instrum. Meth. B, 193, 720

Baragiola, R. A., Vidal, R. A., Svendsen, W., et al. *2003*, *Sputtering of water ice*, Nucl. Instrum. Meth. B, 209, 294

Barstow, J. K. *2020*, *Unveiling cloudy exoplanets: the influence of cloud model choices on retrieval solutions*, Monthly Notices of the Royal Astronomical Society, 497, 4183

—. *2021*, *The curse of clouds*, Astronomy & Geophysics, 62, 1

Barstow, J. K., & Irwin, P. G. J. *2016*, *Habitable worlds with JWST: transit spectroscopy of the TRAPPIST-1 system?*, , 461, L92, doi: 10.1093/mnrasl/slw109

Barucci, M. A., Merlin, F., Guilbert, A., et al. *2008*, *Surface composition and temperature of the TNO Orcus*, Astronomy & Astrophysics, 479, L13

Batalha, N. E., & Line, M. R. *2017*, *Information Content Analysis for Selection of Optimal JWST Observing Modes for Transiting Exoplanet Atmospheres*, , 153, 151, doi: 10.3847/1538-3881/aa5faa

Bauer, J. M., Roush, T. L., Geballe, T. R., et al. *2002*, *The near infrared spectrum of Miranda: Evidence of crystalline water ice*, Icarus, 158, 178

Becker, T. M., Trumbo, S. K., Molyneux, P. M., et al. *2022*, *Mid-ultraviolet Hubble Observations of Europa and the Global Surface Distribution of SO2*, The Planetary Science Journal, 3, 129

Behr, P. R., Tribbett, P. D., Robinson, T. D., & Loeffler, M. J. *2020*, *Compaction of Porous H2O Ice via Energetic Electrons*, The Astrophysical Journal, 900, 147

Beichman, C., Benneke, B., Knutson, H., et al. *2014*, *Observations of Transiting Exoplanets with the James Webb Space Telescope (JWST)*, , 126, 1134, doi: 10.1086/679566

Benneke, B., & Seager, S. *2012*, *Atmospheric retrieval for super-earths: uniquely constraining the atmospheric composition with transmission spectroscopy*, The Astrophysical Journal, 753, 100, doi: 10.1088/0004-637X/753/2/100

Benneke, B., Wong, I., Piaulet, C., et al. *2019*, *Water Vapor and Clouds on the Habitable-zone Sub-Neptune Exoplanet K2-18b*, , 887, L14, doi: 10.3847/2041-8213/ab59dc

Bennett, C. J., & Kaiser, R. I. *2005*, *Laboratory studies on the formation of ozone (O3) on icy satellites and on interstellar and cometary ices*, The Astrophysical Journal, 635, 1362

Bertie, J. E., & Devlin, J. P. *1984*, *The infrared spectra and phase transitions of pure and isotopically impure 2ND3 H2O, 2NH3 D2O, 2NH3 H2O, and 2ND3 D2O between 100 and 15 K*, The Journal of chemical physics, 81, 1559

Bertie, J. E., & Morrison, M. M. *1980*, *The infrared spectra of the hydrates of ammonia, NH3 H2O and 2NH3 H2O at 95° K*, The Journal of Chemical Physics, 73, 4832

Bertie, J. E., & Whalley, E. *1964*, *Infrared Spectra of Ices Ih and Ic in the Range 4000 to 350 cm—1*, The journal of chemical physics, 40, 1637

Bétrémieux, Y., & Swain, M. R. *2016*, *An analytical formalism accounting for clouds and other "surfaces" for exoplanet transmission spectroscopy*, ArXiv e-prints. https://arxiv.org/abs/1610.02049

Blackman, M., & Lisgarten, N. D. *1958*, *Electron diffraction investigations into the cubic and other structural forms of ice*, Advances in Physics, 7, 189

Blitz, L., & Shu, F. H. *1980*, *The origin and lifetime of giant molecular cloud complexes*, The Astrophysical Journal, 238, 148

Boring, J. W., Johnson, R. E., Reimann, C. T., et al. *1983*, *Ion-induced chemistry in condensed gas solids*, Nucl. Instrum. Methods Phys. Res., 218, 707

Bossa, J. B., Duvernay, F., Theulé, P., et al. *2009a*, *Methylammonium methylcarbamate thermal formation in interstellar ice analogs: a glycine salt precursor in protostellar environments*, Astronomy & Astrophysics, 506, 601

Bossa, J.-B., Theulé, P., Duvernay, F., Borget, F., & Chiavassa, T. *2008*, *Carbamic acid and carbamate formation in NH: CO ices–UV irradiation versus thermal processes*, Astronomy & Astrophysics, 492, 719

Bossa, J. B., Theule, P., Duvernay, F., & Chiavassa, T. *2009b*, *NH2CH2OH thermal formation in interstellar ices contribution to the 5–8 μm region toward embedded protostars*, The Astrophysical Journal, 707, 1524

Brown, D. E., George, S. M., Huang, C., et al. *1996*, *H2O condensation coefficient and refractive index for vapor-deposited ice from molecular beam and optical interference measurements*, The Journal of Physical Chemistry, 100, 4988

Brown, M. E., & Calvin, W. M. *2000*, *Evidence for crystalline water and ammonia ices on Pluto's satellite Charon*, Science, 287, 107

Brown, T. M. *2001*, *Transmission spectra as diagnostics of extrasolar giant planet atmospheres*, The Astrophysical Journal, 553, 1006

Brown, W. L., Augustyniak, W. M., Brody, E., et al. *1980*, *Energy dependence of the erosion of H2O ice films by H and He ions*, Nucl. Instrum. Meth., 170, 321

Brown, W. L., Augustyniak, W. M., Marcantonio, K. J., et al. *1984*, *Electronic sputtering of low temperature molecular solids*, Nucl. Instrum. Meth. B, 1, 307

Brown, W. L., Lanzerotti, L. J., Poate, J. M., & Augustyniak, W. M. *1978*, *"Sputtering of ice by MeV light ions*, Phys. Rev. Lett., 40, 1027

Brown, W. L., Augustyniak, W. M., Simmons, E., et al. *1982*, *Erosion and molecule formation in condensed gas films by electronic energy loss of fast ions*, Nucl. Instrum. Meth. Phys. Res., 198, 1

Buch, V., & Devlin, J. P. *1991*, *Spectra of dangling OH bonds in amorphous ice: Assignment to 2-and 3-coordinated surface molecules*, The Journal of chemical physics, 94, 4091

Cadle, R. D., & Ledford, M. *1966*, *The reaction of ozone with hydrogen sulfide*, Int. J. Air Water Pollut, 10, 25

Calvani, P., Cunsolo, S., Lupi, S., & Nucara, A. *1992*, *The near-infrared spectrum of solid CH4*, The Journal of chemical physics, 96, 7372

Calvin, W. M., & Martin, T. Z. *1994*, *Spatial variability in the seasonal south polar cap of Mars*, Journal of Geophysical Research: Planets, 99, 21143

Capalbo, F. J., Bénilan, Y., Fray, N., et al. *2016*, *New benzene absorption cross sections in the VUV, relevance for Titan's upper atmosphere*, Icarus, 265, 95

Capps, R. W., Gillett, F. C., & Knacke, R. F. *1978*, *Infrared observations of the OH source W33 A*, The Astrophysical Journal, 226, 863

Carlson, R. W., Anderson, M. S., Johnson, R. E., Schulman, M. B., & Yavrouian, A. H. *2002*, *Sulfuric acid production on Europa: the radiolysis of sulfur in water ice*, Icarus, 157, 456

Carlson, R. W., Johnson, R. E., & Anderson, M. S. *1999a*, *Sulfuric acid on Europa and the radiolytic sulfur cycle*, Science, 286, 97

Carlson, R. W., Anderson, M. S., Johnson, R. E., et al. *1999b*, *Hydrogen peroxide on the surface of Europa*, Science, 283, 2062

Carmack, R. A., Tribbett, P. D., & Loeffler, M. J. *2023*, *Pore Accessibility in Amorphous Solid Water*, The Astrophysical Journal, 942, 1

Carrasco, N., Tigrine, S., Gavilan, L., Nahon, L., & Gudipati, M. S. *2018*, *The evolution of Titan's high-altitude aerosols under ultraviolet irradiation*, Nature Astronomy, 2, 489

Cartwright, R. J., Beddingfield, C. B., Nordheim, T. A., et al. *2020*, *Evidence for ammonia-bearing species on the Uranian satellite Ariel supports recent geologic activity*, The Astrophysical Journal Letters, 898, L22

Caselli, P., & Ceccarelli, C. *2012*, *Our astrochemical heritage*, The Astronomy and Astrophysics Review, 20, 1

Cassidy, T. A., Paranicas, C. P., Shirley, J. H., et al. *2013*, *Magnetospheric ion sputtering and water ice grain size at Europa*, Planet. Space Sci., 77, 64

Chaabouni, H., Schriver-Mazzuoli, L., & Schriver, A. *2000*, *Infrared spectroscopy of neat solid ozone and that of ozone in interaction with amorphous and crystalline water ice*, The Journal of Physical Chemistry A, 104, 6962

Chandler, C. O., Kueny, J. K., Trujillo, C. A., Trilling, D. E., & Oldroyd, W. J. *2020*, *Cometary Activity Discovered on a Distant Centaur: A Nonaqueous Sublimation Mechanism*, The Astrophysical Journal Letters, 892, L38

Charbonneau, D., Brown, T. M., Noyes, R. W., & Gilliland, R. L. *2002*, *Detection of an extrasolar planet atmosphere*, The Astrophysical Journal, 568, 377

Chen, F. Z., & Wu, C. Y. R. *2004*, *Temperature-dependent photoabsorption cross sections in the VUV-UV region. I. Methane and ethane*, Journal of Quantitative Spectroscopy and Radiative Transfer, 85, 195

Chen, Y.-J., Nuevo, M., Chu, C.-C., et al. *2011*, *Photo-desorbed species produced by the UV/EUV irradiation of an H2O: CO2: NH3 ice mixture*, Advances in Space Research, 47, 1633

Christiansen, J. W., Carpini, D. D., & Tsong, I. S. T. *1986*, *Sputtering of ices by keV ions*, Nucl. Instrum. Meth. B, 15, 218

Cook, J. C., Desch, S. J., Roush, T. L., Trujillo, C. A., & Geballe, T. R. *2007*, *Near-infrared spectroscopy of Charon: Possible evidence for cryovolcanism on Kuiper belt objects*, The Astrophysical Journal, 663, 1406

Cook, J. C., Protopapa, S., Dalle Ore, C. M., et al. *2023*, *Analysis of Charon's spectrum at 2.21-μm from New Horizons/LEISA and Earth-based observations*, Icarus, 389, 115242

Cooper, J. F., Cooper, P. D., Sittler, E. C., Sturner, S. J., & Rymer, A. M. *2009*, *Old Faithful model for radiolytic gas-driven cryovolcanism at Enceladus*, Planetary and Space Science, 57, 1607

Cooper, J. F., Johnson, R. E., Mauk, B. H., Garrett, H. B., & Gehrels, N. *2001*, *Energetic ion and electron irradiation of the icy Galilean satellites*, Icarus, 149, 133

Cruikshank, D. P., Pilcher, C. B., & Morrison, D. *1977*, *Identification of a new class of satellites in the outer solar system*, The Astrophysical Journal, 217, 1006

Cruikshank, D. P., Roush, T. L., Owen, T. C., Quirico, E., & Bergh, C. D. *1998*, The surface compositions of Triton, Pluto, and Charon, in Solar System Ices: Based on Reviews Presented at the International Symposium "Solar System Ices" held in Toulouse, France, on March 27–30, 1995, Springer, 655–684

Cruikshank, D. P., Meyer, A. W., Brown, R. H., et al. *2010*, *Carbon dioxide on the satellites of Saturn: Results from the Cassini VIMS investigation and revisions to the VIMS wavelength scale*, Icarus, 206, 561

Dalba, P. A., Muirhead, P. S., Fortney, J. J., et al. *2015*, *The Transit Transmission Spectrum of a Cold Gas Giant Planet*, , 814, 154, doi: 10.1088/0004-637X/814/2/154

Dalle Ore, C. M., Cruikshank, D. P., Protopapa, S., et al. *2019*, *Detection of ammonia on Pluto's surface in a region of geologically recent tectonism*, Science advances, 5, eaav5731

Dartois, E., Ding, J. J., De Barros, A. L. F., et al. *2013*, *Swift heavy ion irradiation of water ice from MeV to GeV energies-Approaching true cosmic ray compaction*, Astronomy & Astrophysics, 557, A97

Davis, M. R., Meier, R. M., Cooper, J. F., & Loeffler, M. J. *2021*, *The contribution of electrons to the sputter-produced O2 exosphere on Europa*, The Astrophysical Journal Letters, 908, L53

De Pena, R. G., Olszyna, K., & Heicklen, J. *1973*, *Kinetics of particle growth. I. Ammonium nitrate from the ammonia-ozone reaction*, The Journal of Physical Chemistry, 77, 438

De Sanctis, M. C., Raponi, A., Ammannito, E., et al. *2016*, *Bright carbonate deposits as evidence of aqueous alteration on (1) Ceres*, Nature, 536, 54

de Wit, J., Wakeford, H. R., Gillon, M., et al. *2016*, *A combined transmission spectrum of the Earth-sized exoplanets TRAPPIST-1 b and c*, , 537, 69, doi: 10.1038/nature18641

DeColibus, D. R., Chanover, N. J., & Cartwright, R. J. *2022*, *Longitudinal Variation of H2O Ice Absorption on Miranda*, The Planetary Science Journal, 3, 119

Deming, D., Seager, S., Winn, J., et al. *2009*, *Discovery and Characterization of Transiting Super Earths Using an All-Sky Transit Survey and Follow-up by the James Webb Space Telescope*, , 121, 952, doi: 10.1086/605913

Demyk, K., Dartois, E., d'Hendecourt, L., et al. *1998*, *Laboratory identification of the 4.62 mu M solid state absorption band in the ISO-SWS spectrum of RAFGL 7009S*, Astronomy and Astrophysics, 339, 553

Ditchburn, R. W. *1955*, *Absorption cross-sections in the vacuum ultra-violet III. Methane*, Proceedings of the Royal Society of London. Series A. Mathematical and Physical Sciences, 229, 44

Duvernay, F., Dufauret, V., Danger, G., et al. *2010*, *Chiral molecule formation in interstellar ice analogs: alpha-aminoethanol NH2CH (CH3) OH*, Astronomy & Astrophysics, 523, A79

Earle, A. M., Binzel, R. P., Young, L. A., et al. *2017*, *Long-term surface temperature modeling of Pluto*, Icarus, 287, 37

Ehrenfreund, P., Burgdorf, M., d'Hendecourt, L., & Greenberg, J. M. *1993*, *On the possible detection of solid O2 and O3 interstellar grains with ISO*, Advances in Space Research, 13, 465

Emery, J. P., Burr, D. M., Cruikshank, D. P., Brown, R. H., & Dalton, J. B. *2005*, *Near-infrared (0.8–4.0 m) spectroscopy of Mimas, Enceladus, Tethys, and Rhea*, Astronomy & Astrophysics, 435, 353

Erickson, R. E., Yates, L. M., Clark, R. L., & McEwen, D. *1977*, *The reaction of sulfur dioxide with ozone in water and its possible atmospheric significance*, Atmospheric Environment (1967), 11, 813

Esposito, L. W., Barth, C. A., Colwell, J. E., et al. *2004*, *The Cassini ultraviolet imaging spectrograph investigation*, Space science reviews, 115, 299

Falk, M. *1984*, *The frequency of the H O H bending fundamental in solids and liquids*, Spectrochimica Acta Part A: Molecular Spectroscopy, 40, 43

Famá, M., Bahr, D. A., Teolis, B. D., & Baragiola, R. A. *2002*, *Ion beam induced chemistry: the case of ozone synthesis and its influence on the sputtering of solid oxygen*, Nuclear Instruments and Methods in Physics Research Section B: Beam Interactions with Materials and Atoms, 193, 775

Famá, M., Shi, J., & Baragiola, R. A. *2008*, *Sputtering of ice by low-energy ions*, Surf. Sci., 602, 156

Fathe, K., Holt, J. S., Oxley, S. P., & Pursell, C. J. *2006*, *Infrared spectroscopy of solid hydrogen sulfide and deuterium sulfide*, The Journal of Physical Chemistry A, 110, 10793

Feng, Y., & Penner, J. E. *2007*, *Global modeling of nitrate and ammonium: Interaction of aerosols and tropospheric chemistry*, Journal of Geophysical Research: Atmospheres, 112

Feng, Y. K., Line, M. R., Fortney, J. J., et al. *2016*, *The impact of non-uniform thermal structure on the interpretation of exoplanet emission spectra*, The Astrophysical Journal, 829, 52

Ferradaz, T., Bénilan, Y., Fray, N., et al. *2009*, *Temperature-dependent photoabsorption cross-sections of cyanoacetylene and diacetylene in the mid-and vacuum-UV: Application to Titan's atmosphere*, Planetary and Space Science, 57, 10

Ferrante, R. F., Moore, M. H., Spiliotis, M. M., & Hudson, R. L. *2008*, *Formation of interstellar OCS: Radiation chemistry and IR spectra of precursor ices*, The Astrophysical Journal, 684, 1210

Ferraro, J. R., Sill, G., & Fink, U. *1980*, *Infrared intensity measurements of cryodeposited thin films of NH 3, NH 4 HS, H 2 S, and assignments of absorption bands*, Applied Spectroscopy, 34, 525

Filacchione, G., Groussin, O., Herny, C., et al. *2019*, *Comet 67P/CG nucleus composition and comparison to other comets*, Space science reviews, 215, 1

Fink, U., Dekkers, N. H., & Larson, H. P. *1973*, *Infrared spectra of the Galilean satellites of Jupiter*, The Astrophysical Journal, 179, L155

Fink, U., Larson, H. P., Gautier III, T., & Treffers, R. *1976*, *Infrared spectra of the satellites of Saturn-Identification of water ice on Iapetus, Rhea, Dione, and Tethys*, The Astrophysical Journal, 207, L63

Fink, U. W. E., & Larson, H. P. *1975*, *Temperature dependence of the water-ice spectrum between 1 and 4 microns: Application to Europa, Ganymede and Saturn's rings*, Icarus, 24, 411

Flannery, B. P., Press, W. H., Teukolsky, S. A., & Vetterling, W. *1992*, *Numerical recipes in C*, Press Syndicate of the University of Cambridge, New York, 24, 36

Foreman-Mackey, D., Hogg, D. W., Lang, D., & Goodman, J. *2013*, *emcee: the MCMC hammer*, Publications of the Astronomical Society of the Pacific, 125, 306

Fortney, J. J. *2005*, *The effect of condensates on the characterization of transiting planet atmospheres with transmission spectroscopy*, Monthly Notices of the Royal Astronomical Society, 364, 649

Fraine, J., Deming, D., Benneke, B., et al. *2014*, *Water vapour absorption in the clear atmosphere of a Neptune-sized exoplanet*, Nature, 513, 526

Galli, A., Vorburger, A., Wurz, P., et al. *2018*, *0.2 to 10 keV electrons interacting with water ice: Radiolysis, sputtering, and sublimation*, Planet. Space Sci., 155, 91

Gardner, J. P., Mather, J. C., Clampin, M., et al. *2006*, *The James Webb Space Telescope*, , 123, 485

Gaudi, B. S., Seager, S., Mennesson, B., et al. *2018*, *The Habitable Exoplanet Observatory*, Nature Astronomy, 2, 600, doi: 10.1038/s41550-018-0549-2

Gerakines, P. A., Bray, J. J., Davis, A., & Richey, C. R. *2005*, *The strengths of near-infrared absorption features relevant to interstellar and planetary ices*, The Astrophysical Journal, 620, 1140

Gerakines, P. A., & Hudson, R. L. *2015*, *First infrared band strengths for amorphous CO2, an overlooked component of interstellar ices*, The Astrophysical Journal Letters, 808, L40

—. *2020*, *A modified algorithm and open-source computational package for the determination of infrared optical constants relevant to astrophysics*, The Astrophysical Journal, 901, 52

Gerakines, P. A., Schutte, W. A., Greenberg, J. M., & van Dishoeck, E. F. *1995*, *The infrared band strengths of H_2_O, CO and CO_2_ in laboratory simulations of astrophysical ice mixtures.*, , 296, 810. https://arxiv.org/abs/astro-ph/9409076

Ghosh, D., Mondal, B., Bagchi, S., & Kumar Das, A. *2010*, *Isomers of OCS and their reaction with H2O on singlet potential energy surface*, Molecular Physics, 108, 3353

Gibb, E. L., Whittet, D. C. B., Schutte, W. A., et al. *2000*, *An inventory of interstellar ices toward the embedded protostar W33A*, The Astrophysical Journal, 536, 347

Giguère, P. A., & Harvey, K. B. *1956*, *On the infrared absorption of water and heavy water in condensed states*, Canadian Journal of Chemistry, 34, 798

Glavas, S., & Toby, S. *1975*, *Reaction between ozone and hydrogen sulfide*, The Journal of Physical Chemistry, 79, 779

Goodman, J., & Weare, J. *2010*, *Ensemble samplers with affine invariance*, Communications in applied mathematics and computational science, 5, 65

Grasset, O., Dougherty, M. K., Coustenis, A., et al. *2013*, *JUpiter ICy moons Explorer (JUICE): An ESA mission to orbit Ganymede and to characterise the Jupiter system*, Planetary and Space Science, 78, 1

Greeley, R., Chyba, C. F., Head, J. W., et al. *2004*, *Geology of Europa*, Jupiter: The Planet, Satellites and Magnetosphere, 329

Greene, T. P., Line, M. R., Montero, C., et al. *2016*, *Characterizing transiting exoplanet atmospheres with JWST*, , 817, 17, doi: 10.3847/0004-637X/817/1/17

Grundy, W. M., Schmitt, B., & Quirico, E. *2002*, *The temperature-dependent spectrum of methane ice I between 0.7 and 5 μm and opportunities for near-infrared remote thermometry*, Icarus, 155, 486

Grundy, W. M., Young, L. A., Spencer, J. R., et al. *2006*, *Distributions of H2O and CO2 ices on Ariel, Umbriel, Titania, and Oberon from IRTF/SpeX observations*, Icarus, 184, 543

Grundy, W. M., Binzel, R. P., Buratti, B. J., et al. *2016*, *Surface compositions across Pluto and Charon*, Science, 351, aad9189

Hagen, W., Tielens, A. G. G. M., & Greenberg, J. M. *1981*, *The infrared spectra of amorphous solid water and ice Ic between 10 and 140 K*, Chemical Physics, 56, 367

Hales, J. M., Wilkes, J. O., & York, J. L. *1969*, *The rate of reaction between dilute hydrogen sulfide and ozone in air*, Atmospheric Environment (1967), 3, 657

Hand, K. P., & Brown, M. E. *2013*, *Keck II observations of hemispherical differences in H2O2 on Europa*, The Astrophysical Journal Letters, 766, L21

Hanel, R., Conrath, B., Flasar, F. M., et al. *1982*, *Infrared observations of the Saturnian system from Voyager 2*, Science, 215, 544

Hanel, R., Conrath, B., Flasar, F., et al. *1986*, *Infrared observations of the Uranian system*, Science, 233, 70

Hansen, C. J., Esposito, L., Stewart, A. I. F., et al. *2006*, *Enceladus' water vapor plume*, Science, 311, 1422

Hanson, D., & Mauersberger, K. *1988*, *Vapor pressures of nitric acid/water solutions at low temperatures*, The Journal of Physical Chemistry, 92, 6167

Harcke, L. J. 2005, Radar imaging of solar system ices (Stanford University)

Hardin, A. H., & Harvey, K. B. *1973*, *Temperature dependences of the ice I hydrogen bond spectral shifts—I: The vitreous to cubic ice I phase transformation*, Spectrochimica Acta Part A: Molecular Spectroscopy, 29, 1139

Haring, R. A., Kolfschoten, A. W., & De Vries, A. E. *1984*, *Chemical sputtering by keV ions*, Nucl. Instrum. Meth. B, 2, 544

He, C., Hörst, S. M., Lewis, N. K., et al. *2020*, *Sulfur-driven haze formation in warm CO 2-rich exoplanet atmospheres*, Nature Astronomy, 4, 986

Heavens, O. S. 1965, Optical properties of thin solid films (New York: Dover)

Heide, H.-G. *1982*, *On the irradiation of organic samples in the vicinity of ice*, Ultramicroscopy, 7, 299

—. *1984*, *Observations on ice layers*, Ultramicroscopy, 14, 271

Hendrix, A. R., Barth, C. A., & Hord, C. W. *1999*, *Ganymede's ozone-like absorber: Observations by the Galileo ultraviolet spectrometer*, Journal of Geophysical Research: Planets, 104, 14169

Hendrix, A. R., Cassidy, T. A., Johnson, R. E., Paranicas, C., & Carlson, R. W. *2011*, *Europa's disk-resolved ultraviolet spectra: Relationships with plasma flux and surface terrains*, Icarus, 212, 736

Hendrix, A. R., Hansen, C. J., & Holsclaw, G. M. *2010*, *The ultraviolet reflectance of Enceladus: Implications for surface composition*, Icarus, 206, 608

Hendrix, A. R., & Johnson, R. E. *2008*, *Callisto: new insights from Galileo disk-resolved UV measurements*, The Astrophysical Journal, 687, 706

Heng, K., & Kitzmann, D. *2017*, *The theory of transmission spectra revisited: a semi-analytical method for interpreting WFC3 data and an unresolved challenge*, , 470, 2972, doi: 10.1093/mnras/stx1453

Hoffmann, M. R. *1986*, *On the kinetics and mechanism of oxidation of aquated sulfur dioxide by ozone*, Atmospheric Environment (1967), 20, 1145

Hogg, D. W., Bovy, J., & Lang, D. *2010*, *Data analysis recipes: Fitting a model to data*, arXiv preprint arXiv:1008.4686

Horimoto, N., Kato, H. S., & Kawai, M. *2002*, *Stepwise morphological change of porous amorphous ice films observed through adsorption of methane*, The Journal of chemical physics, 116, 4375

Hörst, S. M. *2017*, *Titan's atmosphere and climate*, Journal of Geophysical Research: Planets, 122, 432

Hubbard, W., Fortney, J., Lunine, J., et al. *2001*, *Theory of extrasolar giant planet transits*, The Astrophysical Journal, 560, 413

Hudson, R. L., & Gerakines, P. A. *2018*, *Infrared spectra and interstellar sulfur: New laboratory results for H2S and four malodorous thiol ices*, The Astrophysical Journal, 867, 138

Hudson, R. L., Gerakines, P. A., & Loeffler, M. J. *2015*, *Activation of weak IR fundamentals of two species of astrochemical interest in the T d point group–the importance of amorphous ices*, Physical Chemistry Chemical Physics, 17, 12545

Hudson, R. L., Gerakines, P. A., & Yarnall, Y. Y. *2022*, *Ammonia Ices Revisited: New IR Intensities and Optical Constants for Solid NH3*, The Astrophysical Journal, 925, 156

Hudson, R. L., Loeffler, M. J., & Gerakines, P. A. *2017*, *Infrared spectra and band strengths of amorphous and crystalline N2O*, The Journal of chemical physics, 146, 024304

Hueso, R., Guillot, T., & Sánchez-Lavega, A. *2020*, *Convective storms and atmospheric vertical structure in Uranus and Neptune*, Philosophical Transactions of the Royal Society A, 378, 20190476

Huston, T., Hisatsune, I. C., & Heicklen, J. *1983a*, *Condensed-phase reactions of O3 with NH3 and NH2OH*, Canadian journal of chemistry, 61, 2070

—. *1983b*, *Low-temperature infrared studies of some acid–base reactions*, Canadian journal of chemistry, 61, 2077

Jenniskens, P., & Blake, D. F. *1994*, *Structural transitions in amorphous water ice and astrophysical implications*, Science, 265, 753

Jewitt, D. C., & Luu, J. *2004*, *Crystalline water ice on the Kuiper belt object (50000) Quaoar*, Nature, 432, 731

Jiménez-Escobar, A., & Muñoz caro, G. M. *2011*, *Sulfur depletion in dense clouds and circumstellar regions-I. H2S ice abundance and UV-photochemical reactions in the H2O-matrix*, Astronomy & Astrophysics, 536, A91

Johnson, R. E., Burger, M. H., Cassidy, T. A., et al. *2009*, *Composition and detection of Europa's sputter-induced atmosphere*, Europa, University of Arizona Press, Tucson, 507

Johnson, R. E., Carlson, R. W., Cooper, J. F., et al. *2004*, *Radiation effects on the surfaces of the Galilean satellites*, Jupiter: The planet, satellites and magnetosphere, 485

Johnson, R. E., & Jesser, W. A. *1997*, *O2/O3 microatmospheres in the surface of Ganymede*, The Astrophysical Journal, 480, L79

Johnson, R. E., Quickenden, T. I., Cooper, P. D., McKinley, A. J., & Freeman, C. G. *2003*, *The production of oxidants in Europa's surface*, Astrobiology, 3, 823

Johnson, R. E., Luhmann, J. G., Tokar, R. L., et al. *2006*, *Production, ionization and redistribution of O2 in Saturn's ring atmosphere*, Icarus, 180, 393

Kaňuchová, Z., Boduch, P. H., Domaracka, A., et al. *2017*, *Thermal and energetic processing of astrophysical ice analogues rich in SO2*, Astronomy & Astrophysics, 604, A68

Kass, R. E., & Raftery, A. E. *1995*, *Bayes factors*, Journal of the american statistical association, 90, 773

Keller, W. E., & Halford, R. S. *1949*, *Motions of Molecules in Condensed Systems. IV. The Infra-Red Spectra for Ammonium Nitrate and Thallous Nitrate*, The Journal of Chemical Physics, 17, 26

Kempton, E. M. R., Lupu, R., Owusu-Asare, A., Slough, P., & Cale, B. *2017*, *Exo-Transmit: An Open-Source Code for Calculating Transmission Spectra for Exoplanet Atmospheres of Varied Composition*, , 129, 044402, doi: 10.1088/1538-3873/aa61ef

Kempton, E. M.-R., & Rauscher, E. *2012*, *Constraining high-speed winds in exoplanet atmospheres through observations of anomalous doppler shifts during transit*, The Astrophysical Journal, 751, 117

Khuntia, S., Majumder, S. K., & Ghosh, P. *2013*, *Removal of ammonia from water by ozone microbubbles*, Industrial & Engineering Chemistry Research, 52, 318

King, O., Fletcher, L. N., & Ligier, N. *2022*, *Compositional Mapping of Europa Using MCMC Modeling of Near-IR VLT/SPHERE and Galileo/NIMS Observations*, The Planetary Science Journal, 3, 72

King, T. V. V., Clark, R. N., Calvin, W. M., Sherman, D. M., & Brown, R. H. *1992*, *Evidence for ammonium-bearing minerals on Ceres*, Science, 255, 1551

Knop, O., & Glguère, P. A. *1959*, *Infrared spectrum of ammonium hydroperoxide*, Canadian Journal of Chemistry, 37, 1794

Knutson, H. A., Benneke, B., Deming, D., & Homeier, D. *2014*, *A featureless transmission spectrum for the Neptune-mass exoplanet GJ 436b*, Nature, 505, 66

Koskinen, T. T., Yelle, R. V., Snowden, D. S., et al. *2011*, *The mesosphere and lower thermosphere of Titan revealed by Cassini/UVIS stellar occultations*, Icarus, 216, 507

Kreidberg, L., Bean, J. L., Désert, J.-M., et al. *2014*, *Clouds in the atmosphere of the super-Earth exoplanet GJ 1214b*, Nature, 505, 69

Kruczkiewicz, F., Vitorino, J., Congiu, E., Theulé, P., & Dulieu, F. *2021*, *Ammonia snow lines and ammonium salts desorption*, Astronomy & Astrophysics, 652, A29

Kuo, C.-H., Yuan, F., & Hill, D. O. *1997*, *Kinetics of oxidation of ammonia in solutions containing ozone with or without hydrogen peroxide*, Industrial & Engineering Chemistry Research, 36, 4108

Lane, A. L., Nelson, R. M., & Matson, D. L. *1981*, *Evidence for sulphur implantation in Europa's UV absorption band*, Nature, 292, 38

Lanzerotti, L. J., Brown, W. L., Marcantonio, K. J., & Johnson, R. E. *1984*, *Production of ammonia-depleted surface layers on the saturnian satellites by ion sputtering*, Nature, 312, 139

Lavvas, P., Galand, M., Yelle, R. V., et al. *2011*, *Energy deposition and primary chemical products in Titan's upper atmosphere*, Icarus, 213, 233

Lavvas, P., & Koskinen, T. *2017*, *Aerosol Properties of the Atmospheres of Extrasolar Giant Planets*, The Astrophysical Journal, 847, 32

Lavvas, P., Koskinen, T., Steinrueck, M. E., Muñoz, A. G., & Showman, A. P. *2019*, *Photochemical Hazes in Sub-Neptunian Atmospheres with a Focus on GJ 1214b*, The Astrophysical Journal, 878, 118

Lavvas, P., Yelle, R. V., & Vuitton, V. *2009*, *The detached haze layer in Titan's mesosphere*, Icarus, 201, 626

Lavvas, P. P., Coustenis, A., & Vardavas, I. M. *2008*, *Coupling photochemistry with haze formation in Titan's atmosphere, part I: Model description*, Planetary and Space Science, 56, 27

Lee, A. Y. T., Yung, Y. L., Cheng, B.-M., et al. *2001*, *Enhancement of deuterated ethane on Jupiter*, The Astrophysical Journal Letters, 551, L93

Ligier, N., Paranicas, C., Carter, J., et al. *2019*, *Surface composition and properties of Ganymede: Updates from ground-based observations with the near-infrared imaging spectrometer SINFONI/VLT/ESO*, Icarus, 333, 496

Line, M. R., Knutson, H., Wolf, A. S., & Yung, Y. L. *2014*, *A Systematic Retrieval Analysis of Secondary Eclipse Spectra. II. A Uniform Analysis of Nine Planets and their C to O Ratios*, , 783, 70. `https://arxiv.org/abs/1309.6663`

Line, M. R., Teske, J., Burningham, B., Fortney, J. J., & Marley, M. S. *2015*, *Uniform atmospheric retrieval analysis of ultracool dwarfs. I. Characterizing benchmarks, Gl 570D and HD 3651B*, The Astrophysical Journal, 807, 183

Line, M. R., Stevenson, K. B., Bean, J., et al. *2016*, *No Thermal Inversion and a Solar Water Abundance for the Hot Jupiter HD209458b from HST WFC3 Emission Spectroscopy*, ArXiv e-prints. `https://arxiv.org/abs/1605.08810`

Littenberg, T. B., & Cornish, N. J. *2009*, *Bayesian approach to the detection problem in gravitational wave astronomy*, Physical Review D, 80, 063007

Llama, J., & Shkolnik, E. L. *2015*, *Transiting the Sun: the impact of stellar activity on X-ray and ultraviolet transits*, The Astrophysical Journal, 802, 41

Loeffler, M. J., & Hudson, R. L. *2010*, *Thermally-induced chemistry and the Jovian icy satellites: A laboratory study of the formation of sulfur oxyanions*, Geophysical research letters, 37

—. *2013*, *Low-temperature thermal reactions between SO2 and H2O2 and their relevance to the jovian icy satellites*, Icarus, 224, 257

—. *2015*, *Descent without modification? The thermal chemistry of H2O2 on Europa and other icy worlds*, Astrobiology, 15, 453

—. *2016*, *What is eating ozone? Thermal reactions between SO2 and O3: implications for icy environments*, The Astrophysical Journal Letters, 833, L9

Loeffler, M. J., Hudson, R. L., Chanover, N. J., & Simon, A. A. *2016a*, *The spectrum of Jupiter's Great Red Spot: The case for ammonium hydrosulfide (NH4SH)*, Icarus, 271, 265

Loeffler, M. J., Hudson, R. L., Moore, M. H., & Carlson, R. W. *2011*, *Radiolysis of sulfuric acid, sulfuric acid monohydrate, and sulfuric acid tetrahydrate and its relevance to Europa*, Icarus, 215, 370

Loeffler, M. J., Moore, M. H., & Gerakines, P. A. *2016b*, *The effects of experimental conditions on the refractive index and density of low-temperature ices: solid carbon dioxide*, The Astrophysical Journal, 827, 98

Loeffler, M. J., Raut, U., & Baragiola, R. A. *2006a*, *Enceladus: A source of nitrogen and an explanation for the water vapor plume observed by Cassini*, The Astrophysical Journal, 649, L133

—. *2010*, *Radiation chemistry in ammonia-water ices*, The Journal of chemical physics, 132, 054508

Loeffler, M. J., Raut, U., Vidal, R. A., Baragiola, R. A., & Carlson, R. W. *2006b*, *Synthesis of hydrogen peroxide in water ice by ion irradiation*, Icarus, 180, 265

Loeffler, M. J., Teolis, B. D., & Baragiola, R. A. *2006c*, *A model study of the thermal evolution of astrophysical ices*, The Astrophysical Journal Letters, 639, L103

Loeffler, M. J., Tribbett, P. D., Cooper, J. F., & Sturner, S. J. *2020*, *A possible explanation for the presence of crystalline H2O-ice on Kuiper Belt objects*, Icarus, 351, 113943

Lothringer, J. D., Fu, G., Sing, D. K., & Barman, T. S. *2020*, *UV Exoplanet Transmission Spectral Features as Probes of Metals and Rainout*, arXiv e-prints, arXiv:2005.02528. `https://arxiv.org/abs/2005.02528`

Lu, C.-S., & Lewis, O. *1972*, *Investigation of film-thickness determination by oscillating quartz resonators with large mass load*, J. Appl. Phys., 43, 4385

Lu, H.-C., Chen, H.-K., & Cheng, B.-M. *2004*, *Analysis of c2h4 in c2h6 and c2h5d with vuv absorption spectroscopy and a method to remove c2h4 from c2h6 and c2h5d*, Analytical chemistry, 76, 5965

Lundeen, J. W., & Tobias, R. S. *1975*, *Evidence for ion pairing and solvation from Raman spectra of solutions of ammonium, silver, potassium, sodium, and calcium nitrates in liquid ammonia*, The Journal of Chemical Physics, 63, 924

Lunine, J. I. *2010*, *Titan and habitable planets around M-dwarfs*, Faraday discussions, 147, 405

Macintosh, B., Graham, J. R., Ingraham, P., et al. *2014*, *First light of the Gemini Planet Imager*, , 111, 12661

Madhusudhan, N. *2019*, *Exoplanetary Atmospheres: Key Insights, Challenges, and Prospects*, , 57, 617, doi: 10.1146/annurev-astro-081817-051846

Mahjoub, A., & Hodyss, R. *2018*, *Thermal Reaction in Cometary and Pre-cometary Ices: Formation of Thiocarbamate in OCS-CH3NH2 Mixed Ices*, The Astrophysical Journal, 869, 98

Mark, G., Naumov, S., & von Sonntag, C. *2011*, *The reaction of ozone with bisulfide (HS-) in aqueous solution–mechanistic aspects*, Ozone: science & engineering, 33, 37

Mastrapa, R. M., Bernstein, M. P., Sandford, S. A., et al. *2008*, *Optical constants of amorphous and crystalline H2O-ice in the near infrared from 1.1 to 2.6 μm*, Icarus, 197, 307

Mayer, E., & Pletzer, R. *1986*, *Astrophysical implications of amorphous ice—a microporous solid*, Nature, 319, 298

McClintock, W. E., Lawrence, G. M., Kohnert, R. A., & Esposito, L. W. *1993*, *Optical design of the Ultraviolet Imaging Spectrograph for the Cassini mission to Saturn*, Optical Engineering, 32, 3038

McCord, T. B., Hansen, G. B., Clark, R. N., et al. *1998*, *Non-water-ice constituents in the surface material of the icy Galilean satellites from the Galileo near-infrared mapping spectrometer investigation*, Journal of Geophysical Research: Planets, 103, 8603

McGraw, G. E., Bernitt, D. L., & Hisatsune, I. C. *1965*, *Vibrational spectra of isotopic nitric acids*, The Journal of Chemical Physics, 42, 237

Meier, R. M. *2019*, Sputtering of Planetary Surfaces via Electron Irradiation, PhD thesis, Northern Arizona University

Meier, R. M., & Loeffler, M. J. *2020*, *Sputtering of water ice by keV electrons at 60 K*, Surf. Sci., 691, 121509

Mejía, C., de Barros, A. L. F., Duarte, E. S., et al. *2015*, *Compaction of porous ices rich in water by swift heavy ions*, Icarus, 250, 222

Mejía, C., de Barros, A. L. F., Rothard, H., Boduch, P., & da Silveira, E. F. *2020*, *Radiolysis of Ices by Cosmic-Rays: CH4 and H2O Ices Mixtures Irradiated by 40 MeV 58Ni11+ Ions*, The Astrophysical Journal, 894, 132

Mifsud, D. V., Kaňuchová, Z., Herczku, P., et al. *2021a*, *Sulfur Ice Astrochemistry: A review of laboratory studies*, Space Science Reviews, 217, 1

Mifsud, D. V., Juhász, Z., Herczku, P., et al. *2021b*, *Electron irradiation and thermal chemistry studies of interstellar and planetary ice analogues at the ICA astrochemistry facility*, The European Physical Journal D, 75, 1

Migliorini, A., Kanuchova, Z., Ioppolo, S., et al. *2022*, *On the origin of molecular oxygen on the surface of Ganymede*, Icarus, 115074

Milam, S. N., Stansberry, J. A., Sonneborn, G., & Thomas, C. *2016*, *The James Webb Space Telescope's plan for operations and instrument capabilities for observations in the solar system*, Publications of the Astronomical Society of the Pacific, 128, 018001

Miller, F. A., & Wilkins, C. H. *1952*, *Infrared spectra and characteristic frequencies of inorganic ions*, Analytical chemistry, 24, 1253

Moore, M. H., Ferrante, R. F., Hudson, R. L., & Stone, J. N. *2007a*, *Ammonia–water ice laboratory studies relevant to outer solar system surfaces*, Icarus, 190, 260

Moore, M. H., & Hudson, R. L. *2000*, *IR detection of H2O2 at 80 K in ion-irradiated laboratory ices relevant to Europa*, Icarus, 145, 282

Moore, M. H., Hudson, R. L., & Carlson, R. W. *2007b*, *The radiolysis of SO2 and H2S in water ice: Implications for the icy jovian satellites*, Icarus, 189, 409

Moran, S. E., Hörst, S. M., Vuitton, V., et al. *2020*, *Chemistry of Temperate Super-Earth and Mini-Neptune Atmospheric Hazes from Laboratory Experiments*, The Planetary Science Journal, 1, 17

Moudens, A., Georges, R., Goubet, M., et al. *2009*, *Direct absorption spectroscopy of water clusters formed in a continuous slit nozzle expansion*, The Journal of chemical physics, 131, 204312

Mousavipour, S. H., Mortazavi, M., & Hematti, O. *2013*, *Multichannel RRKM-TST and direct-dynamics CVT study of the reaction of hydrogen sulfide with ozone*, The Journal of Physical Chemistry A, 117, 6744

Muntean, E. A., Lacerda, P., Field, T. A., et al. *2016*, *A laboratory study of water ice erosion by low-energy ions*, Mon. Not. R. Astron. Soc., 462, 3361

Narten, A. H., Venkatesh, C.-G., & Rice, S. A. *1976*, *Diffraction pattern and structure of amorphous solid water at 10 and 77 K*, The Journal of Chemical Physics, 64, 1106

Noble, J. A., Theule, P., Borget, F., et al. *2013*, *The thermal reactivity of HCN and NH3 in interstellar ice analogues*, Monthly Notices of the Royal Astronomical Society, 428, 3262

Noble, J. A., Theule, P., Mispelaer, F., et al. *2012*, *The desorption of H2CO from interstellar grains analogues*, Astronomy & Astrophysics, 543, A5

Noll, K. S., Johnson, R. E., Lane, A. L., Domingue, D. L., & Weaver, H. A. *1996*, *Detection of ozone on Ganymede*, Science, 273, 341

Noll, K. S., Roush, T. L., Cruikshank, D. P., Johnson, R. E., & Pendleton, Y. J. *1997*, *Detection of ozone on Saturn's satellites Rhea and Dione*, Nature, 388, 45

Nordheim, T. A., Jasinski, J. M., & Hand, K. P. *2019*, *Galactic cosmic-ray bombardment of Europa's surface*, The Astrophysical Journal Letters, 881, L29

Olszyna, K. J., de Pena, R. G., Luria, M., & Heicklen, J. *1974*, *Kinetics of particle growth—IV: NH4NO3 from the NH3-O3 reaction revisited*, Journal of Aerosol Science, 5, 421

Olszyna, K. J., & Heicklen, J., The reaction of ozone with Ammonia. 1971, in Photochemical Smog and Ozone Reactions (ACS Publications)

Orlando, T. M., & Sieger, M. T. *2003*, *The role of electron-stimulated production of O2 from water ice in the radiation processing of outer solar system surfaces*, Surf. Sci., 528, 1

Oshagh, M., Santos, N. C., Ehrenreich, D., et al. *2014*, *Impact of occultations of stellar active regions on transmission spectra-Can occultation of a plage mimic the signature of a blue sky?*, Astronomy & Astrophysics, 568, A99

Palumbo, M. E. *2006*, *Formation of compact solid water after ion irradiation at 15 K*, Astronomy & Astrophysics, 453, 903

Palumbo, M. E., & Strazzulla, G. *2003*, *Nitrogen condensation on water ice*, Canadian journal of physics, 81, 217

Paranicas, C., Cooper, J. F., Garrett, H. B., Johnson, R. E., & Sturner, S. J., Europa's radiation environment and its effects on the surface. 2009, in Europa (University of Arizona Press Tucson), 529–544

Phillips, C. B., & Pappalardo, R. T. *2014*, *Europa Clipper mission concept: Exploring Jupiter's ocean moon*, Eos, Transactions American Geophysical Union, 95, 165

Plainaki, C., Milillo, A., Mura, A., et al. *2012*, *The role of sputtering and radiolysis in the generation of Europa exosphere*, Icarus, 218, 956

Poch, O., Istiqomah, I., Quirico, E., et al. *2020*, *Ammonium salts are a reservoir of nitrogen on a cometary nucleus and possibly on some asteroids*, Science, 367, eaaw7462

Podolak, M., Noy, N., & Bar-Nun, A. *1979*, *Photochemical aerosols in Titan's atmosphere*, Icarus, 40, 193

Pontoppidan, K. M., Pickering, T. E., Laidler, V. G., et al. *2016*, Pandeia: a multi-mission exposure time calculator for JWST and WFIRST, in Observatory Operations: Strategies, Processes, and Systems VI, Vol. 9910, International Society for Optics and Photonics, 991016

Poppe, A. R., Fatemi, S., & Khurana, K. K. *2018*, *Thermal and energetic ion dynamics in Ganymede's magnetosphere*, Journal of Geophysical Research: Space Physics, 123, 4614

Porco, C. C., Baker, E., Barbara, J., et al. *2005*, *Imaging of Titan from the Cassini spacecraft*, Nature, 434, 159

Potapov, A., Theulé, P., Jäger, C., & Henning, T. *2019*, *Evidence of surface catalytic effect on cosmic dust grain analogs: The ammonia and carbon dioxide surface reaction*, The Astrophysical Journal Letters, 878, L20

Prasad, S. S., & Tarafdar, S. P. *1983*, *UV radiation field inside dense clouds-Its possible existence and chemical implications*, The Astrophysical Journal, 267, 603

Quirico, E., & Schmitt, B. *1997*, *Near-Infrared Spectroscopy of Simple Hydrocarbons and Carbon Oxides Diluted in Solid N2and as Pure Ices: Implications for Triton and Pluto*, Icarus, 127, 354

Rackham, B. V., Apai, D., & Giampapa, M. S. *2018*, *The Transit Light Source Effect: False Spectral Features and Incorrect Densities for M-dwarf Transiting Planets*, , 853, 122, doi: 10.3847/1538-4357/aaa08c

Rages, K., & Pollack, J. B. *1983*, *Vertical distribution of scattering hazes in Titan's upper atmosphere*, Icarus, 55, 50

Raut, U., Famá, M., Loeffler, M. J., & Baragiola, R. A. *2008*, *Cosmic ray compaction of porous interstellar ices*, The Astrophysical Journal, 687, 1070

Raut, U., Famá, M., Teolis, B. D., & Baragiola, R. A. *2007a*, *Characterization of porosity in vapor-deposited amorphous solid water from methane adsorption*, The Journal of chemical physics, 127, 204713

Raut, U., Loeffler, M. J., Famá, M., & Baragiola, R. A. *2011*, *Photolysis of pure solid O3 and O2 films at 193 nm*, The Journal of chemical physics, 134, 194501

Raut, U., Teolis, B. D., Loeffler, M. J., et al. *2007b*, *Compaction of microporous amorphous solid water by ion irradiation*, The Journal of chemical physics, 126, 244511

Reding, F. P., & Hornig, D. F. *1957*, *Vibrational Spectra of Molecules and Complex Ions in Crystals. X. H2S and D2S*, The Journal of Chemical Physics, 27, 1024

Reimann, C. T., Boring, J. W., Johnson, R. E., et al. *1984*, *Ion-induced molecular ejection from D2O ice*, Surf. Sci., 147, 227

Ritzhaupt, G., & Devlin, J. P. *1977*, *Ionic vs. molecular nature of monomeric ammonium and hydronium nitrate. Infrared spectra of hydronium nitrate (H3O+ NO3-) and ammonium nitrate (NH4+ NO3-) solvated in argon matrices*, The Journal of Physical Chemistry, 81, 521

—. *1991*, *Infrared spectra of nitric and hydrochloric acid hydrate thin films*, The Journal of Physical Chemistry, 95, 90

Ritzhaupt, G., Smyrl, N., & Devlin, J. P. *1976*, *Vibrational spectra of glassy water aggregates and thin films*, The Journal of Chemical Physics, 64, 435

Rivkin, A. S., Marchis, F., Stansberry, J. A., et al. *2016*, *Asteroids and the James Webb Space Telescope*, Publications of the Astronomical Society of the Pacific, 128, 018003

Roberge, A., & Moustakas, L. A. *2018*, *The Large Ultraviolet/Optical/Infrared Surveyor*, Nature Astronomy, 2, 605, doi: 10.1038/s41550-018-0543-8

Robinson, T. D. *2017*, *A Theory of Exoplanet Transits with Light Scattering*, , 836, 236, doi: 10.3847/1538-4357/aa5ea8

Robinson, T. D., Fortney, J. J., & Hubbard, W. B. *2017*, *Analytic Scattering and Refraction Models for Exoplanet Transit Spectra*, , 850, 128, doi: 10.3847/1538-4357/aa951e

Robinson, T. D., Maltagliati, L., Marley, M. S., & Fortney, J. J. *2014*, *Titan solar occultation observations reveal transit spectra of a hazy world*, Proceedings of the National Academy of Sciences, 111, 9042

Rocard, F., Bénit, J., Bibrtng, J. P., Ledu, D., & Meunier, R. *1986*, *Erosion of ices: Physical and astrophysical discussion*, Radiation Effects, 99, 97

Rowland, B., Fisher, M., & Devlin, J. P. *1991*, *Probing icy surfaces with the dangling-OH-mode absorption: Large ice clusters and microporous amorphous ice*, The Journal of chemical physics, 95, 1378

Sandford, S. A., & Allamandola, L. J. *1993*, *H2 in interstellar and extragalactic ices-Infrared characteristics, ultraviolet production, and implications*, The Astrophysical Journal, 409, L65

Satorre, M., Leliwa-Kopystynski, J., Santonja, C., & Luna, R. *2013*, *Refractive index and density of ammonia ice at different temperatures of deposition*, Icarus, 225, 703

Sauder, D. G., Stephenson, J. C., King, D. S., & Casassa, M. P. *1992*, *Nascent product states in the photoinitiated reaction of O3 and H2O*, The Journal of chemical physics, 97, 952

Sceats, M. G., & Rice, S. A. *1982*, In Water: A Comprehensive Treatise, Volume 7; ; Franks, F., Ed, Plenum Press: New York

Schmitt, B., Quirico, E., Trotta, F., & Grundy, W. M., Optical properties of ices from UV to infrared. 1998, in Solar System Ices (Springer), 199–240

Schurath, U., Weber, M., & Becker, K. H. *1977*, *Electronic spectrum and structure of the HSO radical*, The Journal of Chemical Physics, 67, 110

Schutte, W. A., Boogert, A. C. A., Tielens, A. G. G. M., et al. *1999*, *Weak ice absorption features at 7.24 and 7.41 μm in the spectrum of the obscured young stellar object W 33A*, Astron. Ap., 343, 966

Seager, S., & Deming, D. *2010*, *Exoplanet atmospheres*, Annual Review of Astronomy and Astrophysics, 48, 631

Seager, S., & Sasselov, D. D. *2000*, *Theoretical transmission spectra during extrasolar giant planet transits*, The Astrophysical Journal, 537, 916

Sharma, S. *2017*, *Markov Chain Monte Carlo methods for Bayesian data analysis in astronomy*, Annual Review of Astronomy and Astrophysics, 55, 213

Shemansky, D. E., Stewart, A. I. F., West, R. A., et al. *2005*, *The Cassini UVIS stellar probe of the Titan atmosphere*, Science, 308, 978

Shi, J., Famá, M., Teolis, B. D., & Baragiola, R. A. *2010*, *Ion-induced electrostatic charging of ice*, Nucl. Instrum. Meth. B, 268, 2888

Shi, M., Baragiola, R. A., Grosjean, D. E., et al. *1995*, *Sputtering of water ice surfaces and the production of extended neutral atmospheres*, J. Geophys. Res. Planets, 100, 26387

Sieger, M. T., Simpson, W. C., & Orlando, T. M. *1998*, *Production of O 2 on icy satellites by electronic excitation of low-temperature water ice*, Nature, 394, 554

Sigmund, P. *1969*, *Theory of sputtering. I. Sputtering yield of amorphous and polycrystalline targets*, Phys. Rev., 184, 383

Simon-Miller, A. A., Conrath, B., Gierasch, P. J., & Beebe, R. F. *2000*, *A detection of water ice on Jupiter with Voyager IRIS*, Icarus, 145, 454

Sing, D. K., Pont, F., Aigrain, S., et al. *2011*, *Hubble Space Telescope transmission spectroscopy of the exoplanet HD 189733b: high-altitude atmospheric haze in the optical and near-ultraviolet with STIS*, Monthly Notices of the Royal Astronomical Society, 416, 1443

Sing, D. K., Fortney, J. J., Nikolov, N., et al. *2016*, *A continuum from clear to cloudy hot-Jupiter exoplanets without primordial water depletion*, , 529, 59, doi: 10.1038/nature16068

Sing, D. K., Lavvas, P., Ballester, G. E., et al. *2019*, *The Hubble Space T elescope PanCET Program: Exospheric Mg ii and Fe ii in the Near-ultraviolet Transmission Spectrum of WASP-121b Using Jitter Decorrelation*, The Astronomical Journal, 158, 91

Singer, P. C., & Zilli, W. B. *1975*, *Ozonation of ammonia in wastewater*, Water Research, 9, 127

Singer, R. B., McCord, T. B., Clark, R. N., Adams, J. B., & Huguenin, R. L. *1979*, *Mars surface composition from reflectance spectroscopy: A summary*, Journal of Geophysical Research: Solid Earth, 84, 8415

Singh, S. K., Bergantini, A., Zhu, C., et al. *2021*, *Origin of ammoniated phyllosilicates on dwarf planet Ceres and asteroids*, Nature Communications, 12, 2690

Smardzewski, R. R. *1978*, *Chemiluminescent matrix reactions of atomic oxygen, sulfur, and O (3 P)+ H2S*, The Journal of Chemical Physics, 68, 2878

Smardzewski, R. R., & Lin, M.-C. *1977*, *Matrix reactions of oxygen atoms with H2S molecules*, The Journal of chemical physics, 66, 3197

Smith, R. H., Leu, M. T., & Keyser, L. F. *1991*, *Infrared spectra of solid films formed from vapors containing water and nitric acid*, The Journal of Physical Chemistry, 95, 5924

Snellen, I. A. G., De Kok, R. J., De Mooij, E. J. W., & Albrecht, S. *2010*, *The orbital motion, absolute mass and high-altitude winds of exoplanet HD 209458b*, Nature, 465, 1049

Sori, M. M., Bapst, J., Bramson, A. M., Byrne, S., & Landis, M. E. *2017*, *A Wunda-full world? Carbon dioxide ice deposits on Umbriel and other Uranian moons*, Icarus, 290, 1

Spencer, J. R., & Calvin, W. M. *2002*, *Condensed O2 on Europa and Callisto*, The Astronomical Journal, 124, 3400

Spencer, J. R., Tamppari, L. K., Martin, T. Z., & Travis, L. D. *1999*, *Temperatures on Europa from Galileo photopolarimeter-radiometer: nighttime thermal anomalies*, Science, 284, 1514

Spudis, P. D., Bussey, D. B. J., Baloga, S. M., et al. *2013*, *Evidence for water ice on the Moon: Results for anomalous polar craters from the LRO Mini-RF imaging radar*, Journal of Geophysical Research: Planets, 118, 2016

Squyres, S. W. *1980*, *Surface temperatures and retention of H2O frost on Ganymede and Callisto*, Icarus, 44, 502

Stern, S. A., Mullhaupt, J. T., & Kay, W. B. *1960*, *The Physicochemical Properties of Pure Nitric Acid.*, Chemical Reviews, 60, 185

Stern, S. A., Weintraub, D. A., & Festou, M. C. *1993*, *Evidence for a low surface temperature on Pluto from millimeter-wave thermal emission measurements*, Science, 261, 1713

Stevenson, K. B., Harrington, J., Nymeyer, S., et al. *2010*, *Possible thermochemical disequilibrium in the atmosphere of the exoplanet GJ 436b*, , 464, 1161. https://arxiv.org/abs/1010.4591

Stevenson, K. P., Kimmel, G. A., Dohnalek, Z., Smith, R. S., & Kay, B. D. *1999*, *Controlling the morphology of amorphous solid water*, Science, 283, 1505

Strazzulla, G., Garozzo, M., & Gomis, O. *2009*, *The origin of sulfur-bearing species on the surfaces of icy satellites*, Advances in space research, 43, 1442

Strobel, D. F. *2006*, *Gravitational tidal waves in Titan's upper atmosphere*, Icarus, 182, 251

Swain, M. R., Vasisht, G., & Tinetti, G. *2008*, *The presence of methane in the atmosphere of an extrasolar planet*, , 452, 329

Taylor, J. 1997, Introduction to error analysis, the study of uncertainties in physical measurements

Teolis, B. D., Famá, M., & Baragiola, R. A. *2007a*, *Low density solid ozone*, The Journal of chemical physics, 127, 074507

Teolis, B. D., Loeffler, M. J., Raut, U., Fama, M., & Baragiola, R. A. *2006*, *Ozone synthesis on the icy satellites*, The Astrophysical Journal Letters, 644, L141

Teolis, B. D., Loeffler, M. J., Raut, U., Famá, M., & Baragiola, R. A. *2007b*, *Infrared reflectance spectroscopy on thin films: Interference effects*, Icarus, 190, 274

Teolis, B. D., Plainaki, C., Cassidy, T. A., & Raut, U. *2017*, *Water ice, O2, H2 and H2O2 radiolysis and sputtering yields for any projectile species, energy or temperature: a model for icy astrophysical bodies*, J. Geophys. Res., Planets, 122, 1996

Teolis, B. D., Shi, J., & Baragiola, R. A. *2009*, *Formation, trapping, and ejection of radiolytic O 2 from ion-irradiated water ice studied by sputter depth profiling*, J. Chem. Phys., 130, 134704

Teolis, B. D., Vidal, R. A., Shi, J., & Baragiola, R. A. *2005*, *Mechanisms of O2 sputtering from water ice by keV ions*, Phys. Rev. B, 72, 245422

Teolis, B. D., Jones, G. H., Miles, P. F., et al. *2010*, *Cassini finds an oxygen–carbon dioxide atmosphere at Saturn's icy moon Rhea*, Science, 330, 1813

Theoret, A., & Sandorfy, C. *1964*, *Infrared spectra and crystalline phase transitions of ammonium nitrate*, Canadian Journal of chemistry, 42, 57

Theulé, P., Duvernay, F., Danger, G., et al. *2013*, *Thermal reactions in interstellar ice: A step towards molecular complexity in the interstellar medium*, Advances in Space Research, 52, 1567

Tielens, A. G. G. M. 2005, The physics and chemistry of the interstellar medium (Cambridge University Press)

Tinetti, G., Vidal-Madjar, A., Liang, M.-C., et al. *2007*, *Water vapour in the atmosphere of a transiting extrasolar planet*, Nature, 448, 169

Toublanc, D., Parisot, J. P., Brillet, J., et al. *1995*, *Photochemical modeling of Titan's atmosphere*, Icarus, 113, 2

Tremaine, S., Gebhardt, K., Bender, R., et al. *2002*, *The slope of the black hole mass versus velocity dispersion correlation*, The Astrophysical Journal, 574, 740

Tribbett, P. D., & Loeffler, M. J. *2021*, *The sputtering of radiolytic O2 in ion irradiated H2O-ice*, Surface Science, 707, 121797

—. *2022*, *Thermal Reactions between H2S and O3: Implications for Europa Surface chemistry*, Planetary Science Journal, 3, 233 (8pp)

Tribbett, P. D., Tegler, S. C., & Loeffler, M. J. *2021*, *Probing Microporous ASW with Near-infrared Spectroscopy: Implications for JWST's NIRSpec*, The Astrophysical Journal, 915, 40

Trotta, R. *2008*, *Bayes in the sky: Bayesian inference and model selection in cosmology*, Contemporary Physics, 49, 71

Trumbo, S. K., Brown, M. E., & Adams, D. *2021*, *The Geographic Distribution of Dense-phase O2 on Ganymede*, The Planetary Science Journal, 2, 139

Tsiaras, A., Waldmann, I. P., Tinetti, G., Tennyson, J., & Yurchenko, S. N. *2019*, *Water vapour in the atmosphere of the habitable-zone eight-Earth-mass planet K2-18 b*, Nature Astronomy, 3, 1086, doi: 10.1038/s41550-019-0878-9

Verbiscer, A. J., Peterson, D. E., Skrutskie, M. F., et al. *2006*, *Near-infrared spectra of the leading and trailing hemispheres of Enceladus*, Icarus, 182, 211

Vidal, R. A., Bahr, D., Baragiola, R. A., & Peters, M. *1997*, *Oxygen on Ganymede: laboratory studies*, Science, 276, 1839

Vidal, R. A., Teolis, B. D., & Baragiola, R. A. *2005*, *Angular dependence of the sputtering yield of water ice by 100 keV proton bombardment*, Surf. Sci., 588, 1

Vincendon, M., Forget, F., & Mustard, J. *2010*, *Water ice at low to midlatitudes on Mars*, Journal of Geophysical Research: Planets, 115

Voronin, A. A., & Zheltikov, A. M. *2017*, *The generalized Sellmeier equation for air*, Scientific reports, 7, 46111

Vuitton, V., Yelle, R. V., & Lavvas, P. *2009*, *Composition and chemistry of Titan's thermosphere and ionosphere*, Philosophical Transactions of the Royal Society A: Mathematical, Physical and Engineering Sciences, 367, 729

Vyazovkin, S. O., & Wight, C. A. *1997*, *Kinetics in solids*, Annual review of physical chemistry, 48, 125

Waite, J. H., Combi, M. R., Ip, W.-H., et al. *2006*, *Cassini ion and neutral mass spectrometer: Enceladus plume composition and structure*, science, 311, 1419

Wakeford, H. R., Sing, D. K., Stevenson, K. B., et al. *2020*, Into the UV: A precise transmission spectrum of HAT-P-41b using Hubble's WFC3/UVIS G280 grism. https://arxiv.org/abs/2003.00536

Waldron, R. D., & Hornig, D. F. *1953*, *Infrared spectra and structure of crystalline ammonia hydrates*, Journal of the American Chemical Society, 75, 6079

Warren, S. G., & Brandt, R. E. *2008*, *Optical constants of ice from the ultraviolet to the microwave: A revised compilation*, Journal of Geophysical Research: Atmospheres, 113

Watkins, C., & Cho, J. Y. K. *2010*, *Gravity waves on hot extrasolar planets. i. propagation and interaction with the background*, The Astrophysical Journal, 714, 904

Webber, W. R., & Yushak, S. M. *1983*, *A measurement of the energy spectra and relative abundance of the cosmic-ray H and He isotopes over a broad energy range*, The Astrophysical Journal, 275, 391

Wen, L., Chen, J., Yang, L., et al. *2015*, *Enhanced formation of fine particulate nitrate at a rural site on the North China Plain in summer: The important roles of ammonia and ozone*, Atmospheric Environment, 101, 294

West, R. A., Balloch, J., Dumont, P., et al. *2011*, *The evolution of Titan's detached haze layer near equinox in 2009*, Geophysical Research Letters, 38

West, R. A., Seignovert, B., Rannou, P., et al. *2018*, *The seasonal cycle of Titan's detached haze*, Nature Astronomy, 2, 495

Westley, M. S., Baratta, G. A., & Baragiola, R. A. *1998*, *Density and index of refraction of water ice films vapor deposited at low temperatures*, The Journal of chemical physics, 108, 3321

Weston Jr, R. E., & Brodasky, T. F. *1957*, *Infrared spectrum and force constants of the nitrite ion*, The Journal of Chemical Physics, 27, 683

Whittet, D. C. B., Schutte, W. A., Tielens, A. G. G. M., et al. *1996*, *An ISO SWS view of interstellar ices: first results.*, Astronomy and Astrophysics, 315, L357

Wiener, R. N., & Nixon, E. R. *1956*, *Infrared spectrum of solid sulfur dioxide*, The Journal of Chemical Physics, 25, 175

Wood, B. E., & Roux, J. A. *1982*, *Infrared optical properties of thin H 2 O, NH 3, and CO 2 cryofilms*, JOSA, 72, 720

Wu, C. Y. R., Chen, F. Z., & Judge, D. L. *2001*, *Measurements of temperature-dependent absorption cross sections of C2H2 in the VUV-UV region*, Journal of Geophysical Research: Planets, 106, 7629

—. *2004*, *Temperature-dependent photoabsorption cross sections in the VUV-UV region: Ethylene*, Journal of Geophysical Research: Planets, 109

Yarnall, Y. Y., & Hudson, R. L. *2022a*, *Crystalline ices–Densities and comparisons for planetary and interstellar applications*, Icarus, 373, 114799

—. *2022b*, *A New Method for Measuring Infrared Band Strengths in H2O Ices: First Results for OCS, H2S, and SO2*, The Astrophysical Journal Letters, 931, L4

Young, L. A., Kammer, J. A., Steffl, A. J., et al. *2018*, *Structure and composition of Pluto's atmosphere from the New Horizons solar ultraviolet occultation*, Icarus, 300, 174

Yung, Y. L., Allen, M., & Pinto, J. P. *1984*, *Photochemistry of the atmosphere of Titan: Comparison between model and observations*, Astrophysical Journal Supplement Series, 55, 465

Zhang, R., Wooldridge, P. J., Abbatt, J. P. D., & Molina, M. J. *1993*, *Physical chemistry of the sulfuric acid/water binary system at low temperatures: stratospheric implications*, The Journal of Physical Chemistry, 97, 7351

Zheng, W., Jewitt, D., & Kaiser, R. I. *2006*, *Formation of hydrogen, oxygen, and hydrogen peroxide in electron-irradiated crystalline water ice*, The Astrophysical Journal, 639, 534

—. *2009*, *On the state of water ice on Saturn's moon Titan and implications to icy bodies in the outer solar system*, The Journal of Physical Chemistry A, 113, 11174

Zheng, W., & Kaiser, R. I. *2007*, *On the formation of carbonic acid (H2CO3) in solar system ices*, Chemical Physics Letters, 450, 55

Ziegler, J. F., Ziegler, M. D., & Biersack, J. P. *2010*, *SRIM–The stopping and range of ions in matter (2010)*, Nuclear Instruments and Methods in Physics Research Section B: Beam Interactions with Materials and Atoms, 268, 1818